Beyond Lithium: Atomic-Scale Insights into Cathode Materials for Sodium and Magnesium Rechargeable Batteries

Heath, Jenny

Award date:
2018

Awarding institution:
University of Bath

BEYOND LITHIUM: ATOMIC-SCALE INSIGHTS INTO CATHODE MATERIALS FOR SODIUM AND MAGNESIUM RECHARGEABLE BATTERIES

Submitted by

Jennifer Heath

for the degree of Doctor of Philosophy of the

University of Bath

Department of Chemistry

October 2017

COPYRIGHT

Signature of Author: .....

Table of Contents

List of Figures

List of Tables

List of Publications and Presentations

Publications

- C. Tealdi, J. Heath, M. S. Islam, Feeling the strain: enhancing ionic transport in olivine phosphate cathodes for Li- and Na-ion batteries through strain effects, *J. Mater. Chem. A*, **2016**, 4, 6998-7004.

- J. Heath, H. Chen, M. S. Islam, $MgFeSiO_4$ as a potential cathode material for magnesium batteries: ion diffusion rates and voltage trends, *J. Mater. Chem. A*, **2017**, 5, 13161-13167.

- N. Tapia-Ruiz, W. M. Dose, N. Sharma, H. Chen, J. Heath, J. Somerville, U. Maitra, M. S. Islam and P. G. Bruce, High voltage P2-$Na_{2/3}Ni_{1/3-x}Mg_xMn_{2/3}O_2$ ($0 < x < 0.20$) cathodes; insights from neutron and in-situ X-ray diffraction, electrochemical and computational studies, *Energy Environ. Sci.*, **2017** (Submitted).

Oral Presentations

- **June 2017** Solid State Ionics 2017, Padua, Italy, "Olivine-type Cathode Materials for Li^+, Na^+ and Mg^{2+} Batteries: Strain Effects and Ionic Transport"

- **June 2017** Bolland Symposium 2017, University of Bath, "Beyond Lithium? Atomic-Scale Insights into Polyanion Cathode Materials for Na+ and Mg2+ Rechargeable Batteries."
- **December 2016** RSC Annual Solid State Group Meeting, Loughborough University, "Beyond Lithium Atomic-Scale Insights into Polyanion Cathode Materials for Na^{+} and Mg^{2+} Rechargeable Batteries." (**Prize Winner**)
- **April 2016** Advances in Lithium Batteries 2016, University of Bath, "Feeling the Strain: Enhancing Ionic Transport in Li and Na Battery Materials through Strain Effects."
- **September 2015** South West Computational Chemistry Meeting, University of Bristol, "$NaFePO_4$ Cathodes for Sodium Batteries: Why is Olivine More Promising Than Maricite?"

Poster Presentations

- **September 2017** Energy Materials Computational Solutions Symposium, University of Bath (**Flash Presentation Prize Winner**)
- **September 2016** Energy Materials Computational Solutions Symposium, University of Bath
- **June 2016** 17^{th} International Meeting on Lithium Batteries, Chicago, USA
- **September 2015** Energy Materials Computational Solutions Symposium, University of Bath
- **July 2015** CCP5 Methods in Molecular Simulations Summer School, University of Manchester
- **June 2015** Lithium Battery Discussion, Arcachon, France
- **June 2015** Graduate School Research Afternoon, University of Bath
- **June 2015** HPC Conference, University of Bath

- **May 2015** Postgraduate Symposium, University of Bath (**Prize Winner**)
- **March 2015** STFC Early Career Researchers Conference, Abingdon (**Prize Winner**)
- **December 2014** RSC Annual Solid State Group Meeting, University of Glasgow

Abstract

The importance of energy storage worldwide is increasing with the use of renewable energy sources and electric vehicles. With the intermittent nature of wind and solar power, large-scale grid storage is an extremely important progression needed to reduce the use of fossil fuels. For this to become a reality, rechargeable batteries beyond existing Li-ion technologies need consideration. The development of such batteries requires improvement of understanding their component materials. Modern computer modelling techniques enable valuable insights into the fundamental defect, ion transport and voltage properties of battery materials at the atomic level. Atomistic simulation and *ab initio* density functional theory (DFT) techniques have been used to study a number of potential cathode materials for Na-ion and Mg batteries. Firstly, the olivine and maricite forms of $NaFePO_4$ are considered in terms of their defect formation energies and Na ion diffusion. The atomistic study indicates that anti-site disorder is the most favourable type of intrinsic defect. The activation energies for Na-ion migration in the olivine and maricite materials are 0.4 eV and 1.6 – 1.8 eV respectively. Moreover, molecular dynamics (MD) studies reveal that there is only substantial Na-ion diffusion in the olivine structure, with diffusion coefficients (D_{Na}) at 300 K of 7 x 10^{-13} cm^2s^{-1} for maricite and 4 x 10^{-9} cm^2s^{-1} for olivine $NaFePO_4$. The presence of anti-site defects is shown to decrease Na^+ diffusion within the olivine structure, which is of relevance to its rate behaviour. Secondly, the effect of lattice strain on ion transport and defect formation in olivine-type $LiFePO_4$ and $NaFePO_4$ is investigated as a means to enhance their ion conduction properties. It is predicted that lattice strain can have a remarkable effect on the rate performance of olivine cathode materials,

with a major increase in ionic conductivity and decrease in blocking defects at room temperature. Thirdly, DFT techniques have been used to examine surface and grain boundary formation in P2-$NaCoO_2$. The coordination loss experienced by ions present at surfaces is found to influence the resulting surface energy. Layered oxide cathode materials were further investigated by considering the effect of Mg^{2+} doping on P2-$Na_{\frac{2}{3}}[Ni_{\frac{1}{3}}Mn_{\frac{2}{3}}]O_2$. Na vacancy formation energies decreased with 10% Mg^{2+} doping on the Ni site and an increase in Na diffusion was predicted with MD calculations. This positive effect on Na ion conductivity is caused by displacement of the Mg ions from the transition metal layer and the resulting change in electrostatic potential. Finally, Mg ion conduction, doping and voltage behaviour of $MgFeSiO_4$ were studied. The Mg-ion migration activation energy is relatively low for an olivine-type silicate, and MD simulations predict a diffusion coefficient (D_{Mg}) of 10^{-9} cm^2s^{-1}, suggesting favourable electrode kinetics. Partial substitution of Fe by Co or Mn could increase the cell voltage from 2.3 V vs Mg/Mg^{2+} to 2.8 - 3.0 V.

Acknowledgements

'It was like having friends'

J. K. Rowling, Harry Potter and the Half Blood Prince

I would firstly like to extend my greatest thanks to Prof. Saiful Islam for giving me the opportunity to undertake this PhD and his continued support and expertise along the way.

It has been a privilege to work along side the other members of the MSI group (including, but not exclusively: Chris Eames, Stephen Wood, Hungru Chen, Phil Walsh Atkins, James Dawson, Piero Canepa, Jessica Dillon and Eszter Makkos), without whom my experience in the group would no doubt have been considerably less enjoyable and much more difficult without their support academically and personally. I would like to give special thanks to Chris Eames, who had the patience to set me up way back when I was lowly MChem student and without whom I am not sure I would ever have got my head around using the computers. Also special thanks to Jessica Dillon and Phil Walsh Atkins, who I will always consider more as friends than colleagues, who have been there with a supportive cup of tea when things were going wrong and the near constant supply of snacks that they provided.

Last, but by no means least I would like to give my warmest thanks to Ryan and my family. All of whom have been there to support and believe in me when I thought I wasn't capable of completing this work. Ryan thank you for spending weekends listening to practice presentations, rescuing me from the airport after disastrous conference travels and making sure my scientific ramblings were in

'proper' English. This research would not have been possible without all the personal and financial support my parents have given me over the years I cannot express how grateful I am. Thank you.

1 | Introduction

'Understanding is the first step to acceptance'

J. K. Rowling, Harry Potter and the Goblet of Fire

1.1 Background: Energy Storage

The importance of energy storage has grown to an unprecedented level in today's increasingly technologically driven, highly mobile and energy demanding society. The development of rechargeable battery technologies has been primarily influenced by the portable electronics industry, aerospace and military applications and as energy sources for electric vehicles. While these applications for battery systems will remain, pressing needs regarding the efficient use of renewable energy resources in order to reduce fossil fuel consumption have contributed to battery research in recent years.[2,3]

Increasing use of renewable energy sources, such as wind and solar power, bring problems with modulating the resources over time and integrating them into the grid smoothly and safely. It is also important to balance electricity generation and demand between daytime and night-time in order to optimise grid utilisation. Therefore, large-scale energy storage is extremely important to shift electrical energy from peak to off-peak periods. Among the various storage technologies proposed for renewable energy applications, secondary batteries appear to be one of the most promising means for storing electricity on a large

scale because of its flexibility and high energy conversion.[4,5]

Fossil fuel consumption of internal combustion engines gives rise to environmental pollution, resulting in an urgent need for the development of hybrid electric vehicles (HEVs), plug-in hybrid electric vehicles (PHEVs) and electric vehicles (EVs); research into secondary lithium-ion batteries is crucial in the development of these alternatives to petrol and diesel cars, as high energy and power density batteries are required.[3,6]

The limitation of lithium resources, increased cost of mining and reliance on foreign imports have made it necessary to explore alternative battery technologies. Sodium-ion batteries have gained interest in this area as they offer a similar chemistry to lithium-ion systems, since sodium behaves in a comparable way to lithium, but is a much more abundant metal and is therefore lower in cost. Although sodium-ion batteries are a promising alternative, they suffer two major issues when compared with their lithium counterparts. Firstly, Na has a lower ionisation potential than Li, resulting in lower energy densities for sodium-ion batteries. Secondly, Na^+ ions have a larger ionic radius and are heavier than Li^+ ions, which may lead to slower ion diffusion and large volume changes on cycling of the electrode. Despite these factors, sodium-ion batteries would be an optimal choice for use in large scale energy storage systems, where their lower gravimetric capacity is less important, as they could offer cells which are low in cost and long life. The differences between lithium-ion and sodium-ion chemistries also mean that new crystalline solids can be explored to facilitate the intercalation/deintercalation process of the larger ions.[3,4,7–12]

Secondary batteries based on divalent ions, such as magnesium, are also under consideration as alternatives to Li-ion technologies. While the development of these cells is still in its infancy compared to Li-ion batteries, the prospects of increased energy density and the ability to use a metal anode make magnesium batteries promising for future commercial use. However, there are a number of challenges which need to be overcome before this is a possibility, including the development of a suitable cathode material as Mg^{2+} suffers from slow diffusion through more conventional insertion compounds.[13–16]

This introduction chapter will first outline the components and materials in lithium-ion batteries, followed by details on sodium-ion and magnesium battery materials, including the compounds examined in this work.

1.2 Lithium-ion Batteries

Lithium is the most electropositive and lightest metal in the periodic table, meaning it is an ideal component of high energy density rechargeable batteries.[17] Lithium batteries were first developed in the 1950s, after the stability of Li metal in aqueous electrolytes was discovered. These cells were commercialised by the early 1970s for low power applications such as powering watches and calculators. Unsurprisingly, the development of secondary lithium-ion cells was a longer process. Initial cells were based on a Li metal anode, however these were ultimately rejected due to safety concerns caused by dendrite growth on the metal surface.[2] Advances in intercalation compounds led to the development of the first commercial rechargeable lithium-ion battery, the SONY cell, in 1991. This technology was based on the realisation that layered metal oxides could be used as viable electrodes. This cell consisted of a $LiCoO_2$ cathode, a carbon anode and an electrolyte of $LiPF_6$ dissolved in a mixture of organic solvents.[17]

A schematic representation of a standard lithium-ion battery is shown in Figure 1.1. The charging process of a cell such as this forces Li^+ ions to be extracted from the cathode. These ions diffuse through the electrolyte and intercalate between the sheets of the graphite anode. During discharge this process is reversed. Li^+ ions return to the cathode via the electrolyte while electrons pass around an external circuit providing power.

The following sections provide an overview of the three main components of a Li-ion battery and their roles within the cell. As the research presented here focuses on cathode materials these are covered in more detail.

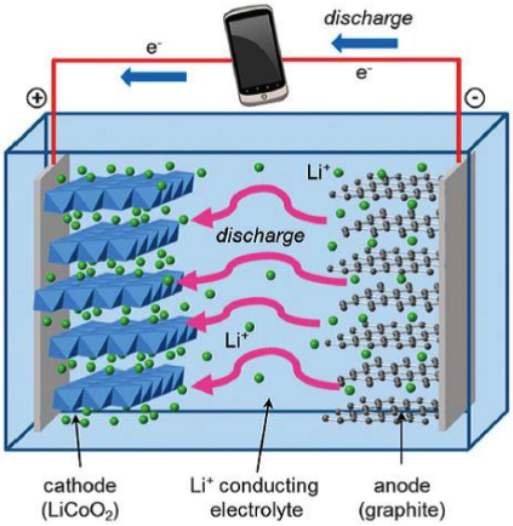

Figure 1.1: *Schematic of a typical rechargeable lithium-ion battery with a $LiCoO_2$ cathode and graphite anode. During charging, Li^+ ions flow to the anode through electrolyte and electrons travel through the external circuit.*[18]

1.3 Electrolyte Materials

The two electrodes in each battery cell must be kept physically separated in order to prevent short circuiting. This is achieved through the use of a porous separator material which allows the flow of lithium ions throughout. The electrolyte is needed to facilitate the movement of lithium ions, not just between the cathode and anode but also through the separator. Therefore the electrolyte needs to be a good ionic conductor but also an electronic insulator otherwise the cell would short circuit.[19]

Conventional lithium-ion batteries contain electrolytes consisting of $LiPF_6$ dissolved in a mixture of organic solvents, since these solutions are compatible with the battery voltage operation window and offer high ionic conductivities. Although the specific mixture of organic solvents used depends on the manufacturer of the battery, ethylene carbonate (EC) is always present. EC is critical for the reversibility of the reaction at the anode; it decomposes on the graphite surface forming a solid electrolyte interface (SEI); a crucial layer that prevents other solvent molecules from co-intercalating with lithium in the

graphite layers.[20]

These typical organic-based electrolytes are thermodynamically stable up to 3.5 V, above this the electrolyte decomposes. Luckily the decomposition process is kinetically controlled, meaning that in practice, cells containing these electrolytes are able to operate at voltages as high as 5.5 V. Even though the process of electrolyte decomposition is slow, it still happens continuously throughout the lifetime of the cell, causing a gradual depletion in performance.[17]

Safety concerns over the use of organic-based liquid electrolytes has led to specific interest in the development of all-solid-state batteries.

1.4 Anode Materials

Li metal was initially thought to be the ideal anode material for Li-ion cells; Li being both the lightest and most electropositive metal facilitated the design of systems with high energy densities. Li metal was initially utilised in a cell along with a TiS_2 cathode. While impeccable operation was displayed at the cathode the cell was not viable. Use of a Li-metal anode along with a liquid electrolyte caused uneven dendrites to form with each charge/discharge cycle; these dendrites were able to penetrate the electrolyte solution and cause the battery to short circuit, leading to major concerns with safety and performance.[17,21,22]

Anode materials in all currently commercially available Li-ion batteries are carbonaceous; but even if these compounds have the same chemical formula, they do not always display the same characteristics. The intercalation process is strongly influenced by their surface area, morphology and crystallinity.[20] When these carbon compounds reversibly intercalate Li ions, the compound LiC_6 is formed, with storage capabilities between 340 mAh and 770 mAh g^{-1}. These values represent a severe storage limitation when compared to Li metal, which has a storage capacity of 3800 Ah kg^{-1}.[21] However, carbon-based cathodes do offer advantages in their use; they are both cheap and readily available and offer excellent electronic conduction properties. Despite the advantages of carbon anodes, research has focused on developing anodes with higher capacities, a few

of which are discussed below.

Metal oxides have been extensively researched as potential anode materials for rechargeable Li-ion batteries due to their ability to deliver high reversible capacities between 500 and 1000 mAh g^{-1}.[23–27] These oxide materials are classified by their reaction mechanisms. One oxide material which has been considered the most important Li-alloy reaction material is SnO_2. The lithium-alloy reaction mechanism is described in equations 1.1 and 12, below.

$$M_xO_y + 2\,yLi^+ + 2\,ye^- \rightleftharpoons xM + yLi_2O \tag{1.1}$$

$$M + zLi^+ + ye^- \rightleftharpoons Li_zMO_x \tag{1.2}$$

Despite the high theoretical capacity of SnO_2 (783 mAh g^{-1}) problems occur when it is cycled continuously.[28–31] Aggregates that form from the delithiation of the Li-Sn alloy cause fast deterioration in the reversible capacity. Developments have been made to improve the cycling performance of SnO_2, including the formation of porous nanostructures, nanocomposites and nanostructured thin films.[32]

Transition metal oxides that store Li via the insertion mechanism (equation 1.3) are attractive anode materials for rechargeable Li-ion batteries due to their low cost and non-toxicity. However, insertion reaction-based oxides have relatively low specific capacities as the number of electrons typically involved in the insertion mechanism is less than one per lithium.

$$MO_x + yLi^+ + ye^- \rightleftharpoons Li_yMO_x \tag{1.3}$$

TiO_2 has been extensively researched as a potential insertion based anode. This material can behave as a low voltage Li-insertion host and also displays fast Li insertion/extraction kinetics.[32] However, TiO_2 suffers from the major drawback of a lower rate capacity than other comparative materials.[33]

1.5 Cathode Materials

Cathode materials are often considered to be the limiting factor in the development of Li-ion batteries. This is because the range of cathode materials available typically do not offer capacities as high as the range of anodes available.[17]

Since rechargeable Li-ion batteries have been commercially available, there have been three main cathode materials that have dominated. These are $LiMO_2$ layered oxides, $LiMn_2O_4$ spinel and olivine $LiFePO_4$.

1.5.1 $LiMO_2$ Layered Oxides

The first commercial rechargeable Li-ion battery (the SONY cell) contained a $LiCoO_2$ cathode coupled with a graphite anode. It was recorded as having a potential of 4 V and a capacity of 130 mAh g^{-1}.[19] The availability of cobalt is limited, meaning that cells based on $LiCoO_2$ are limited to small-scale use, such as in portable laptop computers and mobile phones. If battery technologies are to be scaled up for use in HEVs or grid-scale storage, cathode materials utilising other transition metals must be used.[17,19]

$LiCoO_2$ adopts a layered structure, shown in Figure 1.2. Co^{3+} ions occupy octahedral sites between adjacent layers of oxide ions. Alternative sheets are occupied by the transition metal ions and the remaining sheets are occupied by Li^+ ions. The structure adopts a distorted rhombohedral symmetry and is a member of the $R\bar{3}m$ space group. The structure allows for two-dimensional Li^+ diffusion between the CoO_6 layers. Although a considerable amount of the research attention on the layered oxide family has focused on $LiCoO_2$, other $LiMO_2$ (M = V, Cr, Mn, Fe, Ni) compounds have been studied.[19]

$LiNiO_2$ has been considered as an alternative to $LiCoO_2$ because nickel is both cheaper and more readily available than cobalt. It also has the possibility to offer higher capacities.[22] However, in spite of its potential beneficial properties, it has not been implemented in a lithium-ion battery in its pure state as it is difficult to synthesise.[19] Similarly $LiFeO_2$ has been found to be an unsuitable alternative

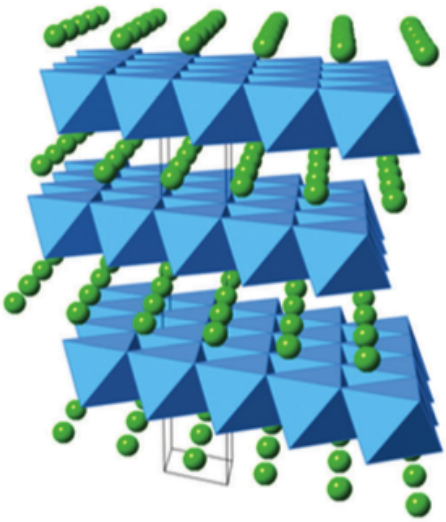

Figure 1.2: *Layered structure of $LiCoO_2$ (green spheres: Li^+ ions; blue octahedra: CoO_6).*

to $LiCoO_2$ due to a low operating voltage, despite Fe being a cheaper and less toxic transition metal.

The enhanced stability of Mn^{4+} in comparison to Co^{4+} would make $LiMnO_2$ an ideal alternative to $LiCoO_2$. However $LiMnO_2$ does not form a layered structure, the more stable spinel phase forms upon cycling.[22]

Mixed layered oxide systems based on cobalt, manganese and nickel, with the general formula $Li(Co_{1-2x}Ni_xMn_x)O_2$, have been used in commercial cells, replacing $LiCoO_2$. Not only is this material cheaper and safer, the storage capacity is higher at 160 mAh g^{-1}. Compositions with $x \approx \frac{1}{3}$ are commercially available, however there is scientific interest in increasing the amount of dopants with the goal of reducing Co content.[34]

1.5.2 Olivine $LiFePO_4$

Goodenough et al.[35] discovered in 1997 that by changing the oxide ions in previously used cathode materials for polyanions, such as phosphates and sulphates, the Fe^{2+}/Fe^{3+} redox potential is increased enough (to 3.5 V) for it to be commercially attractive.[36] It was also established that by developing

abundant iron as a full Fe^{2+}/Fe^{3+} redox system, and by ensuring that all oxide ions are fixed in strong P-O bonds, problems with expense and safety that are seen for other cathode materials are negated.[37,38]

$LiMPO_4$ (M = Mn, Fe, Ni, Co) has an olivine-type structure, space group *Pnma*, and is shown in Figure 1.3. The structure consists of a hcp array of oxygen ions with lithium or iron occupying half of the octahedral sites, and phosphorus sitting in one eighth of the tetrahedral sites. This results in layers of edge-sharing MO_6 octahedra that are linked by PO_4 tetrahedra, forming a one-dimensional channel structure.[2,37,38] This olivine structure has been found to show high voltages and good thermal stability.

$LiFePO_4$ is a commercially available cathode material and has been used for high power applications, such as power tools and mobile phones. It offers a high operating voltage of 3.5 V vs. Li/Li^+, and a large gravimetric capacity of 170 mA g^{-1}. The use of iron as the transition metal also means this compound is low cost and more environmentally friendly than the commonly used $LiCoO_2$

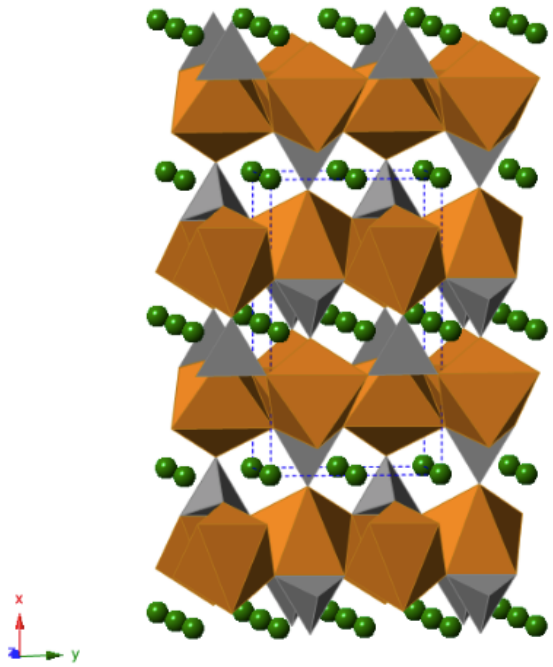

Figure 1.3: *Olivine structure of $LiFePO_4$ (green spheres: Li^+ ions; orange octahedra: FeO_6; grey tetrahedra: PO_4).*

cathode.[2,17,35,39]

The layered cathode materials discussed above display two-dimensional ion diffusion between layers. However $LiFePO_4$ is only able to offer one-dimensional Li^+ diffusion due to its structure. Subsequently, it has a comparatively low rate of lithium conduction. Fortunately, this can be overcome by manipulating its crystal morphology; plate-like particles can be formed which result in lithium channels parallel to the shortest direction. This means that the distance for lithium migration is reduced, and as a consequence the rate of lithium conduction is increased. It is possible that these 1-D channels can become blocked, negatively effecting Li^+ diffusion and reducing the capacity of the battery cell. The formation of anti-site defects, which involve the exchange of sites of neighbouring iron and sodium ions, are energetically favourable in $LiFePO_4$.[38,40] These defects cause the channels in $LiFePO_4$ to be blocked. However, it has been suggested that while anti-site defects are intrinsic within $LiFePO_4$, it may be possible to control their distribution within the structure, limiting their effect on Li^+ diffusion.[41]

Since their discovery, attention on the $LiMPO_4$ (M = Mn, Fe, Ni, Co) olivine phosphates has been focused on $LiFePO_4$. Although each of the alternative systems could, in theory, offer high cell voltages, they each suffer from a number of problems that would need to be overcome before they could be considered viable cathode materials.[31,38,42–45] The major problem for $LiCoPO_4$ and $LiNiPO_4$ is that in order for them to function as cathode materials, advances would need to be made in electrolyte chemistry for their upper voltages to be accessed. $LiNiPO_4$ experiences further problems in that it displays a low charge/discharge capacity and is a poor electronic conductor.[38,46]

1.6 Beyond Lithium: Sodium-ion Batteries

There are several significant challenges facing lithium-ion batteries and their application in grid-scale energy storage systems. One major concern is that conventional lithium-ion battery technology is not sustainable, since global Li

resources are insufficient to satisfy the increasing demands on lithium-battery energy storage. One quarter of Li reserves are predicted to be depleted by electric vehicle applications by 2050. While recycling Li can support its supply, the recycling rate is currently less than 1% and would need to dramatically improve to reach the recycling rate of 50-100% which is predicted to be needed.[47–49]

Research into sodium-ion batteries began in tandem with that of lithium-ion batteries in the late 1970s and through the late 1980s.[50–56] However, the investigation into sodium-ion batteries decreased drastically after the successful commercialisation of rechargeable Li-ion cells in the early 1990s.[2–4] As concerns over the demand on lithium and its resulting high price grow, the sodium alternative has been reintroduced into the battery research community. Sodium-ion batteries are not only able to offer a lower cost alternative to lithium-ion batteries in terms of the alkali metal utilised, but they are also able to use an aluminium current collector, rather than the cooper current collector needed in lithium-ion cells. Aluminium does not form a binary compound with Na as it does with Li, and its use further reduces the cost of sodium-ion technologies.[3] The large ionic size of Na and low standard potential (1.02 Å and $\approx$ 2.71 V vs Na/Na^+, respectively) compared to that Li (0.76 Å and 3.04 V vs Li/Li^+, respectively) has resulted in cells with low energy density and power, which has held back the development of Na-ion batteries. However, as the demand on batteries has increased and the size of cell is not a significant issue when considering grid-scale storage, interest in sodium-ion batteries has resurfaced.

As a relatively large ion, the use of sodium is able to increase the flexibility of materials design. The larger size of sodium compared to lithium not only affects the materials used for electrodes in sodium-ion cells but also means that different electrolytes can be used. The larger ionic radius of sodium means that it is found to have a weak solvation energy in polar solvents.[56] This is considered an important finding for the design of high power sodium-ion batteries, since the desolvation energy influences the kinetics of alkali-ion insertion processes at the electrolyte interface.[57]

It has been established that several chemical structures that do not work as suitable intercalation materials for lithium-ion batteries may do so for their sodium counterparts,[2–4,7,8,58,59] highlighting the importance of the research of novel electrode materials for secondary sodium-ion systems. It is also crucial that fundamental questions regarding these sodium-ion systems are answered, including: (i) the difference in transport and kinetic properties between Na and Li in analogous electrodes; (ii) the insertion/extraction mechanism of Na; (iii) formation of SEI layers on the electrodes from different electrolyte systems; and (iv) charge transfer in the electrolyte-electrode interface and Na^+ migration through the SEI layer.[4]

Sodium has already been successfully implemented in high temperature battery technologies, such as sodium-sulfur and ZEBRA (Na-$NiCl_2$) batteries. Both of these technologies operate at high temperatures, 300-350 °C for Na-S cells and 300 °C for ZEBRA batteries. The high temperatures would need to be lowered due to safety concerns and other problems overcome before these technologies could be used in wide spread applications.[2,12] This review will focus on the component materials for new, room temperature sodium-ion batteries.

1.7 Electrolyte Materials for Sodium-ion Batteries

While the change in alkali-metal ion means that new electrolyte systems can be developed, the conventional systems used in Li-ion batteries are also being adapted for the new Na-ion technology. The choice of a suitable sodium salt depends on a series of important properties. Firstly, the solubility of the salt in the solvent or solvent mixture used is essential for the generation of sufficient charge carriers and conductivity, secondly, the stability of the salt with respect to the other materials employed is crucial and finally, there are toxicity, cost and safety aspects to be considered when it comes to commercial use.[19,60–63]

There is a greater number of potential solvents with sodium salts for use in the electrolytes. These must be polar enough to be able to dissolve the sodium

salts, have a low melting, high boiling point, low viscosity and must be inert with respect to the other materials used in the cell. The choice of solvent can have a significant impact on the performance of the cell and is often electrode specific. Common solvents include dimethoxyethane, diethyleneglycol dimethylether and their mixtures. A more in depth review of sodium-ion electrolyte research can be found elsewhere.[60,61]

1.8 Anode Materials for Sodium-ion Batteries

Replacing lithium with sodium in secondary battery technologies means that completely new anode materials must be developed. Graphite, the most commonly used anode material in Li-ion batteries, is unable to intercalate sodium ions between its sheets. It has also been reported in a theoretical study by Wang et al. that NaC_6 is not an energetically favourable material, like LiC_6.[64] Hard carbon, also known as non-graphitisable carbon, has been reported to intercalate sodium ions with a reversible capacity of 300 $mAhg^{-1}$; Na insertion into the material takes place between parallel layers and into nano-pores between randomly stacked layers.[65–67]

In addition to carbonaceous materials, other anode materials have been investigated with the aim of increasing the specific capacity and cycle life of the anode. These materials fall into three categories that are virtually identical to those for lithium-ion anode materials: (i) oxides and polyanionic compounds (such as phosphates), (ii) p-block elements that show sodiation/desodiation (metals and alloys), (iii) sulphides.[3,9] Alloys of Si, Ge, Sn and Sb have higher specific capacities than carbonaceous materials (Figure 1.4) and have therefore been extensively studied as anode materials.[68] However, these materials exhibit large volume changes on insertion/deinsertion that can result in electrode pulverisation, loss of contact with the current collector and consequent capacity fading.[69] It is clear more extensive work is required in order to overcome the challenges of identifying the best anode material for Na-ion batteries. However, at this stage hard carbon appears to be the most promising.[68–71]

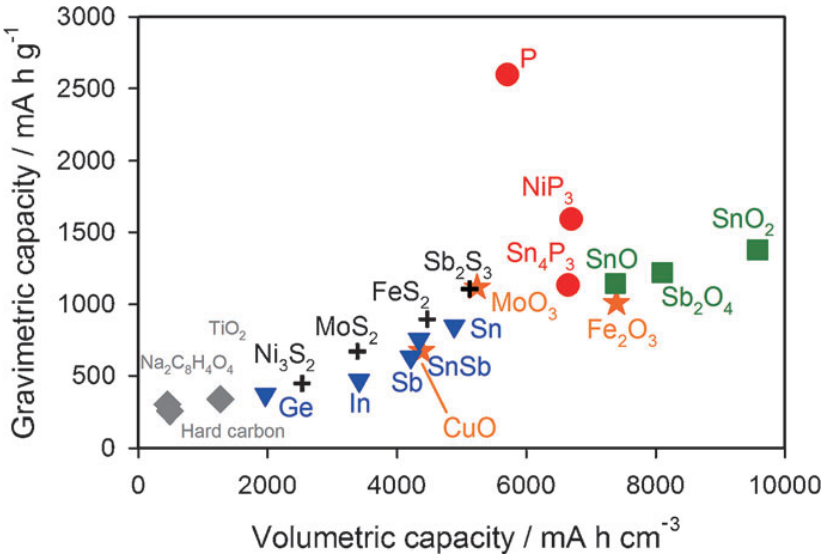

Figure 1.4: *Theoretical gravimetric capacities of various anode materials for Na-ion batteries.*[68]

1.9 Cathode Materials for Sodium-ion Batteries

A large range of materials are being studied as potential cathodes, from layered oxides to polyanion-type compounds. Each family presents its own advantages and disadvantages for application in energy storage systems. Overall, a suitable cathode should exhibit a minimal amount of volume expansion upon de/intercalation if sodium ions are to provide suitable cycling of the cell.[72]

The following sections describe the features of the materials studied in the work reported here.

1.9.1 Layered Oxides

Layered oxide materials have been extensively studied as cathodes for lithium-ion batteries. The success of $LiCoO_2$ unsurprisingly led to extensive investigations into its sodium analogue, $NaCoO_2$.

Layered sodium oxide materials can be classified according to the their arrangement of Na^+ ions.[73] The nomenclature for these materials is as follows: O and P refer to the octahedral and trigonal coordination of Na, while the number 2 or 3 refers to the repeating transition metal layers in the unit cell.

For example, ABBA in P2 and ABCABC in O3, shown in Figure 1.5.[72]

The extraction of sodium ions from O3- and P2-type phases of $NaMO_2$ (M = Co, Ni, Mn, Fe) compounds generally causes phase transitions. Within the O3-type structure sodium ions are originally stabilised in edge-shared octahedral sites. When Na^+ ions are partially extracted from the O3 phase, prismatic sites become energetically stable. This is achieved by the gliding of MO_2 layers without breaking M-O bonds, changing the oxygen packing of the structure and forming a P3-type material. It is, however, impossible in Na cells to transition between the P3/O3-type and P2-type phase as this can only be achieved by breaking and reforming M-O bonds in a high temperature environment.[74]

Layered P2-type compounds have shown enhanced electrochemical performance as generally they undergo fewer phase transitions when de/intercalating Na^+ ions than O3-type compounds.[7]

P2-$NaCoO_2$

The P2-type structure of $NaCoO_2$ is shown in Figure 1.6. The material, analogous to the commercially successful $LiCoO_2$, is the oldest layered oxide studied as a Na^+ ion host. It has a recorded reversible capacity of $\sim$ 120 mAh

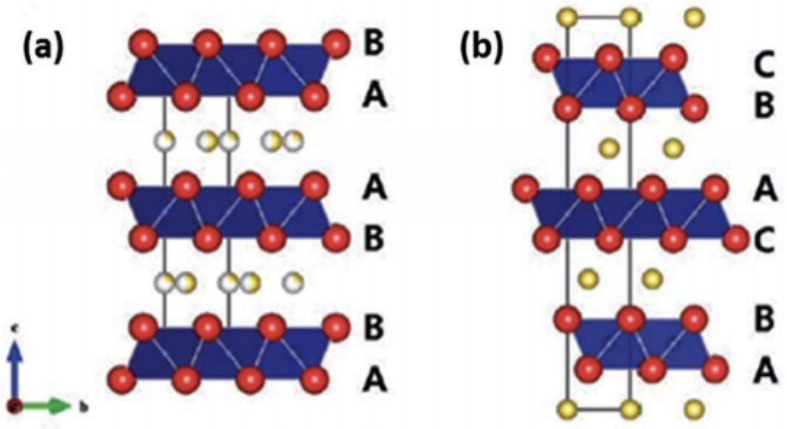

Figure 1.5: *Crystal structure of layered oxide materials a) P2-$NaMO_2$, b) O3-$NaMO_2$ (yellow spheres: Na^+ ions, red spheres: O^{2-} ions, blue octahedra: MO_6).*[10]

g^{-1}.[9,52] P2-$NaCoO_2$ contains two different trigonal prismatic Na sites within its structure: Na1 shares only faces with the CoO_6 octahedra of the adjacent slabs, while Na2 share edges with the surrounding CoO_6 octahedra. These two sites are too close to both be occupied simultaneously when considering the radius of Na^+. The Na2 site is expected to be more stable than Na1, therefore, occupancy of the Na1 site is not required by the overall stoichiometry. However, the simultaneous occupation of both sites minimises in-plane Na^+-Na^+ electrostatic repulsion, leading to stable structures where Na^+ ions occupy both the Na1 and Na2 sites for $0.5 \leq x \leq 1$ in Na_xCoO_2.[75–78]

P2-type $NaCoO_2$ displays complex structural behaviour, evidenced in the galvonostatic cycling curve shown in Figure 1.7, clearly showing that the drops in potential and subsequent voltage plateaus are reversible through charge and discharge. The electronic properties of this material are strongly correlated to the Na^+ content and distribution.[75]

The distribution of Na^+ in the structure results from the culmination of the

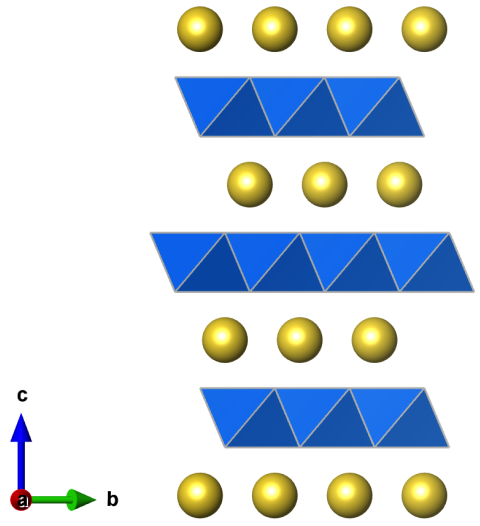

Figure 1.6: *Crystal structure of layered P2-$NaCoO_2$ (yellow spheres: Na^+ ions; blue octahedra: CoO_6).*[79]

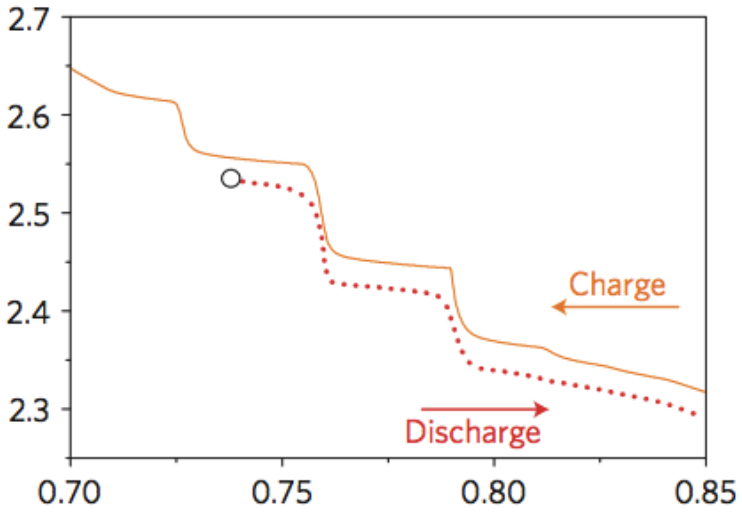

Figure 1.7: *Galvonostatic cycling curve of P2-$NaCoO_2$, showing distinctive phase transitions in the form of plateaus.*[75]

following factors: Na^+-Na^+ electrostatic repulsions, Na^+-Co^{3+} repulsions and the electron-electron interaction in the cobalt layer. All of these are highly sensitive to Na^+ content, resulting in the various Na^+ distributions observed along the composition curve. The high diffusivity of Na^+, even at room temperature, allows for structural rearrangements. A change of as little as 1% in Na concentration can induce a new ordering of ions.[75]

P2-$NaCoO_2$ is studied in **Chapter 5**, where its surface structure and grain boundaries are considered.

P2-$Na_{\frac{2}{3}}[Ni_{\frac{1}{3}}Mn_{\frac{2}{3}}]O_2$

P2-$Na_{\frac{2}{3}}[Ni_{\frac{1}{3}}Mn_{\frac{2}{3}}]O_2$ was used as a precursor material for the layered lithium transition metal oxide compound T2-$Li_{\frac{2}{3}}[Ni_{\frac{1}{3}}Mn_{\frac{2}{3}}]O_2$ as it is low in cost and easy to synthesise.[80] It was found to successfully de/intercalate Na^+ ions in 2001 by Lu and Dahn.[81]

P2-$Na_{\frac{2}{3}}[Ni_{\frac{1}{3}}Mn_{\frac{2}{3}}]O_2$ is a member of the P63/mmc space group.[82,83] With only $\frac{2}{3}$ of the Na-ion sites occupied, the occupied positions and vacancies are able to form an ordered structure, however, the nature of this ordering is still unknown. A cross-section of the structure of P2-$Na_{\frac{2}{3}}[Ni_{\frac{1}{3}}Mn_{\frac{2}{3}}]O_2$ is shown in Figure 1.8, in this example the Na^+ ions are in a "honeycomb" network.

The electrochemical profile of P2-$Na_{\frac{2}{3}}[Ni_{\frac{1}{3}}Mn_{\frac{2}{3}}]O_2$ shows two major intermediate phases upon charging, at 3.5 and 4.0 V. These correspond to Na contents of $\frac{1}{2}$ and $\frac{1}{3}$ respectively. Experimental data has shown that a two-phase reaction occurs during sodium extraction of the material. For $Na_x[Ni_{\frac{1}{3}}Mn_{\frac{2}{3}}]O_2$ the P2-type structure is lowest in energy in the region $\frac{1}{3} < x < \frac{2}{3}$. After the complete extraction of sodium ions ($x = 0$), the O2-type phase is more stable. The two phases coexist in the region $0 < x < \frac{1}{3}$.[82]

Na ions seem to prefer different in-plane orderings at different Na concentrations. The fast self-arrangement that occurs when these orderings change suggests that $Na_{\frac{2}{3}}[Ni_{\frac{1}{3}}Mn_{\frac{2}{3}}]O_2$ has high Na-ion mobility. The P2- and O2-type structures of the material have different Na-ion migration pathways, with different energies. The migration pathway in the P2-type structure is more spacious than that in the O2 structure, and therefore has a lower activation barrier. For the extraction of Na from $Na_x[Ni_{\frac{1}{3}}Mn_{\frac{2}{3}}]O_2$, the smallest sodium diffusion coefficient (D_{Na}) is recorded in the $0 < x < \frac{1}{3}$ region, where the P2 to O2 phase transition takes place. D_{Na} in the $\frac{1}{3} < x < \frac{2}{3}$ region has been recorded between 7 x 10^{-9} - 1 x 10^{-10} cm^2s^{-1}, which is approximately one order

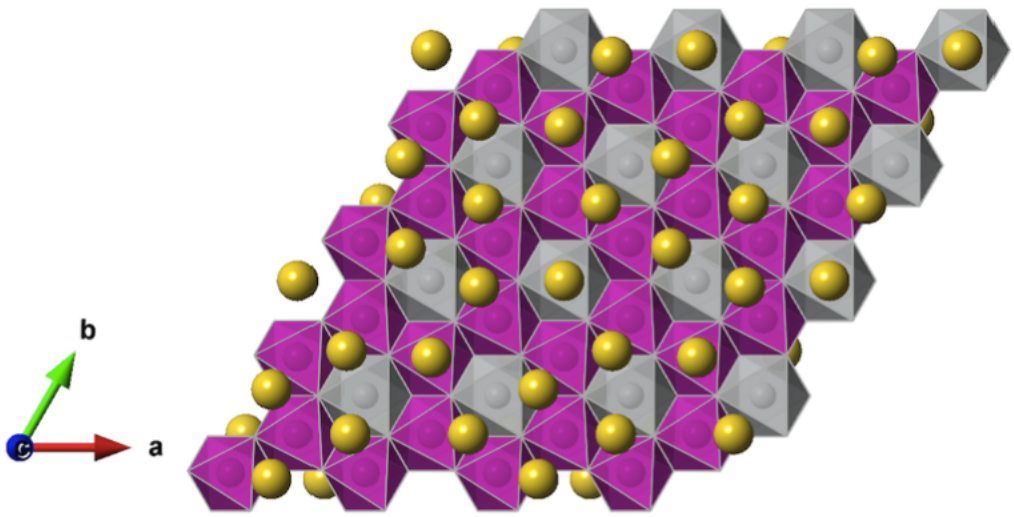

Figure 1.8: *Cross section of P2-$Na_{\frac{2}{3}}[Ni_{\frac{1}{3}}Mn_{\frac{2}{3}}]O_2$ along the c-axis. (Yellow spheres: Na^+ ions; purple octahedra: MnO_6, grey octahedra: NiO_6)*

of magnitude higher than the alkali metal ion diffusion coefficients recorded in similar lithium layered oxide compounds.[82]

P2-$Na_{\frac{2}{3}}[Ni_{\frac{1}{3}}Mn_{\frac{2}{3}}]O_2$ has a theoretical capacity of 173 mA h g^{-1}. The cycling performance of the material is significantly affected by the P2-O2 phase transformation that occurs above 4.2 V. Having the voltage cut-off at 4.1 V prevents this phase transition and avoids the dramatic change in the oxygen framework of the host structure. When the cut-off voltage is 4.5 V, the first discharge capacity is recorded at 134 mA h g^{-1} , with a retention at the second discharge of 89% and only 64% of capacity retained after 10 cycles. Cycling excluding the phase transition shows better retention with a capacity of 87.8 mA h g^{-1} recorded on first discharge, with a retention of 94.9% after 50 cycles.[82]

The structural effect of Mg^{2+} doping on P2-P2-$Na_{\frac{2}{3}}[Ni_{\frac{1}{3}}Mn_{\frac{2}{3}}]O_2$ is investigated in **Chapter 5**.

1.9.2 Olivine $NaFePO_4$

As noted in section 1.5.2, polyanion-based compounds can be used as successful cathodes in secondary Li-ion batteries, with olivine structured $LiFePO_4$ commercially available. Therefore, it is not surprising that sodium metal phosphates have received consideration as potential cathodes in Na-ion cells. The sodium metal phosphate material with the highest theoretical capacity is $NaFePO_4$ (154 mA h g^{-1}), however, unlike its lithium analogue, $NaFePO_4$ does not crystallise in the olivine structure, its most thermodynamically stable form is the maricite polymorph.[7,84]

The olivine and maricite polymorphs have similar structures (shown in Figure 1.9) in terms of phosphate networks, both are members of the Pnma space group. However, in the maricite structure, Na^+ and Fe^{2+} ions occupy the M1 and M2 sites respectively, the reverse of the Na^+ and Fe^{2+} ion occupation in the olivine structure. The difference in the thermodynamically stable forms of $LiFePO_4$ and $NaFePO_4$ is driven by the difference in ionic radius between Li^+ and Na^+, 0.76 and 1.02 Å respectively. In $LiFePO_4$, Fe^{2+}, with an ionic radius of 0.78 Å is essentially the same size as Li^+. The transition metal resides on the M2 site

because of its higher charge. However, sodium has a much larger ionic radius than iron; therefore, in $NaFePO_4$ it is preferential for the Na^+ ion to sit on the M2 site rather than the transition metal ion.[85]

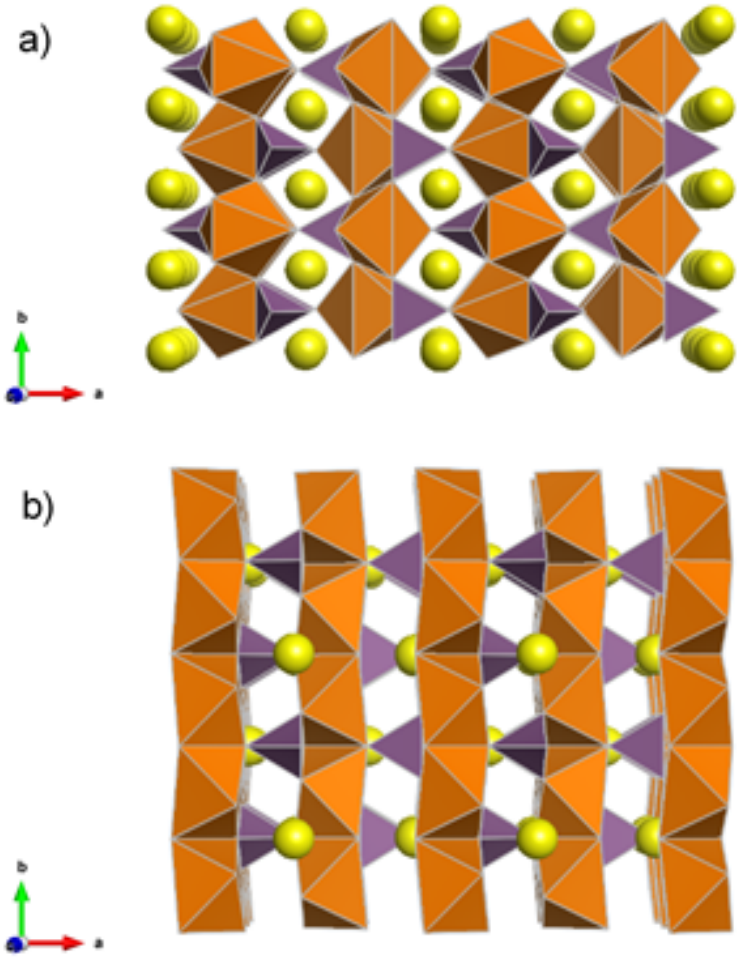

Figure 1.9: *Crystal structures of a) olivine and b) maricite $NaFePO_4$ (Yellow spheres: Na^+ ions; orange octahedra: FeO_6; purple tetrahedra: PO_4).*

In the maricite form of $NaFePO_4$ the Na^+ ions are completely surrounded by PO_4^{3-} tetrahedra and it has been reported that the compound exhibits poor electrochemical behaviour in the bulk crystalline form.[59,86,87] A study on $NaFePO_4$ by Prosini et al.[88] has shown that extraction of sodium from the maricite structure is possible, but with a low discharge rate and with a capacity limited to approximately one third of its theoretical value. It has been reported by Kim et al.[89] that nano-scaled maricite $NaFePO_4$ is able to function as a high-performance electrode through the formation of amorphous $FePO_4$ upon Na extraction. Nanoscale maricite $NaFePO_4$ has also been reported to be electrochemically active after the process of ball milling, due to the formation of structural defeats resulting in an amorphous phase.[90]

Although the maricite phase of $NaFePO_4$ is the more thermodynamically stable form, synthesis methods have been derived in order to prepare the olivine compound. The first method to be successfully implemented was cation exchange from carbon-coated olivine $LiFePO_4$.[84] Other similar techniques have been devised in order to study the electrochemical behaviour of the compound.[86,91,92]

The potential composition curve for olivine $NaFePO_4$ displays a discontinuity at $Na_{\frac{2}{3}}FePO_4$ on both charge and discharge, although it is more visible on the charge curve.[84] Li^+ extraction from $LiFePO_4$ occurs via a biphasic mechanism, while Na^+ extraction from $NaFePO_4$ occurs in two voltage plateaus, separated by the intermediate $Na_{\frac{2}{3}}FePO_4$. This is thought to result from the large cell mismatch between the two end materials ($NaFePO_4$ and $FePO_4$). The $FePO_4$, $Na_{\frac{2}{3}}FePO_4$ and $NaFePO_4$ phases all exist simultaneously.[91,93] There are examples in the literature of the elucidation of the $Na_{\frac{2}{3}}FePO_4$ structure,[91,93–95] which agree that both sodium vacancy and Fe^{2+}/Fe^{3+} ordering occurs in the system. While this phenomenon is not observed in $LiFePO_4$, a similar intermediate formation has been recorded for $Li_{0.7}CoPO_4$ between $LiCoPO_4$ and $CoPO_4$ end members. However, no vacancy ordering has been detected in this structure.[96]

The study presented in **Chapter 3**, provides an outline of defect chemistry and Na diffusion in the olivine and maricite polymorphs of $NaFePO_4$. Olivine

$NaFePO_4$ is further investigated in **Chapter 4**, where the effect of biaxial strain on the system (and $LiFePO_4$) is discussed.

1.10 The Move to Divalent Ions: Magnesium Batteries

As mentioned in section 1.6, the challenges facing lithium-ion batteries have increased research interest in post-lithium technologies. Rechargeable magnesium batteries have been considered a promising technology for energy storage. Magnesium-based technology is promising for a number of reasons. Firstly, Mg is much more abundant in the Earth's crust than Li, making it a cheaper metal to incorporate into electrode materials. Secondly, Mg is more atmospherically stable than Li and has a higher melting point, this makes it safer to handle and manufacture. The divalent nature of the Mg ion means it is also able to offer a potential advantage in terms of energy density.[13–16]

1.11 Electrolyte Materials for Magnesium Batteries

One of the largest challenges facing Mg batteries is the development of a suitable electrolyte that is capable of reversible metal plating/stripping at the anode and supporting reversible intercalation against a high voltage cathode. A multitude of factors has slowed the development of a functional magnesium electrolyte, including limited electrochemical stability with the electrodes (i.e. narrow electrochemical stability window), lack of reversible Mg metal stripping and plating, instability against current collectors and low Mg mobility, leading to the formation of ionic couples.[14,97–99]

A comprehensive evaluation of the development of a suitable electrolyte for Mg batteries is detailed elsewhere.[15,97,99–101]

1.12 Anode Materials for Magnesium Batteries

Unlike the monovalent batteries discussed above, it is possible to use a metal anode with Mg batteries, offering a theoretical capacity of $\sim$ 3833 mAh cm^{-3}. This is because it deposits more uniformly when cycling than for either Li or Na.[13,15] This is a very favourable attribute of magnesium batteries. Mg-metal anodes are only able to operate in electrolytes that are not reduced on metallic Mg^{2+} and therefore do not form passivating films on the surface of the anode. Unlike Li-ion batteries, where a passivation layer is crucial to the operation of the cell, in Mg batteries this layer impedes Mg^{2+} diffusion.[15,102] The challenges in developing a suitable electrolyte are discussed below.

1.13 Cathode Materials for Magnesium Batteries

The development of a suitable cathode material for Mg batteries, which offers a high reversible capacity and an adequate operating voltage, is a major challenge to overcome. The high valency of Mg^{2+} ions results in slow diffusion through inorganic cathode materials, culminating in low reversible capacity and reduced power output. It is thought that the low Mg^{2+} mobility is caused by strong ionic interactions and redistribution of the divalently charged cations in the material. Strategies have been employed in order to address these issues, including the formation of mesoporous and nanostructured materials, in order to reduce the diffusion length for Mg^{2+}.[103] Capabilities of Mg cathodes have also been improved by utilising materials with a high Mg^{2+} diffusivity.[16,104,105] While working multivalent cathodes have been reported in the literature (a few of which are discussed below), Mg^{2+} host materials have been relatively unexplored compared to those for Li^{+} ions.[14]

The first working Mg battery cell was achieved in 2000 by Aurbach et al.[13] consisting of a Mg metal anode, and a Chevrel $Mg_2Mo_6S_8$ cathode. An operating voltage of 1.1 V vs. Mg metal and an energy density of 70 mAh g^{-1} were

reported.

Most Li-ion battery cathodes are made up of close-packed oxygen frameworks, unlike the Chevrel phase that has a 'cluster' structure, as shown in Figure 1.10. The Chevrel structure is made up of Mo_6S_8 blocks that are arranged such that they are separated by "cavities".[14,15,106–108] These "cavities" are the sites upon which Mg^{2+} ions are able to intercalate into. While this material only offers a poor capacity and an average cell voltage, it has provided insight into the desirable characteristics of a successful magnesium cathode.[15,109,110]

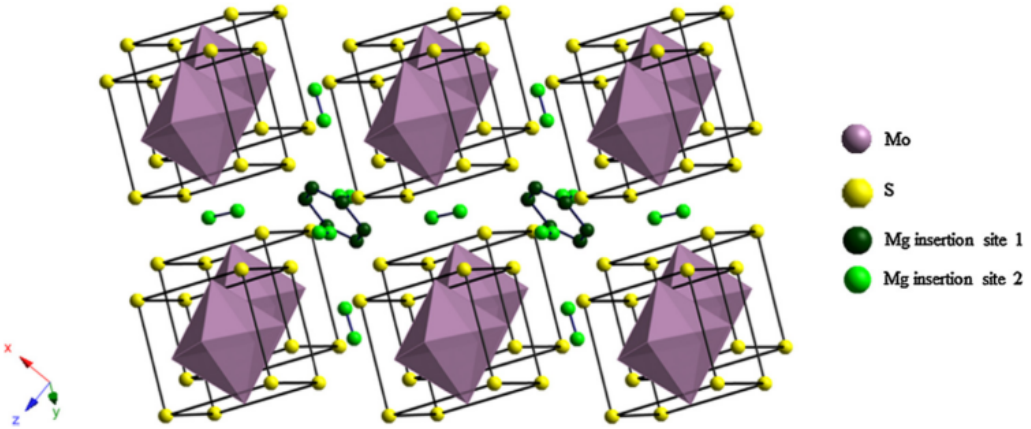

Figure 1.10: *Crystal structure of Chevrel phase Mo_6S_8.*[108]

In order to improve upon the performance of the Chevrel cathodes, other transition metal chalcogenides with the general formula AMT_2 where A is the multivalent ion, M a transition metal and T = S, Se or Te, have been considered. This included work on Mg intercalation spinel-structured Ti_2S_4,[105,111–113] which offers a reversible capacity of 200 mAh g^{-1} and a cell voltage of 1.2 V vs. Mg/Mg^+.[114] The fundamental study of chacogenide compounds and the breakthrough of Mg^{2+} intercalation into chevrel-Mo_6S_8 by Aurbach et al.[13] has led to these materials being the most promising Mg cathode materials in terms of cycling at the present time.[14]

Intercalation materials offering higher theoretical capacities and voltages than the chalcogenide cathodes mentioned above have been targeted. Methods for achieving these desirable properties include switching the anion species from sulfur to oxygen and by increasing the ratio of intercalant to transition metal.[115]

These factors make oxide materials particularly appealing as cathodes.

Oxides are known to exhibit slower Li^+ diffusion than the corresponding sulfides. This poses a more serious problem in Mg^{2+} cathodes as the sluggish mobility of the multivalent ions is generally considered a major hurdle to overcome in the development of suitable materials.[14,105,116] Another concerning issue to overcome with oxide intercalation hosts is the tendency for irreversible oxide conversion reactions to occur rather than reversible Mg^{2+} intercalation. This is due to the low formation energy of MgO.[14]

One oxide material that has attracted interest is layered orthorhombic V_2O_5, shown in Figure 1.11. This is due to the high theoretical capacity of 294.7 mAh g^{-1} and theoretical voltage of 2.5 V.[117,118] However, electrochemical insertion of Mg^{2+} into orthorhombic V_2O_5 has been shown to have poor kinetics,[104,119] which is attributed to slow Mg diffusion in the host material. This has also been shown to be true for Mg intercalation into other oxide cathode materials, such as spinel-type Mn_2O_4.[116,120]

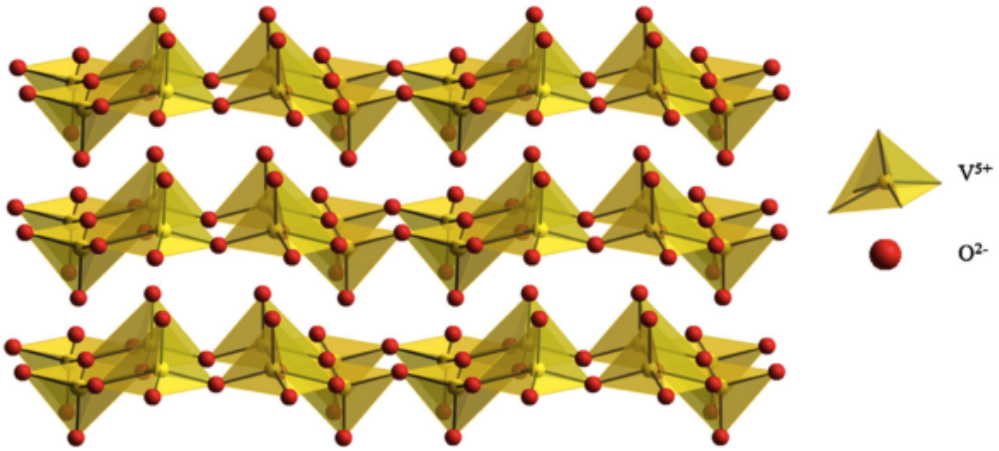

Figure 1.11: *Crystal structure of layered orthorhombic V_2O_5.*[121]

1.13.1 Olivine $MgFeSiO_4$

As discussed in sections 1.5.2 and 1.9.2 polyanion materials, specifically those with an olivine-type structure, have been of great interest as cathode materials for Li- and Na-ion batteries. Recently, olivine magnesium silicates have been reported to promising cathode performance, with indication of reversible Mg^{2+} intercalation.[122–127]

$MgFeSiO_4$ has been considered of interest as a potential cathode material due to its olivine structure (Figure 1.12). However, it exhibits a large degree of mixing between octahedral Mg and Fe crystallographic sites.[128–130] Ordered phases of $MgFeSiO_4$ have been synthesised through high temperature methods, where a synthesis temperature up to 900 °C yields a structure with Mg^{2+} occupying M2 octahedral sites and Fe^{2+} residing in the M1 sites. Above this temperature the site preference switches.[128] Therefore, above 900 °C $MgFeSiO_4$ can be synthesised with a structure analogous to $LiFePO_4$, where the Mg^{2+} ions form one-dimensional channels along the *c*-axis.

It has been reported that Mg^{2+} can be de/intercalated into disorder olivine $FePO_4$ with a capacity of only 13 mAh g^{-1}. This poor performance was found to be linked to surface amorphisation, which prevented electrochemical reaction from penetrating the bulk. A first-principles study by Ling et al.[125] provided insight into the redox and thermodynamic behavior of magnesium silicates, indicating similarities between the insertion processes of Mg and Li ions. However, kinetic processes and Mg diffusion have not previously been considered.

A study of the Mg diffusion and voltage properties of $MgFeSiO_4$ is presented in **Chapter 6**.

Having introduced the materials explored in this work, the next chapter discusses the computational methods used. After which the results of the studies are presented.

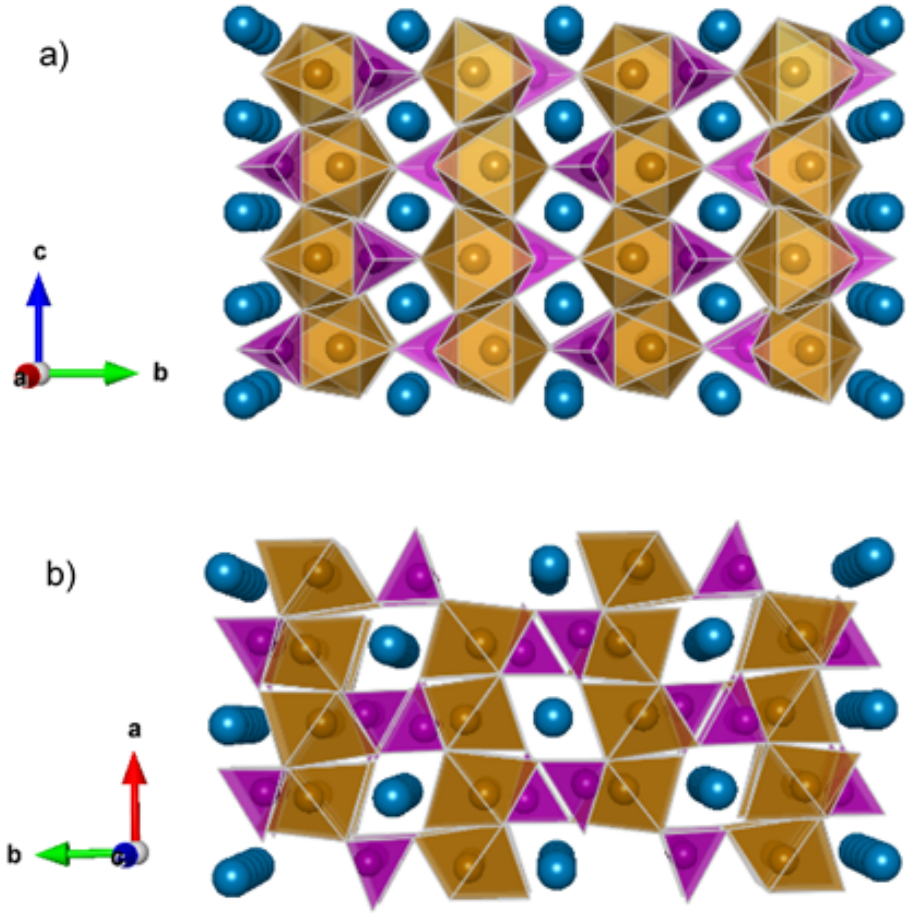

Figure 1.12: *Crystal structure of $MgFeSiO_4$ a) along the a-axis and b) c-axis, showing channels of Mg^{2+} ions. (Blue spheres: Mg^{2+}, purple tetrahedra: SiO_4 and brown octahedra: FeO_6)*

2 | Computational Modelling Methods

'Of course it's happening in your head... but why should that mean it is not real?'

J. K. Rowling, Harry Potter and the Deathly Hallows

2.1 Introduction

Computer modelling techniques are now able to play a crucial role in the prediction of structures and properties of complex materials, and are well-established tools in the field of solid-state chemistry. These techniques provide a means of investigating fundamental structural, transport and defect properties on the atomic scale. There are three main computational techniques used in the studies presented here: potentials-based energy minimisation, molecular dynamics (MD) and density functional theory (DFT). These techniques are implemented in several software packages: here, energy minimisation calculations were carried out using GULP[131,132] , MD simulations using LAMMPS[133] and DFT studies using VASP.[134,135] A general overview of these techniques is given here, as they are described in more detail elsewhere.[136–141]

2.2 Atomistic Simulations

The techniques discussed below require that the interatomic forces are evaluated at each step. The description of these interactions can be separated into two methodologies: atomistic techniques and *ab initio* techniques. Atomistic simulation techniques use simple, empirically derived equations to describe interatomic interactions, while *ab initio* techniques are based on fundamental quantum mechanics and explicitly include electron density. This makes *ab initio* techniques computationally expensive, and therefore means they are more suited to small system sizes. While atomistic techniques are able to easily simulate several thousands of atoms and are often used for modelling defects in large crystal systems.

2.2.1 Interatomic Potentials

The starting point for every atomistic simulation is the development of a potential model; using mathematical terminology it provides a description of the energy of a system as a function of its coordinates. The results obtained from simulations are directly affected by the extent to which the potential model represents the system under study. The lattice energy (U_L) of a system is the property of primary importance; a potential model must calculate it accurately if it is to represent the system well. The expression used to calculate U_L is shown in equation 2.1; a series expansion of pairwise, three-body and increasingly larger body terms.

$$U_L = \sum_{ij} V_{ij}(r_{ij}) + \sum_{ijk} V_{ijk}(r_{ijk}) + ... \tag{2.1}$$

The summation terms account for all ion pairs (i and j) and all ion trios (i, j and k) in a crystal. The equation could, theoretically, include terms to represent a larger number of ions, but in the majority of cases it is not considered necessary to include summations that exceed the "three-body" terms.

The potential model for each crystal system is formed of a number of interatomic equations, which are summed to give the lattice energy. The

parameters of these interatomic potentials can be altered to accurately describe the chemical factors, such as bond strength and atomic mass of the crystal structure they represent.

The potential models used in this work are based on the Born model. The model predominantly includes the pairwise (two-body) terms from the lattice energy series expansion shown above in equation 2.1. The two-body terms can further be divided into short-range and long-range coulombic interactions. The short-range interactions account for both attractive and repulsive forces; the attractive forces are due to the presence of dispersive forces, whilst the overlap of ion charge clouds is what gives rise to the repulsive forces. The first term on the right side of equation 2.2 accounts for the coulombic interactions between pairs of ions, q_i and q_j represent the ionic charges and r_{ij} the interatomic distance. For ionic materials this term is dominant and can represent 90% of the total lattice energy. The $\Phi(r_{ij})$ term accounts for short range interactions.

$$U_L = \sum_{ij} \frac{q_i q_j}{4\pi\epsilon_0 r_{ij}} + \sum_{ij} \Phi_{ij}(r_{ij}) \tag{2.2}$$

Short-range interactions are modelled using simple analytical functions known as interatomic potentials. The best known examples of these potentials are the Buckingham[142] and Morse[143] potentials. The Buckingham potential (Equation 2.3) has been mostly used in this work. The expression which describes the potential can be divided into two components; the exponential repulsive term, containing the A and ρ parameters, represents the repulsion of the electronic charge cloud of the ions. The second part of the equation, containing the C term, accounts for attractive forces.

$$\Phi_{ij}(r_{ij}) = Aexp\frac{-r_{ij}}{\rho_{ij}} - \frac{C_{ij}}{r_{ij}^6} \tag{2.3}$$

The Pedone partial charge model[144] was used to model materials in **Chapters 3, 4 and 7** of this work. This model uses a standardised charge of 0.6 and employs the Morse potential rather than the Buckingham potential described above. Equation 2.4 shows the standard form of the Morse potential. The bond dissociation energy (the depth of the potential well) is denoted by D_e, the width

of the potential well is controlled by the a parameter and the equilibrium bond distance r_0. In order for the interaction energy to have a zero value at infinite separation, the bond dissociation energy is subtracted.

$$\Phi_{ij}(r_{ij}) = D_e[(1 - exp(-a(r_{ij} - r_0))^2) - 1] \tag{2.4}$$

In some instances it is necessary to include a three-body term, for example when modelling phosphate or silicate materials in order to account for the rigidity of the O-P-O and O-Si-O bonds and their angle-dependent nature. The three-body term is defined according to Equation 2.5, where the bond angle for a tetrahedron is represented as Θ_0, and K represents the force constant. The three-body term acts so that any change from the ideal angle is penalised with an increase in energy.

$$\Phi_\Theta = \frac{1}{2}K_{ijk}(\Theta - \Theta_0)^2 \tag{2.5}$$

Coulombic terms can be slow to converge, due to the fact that the coulombic interaction between ion pairs (i and j) decays in a way that is directly proportional to the inverse of their inter-ionic separation ($\frac{1}{r_{ij}}$). The number of interacting ions, however, increases linearly with the surface area of a sphere ($4\pi r^2$). Therefore, whilst it is to be expected that the coulombic interaction term would decay as distance is increased, in fact, the energy density of the interaction between ions increases with interionic separation. Methods have been developed to correct this problem. For three-dimensional materials the most commonly used is the Ewald method; this method divides the sum into real and reciprocal space components, and requires that in addition to being neutral, the unit cell has a zero dipole moment.

2.2.2 Ionic Polarisation

It is not usually possible to assume a fixed dipole moment for an individual atom, as its polarisability is affected by both the magnitude and direction of the dipole within the crystal structure. It is essential that the effect of polarisation is incorporated into the potential model in order to accurately model the crystal strucutre. Polarisation occurs as a result of distortion of an ion's electron charge

cloud, caused by the presence of an applied external field, such as the electrostatic field of the crystal. Accurate modelling of polarisation effects is of particular importance when dealing with defect modelling. The polarisation produced by the electric field as a result of a charge point defect will greatly affect the lattice relaxation around said defect.

The simplest model with the ability to describe polarisation is the Point Polarisable Ion (PPI) model. In this model each ion is assigned a dipole moment (μ_i) which is the product of the ion's point polarisability (α_i) and the magnitude of the applied field (E), as shown in equation 2.6.

$$\mu_i = \alpha_i E \tag{2.6}$$

Problems occur when the PPI model is used for solid state ionic materials as the description of the polarisability it provides is inadequate. This inadequacy is caused by the absence of a term in the equation to account for the coupling between the short-range repulsion and the polarisation, this is a key factor considering that ions are polarised in solids. Short-range repulsion is the product of the overlapping valence shell orbitals of different atoms, since the shape of valence orbitals are directly affected by polarisation, the combination of the two forces can "dampen" the overall effect.

The most successful model for incorporating the key coupling between the short-range repulsion and polarisation is Dick and Overhauser's[145] shell model (Figure 2.1). Within this model each ion is separated into a core and a shell. The core, with a charge of X, effectively accounts for the total mass of the ion, as it represents both the heavy nucleus and the inner electrons of the ion. The shell, with a charge of Y, is considered "mass-less" as it only represents the polarisable valence electrons. Although the core and shell components of the model are coulombically screened from one another, they are connected by a harmonic spring, that has a spring constant of k. The electronic polarisability of a free-ion can be calculated using Equation 2.7.

$$\alpha = \frac{Y^2}{k} \tag{2.7}$$

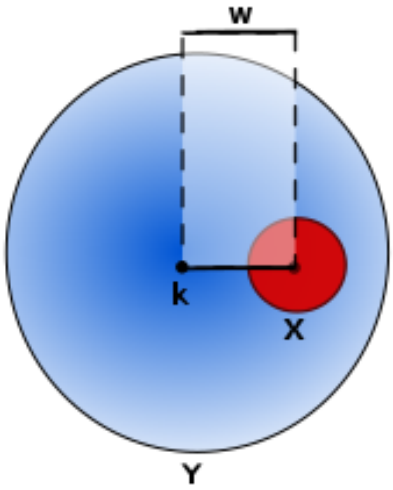

Figure 2.1: *Schematic representation of the shell model. The ion core has a charge of X and the shell a charge of Y. The two are displaced by a distance W and are connected by a harmonic spring, which has a spring constant of k.*

2.2.3 Deriving Interatomic Potentials

In order for atomistic calculations to provide accurate atomic insights it is necessary that the components of potential models are derived so they are able to accurately reproduce the materials they represent. Derivation is possible through empirical fitting to experimental data and/or material properties. Crystal structure information obtained from experiment is often the most easily accessible data with which to make comparisons. That being said, is is not uncommon for other properties such as dielectric and elastic constants to be incorporated in the comparison. The quality of fit of the parameters is judged by the calculation of the sum of squares (SS), shown in equation 2.8. The number of observables is denoted by N_{obs}, the experimental and calculated values of the observables are described by f_i^{obs} and f_i^{calc} respectively, and ω_i is a weighting factor. The weighting factor can be altered for each observable depending on its reliability and importance to the model.

$$SS = \sum_{i=1}^{Nobs} \omega_i (f_i^{obs} - f_i^{calc})^2 \tag{2.8}$$

The sum of squares should, ideally, be equal to zero, this means that the calculated model exactly matches experiment. However, this situation is highly unlikely except for the most simple of models.

The fitting process requires that the potential parameters are adjusted in order to minimise the sum of squares. The fitting process is effectively the reverse of the energy minimisation procedure, as the interactions between the ions are changed to match the starting structure, rather than minimising the energy through structure modification.

2.2.4 Energy Minimisation

The potential energy of a system can be defined as a function of the coordinates of its component atoms. Therefore the potential energies of all solid-state systems are dependent on the positions of all their constituent particles. This function is the potential energy surface, with each position on the surface representing a set of coordinates, corresponding to a particular atomic configuration. The potential energy surface is difficult to visualise and characterise in its entirety, due to its multi-dimensional nature. However, the use of key component coordinates allows a greater understanding of these surfaces, and the chemical systems they represent.

There are two types of stationary points which are of particular importance for the analysis of a given potential energy surface:

i. **Minima:** The lowest energy points on the potential energy surface represent stable states for the chemical systems. For some systems it is possible that multiple minima can be found, each corresponding to a different structure. The lowest energy point on the potential energy surface is the 'global minimum' of the system. This corresponds to the lowest energy, and therefore the most thermodynamically stable structure. All other minima are known as 'local minima'.

ii. **Saddle-Point:**The saddle point is the point of maximum energy found on the lowest energy path between two stable structures (minima). It is also

known as the transition state. The presence of a transition state indicates a possible reaction pathway. Reaction pathways allow activation barriers to be calculated, these are vitally important in the understanding of chemical systems.

It is not possible to distinguish between these two types of stationary points by using their first derivatives, as they both equal zero. However, distinction is possible through the use of second derivatives with respect to distance. The eigenvalues of the Hessian matrix of second derivatives are all positive for minima, whilst one of the eigenvalues will be negative for a saddle-point.

The location of stationary points on the potential energy surface is vital in the field of computational chemistry. Energy minimisation algorithms can be used to find these points. They can, however, experience problems due to the complex nature of the potential energy function. These issues can often be overcome by assuming that when the potential energy function approaches a minimum it is harmonic (quadratic).

Energy minimisation is a relatively simple concept. The structural parameters that define the energy of the crystal (cell dimensions and atomic coordinates) are adjusted in order to find the minimum energy configuration of the system. There are a number of different techniques for energy minimisation. The most simple of these is a 'search' procedure, where the location of the global minimum just requires scanning the parameter space. Due to its simplicity, this method is often not particularly effective, and subsequently is rarely used. Consequently other more involved techniques, which incorporate relatively complicated mathematical formulae are usually favoured. It is vitally important that for large crystal systems the most appropriate technique is chosen, in order for the global minimum of the system to be obtained without the use of an unnecessary amount of computer time.

The gradient (first-order) method is one technique that is often implemented in place of the 'search' procedure. This requires the first derivative of the potential energy function (E_i) in terms of the atomic coordinates to be varied

(x_i), shown in Equation 2.9.

$$g_i = \frac{\delta E_i}{\delta x_i} \tag{2.9}$$

The following subsections will discuss different derivative-based energy minimisation techniques that can be used.

2.2.5 Steepest Descent

The simplest of the first derivative-based energy minimisation techniques is the steepest descent algorithm. This is an iterative technique used to find the minimum of the system. The atomic coordinates are changed in a way that generates the steepest gradient, and therefore the largest decrease in energy. The direction in which the 3N Cartesian coordinates of a system, with N atoms, are moved, can be described using a 3N-dimensional gradient unit vector (r_i), which points in the opposite direction to the gradient vector (g_i), shown in Equation 2.10.

$$r_i = -g_i \tag{2.10}$$

Once in has been determined which direction to the move the coordinates, the distance along the gradient to move them needs to be established. It is not possible to determine this distance analytically, as it has to be assumed that the potential energy is quadratic. There are, however, two approaches that can be used in order to calculate this parameter, either using a step of an arbitrary length or a line search. The arbitrary step method is often preferred over a line search as this is often requires a large amount of computational resources.

The arbitrary step method involves taking a step of arbitrary length α_i along a gradient (r_i) in order to determine a more refined atomic configuration (x_{i+1}). This is shown in Equation 2.11, where the coordinates of the original configuration are denoted using x_i.

$$x_{i+1} = x_i + \alpha_i r_1 \tag{2.11}$$

This method gradually converges on the minimum through a series of right angled turns as a result of using a series of orthogonal successive steps.

The steepest descent algorithms provides a robust method of determining the minimum energy of a system, even if the minimum is far from the initial starting point. However, it can be considered inefficient at finding the minimum of a system, due to these right-angled turns. This is particularly problematic when proceeding down a long narrow energy well, as a large number of small steps will be required.

2.2.6 Conjugate Gradient

The conjugate gradient algorithm is often seen as a theoretical advancement on the steepest descent method, as it avoids the reintroduction of errors with each separate iteration. While the steepest gradient algorithm uses a series of orthogonal lines to minimise the energy of the system, the conjugate gradient method uses a set of orthogonal search vectors $(d_{(0)}, d_{(1)}, ..., d_{(n-1)})$, and only minimises the energy once. The minimum of the energy surface is located by minimising the energy with respect to each direction.

The conjugate gradients algorithm generates a new search vector (d_i), based on the previous search vector (d_{i-1}), the previous gradient (g_{i-1}) and the current gradient (g_i), according to Equations 2.12 and 2.13.

$$d_i = -g_i + \beta_i d_{i-1} \tag{2.12}$$

Where:

$$\beta_i = \frac{g_i \cdot g_i}{g_{i-1} \cdot g_{i-1}} \tag{2.13}$$

Minimising the energy function in this new direction allows a position nearer the minimum (x_{i+1}) to be calculated, shown in Equation 2.14.

$$x_{i+1} = x_i + \alpha_i d_i \tag{2.14}$$

The step length is denoted using α_i and is calculated using the same line search technique for each iteration.

The conjugate gradient algorithm is more efficient than the steepest descent method requiring fewer iterations to locate the minimum energy of the system. Only n steps will be needed to locate the minimum for a quadratic function of

n variables. Unlike with the steepest descent method, convergence towards the minimum is not hindered by the shape of the potential well. Additionally, as only the first derivative information is used in the conjugate gradients algorithm, the time of calculation for each step is relatively quick.

2.2.7 Newton-Raphson

The Newton-Raphson method is a commonly used second-order minimisation technique. It uses both first- and second-order derivative information in order to converge on the minimum of the system. Each new iteration (x_{i+1}) is calculated by taking the atomic coordinates of the current configuration (x_i), and subtracting the corresponding gradient for that point (g_i) multiplied by the reciprocal of the Hessian matrix (H_i^{-1}). Hence the atomic coordinates are continually updated according to Equation 2.15.

$$x_{i+1} = x_i - H_i^{-1} g_i \tag{2.15}$$

If the potential energy surface of the system under study was harmonic (a true quadratic), then the Newton-Raphson approach would only need a single step in order to locate its minimum energy. However, real chemical systems are not perfectly harmonic and therefore this technique, like those mentioned previously, must be applied iteratively. If the configuration under evaluation is close to a minimum, then rapid convergence towards said minimum occurs as it is a valid assumption that the potential well is harmonic. Unfortunately, minimisation can become unstable when the starting configuration is far from the minimum, as the potential energy surface cannot be assumed to be harmonic, hence Newton-Raphson is a less useful technique in these instances. It is therefore of particular importance, that for this method a suitable atomic configuration is chosen before the optimisation is started. When it is likely that the starting configuration is far from the minimum, due to the unavailability or poor quality of experimental structural data, a more robust energy minimisation technique should be used. It is often the case in these situations that either the steepest descent or conjugate gradient method is used initially to provide a configuration

closer to the minimum, before switching to Newton-Raphson to accurately and rapidly locate the minimum.

The use of the Hessian allows for faster convergence when near minima, however, the calculation and inversion of the Hessian matrix can be regarded as relatively computationally expensive.

2.3 Periodic Boundary Conditions

Periodic boundary conditions are considered crucial in order to successfully model large solid state systems, because they are able to reduce the amount of computational time needed. As crystalline solids are symmetrical they can be broken down into unit cells which consist of only a relatively small number of atoms, ions or molecules. Unit cells can then be repeated continuously in all three dimensions.

Using periodic boundary conditions means that during a simulation the unit

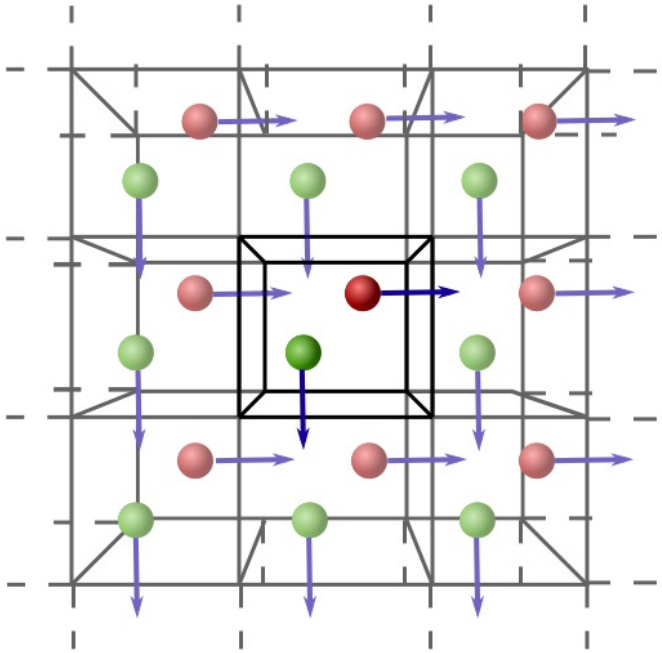

Figure 2.2: *Schematic representation of periodic boundary conditions*

cell is surrounded, in all directions, by identical copies of itself (Figure 2.2). The ions in these images are only able to interact with ions in the original unit cell and not with each other, while ions in the unit cell can interact with all ions in the simulation, including each other. Periodic boundary conditions are essentially used to make a simulation cell 'feel' like it is part of a large solid state system.

2.4 Modelling Point Defects

Before outlining the techniques used to model defect species in crystal systems, it is important to introduce defect chemistry and highlight some of the types of defects likely to be encountered. Every crystal system will contain an intrinsic concentration of defects due to entropy. Figure 2.3 depicts three of the main defect types:

Vacancy: A vacant lattice site.

Interstitial: An ion located at a site that is not usually occupied.

Substitutional: A lattice site occupied by a dopant ion.

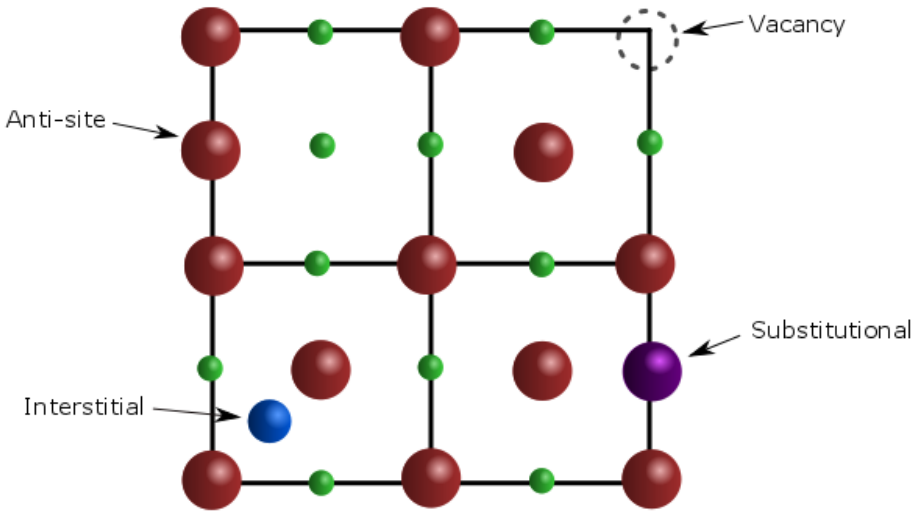

Figure 2.3: *Schematic of a two-dimensional cross-section of a NaCl crystal lattice, depicting types of defect.*

Anti-site: The exchange of sites for two different neighbouring ions.

It is important when modelling defect structures and energies to include an additional relaxation effect. Atoms that directly surround the defect typically experience an extensive perturbation, therefore their relaxed positions are largely effected. The perturbation caused by the defect is effectively coulombic since the field of relaxation is relatively long-range. Lattice relaxation reduces the symmetry of a crystal system, therefore modelling the system as an infinite array of symmetrical unit cells is no longer appropriate.

The Mott-Littleton approximation[146] (Figure 2.4) is a method of defect modelling that attempts to account for lattice relaxation around a defect centre. This method splits the crystal lattice into two regions. The spherical inner region (region I) contains the defect centre and the ions which surround it. The lattice relaxation effect is therefore very strong in this region and all ions are relaxed explicitly.

Region II, which extends to an infinite distance, is further divided into

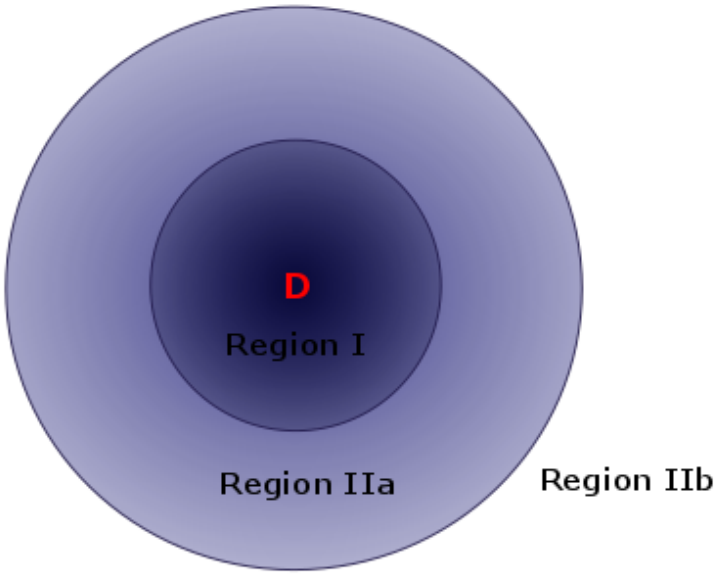

Figure 2.4: *Schematic of the Mott-Littleton approximation, where D represents the defect at the centre of region I.*

sub-regions (IIa and IIb); the ions in the outermost reason (IIb) respond to the defect in a purely dielectric manner (a change in polarisation is experienced, but with no displacement). The relaxation in region IIa is technically a result of all the ions in region I. An approximation is used to allow the relaxation in region IIa to be modelled only as a result of the central charge defect. Region IIa can, therefore, be described as an intermediate region between regions I and IIb, where the modelling of lattice relaxation is very different.

It is important for the validity of this technique that the defect energy has converged significantly with respect to the radius of region IIa, so that the chance that lattice relaxation will occur within region IIb is removed. Ideally both the radius of region I, and the difference between regions I and IIa should exceed the Buckingham potential cutoff radius. This approach, however, may still not provide a completely adequate model of the lattice relaxation, due to the mainly long-range coulombic effect of the defect. Therefore, for these calculations it should always be checked if increasing the region sizes notably changes the values of the defect energies.

2.5 Molecular Dynamics

Energy minimisation (described in section 2.2) is used to simulate systems at absolute zero temperature and, as a result, offers no kinetic energy information about the system under study. These calculations focus entirely on the potential energy of the system; while vast amounts of information can be gained from these processes, the effects of thermal energy are not considered.

Molecular dynamics (MD) explicitly includes the kinetic energy of atoms. All atoms are assigned a velocity, and the variable of temperature is included in the simulation. While energy minimisation techniques are only able to travel downhill on the potential energy surface, a major disadvantage of the technique, MD simulations are able to overcome local energy barriers and potentially find configurations with improved thermodynamic stability. However, it is often only possible to overcome barriers which are in the order of a few k_BT, as MD

calculations are only able to simulate relatively short real-timescales.

Trajectories describe how the positions and velocities of ions vary with time. These variables need to be calculated in order to simulate dynamical properties of a system such as ion transport and crystal vibrations. This essentially requires the integration of Newton's laws of motion for the entire system over a finite period of time. An atom's acceleration ($\boldsymbol{a}$) can be calculated as the second derivative of its position ($\boldsymbol{r}$) with time (t), when the force ($\boldsymbol{f}$) acting on the atom is known, according to Equation 2.16.

$$f = m\frac{d^2r}{dt^2} = ma \tag{2.16}$$

MD simulations proceed by solving Newtonian equations of motion in an iterative manner. After a time step (Δt), with an infinitesimal value, each iteration (x_i) and velocity (v_i) are updated. The acceleration, determined from the force, is combined with the velocities at time t, to generate updated velocities at time $t + \Delta t$. This is shown in the simple update expressions, equations 2.17 and 2.18. It is assumed that the force remains constant between each value of t and $t + \Delta t$, this produces the main source if inaccuracy in this method.

$$x_i(t + \Delta t) = x_i(t) + v_i(t)\Delta t \tag{2.17}$$

$$v_i(t + \Delta t) = v_i(t) + a(t)\Delta t \tag{2.18}$$

The value of Δt must be infinitesimal, because in real systems the forces acting on an ion will vary depending on its distance from other ions; in these cases equations 2.17 and 2.18 are only accurate over infinitesimal values of time. As this is a many-body problem, accurately describing the motion of the ions over larger, more statistically relevant time-scales requires the use of numerical integration algorithms.

2.5.1 Integration Algorithms

A number of different algorithms are available to integrate the Newtonian equations of motion. All of these methods involve the use of a Taylor expansion to approximate the velocities, positions and accelerations. The accuracy of

these properties calculated using the algorithms can be improved by reducing the time step and including higher terms from the Taylor expansion.

The Verlet algorithm[147] is widely used in MD simulations. The Verlet algorithm is derived by approximating the trajectory of ions as a Taylor series about the current set of ion positions (r_i) which is truncated at the third derivative. This is shown in equation 2.19, where v_t, a_t and b_t represent the velocities, accelerations and jerks (acceleration changes) respectively and θ represents an error term.

$$r_{t+\Delta t} = r_t + v_t\Delta t + \frac{a_t}{2}\Delta t^2 + \frac{b_t}{6}\Delta t^3 + \theta(\Delta t^4) \tag{2.19}$$

The b term accounts for the change in force, but is difficult to compute. However there is a mathematical trick, developed by Verlet, that is able to overcome this obstacle. By using information gained from the previous step ($t_{t-\Delta t}$) the third derivative can be included implicitly. Using the same derivation strategy as in the above Equation the Taylor series at $t - \Delta t$ is expressed by equation 2.20.

$$r_{t-\Delta t} = r_t - v_t\Delta t + \frac{a_t}{2}\Delta t^2 - \frac{b_t}{6}\Delta t^3 + \theta(\Delta t^4) \tag{2.20}$$

The overall Verlet algorithm is therefore given by the sum of equations 2.19 and 2.20, as shown below in 2.21.

$$r_{t+\Delta t} = 2r_t - r_{t-\Delta t} + a_t t^2\Delta t^2 + \theta(\Delta t^4) \tag{2.21}$$

By using information gained in the previous step, the Verlet algorithms remove the need to calculate the problematic third derivative term. However, the use of this technique causes the total error to increase, because the errors from both the calculation of r_t and $\mathrm{r}_{t-\Delta t}$ are carried forward into the calculation of $r_{t+\Delta t}$.

The Verlet algorithm does not necessarily calculate the ion velocities, as the ion trajectories can be determined without them. However they remain important values to calculate, since they are scaled to maintain the temperature of the system. It is also necessary to compute the kinetic energy in order to calculate the total energy of the system. The velocities can be determined using the Verlet trajectory by subtracting equation 2.19 from equation 2.20 to yield

equation 2.22.

$$v_t = \frac{r_{t+\Delta t} - r_{t-\Delta t}}{2\Delta t} + \theta(\Delta t^2) \tag{2.22}$$

It is clear from this equation that, until the ion positions have been calculated at the next step, the velocities cannot be determined. It is also important to note that the calculation of velocities using this method introduces a large degree of numerical inaccuracy, with the error being in the order of Δt^2.

The Verlet algorithm is not self starting, information from the previous step is required. This means that initial velocities are assigned to the system. In practice, these values are assigned randomly, whilst ensuring that the system starts at the desired temperature, and with no translational momentum.

2.5.2 Time Step and Equilibrium

The choice of the time step (Δt) is significant for molecular dynamics calculations. The value must be smaller than the timescale of any important dynamical process at the atomic or molecular level. The value chosen must be at least an order of magnitude smaller than the typical period of atomic vibrations (10^{-12} - 10^{-13}). A short time step means that the numerical integration of the equations of motion is more accurate, but also that the process requires more computational effort than if a longer time step was selected. However, the use of too large a time step can generate instabilities in the system, which cause atoms to move unphysical distances or collide with too much energy, ultimately resulting in failure of the simulation. In practice, a time step between 0.1 and 1 femto seconds is typically chosen; this is the ideal choice as it is large enough to cover as much "real time" as quickly as possible, but without any instability in the system.

The initial stage of an MD simulation is the equilibrium period. This period allows the starting configuration of the system to reach a state of equilibrium. During this period several properties of the system are monitored, these include the total energy, which is the sum of the potential energy from the atomic arrangement, and the kinetic energy due to atomic motion. Equilibrium is

achieved when these properties have 'settled' into a steady pattern. The equilibrium period normally lasts for tens of thousands of time steps in order to ensure a satisfactory level of convergence. Once equilibrium is achieved and the equilibrium phase has ended, the production phase can commence. It is from this phase that the desirable statistics of the calculation can be obtained.

2.5.3 Ensembles

An ensemble is used to describe the set of constraints applied to a system that give rise to the distribution of thermally accessible states. The atomic coordinates of the system under study vary with time throughout the duration of a MD simulation. This means that the different atomic arrangements of the system correspond to independent states. Different types of ensembles require different sets of constraints.

The micro-canonical ensemble (NVE) keeps the number of atoms (N) constant, as well as the volume of the simulation cell (V) and the total energy of the system (E). While the total energy of the system is kept at a constant value, the potential and kinetic energy contributions towards this value can change. The conserved value of the total energy can be represented by equation 2.23, where the Hamiltonian ($\mathcal{H}$) corresponds to the total energy of the system, consisting of contributions from the kinetic energy ($\mathcal{K}$) and the potential energy ($\mathcal{V}$).

$$\mathcal{H} = \mathcal{K} + \mathcal{V} \tag{2.23}$$

The micro-canonical ensemble allows large variations in temperature and pressure; this does not accurately represent "real" conditions under which most experimental investigations take place. Alternatives to the micro-canonical ensemble include the commonly used canonical (NVT) and isobaric-isothermal (NPT) ensembles. The canonical ensemble allows the system to be studied as a function of temperature, while the isobaric-isothermal ensemble allows the system to be probed as a function of pressure. It is important to control both the temperature and the pressure during simulations of a system. This is

achieved using mathematical thermostats and barostats. An added benefit to studying systems under controlled conditions is that they help to compensate for the slow accumulation of rounding errors that develop over time.

2.5.4 MD Data Analysis

The production phase of MD simulations can provide useful information in the form of diffusivity of ions and time averaged structures. These properties can be directly extracted from the simulated ion trajectories.

Mean Square Displacement

The means squared displacement (MSD) is a measure of the distance atoms in the simulation cell have moved from their initial conditions. This provides information about the diffusion rate of atoms in the system. The MSD can be defined using equation 2.24, where N is the number of atoms, and $r_i(0)$ and $r_i(t)$ are the initial and current positions of atom i respectively.

$$MSD(t) = \frac{1}{N}\sum_{i=0}^{N} |r_i(t) - r_i(0)|^2 \tag{2.24}$$

The gradient of the MSD is related to the self-diffusion coefficient D according to equation 2.25, where d is the dimensionality of the system.

$$MSD(t) = 2dDt \tag{2.25}$$

Therefore the MSD for a three dimensional system at time t can be described by equation 2.26.

$$MSD(t) = MSD(0) + 6Dt \tag{2.26}$$

It is possible to estimate the activation barrier for ion migration using an Arrhenius plot of diffusion data obtained from a set of MSD plots at several different temperatures. Equation 2.27 is used to generate the plot. LnD plotted versus $\frac{1}{T}$ provides a slope which is proportional to the activation energy Ea.

$$lnD = \frac{-E_a}{RT} + lnA \tag{2.27}$$

It is possible through this method for MD simulations to provide new information about migration barriers that static lattice calculations are unable to access.

Time Averaged Atomic Densities

MD simulations are able to offer the study of ion migration in crystalline materials. It is imperative to be able to visualise the spatial properties of this migration in order to derive the nature and mechanics of diffusion. A useful method of visualisation is through a time-averaged atomic density plot, generated from trajectory data and used to determine diffusion pathways in crystals. The trajectory data needs to contain the ion positions for a series of time steps, in order to show the movement of ions over the simulation.

2.6 Density Functional Theory

While potential-based methods aim to reproduce observed characteristics of real systems, *ab initio* techniques are based on developing models directly from theoretical properties.They allow insights into various ground-state properties which empirical methods do not provide, such as: charge distribution, orbital occupancies, band structure and bonding.

All quantum mechanical techniques aim to solve the Schrödinger equation and therefore derive an exact wave-function for a system. The simplest form of the Schrödinger equation is shown below (Equation 2.28), where $\mathcal{H}$ is the Hamiltonian operator, ψ corresponds to the wave-function and $\mathcal{E}$ is the total energy of the system.

$$\mathcal{H}\psi = \mathcal{E}\psi \tag{2.28}$$

The wave-function contains all information with respect to the positions and spins of the particles within the system. Therefore theoretically all material properties can be related to the wave-function of a system and identification of the wave-function allows all material properties to be calculated. As the eigenvalue of the Hamiltonian operator equals the total energy of the system, by identifying the appropriate form of the Hamiltonian the exact solution can be found. The full Hamiltonian can be expressed by Equation 2.29. Here $\mathcal{T}_e$ describes the electronic kinetic energy, $\mathcal{T}_n$ is the nuclear kinetic energy and

the following three terms ($\mathcal{V}_{int}, \mathcal{V}_{nn}, \mathcal{V}_{ext}$) can be summed together to make the potential energy of the system. $\mathcal{V}_{int}$ is used to describe the electron-electron interactions, while $\mathcal{V}_{ext}$ is the electron-nuclei interactions. The final term, $\mathcal{V}_{nn}$ defines nuclear-nuclear repulsions.

$$\mathcal{H} = \mathcal{T}_e + \mathcal{T}_n + \mathcal{V}_{int} + \mathcal{V}_{nn} + \mathcal{V}_{ext} \tag{2.29}$$

Summing together these terms over all the nuclei and electrons present leads to Equation 2.30, which provides a complete description of the system under study. Where the mass and position of nucleus I, of charge Z_I are defined by M_I and R_I respectively. m_e and r_i describe the mass and position of electron i, respectively.

$$\mathcal{H} = -\frac{h^2}{2m_e}\sum_i \nabla_i^2 - \sum_I \frac{h^2}{2M_I}\nabla_I^2 + \frac{1}{2}\sum_{i\neq j}\frac{e^2}{|r_i - r_j|} + \frac{1}{2}\sum_{I\neq J}\frac{Z_I Z_J . e^2}{|R_I - R_J|} - \sum_{i,I}\frac{Z_I . e}{|r_I - R_I|} \tag{2.30}$$

As can be seen from Equation 2.30, the evaluation of the Hamiltonian operator of a many-bodied system is a convoluted procedure which involves many independent terms. While the basic Schröndinger equation is relatively simple, a full solution is extremely complicated for anything but a basic system. These full analytical solutions are beyond current computational capability and hence a series of approximations are needed in order to make the problem manageable. The first approximation employed is the Born-Oppenheimer which is used to decouple nuclear and electronic motion. The large difference in mass between the nucleus and surrounding electrons is reflected in their motion; the electrons move much faster than the nuclei and therefore we can assume that the system has a fixed nuclear arrangement when calculating the electronic wavefunction. Use of this approximation allows the Hamiltonian to be rewritten as the electronic Hamiltonian, as outlined in Equations 2.31, 2.32 and 2.33.

$$\mathcal{H}_{elec} = \mathcal{T} + \mathcal{V}_{int} + \mathcal{V}_{ext} \tag{2.31}$$

$$\mathcal{H}_{elec} = -\frac{h^2}{2m_e}\sum_i \nabla_i^2 + \frac{1}{2}\sum_{i\neq j}\frac{e^2}{|r_i - r_j|} - \sum_{i,j}\frac{Z_I . e}{|r_I - R_I|} \tag{2.32}$$

$$\mathcal{H}_{elec} = -\frac{h^2}{2m_e}\sum_i \nabla_i^2 + \frac{1}{2}\sum_{i\neq j}\frac{e^2}{|r_i - r_j|} + \sum_i V_{ext}(r_i) \tag{2.33}$$

This acts to significantly simplify the problem by removing the cross terms from the original Hamiltonian. The nuclear configuration of the system is now only included as part of the external potential (V_{ext}). Even though the wave-function is now only dependent on the electronic configuration of the system, this formulation is still beyond all but the simplest systems, due to the large number of electron-electron interactions.

2.6.1 Hohenberg-Kohn Theorems

The Hohenberg-Kohn Theorems provide a viable framework for calculating a wave-function, and form the elementary principles of DFT. The two theorems are defined as:

i. The three-dimensional electron density of a many electron system uniquely determines all the ground state properties of the system.

ii. The energy of a system can be defined as a functional of the electron density, with the minimum energy functional corresponding to the ground-state electron density.

The first theorem means that solutions for the N electron wave-function ($\psi(r)$) are no longer required. All that is needed is the the much simpler knowledge of the three-dimensional electron density $\rho(r)$. The second theorem states that by defining the energy functional of the system the ground state electron density of the system can be calculated. This defines all the other properties of the system. Hohenberg and Kohn define the energy functional which now encompasses much of the complexity of the original problem according to Equation 2.34.

$$E[\rho(r)] = \int V_{ext}(r)\rho(r)dr + F[\rho(r)] \tag{2.34}$$

The first term defines the interactions between electrons and the external potential, including nuclear interactions. The second term ($F[\rho(r)]$), contains the kinetic information of the electrons in the system, as well as terms resulting from electron-electron interactions.

While the Hohenberg-Kohn theorems provide a simplified model for the calculation of the many-electron Schrödinger equation, and hence the foundations for the development of DFT, they are unable to provide a form for $F[\rho(r)]$. Therefore information needed to calculate the ground-state of the system is still missing.

2.6.2 Kohn-Sham Equations

A series of equations were published by Kohn and Sham which built on the Hohenberg-Kohn theorems, allowing for the calculation of the ground state of a system.[148] These are known as the Kohn-Sham equations and have formed the base for modern DFT. They theorised that through the knowledge of the electron density ($\rho(r)$) of a given system with a set of interacting electrons, an equivalent system with the same electron density could be derived with non-interacting electrons. Applying this approach to the problem presented by the Hohenberg-Kohn theorems of the unknown energy functional $F[\rho(r)]$ allows it to be split into a series of terms shown in Equation 2.35. Where $E_{ke}[\rho(r)]$ describes the kinetic energy of the non-interacting electrons and the Hartree term is denoted by $E_H[\rho(r)]$, which contains the Coulombic energy of the electron-electron interactions. The final term ($E_{xc}[\rho(r)]$) is used to describe the contribution to the energy functional from the exchange-correlation term and the energy difference between the real interacting electrons and the hypothetical non-interacting system. Essentially the exchange-correlation term works by collecting together the unknowns of the problem into a single contribution which can be approximated.

$$F[\rho(r)] = E_{ke}[\rho(r)] + E_H[\rho(r)] + E_{xc}[\rho(r)] \tag{2.35}$$

It is important to note that the Hartree term ($E_H[\rho(r)]$) does not account for the correlation of electron motion; it is the summation of the classical pairwise interactions between charge densities as shown in Equation 2.36.

$$E_H[\rho(r)] = \frac{1}{2}\int\int \frac{\rho(r_1)\rho(r_2)}{r_1 - r_2} dr_1 dr_2 \tag{2.36}$$

Importantly two of the terms within the Kohn-Sham approximation (E_{ke} and E_H) are known. While the exchange-correlation term is only known for a few simple systems, its definition is vital for DFT research and is discussed in Section 2.6.3 below.

The combination of the Hohenberg-Kohn theorems and the Kohn-Sham energy functional yields the Schrödinger-like Kohn-Sham equation (Equation 2.37), where $\psi_i(r)$ denotes the Kohn-Sham orbitals of non-interacting electrons, ϵ_i is used to describe the orbital energies and V_{eff} is the effective potential of the system.

$$[\frac{-h}{2m_e}\nabla^2 + V_{eff}(r)]\psi_i(r) = \epsilon_i\psi_i(r) \tag{2.37}$$

This equation can be simplified to derive a stationary solution of the Schrödinger equation (Equation 2.38), subject to assumptions. Here $V_{ext}(r)$ and $V_{xc}(r)$ denote the external potential and the exchange correlation potential respectively. $V_{xc}(r)$ is related to the exchange-correlation energy by Equation 2.39.

$$V_{eff}(r) = V_{ext}(r) + \int \frac{\rho(r')}{[r - r']}dr' + V_{xc}(r) \tag{2.38}$$

$$V_{xc}(r) = \frac{\delta E_{xc}[\rho(r)]}{\delta\rho(r)} \tag{2.39}$$

This method allows DFT to find solutions to the Schrödinger equation through an iterative approach. An initial 'guess' is made for the electron density, usually by superimposing all the single electron densities. This is used to calculate an initial effective potential (V_{eff}) which is subsequently used to generate the Kohn-Sham orbitals of the system, using Equation 2.37. The orbitals can then estimate an improved electron density for the system through Equation 2.40.

$$\rho(r) = \sum_{i}^{N} |\psi_i(r_i)|^2 \tag{2.40}$$

The improved estimate of the electron density is then used to update $V_{eff}(r)$ in a iterative process until a converged value of the electron density is obtained. This electron density (which corresponds to the ground state energy) allows all ground state properties to be defined, as stated in the second of the Hohenberg-Kohn theorems. It is important to note that to be able to generate an accurate value

of V_{eff} at each step, an appropriate exchange-correlation function ($V_{xc}(r)$) needs to be specified. As the exact form of this term is unknown, it is crucial that an valid approximation is made in order for a accurate ground state electron density to be obtained.

2.6.3 Exchange-Correlation Functionals

The exact form of the exchange-correlation functional is not known for most systems. However, there are a few examples for which it has been accurately calculated. The most useful of these being the uniform electron gas, for which the exchange energy has been calculated analytically and the correlation energy has been accurately simulated using Monte Carlo methods. In all cases where the exchange-correlation functional is not known an approximation must be used. The value chosen is not trivial, as this approximation is often a source of significant error in DFT calculations; different exchange-correlation functional can give wildly different results.

There are a vast number of exchange-correlation functionals available for typical DFT calculations which vary in suitability, accuracy and computational expense. These can either be derived semi-empirically or theoretically. The type that is used depends on the calculations being carried out. Commonly used functionals include those based on the Local Density Approximation (LDA), its expansion the Generalised Gradient Approximation (GGA) and their Hubbard U corrected versions (LDA+U/GGA+U); these will be discussed in further detail below.

Local Density Approximation (LDA)

The Local Density Approximation is considered one of the simplest exchange-correlation functionals. However, it has proved remarkably accurate at calculating a range of ground state properties and has therefore become one of the most popular approximations.[149] It is assumed within LDA that the exchange-correlation per electron of a system with an electron density of $\rho(r)$, is equivalent to that of the homogeneous electron gas with the same

electron density of $\rho(r)$, as shown in Equation 2.41. Where ϵ_{xc}^{hom} is the exchange-correlation energy of the homogeneous electron gas per particle.

$$E_{xc}^{LDA}[\rho(r)] = \int \rho(r)\epsilon_{xc}^{hom}(\rho(r))dr \tag{2.41}$$

This approximation relies entirely on local density to approximate the exchange-correlation functional, hence it is named as so. Surprisingly this method is able to accurately reproduce inhomogeneous systems where the electron density does not resemble that of a homogeneous electron gas. This is partly due to the fact that LDA consistently underestimates the correlation energy, but overestimates the exchange energy. This results in the cancellation of some errors. There are, however, considerable limitations to the LDA method. It generally underestimates band gaps, overestimates binding energies and incorrectly predicts some electronic ground states. Therefore, when these properties are of importance an expanded method is required, commonly the Generalised Gradient Approximation (GGA).

Generalized Gradient Approximation

The homogeneous gas concept used for the LDA can be considered flawed, as real systems always exhibit some variation in the electron density with respect to position. More advanced functionals include this information and are therefore semi-local functionals. These consider the local density ($\rho(r)$) at position r, but also account for variations, unlike the LDA functionals, and are known as gradient-correlated. The simplest gradient-correlated functional is the Generalised Gradient Approximation (GGA) functional, and it can be used to calculate the exchange-correlation energy term according to Equation 2.42.

$$E_{xc}^{GGA}[\rho] = \int \rho(r)\epsilon_{xc}^{GGA}(\rho(r), \nabla\rho(r))dr \tag{2.42}$$

Unlike for the LDA where there is only one form for ϵ_{xc} (ϵ_{xc}^{hom}) and the functional can only take one form, there are many different potential forms of ϵ_{xc} within GGA. Therefore, there are many different types of GGA functionals. One of the most popular of these is the PBE functional, based on the work of Perdew, Burke and Ernzerhof.[150]

The GGA approach has been able to more accurately reproduce properties such as crystal structure and binding energies than LDA. While GGA is able to produce a more realistic model for the band gap of materials than LDA, it still tends to underestimate band gap energies. This particularly problematic when dealing with materials with partially filled d- and f-orbitals, such as transition metals and rare earth elements. The so-called hybrid functionals or the Hubbard U corrections are often applied to remedy this. The latter is described in more detail below as only this correction has been used in this work.

GGA+U

The use of an LDA exchange-correlation functional on a transition metal containing system results in a metallic type electronic structure with 'roaming' d-electrons. It is well known that experimentally, transition metal compounds contain localised d-electrons which lead to distinct occupied and unoccupied bands. In order to more accurately reproduce experiment, the exchange-correlation functional is modified for the strong correlation of d-electrons. To achieve this, the s, p and d electrons are treated separately, and their Coulombic interactions are accounted for using a Hartree-Fock mean-field approximation. The strength of the correction of the exchange-correlation functional is described using the Hubbard Coefficient (U), resulting in LDA+U and GGA+U approaches. The value of U needs to be carefully chosen for each element in order to accurately reproduce the system under study, as it is directly associated with the energy gap between the occupied and unoccupied bands in the system. The value is usually chosen empirically to reproduce the properties of the material being investigated.

2.6.4 Application of DFT to Solids

Solid state systems pose a problem when attempting to solve the Schrödinger equation; these calculations tend to simulate the bulk of the system and therefore the cell is treated as being infinite. As the electron wavefunction extends over the entire lattice, this too would be infinite and an infinite number of basis sets would

be required for its accurate description. This can be solved, however, through the use of periodic boundary conditions which allow the system to be considered as a finite crystal. The use of periodic boundary conditions also increases the speed of the calculation by describing aspects of the problem in reciprocal space rather than real space.

The Reciprocal Lattice and k-space

While crystal systems are conventionally described in real space, computational techniques may require the lattice properties to be defined using reciprocal space, or k-space. Lattice vectors a, b and c can be expressed in reciprocal space by a^*, b^* and c^* and are related according to equations 2.43, 2.44 and 2.45 respectively.

$$a^* = 2\pi \frac{b \times c}{a \cdot b \times c} \tag{2.43}$$

$$b^* = 2\pi \frac{a \times c}{b \cdot a \times c} \tag{2.44}$$

$$c^* = 2\pi \frac{a \times b}{c \cdot a \times b} \tag{2.45}$$

In real space a unit cell, with lattice vectors a, b and c, is used to describe the infinitely repeating lattice of a crystal system. Similarly in reciprocal space this primitive cell can be defined as the Brillouin Zone. This is a fundamental concept for the description of periodic systems, as within its volume a complete description of the wave-function can be provided. This concept is described by Blochl's Theorem.[151]

Blochl's Theorem

Blochl's Theorem states that the wavefunction of an electron (i), within a periodic field can be written as a product of two components. One wave-like term and another with the same periodicity as the external field (the periodicity of the unit cell) as shown in Equation 2.46.

$$\psi_i(r) = e^{ikr} f_i(r) \tag{2.46}$$

Where k denotes a wave-vector in the Brillouin zone and controls the frequency and the direction of the wave-like term, and r is used to describe the position

vector. The periodic component of the wave-function combines a basis set of discrete planewaves (e^{iGr}) where the wave-vectors (G) represent all translations to symmetrically identical lattice points. As a result $f_i(r)$ becomes:

$$f_i(r) = \sum_G c_i G e^{iGr} \tag{2.47}$$

Combining this with equation 2.46 leads to the planewave description of the wave-function given in equation 2.48.

$$\psi_i(r) = \sum_G c_{ik} + G e^{i(k+Gr)} \tag{2.48}$$

The solution is defined by the coefficient c_{ik+G}. This summation should be performed using a suitable value of G, to ensure the system is adequately represented.

Planewaves

The choice of the planewave basis set is essential to providing accurate results with reasonable computational expense. Two approximations are applied in order to reduce the complexity of the problem. Firstly, higher order planewaves (those with a large $|G|$) will have a higher kinetic energy and therefore will contribute less to the ground state wave-function. Consequently, a $|G|$ (or energy) cutoff is applied to the summation in equation 2.48; above this value planewaves are not considered to contribute significantly to $\psi_i(r)$ and are not evaluated. Secondly, as ψ is a continuous function of k, small changes in the value of k will result in a minimal impact on ψ. Therefore, a suitable description of k-space can be given by sampling a finite number of points in k-space. The 'k-points' to be sampled can usually be made smaller than the sampling points that would be required for a real space projection of the wave-function. The symmetry of most solid-state systems results in many k-points sampling the same points in the Billouin zone. As double sampling is redundant, the number of k-points can be further reduced through symmetry operations. This can be achieved either through the use of a Gamma point centred k-point mesh ((0, 0, 0) in the Brillouin zone) or one chosen through the Monkhurst-Pack method, where the k-point mesh is shifted from the Gamma point.

In practice, it is essential to check the validity of these approximations in a process known as convergence testing. This requires the variation of the planewave cutoff and the k-point mesh, and the resulting effect on the ground-state properties of the system to be recorded. Convergence is considered to be achieved when the property of interest no longer varies with further alteration of the k-point mesh or planewave cutoff. The lowest planewave cutoff and coarsest k-point mesh which satisfy convergence are typically chosen in order to minimise computational expense.

Pseudopotentials

Near the nuclei of an atom there is significant variation in the electron wave-function. A large number of planewaves would be required to provide an adequate representation of the fine spatial detail associated with the wave-function at small distances from the nuclei. This would result in a reduced calculation speed and therefore increased computational cost. However, as the core electrons are not typically involved in chemical bonding they can be considered essentially constant. Therefore, it is common practice to separate the treatment of the core and valence electrons into two distinct regions by using pseudopotentials.

The pseudopotential is a smooth function which is used to describe the core potential, and can be represented by a reduced set of planewaves, lowering the overall computational expense of the calculation. The distinction between the core and valence electrons is made through the use of a cutoff radius. Within this radius a pseudopotential description is applied which is able to accurately describe the original core potential. This approximation uses an exact representation only for the valence electrons. However, if the cutoff radius has been correctly chosen it is considered acceptable for many ground-state properties of real systems.

The 'softness' of a pseudopotential describes both the smoothness of the function and the size of the cutoff radius from the nuclei. The softer the pseudopotential, the fewer planewaves needed for an adequate description.

However, a very soft potential does not transfer well between systems as it requires a large cutoff radius and can lead to an inaccurate representation of the atom. An ideal pseudopotential will accurately reproduce the wavefunction of an atom across a wide range of chemical systems.

2.7 Surface Calculations

The above sections describe a computational methodology dealing exclusively with bulk crystal simulations, which consider the lattice to extend infinitely in three-dimensions. However, it is often the case that the electrochemical performance of a cathode material is linked to its surface structure and energetics. Computational techniques are an important tool for obtaining detailed surface information, as it is difficult to extract from experiment alone. Simulation can be used to explore surfaces on an atomic level, detailing their energetics and their local surface relaxation, this allows information on particle morphology to be gained.

There are two different methods for computationally generating surfaces. The first produces a series of non-interacting 'slabs' by upholding periodic boundary conditions, while the second breaks symmetry along one lattice vector in order to simulate a bulk vacuum transition with two-dimensional periodic boundary conditions. Three-dimensional periodic surfaces are discussed below as this is the method used in this work.

A number of different types of surface exist, as defined by Tasker[152]; the type of surface needs to be considered when setting up the simulation cell. Type I surfaces are formed by stoichiometric charge-neutral layers, and therefore no dipole moment is present normal to the surface. In Type II surfaces, although each layer is not charge neutral, a finite group of layers form a repeating unit which is charge-neutral, with a zero net dipole moment orthogonal to the surface. For Type III surfaces there is always a dipole moment present normal to the surface, independent of how the surface is cleaved and how many layers make up the repeat unit, therefore these are not stable surfaces. However,

Type III surfaces are able to form naturally when surface reconstruction or oxidation/reduction occurs, removing the dipole moment and leading to a non-stoichiometric surface.

2.7.1 Three-Dimensional Periodic Surfaces

Three-dimensional surface calculations maintain full periodic boundary conditions and generate images of the cell along all Cartesian vectors. Each cell is made of two regions: a slab region contains all the ions, and a vacuum region that separates the slabs from their periodic images. It is important that the vacuum is large enough to ensure that the slabs are not influenced by their periodic images, but the use of an arbitrarily large vacuum region adds considerably to the computational expense of the technique. Therefore a compromise is needed and is obtained through convergence testing, where the vacuum thickness is increased until the surface energies remain constant, at which point the slabs are considered isolated from each other. The slab is composed of two identical surfaces with exactly opposite Miller indices, such that inversion symmetry exists through the centre of the slab.

The surface energy per unit area ($E_{sirface}$) can be calculated using equation 2.49. Where E_S defines the total energy of the slab, E_B the energy of the bulk and A the area of one surface of the slab. The factor of 2 originates from the fact that each slab contains two identical surfaces.

$$E_{surface} = \frac{E_S - E_B}{2A} \tag{2.49}$$

The thickness of the slab is an essential parameter needed to calculate accurate results. Ideally, ions in the centre of the slab should be able to demonstrate bulk behaviour to ensure that all surface related relaxation is correctly accounted for. Therefore the slab should be sufficiently thick. However, increasing the slab thickness beyond a certain point will not give more accurate results but will increase the computational expense of the calculation. Therefore, convergence testing of the slab thickness is needed.

2.8 Computational Equipment

The different types of calculations carried out (atomistic, large scale MD and DFT) require different hardware to be used, due to their differing computational demands. Atomistic calculations (using GULP) can run on a a local desktop machine. These jobs typically use a single core on a Quad-core processor with 8GB of RAM.

The more computationally expensive MD and DFT calculations were carried out on either the UK's high performance computing facility ARCHER, or the high performance computing facility located at the University of Bath, BALENA. These calculations required 3-144 cores and ran in parallel for 3-48 hours. MD calculations were carried out using the LAMMPS code[133], and all DFT simulations used VASP.[134,135]

3 | Defect Chemistry and Na ion diffusion in $NaFePO_4$

'Dark and difficult times lie ahead.'

J. K. Rowling, Harry Potter and the Goblet of Fire

3.1 Background

As discussed in **Chapter 1**, $NaFePO_4$ has been considered a possible cathode material for Na-ion batteries, based on the success of olivine $LiFePO_4$. However, the olivine structure is not the most thermodynamically stable form of $NaFePO_4$ which crystallises as the maricite polymorph. Both structures are shown in Figure 3.1. The olivine and maricite polymorphs have similar structures in terms of phosphate networks. In the maricite form Na^+ and Fe^{2+} ions occupy the M1 and M2 sites respectively. In the olivine structure the positions of Na^+ and Fe^{2+} are reversed. The thermodynamically stable forms $LiFePO_4$ and $NaFePO_4$ differ due to the variation in ionic radius between Li^+ and Na^+, 0.76 Å and 1.02 Å respectively. Fe^{2+} is similar in size to Li^+ with an ionic radius of 0.78 Å. As a result the transition metal resides in the M2 sites because of its higher charge. However, Na^+ has a much larger ionic radius than Fe^{2+}, therefore in $NaFePO_4$

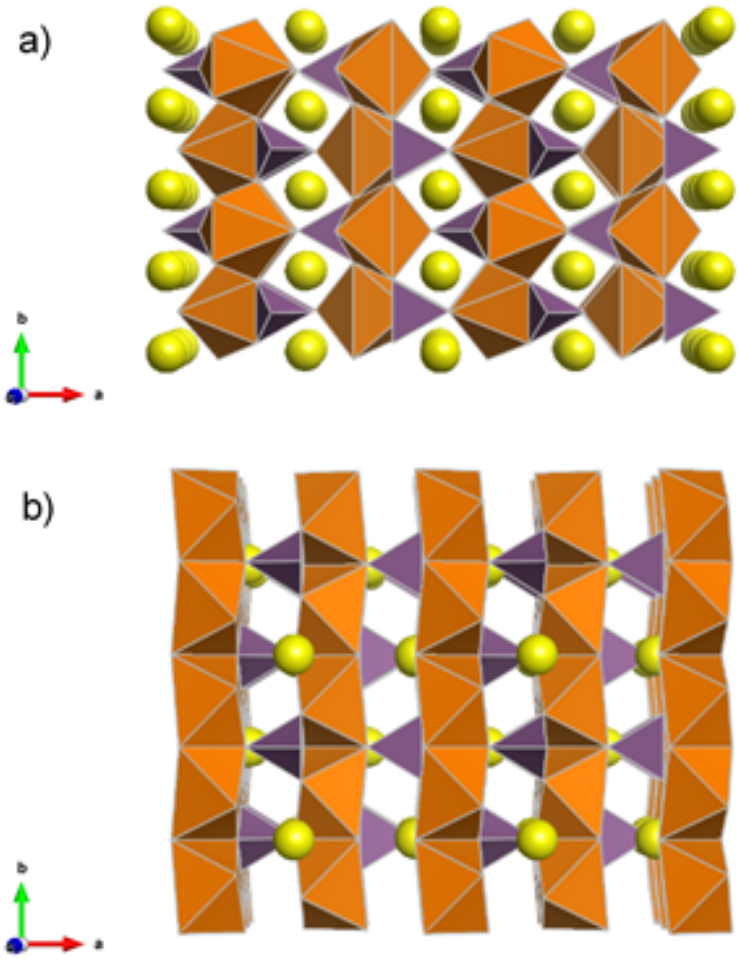

Figure 3.1: *Crystal structures of $NaFePO_4$, a) olivine and b) maricite (Yellow spheres: Na^+ ions; orange octahedra: FeO_6; purple tetrahedra: PO_4).*

it is preferential for the Na^+ ion to sit on the M2 site rather than the transition metal.[85]

The structure of the maricite form of $NaFePO_4$ is such that the Na^+ ions are completely surrounded by PO_4^{3-} tetrahedra and it has been reported that the compound exhibits poor electrochemical behaviour in the bulk crystalline form.[59,86,87] A study on $NaFePO_4$ by Prosini et al.[88] has shown that extraction of sodium from the maricite structure is possible, but with a low discharge rate and with a capacity limited to approximately one third of its theoretical value. Work by Kim et al.[89] reports that nano-scaled maricite $NaFePO_4$ is able to function as a high-performance electrode through the formation of amorphous

$FePO_4$ upon Na extraction. Here maricite $NaFePO_4$ is considered in the bulk crystalline form only.

Although the maricite phase of $NaFePO_4$ is its more thermodynamically stable form, synthesis methods have been devised in order to prepare the olivine polymorph. The first method to be successfully implemented was cation exchange from carbon-coated olivine $LiFePO_4$[84]. Similar techniques have been devised in order to study the electrochemical behaviour of the compound.[86,91,92,153,154]

Our focus here is to probe the defect and diffusion properties of both the olivine and maricite forms of $NaFePO_4$. In this study a combination of atomistic energy minimisation and molecular dynamics methods have been applied to examine the processes governing the defect chemistry and ion migration.

3.2 Structural Modelling

Both olivine and maricite $NaFePO_4$ are orthorhombic members of the *Pnma* space group.[59,85,155,156] The olivine structure consists of FeO_6 octahedra which are linked by corner sharing along the *ab*-plane; PO_4 tetrahedra sit between these planes and share both corners and edges with the FeO_6 octahedra. The Na^+ ions are located in the open channels along the *b*-axis. Na^+ ions occupy M2 sites in the maricite structure while Fe^{2+} sits in M1 positions, the opposite to that observed in the olivine structure. In the maricite framework FeO_6 edge-sharing octahedra lie in ordered layers along the *b*-axis. These are linked by corner-sharing PO_4 tetrahedra, and by corner sharing between the FeO_6 octahedra of one layer and the sodium octahedra of the adjacent layer.

The starting point for any potentials based study is to reproduce experimentally observed structures. The potential parameters used to model $NaFePO_4$ were taken from a previous study on the olivine polymorph by Tripathi et al.[85] and are listed in Tables 3.1 and 3.2.

The lattice parameters of the two structures were calculated with good agreement to experimental data (within 2.2%), shown in Table 3.3.[85,155,157]

Table 3.1: *Two-body short-range potential parameters for $NaFePO_4$.*[85]

Interaction	**A (eV)**	**ρ (Å)**	**C (eV.Å^6)**	**Y (e)**	**K (eV.Å^{-2})**
Na^{+}-O^{2-}	560	0.32	0.0	1.0	99999.0
Fe^{2+}-O^{2-}	1105.2409	0.3106	0.0	2.997	19.26
P^{5+}-O^{-2}	897.2648	0.3577	0.0	5.0	99999.0
O^{2-}-O^{-2}	22764.3	0.149	44.53	-2.96	65.0

Table 3.2: *Three-body interaction for $NaFePO_4$.*[85]

Bond type	**K (eV.rad^{-2})**	**θ_0 (deg)**
O^{2-}-P^{5+}-O^{2-}	1.3226	109.47

Table 3.3: *Calculated lattice parameters for olivine and maricite $NaFePO_4$ and comparison to previously reported experimental values.*

Lattice Parameters	**a (Å)**	**b (Å)**	**c (Å)**	**Na-O (Å)**	**Fe-O (Å)**	**P-O (Å)**
Olivine $NaFePO_4$						
Experimental[85,155]	10.4109	6.2283	4.9521	2.3443	2.1852	1.5393
Calculated	10.3402	6.1647	4.8872	2.3352	2.1478	1.5510
% Δ	-0.7	-1.0	-1.3	-0.004	-0.02	0.008
Maricite $NaFePO_4$						
Experimental[157]	8.9628	6.8429	5.2827	2.4443	2.1761	1.5443
Calculated	8.7737	6.7353	4.9579	2.4029	2.1271	1.5481
% Δ	-2.2	-1.6	-1.4	-0.02	-0.02	0.002

3.3 Intrinsic Defects

A series of isolated point defect energies were calculated for both olivine and maricite structures of $NaFePO_4$. The combination of these values with the necessary lattice energies allows the energies of formation for Schottky, Frenkel and anti-site type defects to be calculated. The formation of these defects are shown below (equations 3.1-3.6), using Kröger-Vink notation.

Na Frenkel:

$$Na_{Na}^{X} \rightarrow Na_{i}^{\bullet} + V_{Na}^{/} \tag{3.1}$$

Fe Frenkel:

$$Fe_{Fe}^{X} \rightarrow Fe_{i}^{\bullet\bullet} + V_{Fe}^{//} \tag{3.2}$$

Full Schottky:

$$Na_{Na}^{X} + Fe_{Fe}^{X} + P_{P}^{X} + 4O_{O}^{X} \rightarrow V_{Na}^{/} + V_{Fe}^{//} + V_{P}^{/////} + 4V_{O}^{\bullet\bullet} + NaFePO_{4(surface)} \tag{3.3}$$

FeO Schottky-like:

$$Fe_{Fe}^{X} + O_{O}^{X} \rightarrow V_{Fe}^{//} + V_{O}^{\bullet\bullet} + FeO_{(surface)} \tag{3.4}$$

Na_2O Schottky-like:

$$2Na_{Na}^{X} + O_{O}^{X} \rightarrow 2V_{Na}^{/} + V_{O}^{\bullet\bullet} + Na_2O_{(surface)} \tag{3.5}$$

Na/Fe antis-site pair:

$$Na_{Na}^{X} + Fe_{Fe}^{X} \rightarrow Fe_{Na}^{\bullet} + Na_{Fe}^{/} \tag{3.6}$$

The calculated energies for intrinsic defect formation in the olivine and maricite structures of $NaFePO_4$ are listed in Table 3.4, from which two main points emerge. Firstly, it can be concluded from the high energies of formation for the Frenkel and Schottky-type defects that such intrinsic defects would be effectively non-existent in both phases of the $NaFePO_4$ structure. Secondly, the lowest formation energy is found for the Na/Fe anti-site defect pair in both systems, indicating that this is the most favourable type of intrinsic disorder. A smaller formation energy is calculated for anti-site defects in the maricite phase

Table 3.4: *Calculated defect formation energies for the olivine and maricite phases of $NaFePO_4$.*

Defect type	Olivine (eV)	Maricite (eV)
Na Frenkel	2.42	2.28
Fe Frenkel	5.63	5.82
Full Schottky	29.38	20.63
FeO Schottky	6.64	4.19
Na_2O Schottky-like	11.35	9.93
Na/Fe anti-site pair	0.88	0.29

than the olivine phase, suggesting that these defects are likely to occur in higher concentration in the maricite compound.

In the context of ion diffusion, the anti-site defects bear more significance in the case of olivine materials, as their presence blocks the only available 1D channel for alkali ion migration.[85,158] Due to the lack of open migration pathways in the maricite structure, anti-site defects are unlikely to negatively affect the diffusion properties. Anti-site defects in olivine $NaFePO_4$ are further explored using molecular dynamics in section 3.5.

3.4 Energetics and Pathways for Na ion Migration

Examination of the intrinsic Na^+ ion mobility in $NaFePO_4$ systems is of vital interest when considering their use as cathode materials in sodium-ion batteries.

The activation energies of Na^+ migration along the lowest energy pathway for both the olivine and maricite compounds are listed in Table 3.5, along with the Na-Na site distances. The activation energy is significantly lower in the olivine structure (E_a = 0.37 eV) than in the maricite structure (E_a = 1.78 eV).

In olivine $NaFePO_4$, sodium diffusion is along a curved one-dimensional pathway in the [010] direction, between sites 3.08 Å apart (Figure 3.2a).

In maricite $NaFePO_4$, sodium diffusion is along the [011] direction, in a two-dimensional network between sites 4.64 Å apart (Figure 3.2b). Thus, the

Table 3.5: *Na-Na separations and activation energies of Na migration in both olivine and maricite $NaFePO_4$.*

Compound	Na-Na distance (Å)	E_a (eV)
Olivine	3.08	0.37
Maricite	4.63	1.78

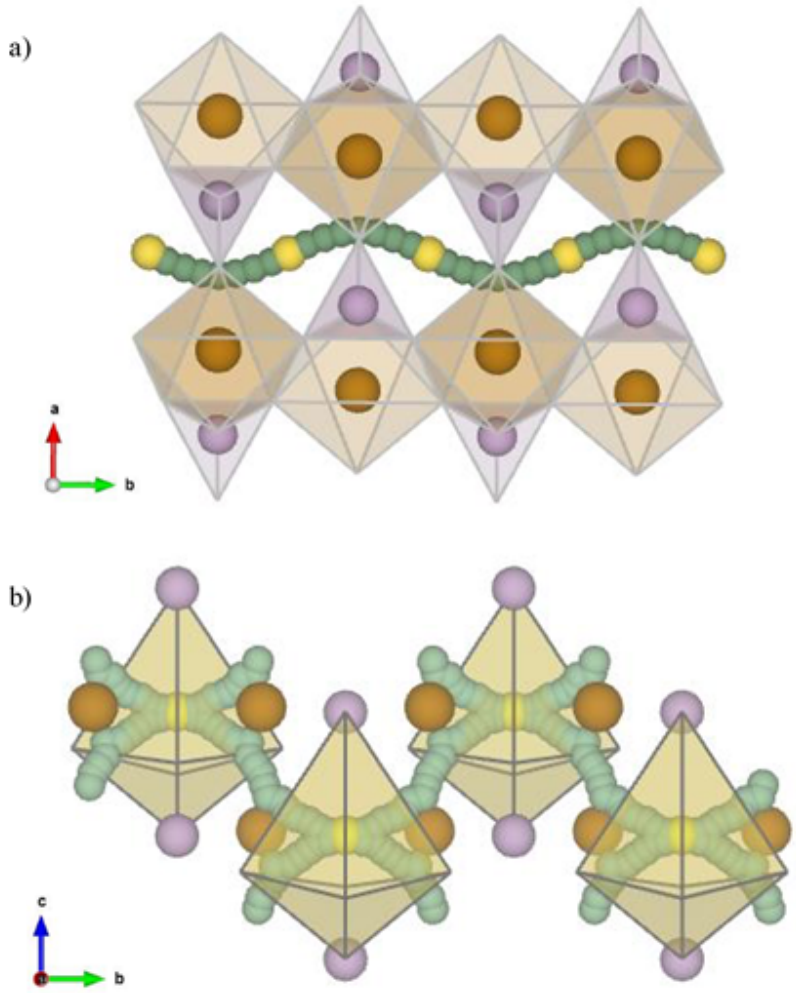

Figure 3.2: *Lowest energy Na migration pathway in a) olivine and b) maricite $NaFePO_4$ (yellow octahedra: NaO_6; purple tetrahedra: PO_4; purple spheres: P^{5+}; brown octahedra: FeO_6; brown spheres: Fe^{2+}; green channels: Na-ion migration pathways*

low discharge rate observed by Prosini et. al.[88] is an atomic-scale feature of the material related to the fundamental difference in crystal structure.

The curved one-dimensional pathways in olivine $NaFePO_4$ are in agreement with experimental diffraction studies on $LiFePO_4$, shown in Figure 3.3.[37] It had previously been assumed that ion migration would take the shortest pathway between adjacent sites, a linear path. Although migration via a curved pathway will require ions to cover greater migration distances, a non-linear trajectory allows the ions to minimise their repulsions with surrounding octahedra and tetrahedra.[158]

MD calculations were carried out using the LAMMPS code.[133] The calculations were carried out on a simulation box, with periodic boundary conditions, made up of 6 x 10 x 12 unit cells for the olivine structure and 6 x 8 x 10 unit cells for maricite consisting of 20160 and 13440 atoms respectively. The initial configurations of both structures contained 10% Na vacancies (and corresponding Fe^{3+} species), which were randomly distributed. The Pedone partial charge model[144] was used for these simulations. Three initial configurations were investigated for each structure and the results were averaged

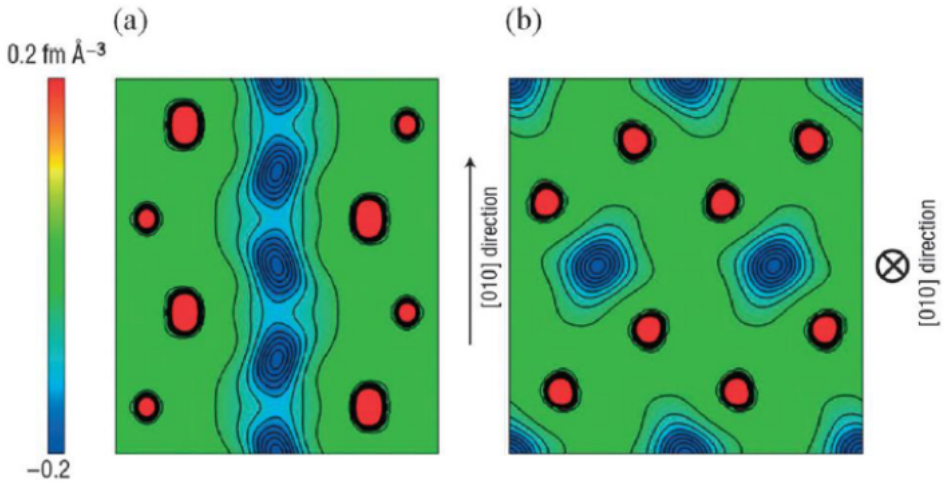

Figure 3.3: *Experimental visualisation of the Li-ion diffusion pathway in $LiFePO_4$. a) Contour map along [001] plane, Li-ions diffuse along the curved one-dimensional pathway along the [010] direction. b) Contour map along [010] plane; all atoms remain near their original positions.*[18,37]

for each system. Simulation runs were carried out using an NPT ensemble and a time step of 2 fs, for long runs of 10 ns, at temperatures in the range 300-873 K. The mean squared displacements (MSDs) of sodium in both olivine and maricite structures of $NaFePO_4$ are shown in Figure 3.4. The results clearly indicate that there is only significant ion diffusion in olivine $NaFePO_4$. The lack of Na^+ ion diffusion within the maricite structure is in accord with the high migration energy (Table 3.5).

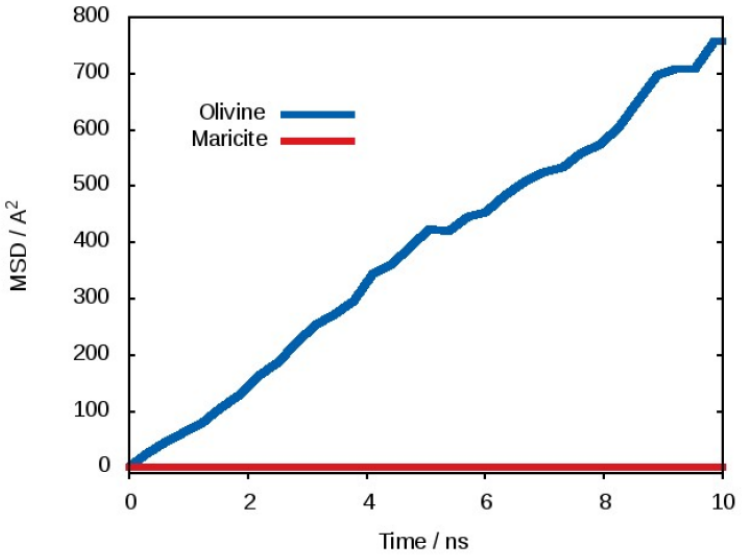

Figure 3.4: *Mean squared displacement (MSD) of sodium ions in olivine (blue) and maricite (red)* $Na_{0.9}FePO_4$ *at 673 K.*

The Na-ion diffusion coefficients (D_{Na}) for both olivine and maricite $NaFePO_4$, calculated using equation 3.7, at a range of temperatures are listed in Table 3.6.

$$D = (\frac{1}{6t}) < [r(t)]^2 > \tag{3.7}$$

At 300 K, D_{Na} values of 4.3 x 10^{-9} cm^2s^{-1} and 6.7 x 10^{-13} cm^2s^{-1} were calculated for the olivine and maricite structures respectively. As there is no lithium analogue of the maricite structure, there is no data for direct comparison between $NaFePO_4$ and $LiFePO_4$ for this polymorph. Experimentally obtained values of D_{Li} for olivine $LiFePO_4$ have been reported at approximately 10^{-9} cm^2s^{-1} at 150 °C,[159] in the same range as those calculated for olivine $NaFePO_4$.

Table 3.6: *Calculated diffusion coefficients (D_{Na}) for maricite and olivine $NaFePO_4$.*

Temperature (K)	Olivine (cm^2s^{-1})	Maricite (cm^2s^{-1})
300	4.3 x 10^{-9}	6.7 x 10^{-13}
400	5.7 x 10^{-8}	1.8 x 10^{-12}
500	1.9 x 10^{-7}	2.7 x 10^{-13}
673	1.2 x 10^{-6}	2.7 x 10^{-13}
773	2.3 x 10^{-6}	2.8 x 10^{-13}
873	3.1 x 10^{-6}	9.5 x 10^{-11}

Previous experimental reports on other potential Na-ion cathode materials have quoted sodium diffusion coefficients in similar ranges as calculated for olivine here. For example, layered oxide based materials have reported diffusion coefficients at approximately 10^{-11} cm^2s^{-1} and 10^{-10} cm^2s^{-1} for $NaCoO_2$ [160] and $NaMnO_2$ [161] respectively.

Figure 3.5 shows the MSD plots of Na^+ ions in olivine $Na_{0.9}FePO_4$ at different temperatures. It is clear that the gradient of the MSD is increasing as the temperature increases. This trend is also present in the calculated diffusion coefficients (Table 3.6). However, it is not as clear in the diffusion coefficients calculated for the maricite structure. The calculated difference between D_{Na} for the different temperatures is small, indicating that even at high temperatures significant motion is not introduced to Na^+ ions.

An Arrhenius plot for Na diffusion in the olivine system is shown in Figure 3.6. This data can be used to estimate the activation energy of migration using equation 3.8.

$$lnD = \frac{-E_a}{k_B T} + lnA \tag{3.8}$$

An activation energy of 0.26 eV was calculated, indicating that there would be high Na^+ ion mobility within this olivine structure. This can be compared with a previous theoretical study on olivine $LiFePO_4$ that reported an activation energy for Li migration of 0.29 eV.[162] This implies that the alkali metal ion migration

within $NaFePO_4$ is slightly more favourable than that in olivine $LiFePO_4$.

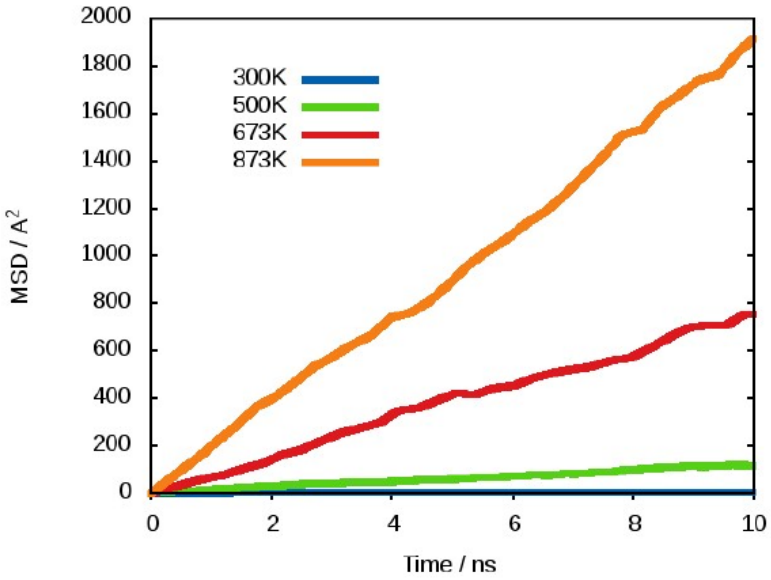

Figure 3.5: *Mean squared displacement (MSD) of sodium ions in olivine $Na_{0.9}FePO_4$ at different temperatures, 300 K (blue), 500 K (green), 673 K (red) and 873 K (orange).*

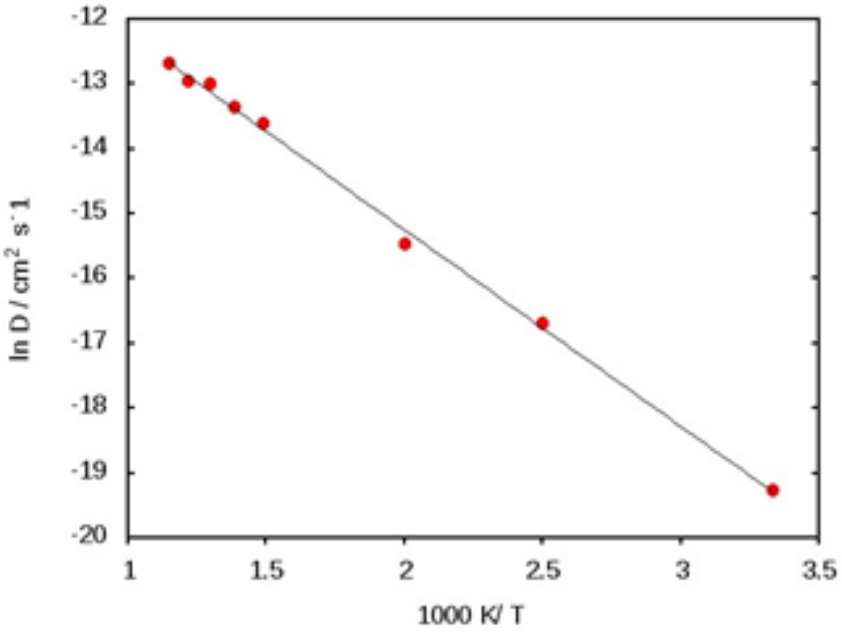

Figure 3.6: *Arrhenius plot (lnD vs. $\frac{1}{T}$) for $Na_{0.9}FePO_4$.*

3.5 Effect of Anti-site Defects on Na Diffusion

As shown in Table 3.4, the most favourable type of intrinsic defect is the Na/Fe anti-site defect in both the olivine and maricite structures. The presence of these defects potentially blocks the open channels through which Na diffusion takes place in the olivine material. MD simulations were used to determine the effect this blocking would have on the diffusion of the Na^+ ions.

Calculated Na^+ diffusion coefficients for the olivine system with 10% vacancies and with 10% vacancies and 2% anti-site defects, are listed in Table 3.7. Figure 3.7 shows a comparison of MSDs. It is clear that the presence of the anti-site defects decreases the gradient of the MSD. A D_{Na} of 7 x 10^{-10} cm^2s^{-1} was calculated for the system with 2% anti-site defects at 300 K. The comparison of this value with that calculated for the 10% Na^+ vacancy system shows that the presence of anti-site defects slows the diffusion of the Na^+ ions by an order of magnitude. This is likely due to the blocking of the *b*-axis channels.

Figure 3.8 shows the Arrhenius plot for both the 10% Na vacancy model and the 2% anti-site defect model. The additional effect of the anti-site defects can also be seen here. An increase in the activation energy of Na diffusion of 0.32 eV was calculated for the anti-site containing system. This indicates that Na mobility in this system is lower than predicted with only vacancy defects present, where an activation energy of 0.26 eV was calculated.

Table 3.7: *Calculated diffusion coefficients (D_{Na}) for olivine $NaFePO_4$ with and without 2% anti-site defects.*

Temperature (K)	**No Anti-site Defects (cm^2s^{-1})**	**2% Anti-site Defects (cm^2s^{-1})**
300	4.3 x 10^{-9}	7.2 x 10^{-10}
400	5.7 x 10^{-8}	1.7 x 10^{-8}
673	1.2 x 10^{-6}	8.8 x 10^{-7}
873	3.1 x 10^{-6}	2.4 x 10^{-6}

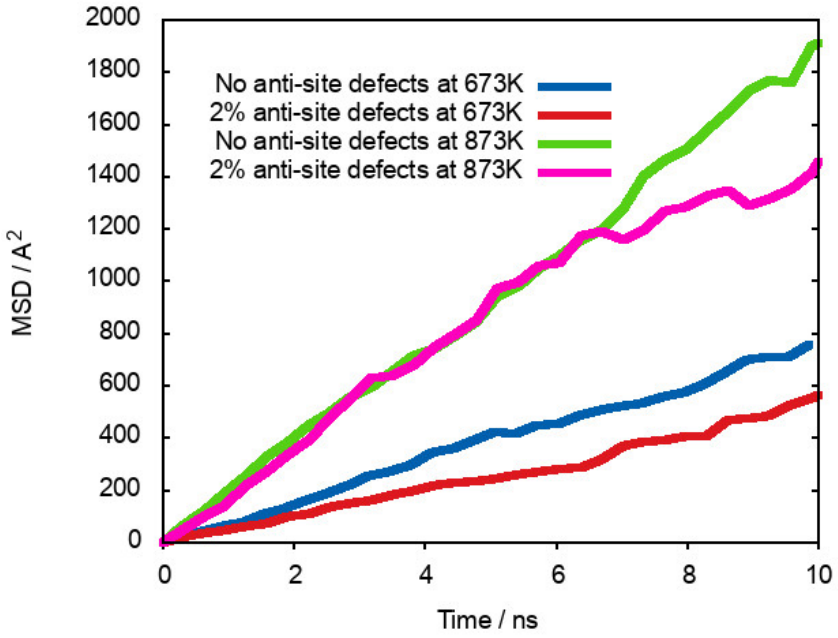

Figure 3.7: *Mean squared displacement (MSD) of sodium ions in olivine $Na_{0.9}FePO_4$ at 673 K (blue) and 873 K (green), and with 2% anti-site defects present at 673 K (red) and 873 K (pink).*

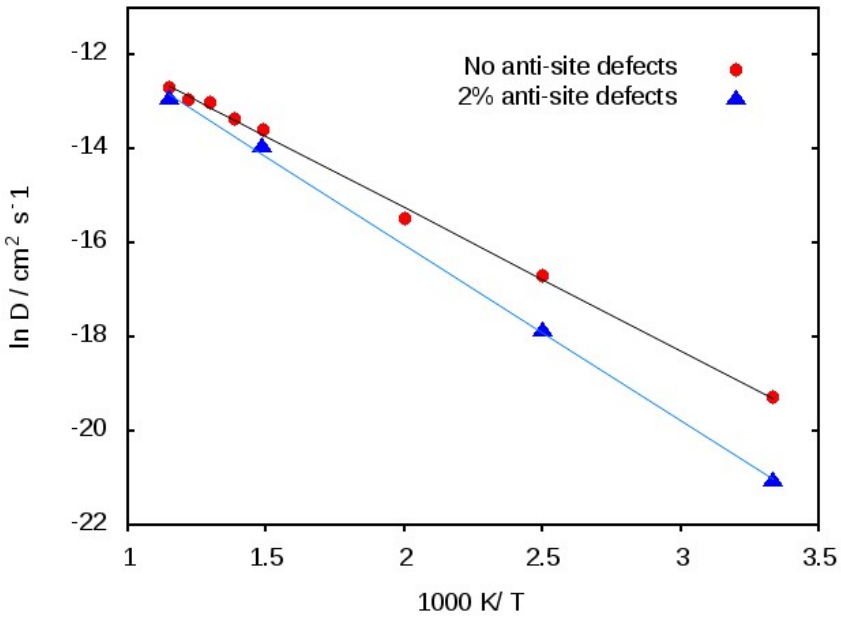

Figure 3.8: *Arrhenius plot (lnD vs. $\frac{1}{T}$) for $Na_{0.9}FePO_4$ with no anti-site defects present (red circles), and with 2% anti-site defects present (blue triangles).*

MD density plots of the Na^+ ion trajectory averaged over the simulated timescale show the migration pathways taken by the mobile Na-ions in the olivine systems and allow the effect of the anti-site defects to be visualised. Figure 3.9a shows the sodium density plot of the $Na_{0.9}FePO_4$ systems. Curved pathways running parallel to the *b*-axis are observed with no inter-channel diffusion. This is in excellent agreement with the pathway predicted using energy minimisation techniques (Fig. 3.2a).

Figure 3.9b shows the sodium density plot for the $Na_{0.9}FePO_4$ system containing 2% anti-site defects. The presence of an Fe^{2+} ion within the channel (as part of the anti-site defect) interrupts the migration of sodium. This blocking effect has also been seen using MD simulations of olivine $LiFePO_4$.[162] However, in $LiFePO_4$ the blocking was partly mitigated by Li^+ ions migrating locally between the *b* -axis channels either along the *a*- or *c*-axes depending on the location of the defect. Here, there is no indication that any inter-channel migration occurs. This is likely due to the difference in ion size between Na^+ and Li^+. The larger ionic radius of the Na^+ ion could prevent the ions from being able to migrate along pathways between *b*-axis channels.

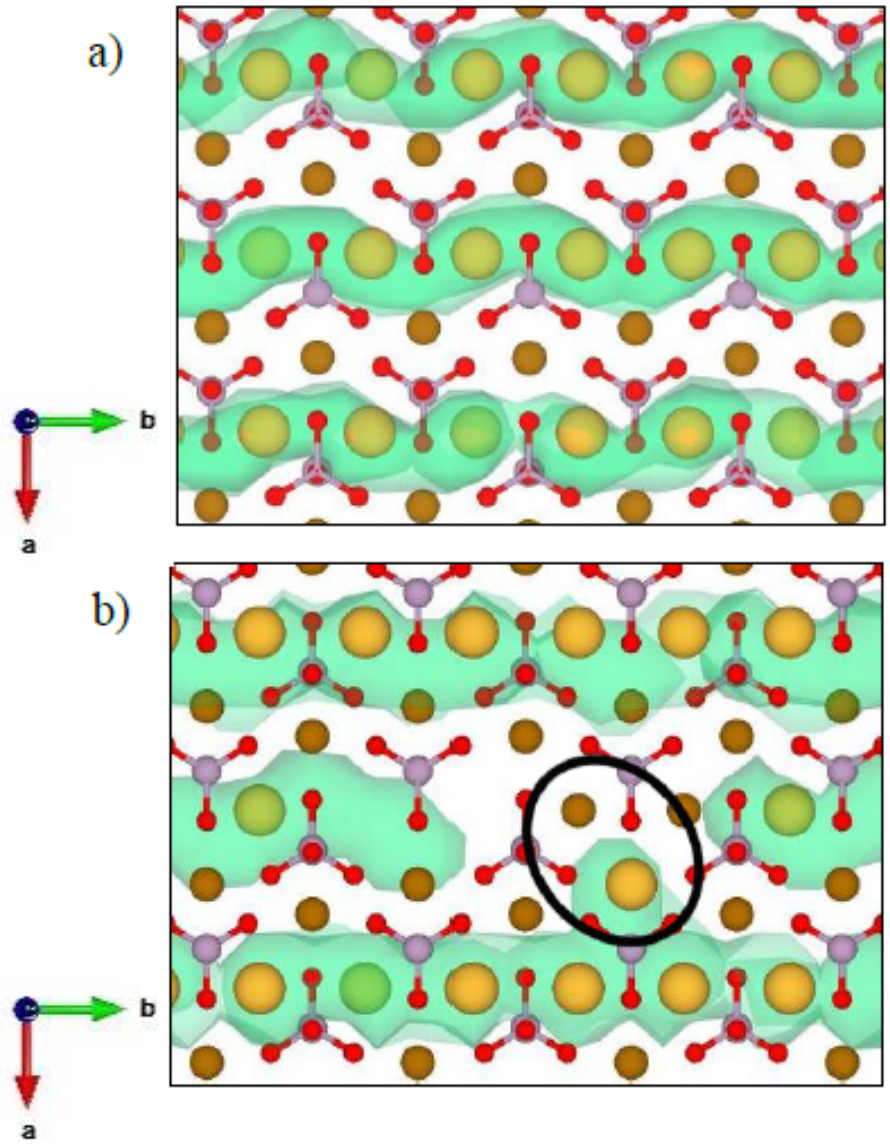

Figure 3.9: *Sodium density plot for olivine $Na_{0.9}FePO_4$ with a) no anti-site defects present and b) with 2% anti-site defects, anti-site defect highlighted (yellow spheres: Na^+ ions; brown spheres: Fe^{+2} ions; purple spheres: phosphorus; red spheres: oxygen and green channels: Na pathways).*

3.6 Chapter Summary

A combination of energy minimisation and molecular dynamics (MD) techniques have been used to provide insight into the defect and migration properties of both olivine and maricite structured $NaFePO_4$.

(a) Firstly, the atomistic potential model accurately reproduced the experimental structures of both olivine and maricite $NaFePO_4$. The most favourable intrinsic defect was found to be the Na/Fe anti-site pair in both structures.

(b) Secondly, the activation barrier for Na-ion diffusion in the olivine polymorph is much lower than that calculated for the maricite analogue. The lowest energy Na^+ ion migration pathway predicted for the olivine structure is along the *b*-axis channel, in line with that observed in olivine $LiFePO_4$. The high-energy barriers predicted in the maricite framework predict that there will be no substantial Na^+ ion diffusion within this structure, which would impede its electrochemical performance. This was confirmed by the MD simulations on maricite $NaFePO_4$, where a very low diffusion coefficient (D_{Na}) of approximately 7 x 10^{-13} cm^2s^{-1} at 300 K was calculated. The lack of Na-ion diffusion within the maricite structure would make it a poor bulk cathode material.

(c) Finally, MD simulations on olivine $NaFePO_4$ indicate a relatively high D_{Na} of 4 x 10^{-9} cm^2s^{s-1} (300 K), which is consistent with a high rate cathode material. However, the presence of anti-site defects is shown to impede Na-ion diffusion in olivine $NaFePO_4$ to a much greater extent than in $LiFePO_4$. There is no evidence of inter-channel hopping in $NaFePO_4$.

Overall our atomic-scale study of olivine and maricite phosphates indicates clear fundamental differences in their intrinsic defect chemistry, and bulk Na diffusion rates, which help to rationalise their electrochemical behaviour.

4 | Effect of Strain on Ion Migration and Defect Formation in Olivine $NaFePO_4$ and $LiFePO_4$

'We must all face the choice between what is right and what is easy.'

J. K. Rowling, Harry Potter and the Goblet of Fire

4.1 Background

As covered in **Chapter 1**, the development of cheap and safe cathode materials is of particular importance for large-scale batteries. For olivine-type cathode materials to be considered for portable electronic or electric vehicle applications, an improvement of their rate performance would be required. Both $LiFePO_4$ and $NaFePO_4$ would require significant improvement in their ionic conductivities.

Previous strategies to optimise intercalation properties have largely involved chemical doping and morphology modulation. The most successful approaches at the current time involve nanosizing or carbon coating.[163,164] The charge/discharge rate performance of olivine $LiFePO_4$ has been improved by

shortening the diffusion distances by preparing nanosized particles, but higher rates are required for certain applications, such as electric vehicles.[165]

The effect of strain on the ionic conductivity of materials has mostly been studied in the solid oxide fuel cell (SOFC) field. The controlled use of strain has attracted interest as a means of lowering the operating temperature of solid electrolyte materials based on Y/ZrO_2 for SOFCs, while still offering high ionic conductivity.[166,167] The report that the formation of thin layers of YSZ greatly improved its conductivity prompted both experimental and theoretical studies on the transport properties of functional oxides.[168–173]

The manipulation of lattice strain has increasingly become considered as a possible design strategy to improve the functional properties of various materials, this has included superconductivity,[174–176] ionic conductivity,[177] and ferroelectricity.[178,179] However, the effect mechanical strain on battery cathode materials has not been extensively studied, with only a limited number of reports in the literature.[180–189]

Experimentally, lattice strain in thin films is introduced by substrate film mismatch (*i.e.* differences in d spacing), as shown in Figure 4.1. Lattice mismatch results in in-plane tensile or compressive strain in the deposited layer. This will be biaxial strain for thin films deposited onto a crystalline substrate. In the case of a perfectly elastic system, the unit cell volume is unchanged and the out-of-plane cell parameters increase or decrease appropriately (Figure 4.1b). Lattice strain introduced by film/substrate mismatch is limited to thin films on the nanoscale. When dealing with samples of thicker films, the strain is released as the distance from the film/substrate interface increases into the bulk of the material (Figure 4.1c).

Calculations were carried out, for the first time on strained olivine $LiFePO_4$ and $NaFePO_4$ systems using energy minimisation and MD techniques.[190] A previous experimental study of olivine $LiFePO_4$ by Shahid et. al.[183] reports that the application of strain on the material (achieved by reducing particle size to the nanoscale) increases electronic conductivity, however ion transport was not fully characterised. Here the application of biaxial strain on the two olivine

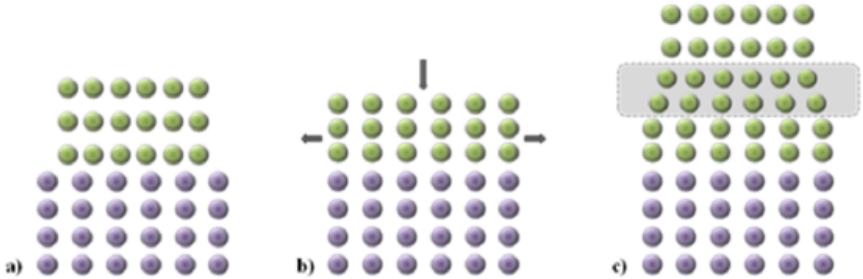

Figure 4.1: *Schematic representation of the effect of tensile lattice strain between a thin film (green) and substrate (purple), due to lattice mismatch. a) no mismatch; b) tensile-strained thin film; c) partially strained film, showing strain release far from the substrate interface.*

systems is examined. The author acknowledges Dr. Cristina Tealdi (University of Pavia, Italy) who performed the calculations relating to $LiFePO_4$. A published version of this work[190] is given in **Appendix E**.

4.2 Structural Modelling

The unstrained olivine unit cell used for the static lattice calculations in section 3.2 were the starting point for $NaFePO_4$. The potential parameters used for $LiFePO_4$ are give in Table 4.1. The structure was reproduced to a high degree of accuracy as shown in Table 4.2.

Strain was applied biaxially, with the two strained axes fixed at values between -4% and +4%. The third axes was allowed to relax at each point to account for this strain. Figure 4.2 shows the influence the application of biaxial

Table 4.1: *Two-body short-range potential parameters for $LiFePO_4$.*[85]

Interaction	A (eV)	ρ (Å)	C (eV.Å^6)	Y (e)	K (eV.Å^{-2})
Li^+-O^{2-}	632.1018	0.2906	0.0	1.0	99999.0
Fe^{2+}-O^{2-}	1105.2409	0.3106	0.0	2.997	19.26
P^{5+}-O^{-2}	897.2648	0.3577	0.0	5.0	99999.0
O^{2-}-O^{-2}	22764.3	0.149	44.53	-2.96	65.0

Table 4.2: *Calculated lattice parameters for olivine $LiFePO_4$ and comparison to previously reported experimental values.*

	Experimental	Calculated	% Δ
a (Å)	10.3380	10.3701	0.30
b (Å)	6.0110	6.0136	0.04
c (Å)	4.6950	4.6722	-0.49

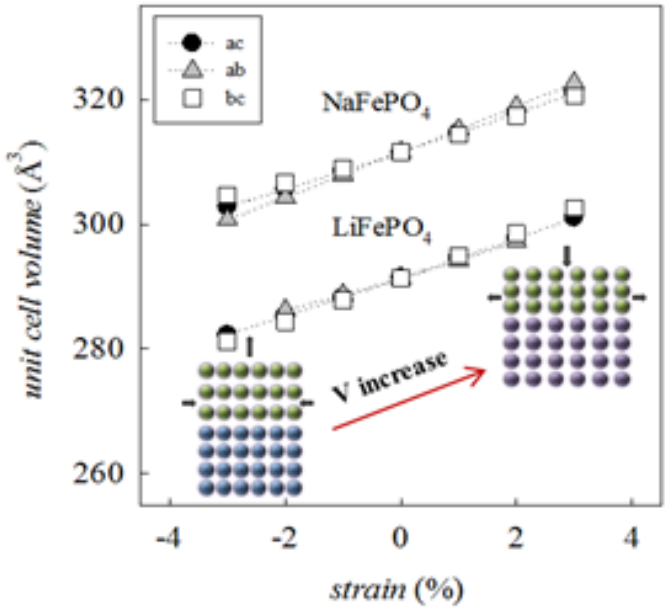

Figure 4.2: *Calculated unit cell volume as a function of strain for $LiFePO_4$ and $NaFePO_4$ with a schematic of the effect of compressive (<0%) and tensile (>0%) lattice strain.*

strain has on the unit cell volume for $NaFePO_4$ and $LiFePO_4$. As expected, compressive strain causes the unit cell volume to decrease while tensile strain is accompanied by an increase in volume.

4.3 Li^+/Na^+ Ion Conduction

The migration pathways in bulk $NaFePO_4$ are shown in section 3.4. The Li^+ migration pathways in $LiFePO_4$ were initially predicted using calculations[158] and were subsequently confirmed using neutron diffraction methods.[37] Li^+/Na^+

diffusion follow the same pathways in both structures, a curved path in the [010] direction, B in Figure 4.3. The calculated migration energies are 0.55 and 0.37 eV for $LiFePO_4$ and $NaFePO_4$ respectively.

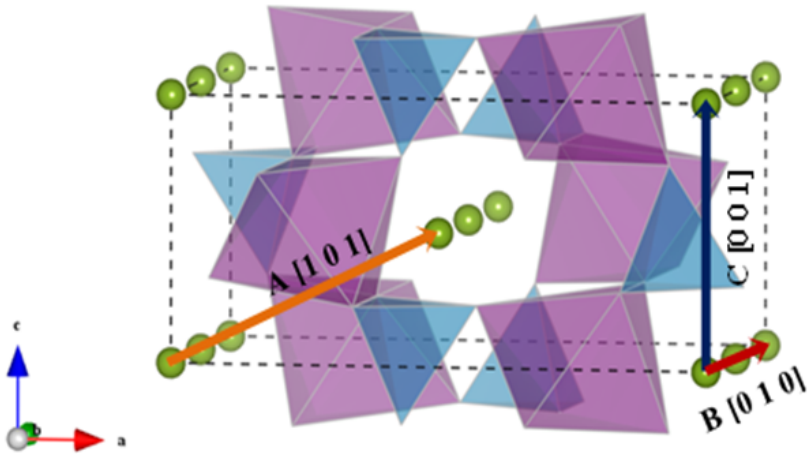

Figure 4.3: *Schematic of the possible migration paths in olivine $LiFePO_4$/$NaFePO_4$. Blue tetrahedra: PO_4; purple octahedra: FeO_6 and green spheres: Li^+/Na^+.*

The effect different types of biaxial strain have on the calculated migration energy in the [010] direction is shown in Figure 4.4 for both $LiFePO_4$ and $NaFePO_4$. For both systems the migration energy is increased slightly with the application of tensile *ab* and *bc* strain. However, the energy barriers decrease with *ac* strain, reaching a value of approximately half that of the unstrained system with the application of 3% tensile strain. For $LiFePO_4$ the calculated energy migration barrier for Li^+ decreases from 0.55 eV to 0.28 eV, while the barrier for migration of Na^+ decreases from 0.37 eV to 0.16 eV for $NaFePO_4$. These reductions in migration energy with tensile strain is in agreement with a previous DFT study on $LiFePO_4$ by Lee et al.[182]

The changes predicted in the migration barriers for diffusion can be interpreted in terms of structural modifications. In particular, there is a relation between the variation in the migration barrier and the ion-ion hopping distance along with applied strain. The energy barrier for migration is also directly

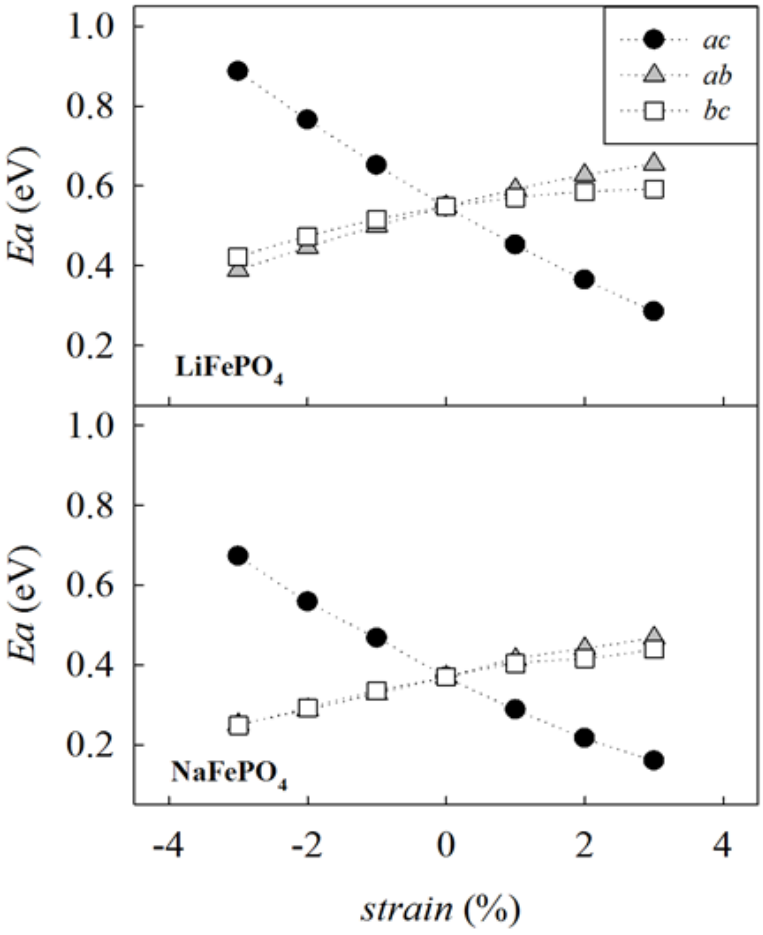

Figure 4.4: *Alkali-ion migration barrier along the [010] direction as a function of strain for $LiFePO_4$ (above) and $NaFePO_4$ (below).*

affected by the strength of the bond to be broken during the hopping of the ion, and the space available for migration at the saddle point configuration. For these final two aspects, elongation of the bonds around the migrating ion results in a decreased migration barrier. These three factors are shown in Figure 4.5 for $LiFePO_4$.

For $LiFePO_4$, the Li-Li hopping distance for migration along the [010] direction decreases when *ac* tensile strain is applied, while it increases for the other two cases (Figure 4.5a). The average bond length of the LiO_6 octahedral

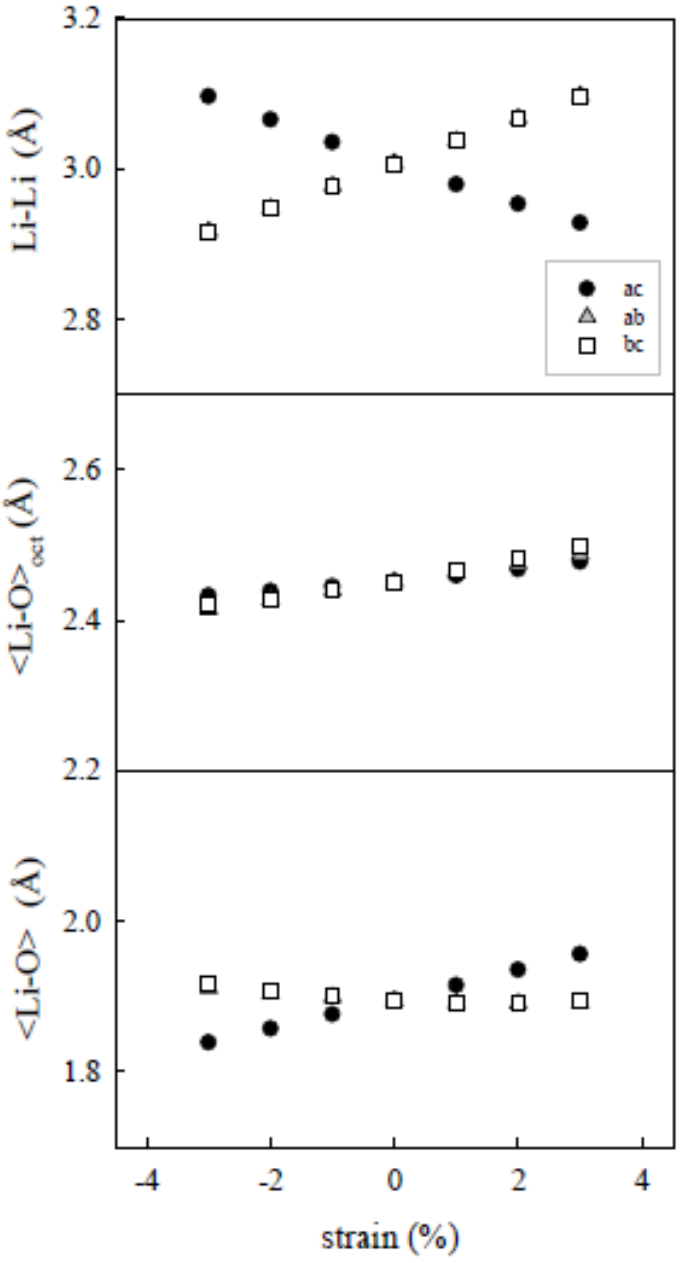

Figure 4.5: *The structural variation of olivine $LiFePO_4$ as a function of applied strain, related to the diffusion pathway in the [010] direction. a) Li-Li hopping distance; b) average Li-O distance for the octahedral LiO_6 environment at the saddle point configuration; c) average of shortest Li-O distances at the saddle point configuration.*

environment is shown in Figure 4.5b, the average bond length increases with the application of strain in all three cases. Hence this parameter tends to lower the migration Li^+ migration barrier along with strain. Figure 4.5c shows the the average of the shortest two Li-O distances at the saddle point configuration (using the relaxed positions around the migrating ion) as a function of applied strain. These distances represent the effective bottleneck for the migrating ion at the saddle point configuration. It is a balance between the three parameters presented in Figure 4.5 which results in a considerable lowering of the activation energy for Li^+ migration in the case of *ac* tensile strain.

There are two other possible migration pathways in the olivine structure (labelled A and C in Figure 4.3), along the [101] and [001] directions. These pathways are characterised by high energy barriers in the unstrained systems of both $LiFePO_4$ and $NaFePO_4$ (>2.5 eV). Therefore, alkali-ion transport is considered a one-dimensional process in these materials. The activation energies of pathways A and C, as a function of applied strain, were calculated in order to determine if the dimensionality of Li^+/Na^+ ion transport is affected by strain. Shown in Figure 4.6. The calculated activation energies for the [101] and [001] pathways remain above 2 eV for the systems with 3% tensile strain applied. They are, therefore, not comparable to the favourable [010] migration pathway. This result predicts that strained olivine systems of $LiFePO_4$ and $NaFePO_4$ remain 1-D conductors with the application of strain.

MD simulations were performed on the unstrained and *ac* strained systems. 4 x 4 x 8 Supercells of $Li_{0.9}FePO_4$ and $Na_{0.9}FePO_4$ were constructed and minimised at both zero and 3% *ac* tensile strain. The alkali metal vacancies were randomly distributed within the supercells and charge compensation was achieved using randomly distributed Fe^{3+} species. The shell model was used to include electronic polarisability and was applied to the oxygen ions using a spring constant of 130 eV $Å^{-2}$. An elevated temperature of 500 K was chosen to allow sufficient ionic diffusion within the time span of the simulation and to improve the statics of the calculations.

The MD calculations confirm the curved pathways in the [010] direction, and

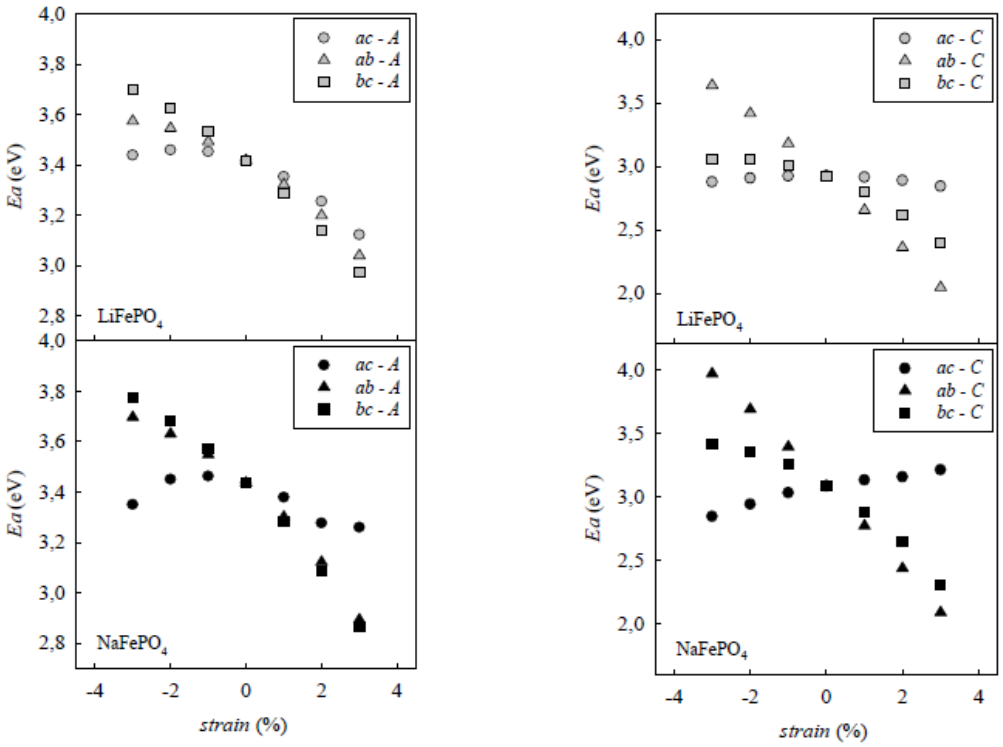

Figure 4.6: *Change in the alkal-ion migration barrier along the [101] direction (left) and the [001] direction as a function of strain for $LiFePO_4$ (upper) and $NaFePO_4$ (lower).*

predict that the nature of these paths are not altered by the application of tensile strain, this is shown in Figure 4.7 for $NaFePO_4$. The difference in the density of the Na^+ channels between the strained and unstrained system can be clearly seen, indicating that the tensile strain has a positive effect on the alkali-ion mobility in the olivine system. This effect can be quantified using Li^+ and Na^+ diffusion coefficients derived from mean square displacement (MSD) data.

A plot of MSD vs. simulation time is shown in Figure 4.7. The diffusion coefficients of Li^+/Na^+ ions were derived using equation 3.7. The simulated diffusion coefficients (D) are given in Table 4.3. There is significant scatter in reported experimental values of diffusion coefficients for these systems, however, the calculated values are consistent with observed values for olivine $LiFePO_4$ and related Na-ion cathode materials.[159,191–194]

From these results it can be predicted that firstly, values of D_{Na} are higher

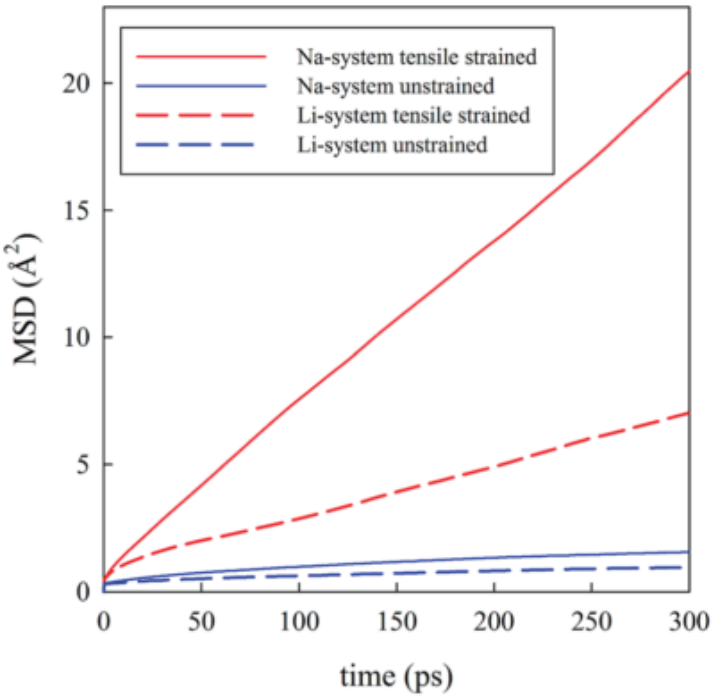

Figure 4.7: *Mean square displacement (MSD) vs. time for $Li_{0.9}FePO_4$ (dashed lines) and $Na_{0.9}FePO_4$ (solid lines).*

Table 4.3: *Calculated Li and Na diffusion coefficients at 500 K for the unstrained and 3% ac tensile strained systems.*

Strain (%)	$\mathbf{D}_{Li}$ **(cm^{2}s^{-1})**	$\mathbf{D}_{Na}$ **(cm^{2}s^{-1})**
0.0	3.36 x 10^{-8}	6.69 x 10^{-8}
3.0	3.42 x 10^{-7}	1.08 x 10^{-6}

than D_{Li} in the same olivine system, which is in agreement with the calculated difference between Na^+ and Li^+ migration barriers. Secondly, the application of tensile strain in the *ac* direction increases alkali-ion diffusion in both systems. At this simulation temperature (500 K) the difference between D_{Li} and Na^+ is around one order of magnitude.

Using the calculated changes in activation energy with applied strain, the change in ionic conductivity with this strain can be predicted using the standard Arrhenius equation. It has previously been reported by De Souza[173] that the change in the enthalpy of migration (ΔH_{mig}) can be approximated using the

calculated value of E_{mig} within a certain range of applied biaxial strain. This is because, in a strained structure, the maximum possible increase in the value of H_{mig} depends only upon the calculated migration enthalpy in the absence of strain. For $LiFePO_4$ and $NaFePO_4$ these values are 0.55 eV and 0.37 eV respectively.

4.4 Defect Formation

The 1D nature of the ion transport in olivine materials means that the presence of anti-site defects (equation 4.1) can be detrimental to the intercalation properties of the systems. This exchange of cations on neighbouring sites represents the most energetically favourable intrinsic defect in olivine materials.[158] These defects have been observed experimentally[40,195] and due to the one-dimensional nature of diffusion in the olivine structure they negatively affect the intercalation properties by blocking the diffusion pathways.

$$M_M^X + Fe_{Fe}^X \rightarrow Fe_M^{\bullet} + M_{Fe}^{/} \tag{4.1}$$

The anti-site cluster formation and binding energies were calculated for $LiFePO_4$ and $NaFePO_4$ as a function of applied strain, in order to investigate whether the application of biaxial strain affects the formation of these defects. The results are given in Figure 4.8. Firstly, it is important to note that the formation of anti-site defects is more favourable in $NaFePO_4$ than for the Li analogue, this is in agreement with previous studies[85] and the work presented in Chapter 3. The predicted change in the defect formation is more pronounced for the Na-based system; as the applied strain increases from compressive to tensile for $LiFePO_4$ the cluster formation energy does not greatly change, suggesting that, in this system, strain is not a crucial parameter to modulate anti-site defect population. The effect is larger for $NaFePO_4$, with tensile strain making the formation of anti-site defects less favourable. The application of compressive strain increases the energy required for a Na^+ ion to occupy an Fe site, due to size restraints with the large Na^+ ion. However, the energy needed for an Fe ion

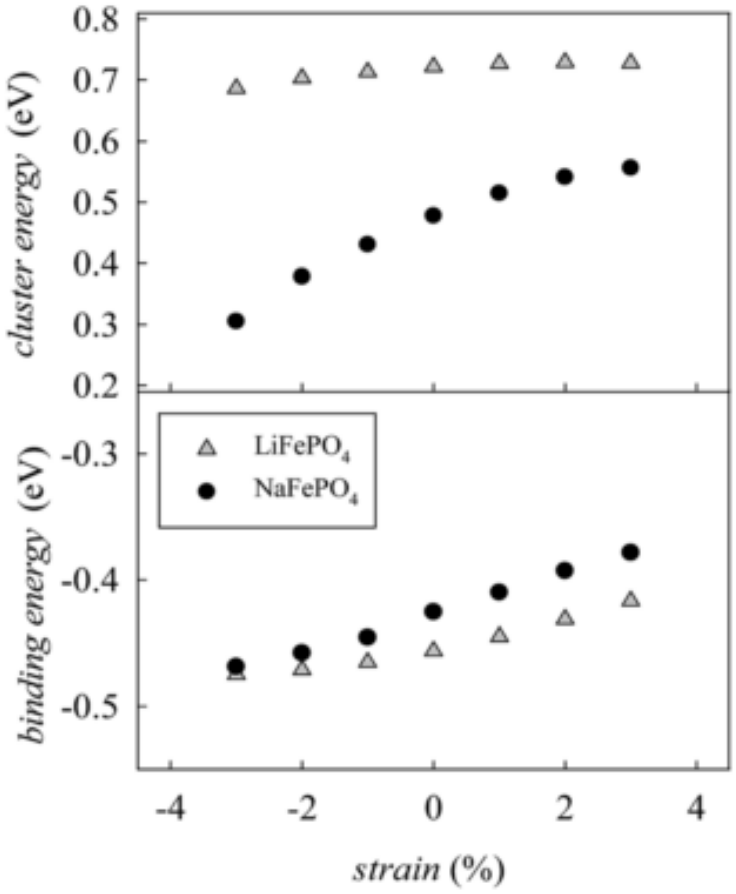

Figure 4.8: *Cluster formation energies for anti-site defectis in olivine $LiFePO_4$ and $NaFePO_4$ as a function of applied biaxial strain in the ac plane (upper panel) and binding energies (lower panel).*

to reside on a Na site is reduced to a greater extent, resulting in the predicted reduction in cluster energy. This change in formation energy is attributed to the elongation of the *b*-axis.

The binding energies for the anti-site clusters were calculated using the difference between the cluster energy and the sum of the energies of the isolated defects. The cluster is said to be bound if the binding energy is negative. The binding energies for both systems studied here become less negative as the applied strain increases (Figure 4.8). This suggests that tensile strain makes the Li/Na-Fe clusters less strongly bound.

4.5 Chapter Summary

Atomistic modelling techniques were used to investigate the effect lattice strain has on the ion conduction properties of olivine-type cathode materials for lithium- and sodium-ion batteries. The results are as follows:

(a) The application of compressive or tensile strain is not found to affect the dimensionality of ion transport in either $LiFePO_4$ or $NaFePO_4$. Ionic diffusion remains one-dimensional, through channels parallel to the *b*-axis. It is of greater importance that Li^+ and Na^+ migration barriers along the [010] direction significantly decrease when tensile strain is applied in the *ac* plane. It is predicted that this decrease in activation energy would correspond to an enhancement in ionic conductivity at room temperature. The effect of tensile strain on ionic diffusion was confirmed using molecular dynamics.

(b) The binding energies of blocking anti-site defects are reduced with the application of tensile strain and their formation energies are slightly increased (this is particularly prominent for $NaFePO_4$).

This study suggests that the application of tensile strain perpendicular to the alkali-ion migration channels would improve the intercalation properties of olivine-type cathode materials. It is important to recognise that interfacial effects such as grain boundaries and dislocations, may influence the effective enhancement predicted in this work.

In general, the results presented here suggest that lattice strain can lead to enhancements in ionic conduction and rate performance of both $LiFePO_4$ and $NaFePO_4$. These insights provide a framework for the design and optimisation of future high rate cathodes.

5 | Structural, Diffusion and Surface Properties of Layered Sodium Oxides

'You start thinking anything's possible if you've got enough nerve.'

J. K. Rowling, Harry Potter and the Half Blood Prince

5.1 Background

Layered oxide materials have been extensively studied as cathodes for lithium-ion batteries. The success of $LiCoO_2$ unsurprisingly led to extensive investigations into sodium materials with the same general structure. As described in **Chapter 1**.

P2-$Na_{\frac{2}{3}}[Ni_{\frac{1}{3}}Mn_{\frac{2}{3}}]O_2$ is considered a potential cathode material for Na-ion batteries due to its high theoretical capacity (approximately 170 mAh g^{-1}) and high average voltage (approximately 3.5 V), which is attributed to the Ni^{2+}/Ni^{4+} redox couple. However, the material suffers from poor cycle life, which is thought to be caused by the 'gliding' of transition metal layers to form the O2-phase.[80,196] Efforts have been made to improve the electrochemical performance of P2-$Na_{\frac{2}{3}}[Ni_{\frac{1}{3}}Mn_{\frac{2}{3}}]O_2$ through cation doping on the Ni^{2+}

site.[58,197–200] One of the most studied approaches is substitution of Ni^{2+} for Mg^{2+}.[201–203] However, as Mg is redox inactive it is possible that this could decrease the overall stored charge in the material. Without doping, theoretically all Na^+ ions can be extracted from P2-$Na_{\frac{2}{3}}[Ni_{\frac{1}{3}}Mn_{\frac{2}{3}}]O_2$, accompanied by the oxidation of Ni^{2+} to Ni^{4+}. The resulting empty Na layers enable the gliding of the MO_2 sheets, which causes the phase transformation from P2 to O2. By doping the structure with Mg^{2+} on the Ni site, a small amount of Na is forced to remain within the structure when it is fully charged, in order to maintain charge neutrality. This prevents the formation of two consecutive empty Na layers forming and stops the material from undergoing a phase transition into the O2-type. There is a need to understand the structural role Mg has in the Ni/Mn layers and how its presence may affect the Na/vacancy ordering and the phase transitions which usually occur at the end of charge.

Layered P2-$NaCoO_2$ has been considered a potential cathode material for Na-ion batteries, due to the commercial success of its Li analogue $LiCoO_2$. This Na-ion material has complex structural behavior, which is strongly correlated to Na^+ concentration and distribution. This is clearly demonstrated in the galvonistic cycling curve of the material, as discussed in **Chapter 1.9.1**, and is noticeably different from the biphasic reaction reported for $LiCoO_2$.[9]

Solid-solid interfaces are present in all battery devices, between cathode/anode and electrolyte in all solid-state cells or at grain boundaries in any solid component. They are expected to strongly influence battery performance, but to date have not been extensively characterised, particularly for Na-ion technologies. This is, in part, due to the difficultly of extracting surface information solely from experimental data.

The lowest energy surfaces of $LiCoO_2$ have previously been studied with DFT by Kramer et. al.[204] In this study low index surfaces, which minimise coordination loss at the transition metal, are considered. The properties of a high symmetry grain boundary have also been considered in $LiCoO_2$ by Moriwake et al.[1] However, there are no equivalent detailed simulation studies of $NaCoO_2$ surfaces or grain boundaries.

Here, a study on the effect of Mg^{2+} doping on Na^+ diffusion and structural properties of P2-$Na_{\frac{2}{3}}[Ni_{\frac{1}{3}}Mn_{\frac{2}{3}}]O_2$ is presented. A series of P2-$Na_{\frac{2}{3}}[Ni_{\frac{1}{3}-x}Mg_xMn_{\frac{2}{3}}]O_2$ structures ($0 \leq x \geq 0.2$) were synthesised and cycled in Na half cells by Nuria Tapia-Ruiz at Oxford University. *Ab initio* studies were completed by Hungru Chen at the University of Bath and these have been complemented using potential-based techniques. This study is extended by a computational investigation of the surface structures and energetics of $NaCoO_2$ for a range of low indexed surface orientations. The grain boundaries formed between low energy surfaces were also considered and compared to previous studies of analogous $LiCoO_2$.

5.2 Structural Modelling of P2-$Na_{\frac{2}{3}}[Ni_{\frac{1}{3}}Mn_{\frac{2}{3}}]O_2$

There are two different Na sites in the P2-$Na_{\frac{2}{3}}[Ni_{\frac{1}{3}}Mn_{\frac{2}{3}}]O_2$ structure: Na1 which is face sharing with MO_6 (M = Mn or Ni) and Na2 which is edge sharing. The Na2 site is more energetically favourable than Na1 due to lower electrostatic repulsions between Na and the transition metal. During charging the Na1 sites extract slightly faster than Na2 until the Na concentration approaches $\frac{1}{3}$, but both sites are extracted uniformly after this point. The reverse of this is true upon discharge. The overall occupancy ratio is determined by the competition between the site energy and the electrostatic repulsions, which also affects the in-place distribution of Na^+ ions. At Na = $\frac{2}{3}$, Na^+ ions from an ordered structure, known as "large zig-zag" (LZZ) due to the pattern of Na1 sites, as shown in Figure 5.1.[78,82,205]

The starting point of this study was to reproduce the experimental structure of $Na_{\frac{2}{3}}[Ni_{\frac{1}{3}}Mn_{\frac{2}{3}}]O_2$ and its Mg doped analogue. The synthesised materials had been refined using neutron diffraction and were assigned to the $P6_3$ space group. From the data obtained it was established that these samples displayed LZZ Na^+/vacancy ordering (Figure 5.1) and a level of Ni^{2+}/Mn^{4+} ordering in the transition metal layer. The structure of un-doped $Na_{\frac{2}{3}}[Ni_{\frac{1}{3}}Mn_{\frac{2}{3}}]O_2$ is shown in Figure 5.2, this was the structure reproduced computationally. The interatomic

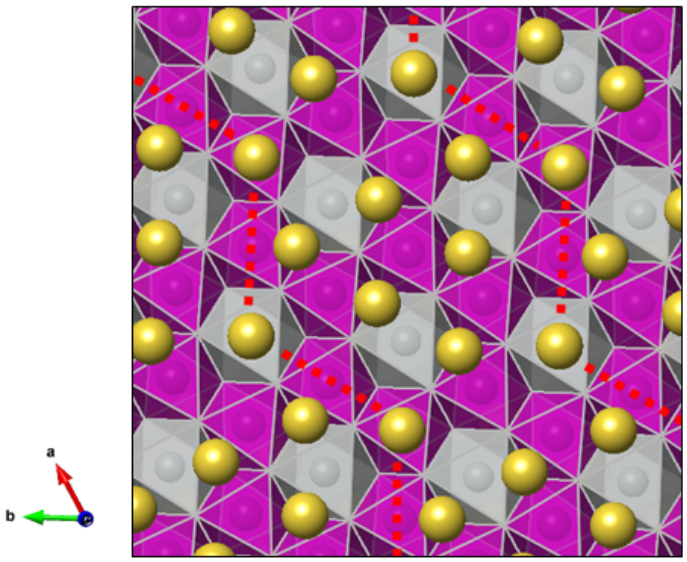

Figure 5.1: *LZZ ordering in* $Na_{\frac{2}{3}}[Ni_{\frac{1}{3}}Mn_{\frac{2}{3}}]O_2$. *(Purple octahedra:* MnO_6*,grey octahedra:* NiO_6 *and yellow spheres:* Na^+ *ions. Red dashed lines show LZZ ordering)*

potentials used were taken from previous studies on related oxides and are give in Table 5.1.[38,85,206,207] For static lattice calculations, carried out using the GULP program, a shell model was used. While for MD a rigid ion model was applied using the same potentials.

Table 5.1: *Short-range potential parameters for* $Na_{\frac{2}{3}}Ni_{\frac{1}{3}}Mn_{\frac{2}{3}}O_2$.

Interaction	A (eV)	ρ (Å)	C (eV.Å^6)
Na^+-O^{2-}	560	0.32	0.0
Ni^{2+}-O^{2-}	1760	0.28	0.0
Mn^{4+}-O^{2-}	1345.15	0.318	0.0
Mg^{2+}-O^{2-}	821.6	0.3242	0.0
O^{2-}-O^{2-}	22764.3	0.149	44.53

A comparison between the experimental and calculated cell parameters is given in Table 5.2. The lattice parameters were reproduced to within 2.3% of the experimental values and bond lengths were reproduced within 5%. This adds

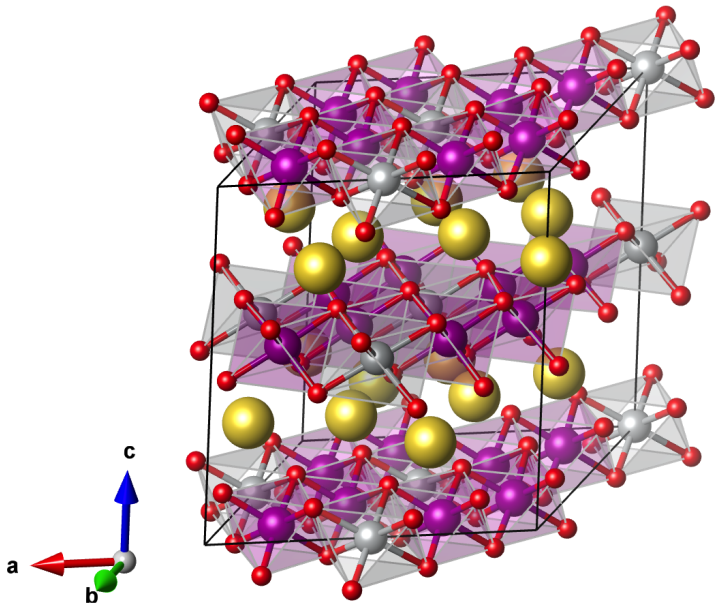

Figure 5.2: *Unit cell of LZZ ordered* $Na_{\frac{2}{3}}[Ni_{\frac{1}{3}}Mn_{\frac{2}{3}}]O_2$ *(Purple octahedra:* MnO_6*,grey octahedra:* NiO_6*, yellow spheres:* Na^+ *ions, red spheres:* O^{2-} *ions).*

Table 5.2: *Experimental and calculated lattice parameters and mean bond-lengths of* $Na_{\frac{2}{3}}[Ni_{\frac{1}{3}}Mn_{\frac{2}{3}}]O_2$*.*

Parameter	**Experimental (Å)**	**Calculated (Å)**	**% Δ**
a	10.00	9.78	-2.20
b	10.00	9.78	-2.21
c	11.11	10.93	-1.61
Na-O	2.37	2.38	0.25
Mn-O	1.92	1.84	-4.58
Ni-O	2.04	2.04	0.0

validity to the potential model derived.

MD calculations were carried out on cells made up of 4 x 4 x 8 unit cells (5632 atoms). The initial configuration contained 10% Na vacancies (and corresponding Ni^{3+} species), which were randomly distributed. Three initial configurations were investigated and the results were averaged.

In order to generate Mg doped structures ($Na_{\frac{2}{3}}[Ni_{\frac{1}{3}-x}Mg_xMn_{\frac{2}{3}}]O_2$, where x = 0.1 0r 0.2), Ni^{2+} ions were randomly substituted for Mg^{2+}. For each level of doping three different random Ni^{2+}/Mg^{2+} configurations were used and the results were then averaged. Much like for the un-doped systems, MD calculations were carried out on structures where 10% Na vacancies and Ni^{3+} species had been incorporated randomly. Again three different configurations were chosen and the results were averaged.

5.3 Na^+ Vacancy Formation in P2-$Na_{\frac{2}{3}}[Ni_{\frac{1}{3}}Mn_{\frac{2}{3}}]O_2$

Sodium vacancy defect energies were calculated for both un-doped and 10% Mg doped P2-$Na_{\frac{2}{3}}Ni_{\frac{1}{3}}Mn_{\frac{2}{3}}O_2$. As mentioned above, there are two different Na positions within the P2-$Na_{\frac{2}{3}}Ni_{\frac{1}{3}}Mn_{\frac{2}{3}}O_2$ structure. Within this division Na1 type ions are able to either share faces with either NiO_6 or MnO_6 octahedra, both of which have been considered and are denoted as such.

The calculated formation energies for sodium vacancies of each Na-type are given in Table 5.3 for $Na_{\frac{2}{3}}[Ni_{\frac{1}{3}-x}Mg_xMn_{\frac{2}{3}}]O_2$ where x = 0.0 or 0.1. A 2 x 2 x 1 supercell was used for these calculations. The formation energies for both types of Na1 defect are slightly higher than that calculated for Na2. The formation energies of Na vacancies in all three positions are lowered by the addition of 10% Mg^{2+} on the Ni site. This suggests that doping the structure with Mg should increase Na^+ diffusion as has been reported experimentally.[203]

Investigations as to how the proximity of the doped Mg site to the Na vacancy in question affects the calculated formation energy were also carried out. All three

Table 5.3: *Na vacancy formation energies in $Na_{\frac{2}{3}}[Ni_{\frac{1}{3}-x}Mg_xMn_{\frac{2}{3}}]O_2$ (x = 0.0 or 0.1).*

x	**Na1(Mn) (eV)**	**Na1(Ni) (eV)**	**Na2 (eV)**
0.0	5.85	5.87	5.73
0.1	5.73	5.73	5.61

types of Na site were considered and the closest Ni site was doped with Mg^{2+}. This was the only Mg impurity included in the structure for these calculations. Table 5.4 summarises these results. The largest % difference in vacancy formation energy is predicted for Na1(Mn), which also happens to be the Na vacancy furthest from the Mg^{2+} impurity. While Na1(Ni) displays the smallest % change and is closest to the Mg impurity. These results suggest that while Mg doping generally decreases the formation energy of all types of Na vacancies, the effect is most prominent for Na1(Mn) vacancies. This is due to an elongated Na-Mg distance when compared to the other Na vacancies.

Table 5.4: *Effect on Na vacancy formation energy according to proximity to given Mg impurity in P2-$Na_{\frac{2}{3}}Ni_{\frac{1}{3}}Mn_{\frac{2}{3}}O_2$.*

Na type	**Mg impurity**			**Distance from**	**Defect energy**	**% Δ**
	x	y	z	**Mg ion (Å)**	**(eV)**	
Na1(Ni)	0.5	0.5	0.5	2.8	5.715	-2.64
Na1(Mn)	0.5	0.25	0.5	4.0	5.625	-3.90
Na2	0.25	0.5	0.5	3.3	5.533	-3.45

5.4 Na^+ Diffusion and Structural Changes in P2-$Na_{\frac{2}{3}}[Ni_{\frac{1}{3}}Mn_{\frac{2}{3}}]O_2$

Long time-scale potentials based MD was carried out on the P2-$Na_{\frac{2}{3}}Ni_{\frac{1}{3}}Mn_{\frac{2}{3}}O_2$ structure, in order to calculate Na diffusion coefficients (D_{Na}) and help visualise any structural changes that occur due to Mg doping. 10% Na vacancies were introduced yielding a structural configuration of $Na_{0.6}[Ni_{0.33}Mn_{0.67}]O_2$, which was then doped with 10% Mg on the Ni site to form $Na_{0.6}[Mg_{0.03}Ni_{0.3}Mn_{0.67}]O_2$.

The MSD plots for Na^+ in the un-doped and 10% Mg doped forms of P2-$Na_{\frac{2}{3}}Ni_{\frac{1}{3}}Mn_{\frac{2}{3}}O_2$ are shown in Figure 5.3. In agreement with the galvonostatic intermittent titration technique (GITT) and nuclear magnetic resonance (NMR) measurements on this family of compounds, our simulations suggest that Mg

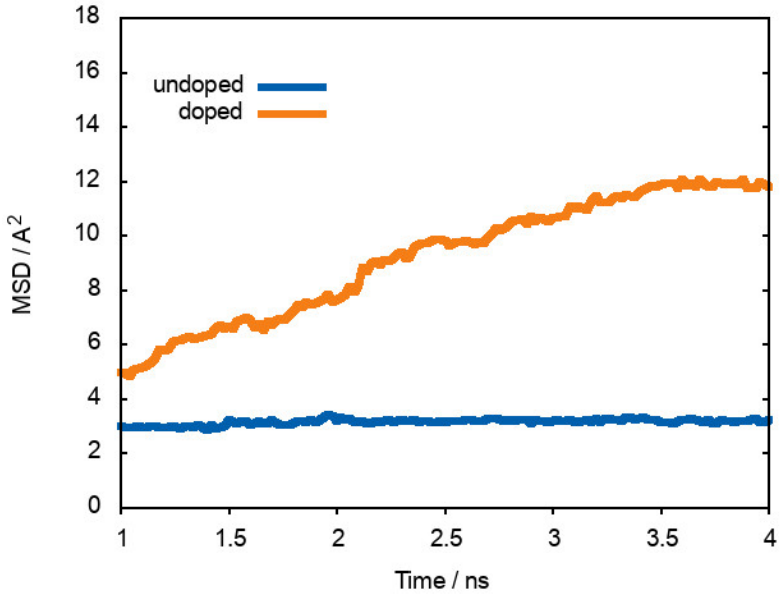

Figure 5.3: *Mean squared displacement (MSD) of sodium ions in* $Na_{0.6}[Ni_{0.33}Mn_{0.67}]O_2$ *(blue) and* $Na_{0.6}[Mg_{0.03}Ni_{0.3}Mn_{0.67}]O_2$ *(orange) at 300 K. Indicating greater* Na^+ *ion diffusion in the doped system.*

doping leads to an increase in Na^+ ion diffusivity. These results were used to derive values of D_{Na}. Values of 2.5 x 10^{-9} cm^2s^{-1} and 4.2 x 10^{-8} cm^2s^{-1} were obtained for $Na_{0.6}[Ni_{0.33}Mn_{0.67}]O_2$ and $Na_{0.6}[Mg_{0.03}Ni_{0.3}Mn_{0.67}]O_2$, respectively at 300 K. The difference between these values is slightly lower than the two orders of magnitude which has been observed experimentally,[203] but an increase in Na^+ diffusion is still predicted.

The increase in Na^+ diffusion with Mg^{2+} doping has previously been attributed to the enlargement of interlayer spacing upon Mg incorporation.[208] However, in this work the interlayer enlargement recorded was very small, at less than 0.05 Å.

Visualisation of the final $Na_{0.6}[Mg_{0.03}Ni_{0.3}Mn_{0.67}]O_2$ structure after 10 ns shows that Mg ions are able to displace in the z-direction to a greater degree than either Mn or Ni ions. Energy density plots for the un-doped and doped structures are shown in Figure 5.4, where the displacement of the Mg ions from the transition metal layer is clear. This effect was also seen in *ab initio* MD calculations. Figure 5.5 shows the degree of displacement of Mg, Ni and Mn ions

in the z-direction in a 50 ps *ab initio* simulation of $Na_{0.6}[Mg_{0.03}Ni_{0.3}Mn_{0.67}]O_2$.

The displacement of the Mg ions can be attributed to the ionic nature of the Mg-O bond. This results in the MgO_6 octahedra being less rigid than either NiO_6 or MnO_6 as their oxygen bonds are more covalent and therefore more rigid. The large displacement of Mg^{2+} in the z-direction consequently alters the electrostatic potential felt by Na^+ ions and has a positive effect on Na diffusion. A similar effect has been reported in P2-$Na_x[Li_yNi_zMn_{1-y-z}]O_2$, where the Li^+ ions (which have a very similar ionic radius to Mg^{2+}) are displaced from the transition metal layers into the Na layers.[209]

As the Mg^{2+} ions displace from the transition metal layer into the Na layer they move from an octahedral to a tetrahedral site. This movement results in an elongation of the Mg-O bond, as recorded in Table 5.5. The shorter Mn/Ni-O bonds reflect their more covalent nature.

Table 5.5: *Average M-O (M = Mg, Mn or Ni) bond lengths for* $Na_{0.6}[Mg_{0.03}Ni_{0.3}Mn_{0.67}]O_2$.

Mg-O (Oh) (Å)	**Mg-O (Td) (Å)**	**Mn-O (Å)**	**Ni-O (Å)**
2.0651	2.1033	1.7781	2.0515

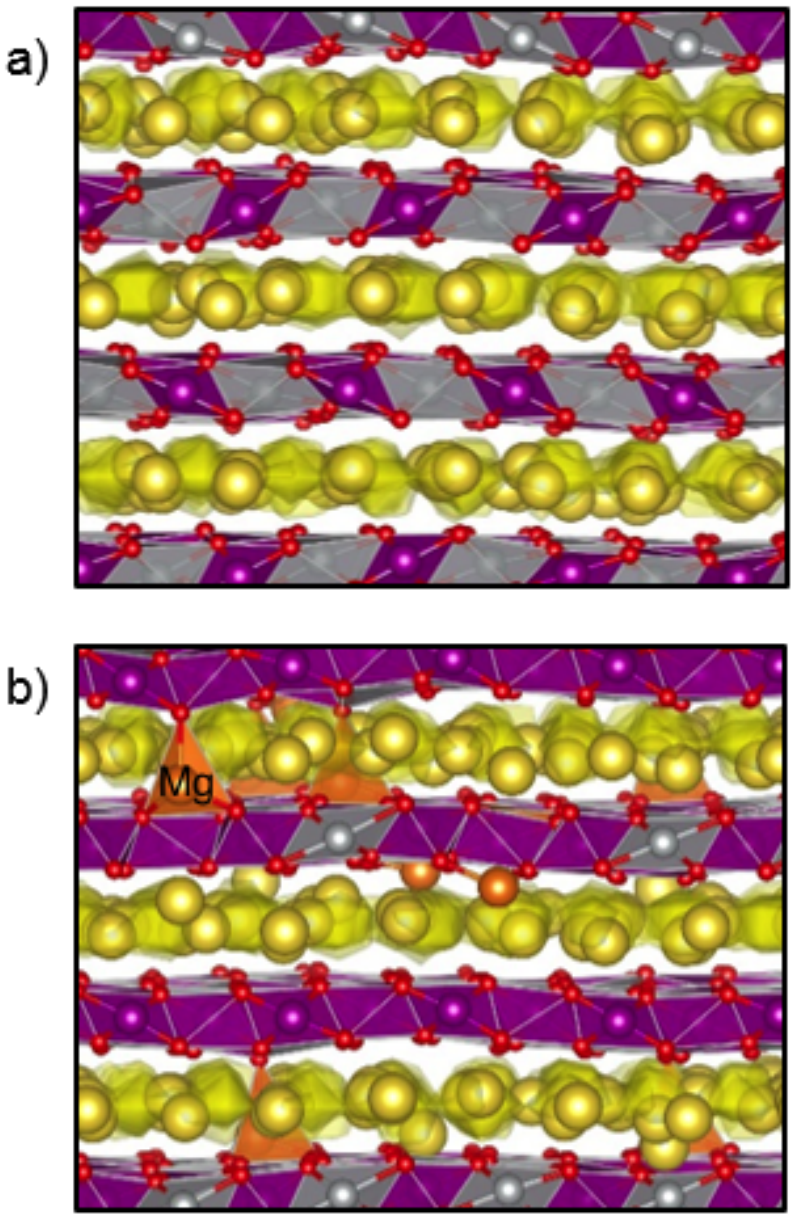

Figure 5.4: *Sodium density plots for a) $Na_{0.6}[Ni_{0.33}Mn_{0.67}]O_2$ and b)$Na_{0.6}[Mg_{0.03}Ni_{0.3}Mn_{0.67}]O_2$. Mg ions have displaced from transition metal layer into Na layer. (Purple octahedra: MnO_6; grey octahedra: NiO_6; orange tetrahedra:MgO_4; yellow spheres: Na^+ ions and yellow channels: Na^+ diffusion).*

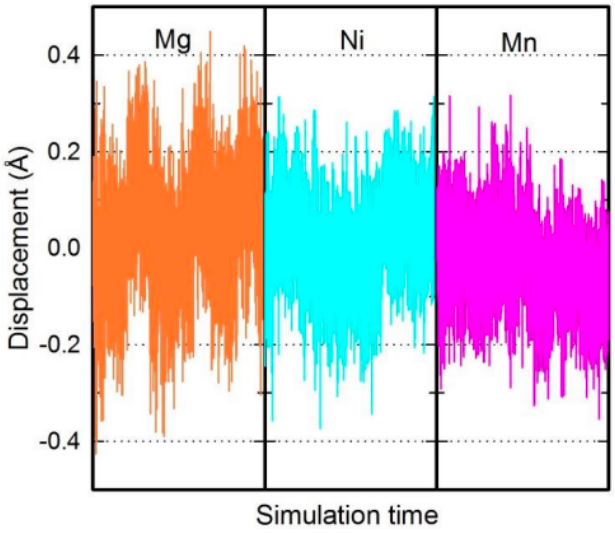

Figure 5.5: *Displacement of Mg, Ni and Mn along the z-direction in* $Na_{0.6}[Mg_{0.03}Ni_{0.3}Mn_{0.67}]O_2$ *during a 50 ps ab initio MD simulation, indicating larger amplitudes for Mg.*

5.5 Structural Modelling of P2-$NaCoO_2$

Layered P2-$NaCoO_2$, which is a member of the R$\bar{3}$mH space group, contains alternating layers of CoO_6 octahedra and Na^+ ions shown in Figure 1.6. There are two different Na sites within this structure: Na1, which shares only faces with CoO_6 octahedra, and Na2 that shares both faces and edges.

It is worth noting that while $Na_{0.7}CoO_2$ is more commonly utilised as a cathode material, $NaCoO_2$ was chosen as the focus of this initial study for structural reasons. Once Na vacancies are introduced into the system the Na^+ ions become highly mobile, making the determination of the surface structures considerably more complex.

The $NaCoO_2$ unit cell (obtained from previous experimental work[79]) was minimised in the VASP code, using PAW potentials and the Generalized Gradient Approximation (GGA) of the PBE functional. A Hubbard U correction (Ueff = U-J = 3.3 eV) was used, this value has been used previously to accurately reproduce other Co containing oxides including $LiCoO_2$.[204] A cut off energy of 520 eV, set on a planewave basis, and a k-point grid of 8 x 3 x 1 were used to

converge the forces in this bulk calculation. Table 5.6 shows the experimental and calculated cell parameters and mean bond lengths of $NaCoO_2$. The experimental structure was reproduced to a high degree of accuracy (within approximately 3%) with this method.

Table 5.6: *Calculated (DFT) and experimental lattice parameters and mean bond lengths for $NaCoO_2$.*

Parameter	**Experimental (Å)**[79]	**Calculated (Å)**	**%Δ (Å)**
a	2.89	2.88	-0.44
b	2.50	2.49	-0.48
c	15.61	15.25	-2.27
Na-O	2.32	2.25	-3.06
Co-O	1.94	2.0	2.89

The METADISE code[210] was utilised to generate all Type I surfaces of $NaCoO_2$ with a Miller index of four or less. The surfaces with lowest energy were further minimised with VASP, using the setup outlined above. The k-point was scaled appropriately for the size of each surface cut studied. K-point testing was carried out to ensure that the forces were minimised for each surface. A vacuum gap of 10 Å was found to be adequate for all surfaces to ensure isolation of the surface slabs.

Grain boundaries were created for low energy surfaces. These were formed by combining two mirroring surfaces, for example $(10\bar{1}4)$ and $(10\bar{1}\bar{4})$. The consequent structures were minimised in the same way as the surfaces and bulk. Again, the k-point grid used for each cell was tested to ensure the convergence of forces.

5.6 Surface Structures and Energies of P2-$NaCoO_2$

Surface structures and energies were considered for the eleven configurations with lowest energy and a Miller index of four or less. The minimised surface energies are given in Table 5.7. The structures of the four lowest energy surfaces are discussed below. The highest energy surface of those considered, $(10\bar{1}0)$, was included for comparison. In this work hexagonal notation is primarily used. The corresponding Miller-indices are included in Table 5.7 for reference. The introduction of the fourth index i is explained in **appendix C**.

Table 5.7: *Surface energies of $NaCoO_2$ and their notation in order of increasing energy.*

Plane (hkl)	**Plane** $(hkil)$	**Surface energy** $\mathbf{Jm^{-2}}$
(104)	$(10\bar{1}4)$	0.98
$(12\bar{4})$	$(12\bar{3}\bar{4})$	1.35
(324)	$(32\bar{5}4)$	1.48
(110)	$(11\bar{2}0)$	1.51
$(13\bar{4})$	$(13\bar{4}\bar{4})$	1.57
(112)	$(11\bar{2}2)$	1.59
(232)	$(23\bar{5}2)$	1.60
(122)	$(12\bar{3}2)$	1.64
$(1\bar{3}\bar{2})$	$(1\bar{3}2\bar{2})$	1.67
$(23\bar{4})$	$(23\bar{5}\bar{4})$	1.72
(100)	$(10\bar{1}0)$	2.38

$(10\bar{1}4)$

The $(10\bar{1}4)$ surface was found to be the lowest energy surface for P2-$NaCoO_2$ with a calculated value of 0.98 Jm^{-2}. This surface termination is shown in Figure 5.6. Each NaO_6 octahedra at the surface has one Na-O bond cleaved, as does each CoO_6 octahedra. Meaning that Na and Co at the surface both have a coordination loss of one.

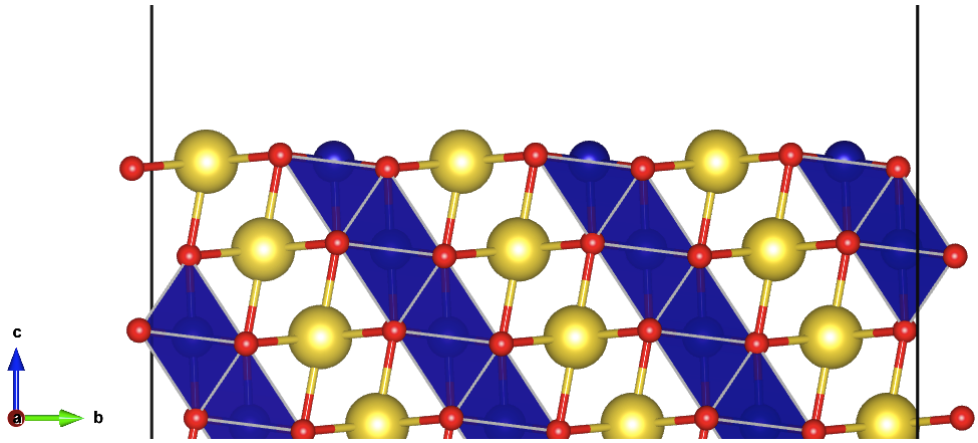

Figure 5.6: *Structure of* $(10\bar{1}4)$ *surface of* $NaCoO_2$ *(side view). Blue octahedra:* CoO_6*, yellow spheres:* Na^+ *ions, red spheres:* O^{2-} *ions.*

$(12\bar{3}\bar{4})$

The second lowest energy surface termination was calculated to be the $(12\bar{3}\bar{4})$ (depicted in Figure 5.7), with an energy of 1.35 Jm^{-2}. At this surface, one third of the Co octahedra remain fully coordinated, one third experience a coordination loss of one and one third a loss of two. This results in three separate Co positions with coordination numbers of four, five and six. The Na ions at this surface experience the same coordination loss.

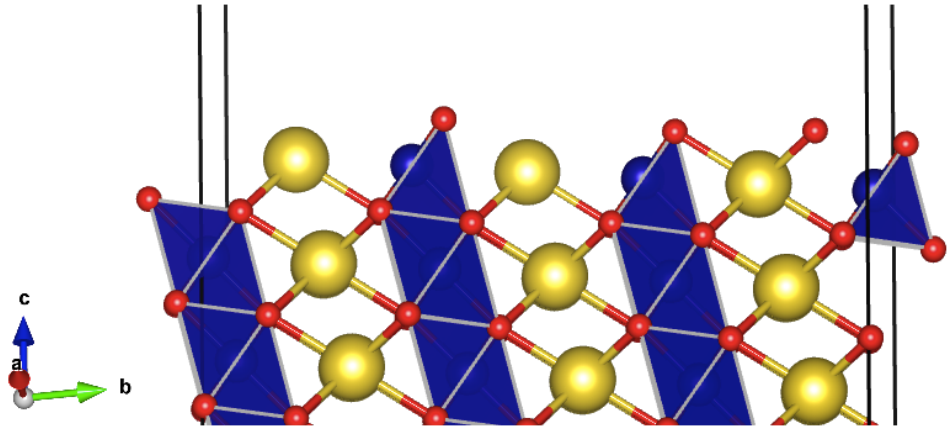

Figure 5.7: *Structure of* $(12\bar{3}4)$ *surface of* $NaCoO_2$ *(side view). Blue octahedra:* CoO_6*, yellow spheres:* Na^+ *ions, red spheres:* O^{2-} *ions.*

$(32\bar{5}4)$

The $(32\bar{5}4)$ surface is predicted to be the third lowest in energy, with a calculated value of 1.48 Jm^{-2}, shown in Figure 5.8. This termination results in half of the CoO_6 octahedra at the surface preserving their full coordination, one quarter experiencing the loss of one oxygen bond and one quarter the loss of two bonds. NaO_6 octahedra experience the same level of coordination loss at this surface.

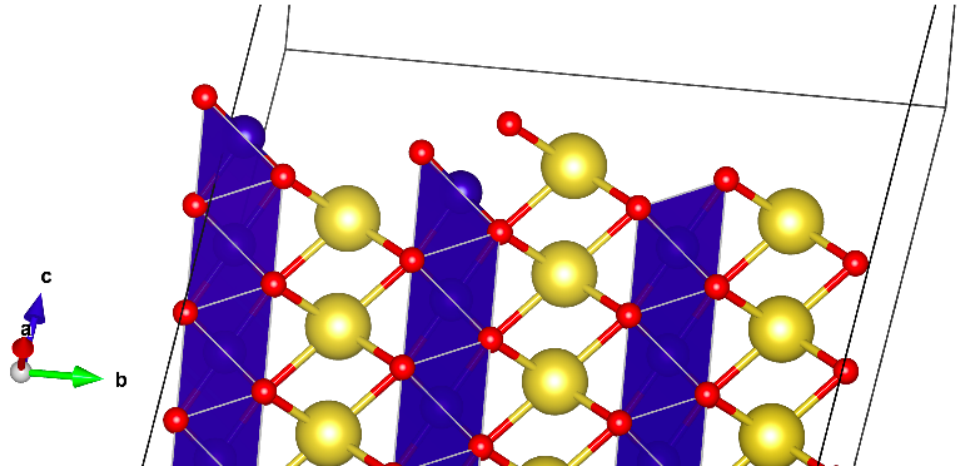

Figure 5.8: *Structure of* $(32\bar{5}4)$ *surface of* $NaCoO_2$ *(side view). Blue octahedra:* CoO_6*, yellow spheres:* Na^+ *ions, red spheres:* O^{2-} *ions.*

$(11\bar{2}0)$

The $(11\bar{2}0)$ termination has a calculated surface energy of 1.51 Jm^{-2} and is shown in Figure 5.9. At this surface half of the CoO_6 octahedra remain fully coordinated while the other half experience a coordination loss of two. The same is observed for the NaO_6 octahedra.

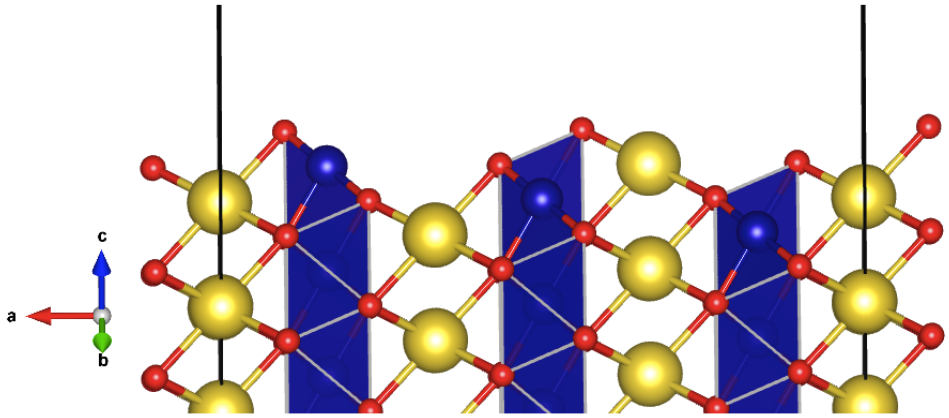

Figure 5.9: *Structure of* $(11\bar{2}0)$ *surface of* $NaCoO_2$ *(side view). Blue octahedra:* CoO_6*, yellow spheres:* Na^+ *ions, red spheres:* O^{2-} *ions.*

$(10\bar{1}0)$

The highest energy termination considered was $(10\bar{1}0)$ (shown in Figure 5.10) with an energy of 2.38 Jm^{-2}. This termination results in two different Na coordinations; one with a coordination of three (three Na-O bonds broken) and the other of coordination of five (one Na-O bond broken). The same coordinations are observed for the Co ions. For the surfaces examined this is the largest coordination loss observed.

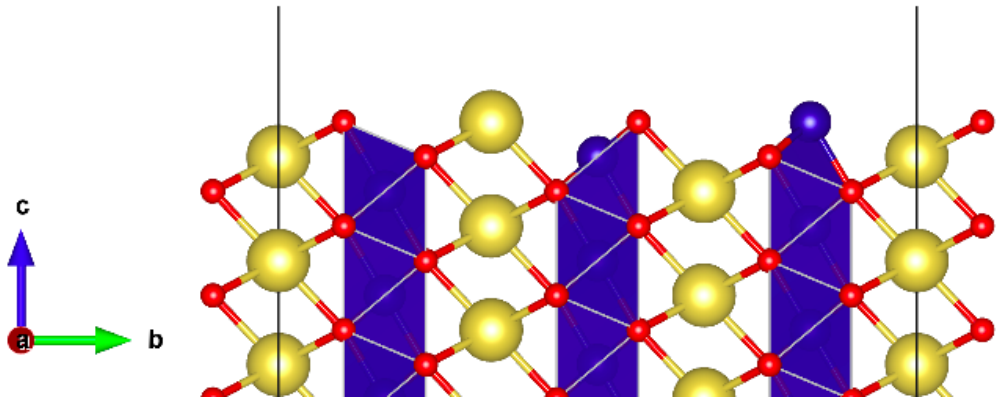

Figure 5.10: *Structure of* $(10\bar{1}0)$ *surface of* $NaCoO_2$ *(side view). Blue octahedra:* CoO_6*, yellow spheres:* Na^+ *ions, red spheres:* O^{2-} *ions.*

From the inspection of the above surfaces, it can be concluded that the coordination loss experienced by Na and Co ions at the surface, is a contributing factor to the magnitude of the surface energy. For example, the minimum coordination loss is experienced at the $(10\bar{1}4)$ surface, which also has the lowest surface energy. The largest coordination loss is found for the highest energy termination, $(10\bar{1}0)$. The coordination of cobalt at the surface it is expected to have the largest effect on the surface energy, as Co-O bonds are known to be much stronger than Na-O.

This same trend has been found for $LiCoO_2$ through DFT calculations.[204] Three Type I surfaces where considered for this material, $(10\bar{1}4)$, $(10\bar{1}0)$ and $(11\bar{2}0)$. Of these three terminations, it was found that the lowest in energy was $(10\bar{1}4)$ at 1.048 Jm^{-2} where the Co coordination at the surface is either five or six. The highest energy was recorded for $(10\bar{1}0)$ where the surface coordination of Co ranges between three and five. It has also been reported that the coordination loss of Fe at the surface of $LiFePO_4$ has a direct consequence on the surface formation energy.[211]

5.7 Grain Boundaries of P2-$NaCoO_2$

It is important to understand the formation of grain boundaries within cathode materials as they are likely to affect conduction properties. From the surfaces discussed above, two grain boundaries were built by combining mirroring surfaces.

The $(10\bar{1}4)$ and $(11\bar{2}0)$ surfaces were selected to form the grain boundaries as they represent the overall lowest energy termination and the low index surface with lowest energy respectively. The minimised grain boundary models are shown in Figures 5.11 and 5.12.

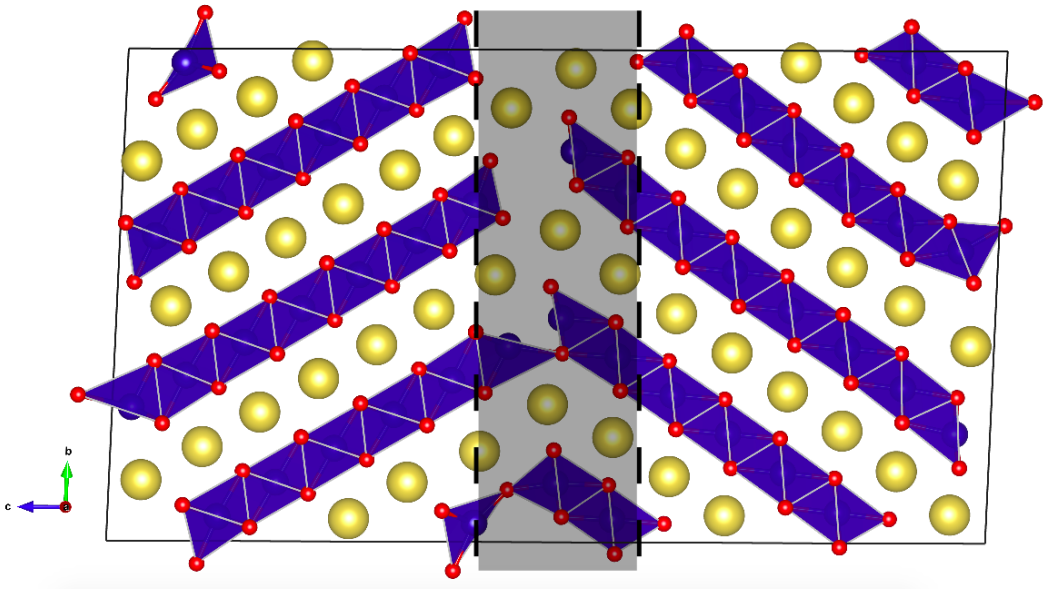

Figure 5.11: *Minimised structure of the grain boundary for* $(10\bar{1}4)$ *surfaces of P2-*$NaCoO_2$*. Blue octahedra:* CoO_6*, yellow spheres:* Na^+ *ions, red spheres:* O^{2-} *ions. Grey area highlights central grain boundary.*

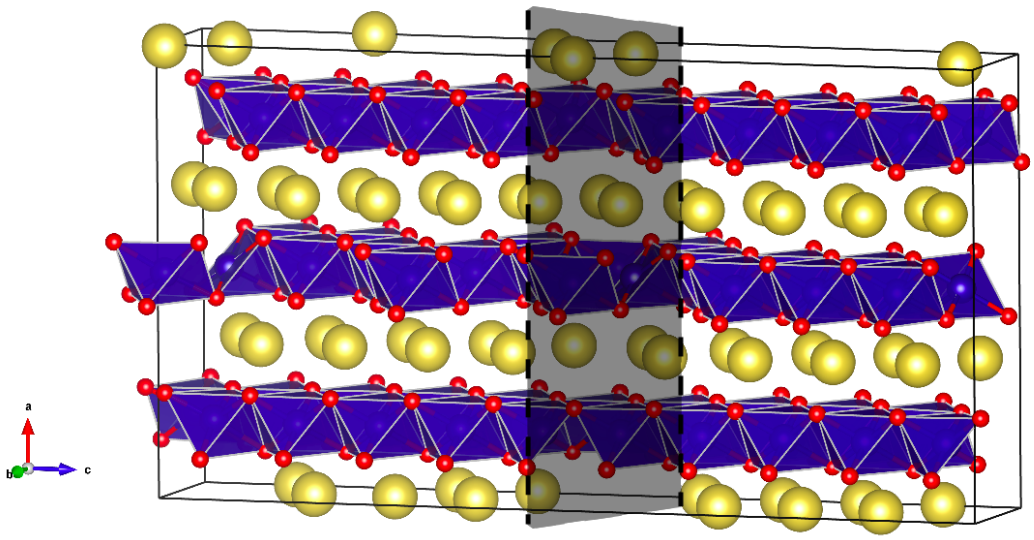

Figure 5.12: *Minimised structure of the grain boundary for* $(11\bar{2}0)$ *surfaces of P2-*$NaCoO_2$*. Blue octahedra:* CoO_6*, yellow spheres:* Na^+ *ions, red spheres:* O^{2-} *ions. Grey area highlights central grain boundary.*

The calculated grain boundary energies of the two configurations are given in Table 5.8. Surprisingly, the boundary formed at the $(11\bar{2}0)$ surface is lower in energy than that formed from the $(10\bar{1}4)$ termination, despite the $(11\bar{2}0)$ surface being lower in energy. However, it is worth noting that the difference in energy is small and as the formation energy of the $(10\bar{1}4)$ surface is considerably lower this is likely to be the dominant grain boundary in P2-$NaCoO_2$.

In general, these grain boundary energies are low compared to other boundaries in oxide materials such as $SrTiO_3$.[212,213] This suggest that Na and Co ions are able to easily adapt to the different coordinations experienced at the surfaces. These low energies indicate that grain boundaries will form with ease and in high concentrations in $NaCoO_2$, and will therefore noticeably influence

Table 5.8: *Grain boundary energies of* $NaCoO_2$*.*

Surface at grain boundary	Energy (eV)
$(10\bar{1}4)$	0.36
$(11\bar{2}0)$	0.32

Na ion diffusion.

Moriwake et. al. have reported a low energy grain boundary in $LiCoO_2$, made when the $(\bar{1}\bar{1}20)$ and $(11\bar{2}0)$ surfaces meet. This is shown in Figure 5.13. The similarity between this and the $(10\bar{1}4)$ boundary in P2-$NaCoO_2$ (Figure 5.11) can clearly be seen in the symmetry of the transition metal layers.The grain boundary was observed using scanning transmission electron microscopy. The voltage, layer spacing and migration energies were all considered as a function of distance from the boundary. Increases in both voltage and Li^+ migration energy are recorded in the vicinity of the grain boundary. To date there are no experimental reports of the grain boundaries present in P2-$NaCoO_2$.

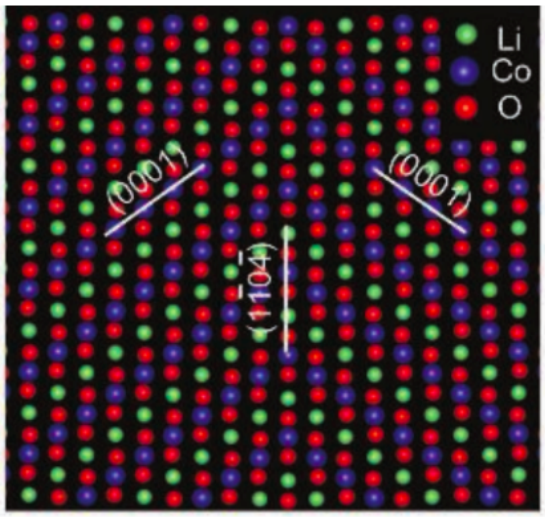

Figure 5.13: *Low energy grain boundary formed at the* $(11\bar{2}0)$ *surface of* $LiCoO_2$.[1]

5.8 Chapter Summary

This part of the project considered layer-structured oxides for Na-ion batteries. Firstly, the effect of Mg^{2+} doping on Na^+ diffusion and structural properties of P2-$Na_{\frac{2}{3}}Ni_{\frac{1}{3}}Mn_{\frac{2}{3}}O_2$ was investigated, using a combination of energy minimisation and molecular dynamics (MD) techniques. The key results are summarised below.

(a) The formation energies of all three types of Na vacancy were reduced by doping the P2-$Na_{\frac{2}{3}}Ni_{\frac{1}{3}}Mn_{\frac{2}{3}}O_2$ structure with 10% Mg^{2+} on the Ni site.

(b) Na^+ diffusion coefficients were calculated for $Na_{0.6}[Ni_{0.33}Mn_{0.67}]O_2$ and $Na_{0.6}[Mg_{0.03}Ni_{0.3}Mn_{0.67}]O_2$. An order of magnitude increase was recorded with Mg doping. Therefore an increase in Na^+ diffusion would be expected with 10% Mg doping of P2-$Na_{\frac{2}{3}}Ni_{\frac{1}{3}}Mn_{\frac{2}{3}}O_2$. Displacement of Mg ions from the transition metal layers was found in both potentials based and *ab initio* MD.

Secondly, *ab initio* calculations were performed on P2-$NaCoO_2$ in order to investigate, for the first time, surface and grain boundary properties of this Na-ion cathode material.

(c) The lowest energy surfaces of P2-$NaCoO_2$ were determined. It was found that the calculated energies were dependent on the coordination loss experienced by both Na and Co ions at the surface. Of the surfaces investigated, $(10\bar{1}4)$ was found to be lowest in energy and $(10\bar{1}0)$ the highest. This is consistent with surface studies on $LiCoO_2$.

(d) Grain boundary models were built for the lowest energy $(10\bar{1}4)$ and low index $(11\bar{2}0)$ terminations and their energies were calculated. The low energies predicted suggest high concentrations of these grain boundaries in $NaCoO_2$.

6 | Diffusion Rates and Voltage Trends of $MgFeSiO_4$

'There was some important stuff hidden in the waffle.'

J. K. Rowling, Harry Potter and the Order the Phoenix

6.1 Background

As covered in **Chapter 1**, the development of magnesium batteries would offer improved energy density over Li- and Na-ion systems. However, the choices of cathode materials for Mg batteries are limited, due to the difficulty of Mg^{2+} insertion/extraction in host structures.

Olivine-type Mg silicates have been reported to show promising performance as cathode materials for Mg batteries, with some indication of reversible Mg intercalation.[122–127,214] This is following extensive work on lithium-based silicates, Li_2FeSiO_4 and Li_2MnSiO_4 as low cost cathodes, due to the abundance of silicon and its ability to form strong Si-O bonds.[215]

$MgFeSiO_4$ exhibits a degree of mixing between octahedral Mg and Fe crystallographic sites.[128,129,216] However, ordered phases of $MgFeSiO_4$ have been synthesised through both high temperature and ion exchange

methods.[126,128] Using high temperature methods above 900 ° C, $MgFeSiO_4$ can be synthesised with a structure analogous to $LiFePO_4$, where the Mg^{2+} ions form one-dimensional channels along the *c*-axis.

It has previously been reported that Mg^{2+} inserted into disordered olivine $FePO_4$ yields a measured capacity of only 13 mA h g^{-1}. This poor performance was found to be linked to surface amorphisation, which prevented the electrochemical reaction from penetrating the bulk rather than poor Mg^{2+} mobility in the structure.[217] A first principles study on the magnesium silicates reports their redox and thermodynamic properties, revealing a similarity between lithium- and magnesium-insertion processes.[125] However, this study did not consider kinetic processes, such as the transport of Mg^{2+} ions through the host lattice, which are essential to the performance of ion intercalation electrodes.

Our focus with this work is to investigate the solid-state features, which influence the electrochemical performance of ordered $MgFeSiO_4$ (with a structure analogous to olivine $LiFePO_4$). We have employed a combination of atomistic energy minimisation, molecular dynamics and density functional theory methods in order to investigate the Mg ion transport properties and voltage trends from transition metal doping of this material. A published version of this work[218] is given in **Appendix E**.

6.2 Structural Modelling

The olivine-type structure of the cation-ordered $MgFeSiO_4$ belongs to *Pmnb* space group, shown in Figure 6.1. The structure consists of corner sharing FeO_6 octahedra, SiO_4 tetrahedra which share corners and edges with FeO_6 and Mg^{2+} ions that are located in channels along the *c*-axis.

The starting point of this study was to reproduce the experimental structure of ordered $MgFeSiO_4$ using a shell model. The interatomic potentials used were taken from previous studies on related oxides and silicates and include a three-body O-Si-O potential (Tables 6.1 and 6.2).[207,219,220]

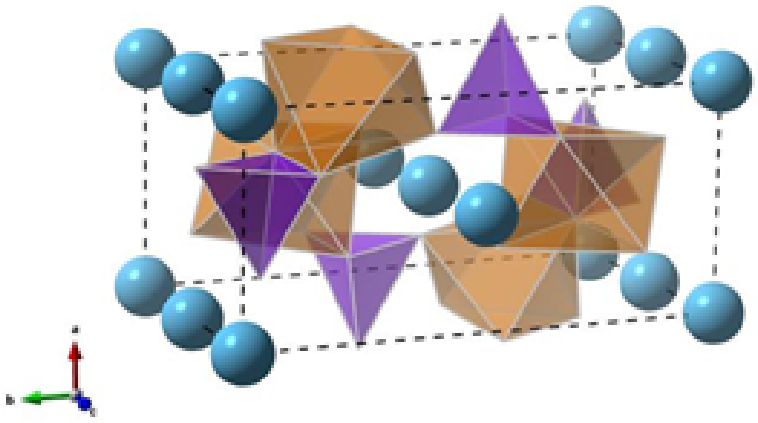

Figure 6.1: *Unit cell of olivine-type, cation ordered $MgFeSiO_4$ (brown octahedra: FeO_4, purple tetrahedra: SiO_4, light blue spheres: Mg^{2+} ions).*

Table 6.1: *Two-body short-range potential parameters for $MgFeSiO_4$.*

Interaction	**A (eV)**	**ρ (Å)**	**C (eV.Å^6)**	**Y (e)**	**K (eV.Å^{-2})**
Mg^{2+}-O^{2-}	946.627	0.31813	0.0	2.0	99999.0
Fe^{2+}-O^{2-}	1105.2409	0.3106	0.0	2.997	19.26
Si^{4+}-O^{-2}	1283.91	0.32052	10.66	4.0	99999.0
O^{2-}-O^{-2}	22764.3	0.149	27.89	-2.96	74.92

Table 6.2: *Three-body interaction for $MgFeSiO_4$.*

Bond type	**K (eV.rad^{-2})**	**θ_0 (deg)**
O^{2-}-Si^{4+}-O^{2-}	2.09724	109.47

A comparison between the experimental and calculated cell parameters are shown in Table 6.3. The lattice parameters were reproduced to within 1% of the experimental values, which adds validity to the interatomic model used for simulating Mg^{2+} diffusion.

Molecular dynamics (MD) calculations were carried out on cells made up of 12 x 6 x 10 unit cells (20160 atoms). The initial configuration contained 10% Mg vacancies (and corresponding Fe^{3+} species), which were randomly distributed. Three initial configurations were investigated and the results were averaged.

Table 6.3: *Calculated (using both rigid ion and Pedone partial charge models) and experimental lattice parameters and bond lengths for $MgFeSiO_4$.*

Parameter	**Experimental[128] (Å)**	**Calculated (R. I.) (Å)**	**Δ (Å)**	**Calculated (Pedone) (Å)**	**Δ (Å)**
a	4.807	4.854	0.047	4.863	-0.056
b	10.376	10.336	-0.040	10.125	-0.251
c	6.061	6.026	-0.035	6.005	-0.056
Mg-O	2.168	2.131	-0.037	2.132	-0.036
Fe-O	2.125	2.140	0.015	2.148	0.023
Si-O	1.624	1.639	0.015	1.600	-0.024

The Pedone partial charge model[144] was used for the MD simulations, this was chosen as it has shown previously to work well for MD simulations of polyanionic materials,[221,222] while still reproducing the structure well (Table 6.3). Simulation runs were carried out using the NVT ensemble and a time step of 2 fs, for runs of 6 ns, at temperatures between 300 and 1500 K. Pre-equilibrium runs of 4 ps with NVE and NPT ensembles were first used to obtain stable configurations.

Additionally, DFT was used to investigate voltage trends from transition metal doping. These calculations were performed using a plane wave basis set implemented in the VASP code.[134] PAW potentials and the Generalised Gradient Approximation of the PBE functional were used. DFT+U methodology was used to account for the metal d-orbitals with an effective Hubbard U_{eff} = U - J = 4.3, 3.9, 3.3 and 6.0 eV (J = 1.0 ev) for Fe, Mn, Co and Ni respectively.[222] A ferromagnetic arrangement of the unpaired 3d electrons was assumed. A cutoff energy of 440 eV and k-point mesh of 2 x 4 x 5 were needed to converge the forces and energies. Similar to the potentials based calculations, the experimental structure was reproduced to a high degree of accuracy, shown in Table 6.4.

Table 6.4: *Calculated (DFT) and experimental lattice parameters for $MgFeSiO_4$.*

Parameter	Experimental (Å)[128]	Calculated (Å)	Δ (Å)
a	4.807	4.756	-0.051
b	10.376	10.262	-0.114
c	6.061	6.047	-0.014

6.3 Energetics and Pathways for Mg ion Migration

There are three potential pathways for Mg^{2+} diffusion in $MgFeSiO_4$, as shown in Figure 6.2. The activation energies for these pathways are given in Table 6.5, along with the Mg-Mg distances. The activation energy for pathway A (parallel to the *c*-axis) is significantly lower than that for pathways B and C. This is in agreement with results obtained for $LiFePO_4$,[158] where the lowest energy pathway is parallel to the *b*-axis; $LiFePO_4$ is a member of the *Pmna* space group, unlike $MgFeSiO_4$ which is characterised as *Pmnb*, hence the disagreement in the axis along which the open channels of Li^+/Mg^{2+} ions lie. The activation energies for pathways B and C are both high enough that it can be concluded

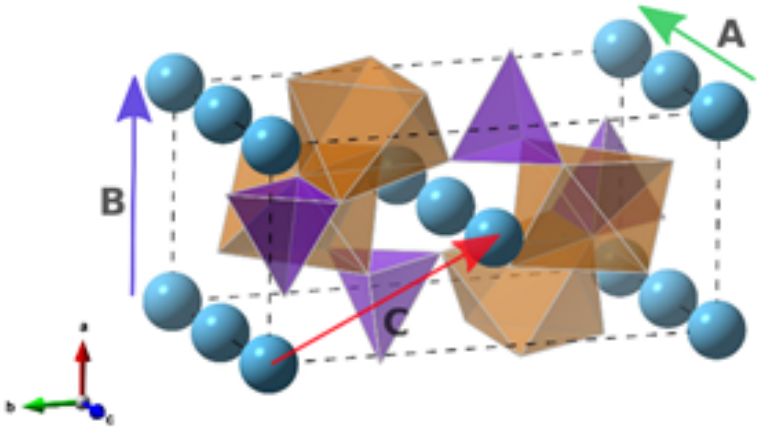

Figure 6.2: *Mg migration pathways in olivine $MgFeSiO_4$ (brown octahedra: FeO_6, purple tetrahedra: SiO_4 and blue spheres: Mg^{2+} ions).*

Table 6.5: *Activation energies and Mg-Mg separations in $MgFeSiO_4$.*

Pathway	Mg-Mg distance (Å)	E_a Mg^{2+} (eV)
A	3.01	0.60
B	4.85	5.18
C	5.71	5.43

that Mg ion migration is unlikely to occur in these directions. The distances between neighbouring Mg^{2+} ions in pathways B and C are larger than pathway A. Additionally, pathway B has a smaller channel size than pathway A. Pathway C would involve migration directly past both Fe-O ans Si-O bonds, both of which would contribute to the high migration energy.

The shape of the migration pathway parallel to the *c*-axis predicted using energy minimisation calculations is shown in Fig 6.3. This is the same as the curved pathway characteristic of olivine $LiFePO_4$, first predicted computationally,[158] and subsequently confirmed by diffraction measurements and maximum entropy studies.[37] This pathway was calculated to have a migration of 0.60 eV in $MgFeSiO_4$, just 0.05 eV higher than the equivalent calculated energy in $LiFePO_4$.[158]

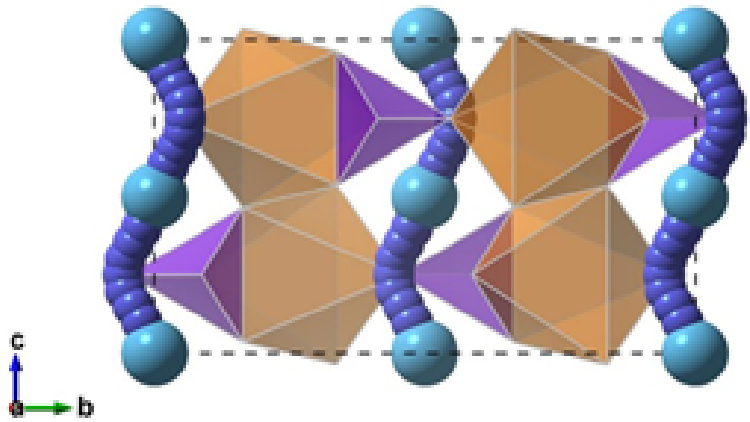

Figure 6.3: *Lowest energy Mg^{2+} pathway in olivine $MgFeSiO_4$ (brown octahedra: FeO_6, purple tetrahedra: SiO_4 and blue spheres: Mg^{2+} ions).*

The migration of different multivalent ions in three possible cathode frameworks has been investigated by Rong et al. using first principles techniques.[116] The three frameworks were olivine $FePO_4$, layered NiO_2 and spinel Mn_2O_4, covering the major structures considered as cathode materials for Li-ion batteries. It was reported that Mg^{2+} diffusion in the olivine structure required approximately 0.7 eV, lower than multivalent cation migration in both the layered and spinel structures, calculated at aprroximately 1.1 and 0.8 eV respectively. The relatively low migration energies predicted previously for olivine $FePO_4$ and here for $MgFeSiO_4$, suggest favourable Mg^{2+} transport in the olivine structure.

We continued our study on $MgFeSiO_4$ using long timescale MD in order to examine Mg^{2+} motion. The same curved pathway as that predicted with energy minimisation techniques was generated using MD, this is shown using an energy density plot in Fig. 6.4.

A degree of anti-site disorder (the exchange of Mg^{2+}/Fe^{2+}) was observed when visualising the MD calculations; an example of this can be seen in the lower part of Fig. 6.4, where Mg ion density is found near the Fe site. These defects were expected given the high levels of Mg/Fe mixing in the thermodynamically stable form of $MgFeSiO_4$.[128?,129] Energy minimisation was used to calculate the formation energy of these defects and a value of 0.036 ev was obtained. This low energy energy again reflects the highly disordered thermodynamically form of $MgFeSiO_4$.

Anti-site defects have been reported to cause blocking of the 1D migration pathways in $LiFePO_4$.[162] However, major blocking of the Mg^{2+} was not observed in our MD simulations. We predict that while the anti-site defects are able to form and cause a localised blocking effect, the Fe^{2+} ions are then able to migrate back into their original sites allowing Mg^{2+} ions to diffuse through uninterrupted channels, due to the low formation energy that has been predicted. There is no evidence of inter-channel hopping of the displaced Mg^{2+} ions.

The MSD for Mg^{2+} in $MgFeSiO_4$ is given in Fig 6.5. These data were used to derive the Mg ion diffusion coefficient (D_{Mg}). A value of 1.1 x 10^{-9} cm^2s^{-1}

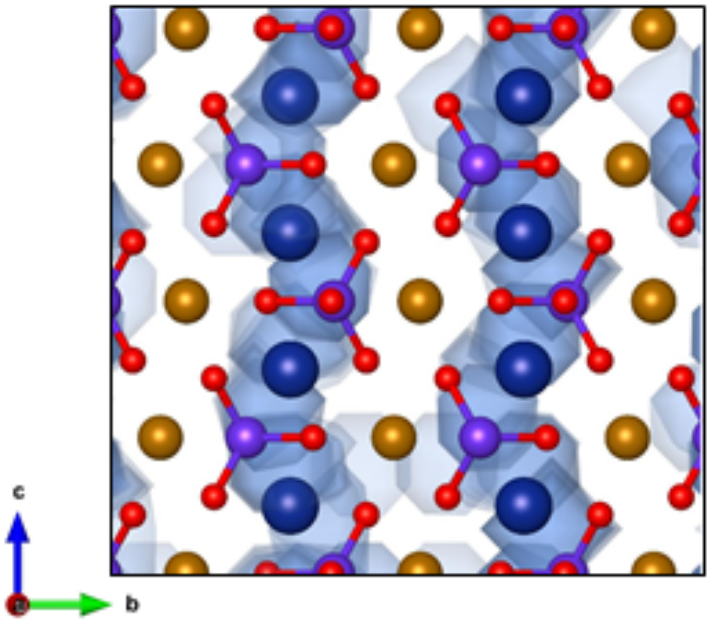

Figure 6.4: *Mg density plot from MD simulations showing Mg diffusion pathways (brown spheres: Fe^{2+} ions; dark blue spheres: Mg^{2+} ions; purple spheres: silicon; red spheres: oxygen. Light blue channels mark diffusion pathway.)*

was calculated at 300 K. To our knowledge there are no experimental diffusion coefficients for ordered $MgFeSiO_4$ to allow direct comparison at the current time. Tavorite structured $FeSo_4F$ has been considered as a potential cathode material for Mg batteries, it is quoted as having a D_{Mg} in the range of 10^{-9} cm^2s^{-1}, the same order of magnitude as observed for Li diffusion in the same structure.[223]

The activation energy of Mg^{2+} diffusion was estimated using an Arrhenius plot, which is shown in Fig. 6.6. A value of 0.79 eV was derived. While this value is slightly higher than that predicted using energy minimisation methods, it is still relatively low for a Mg cathode material.

The prediction of a comparatively low migration energy for Mg-based cathode material and a D_{Mg} in the range of Li-ion cathodes suggests favourable Mg^{2+} intercalation kinetics for ordered $MgFeSiO_4$.

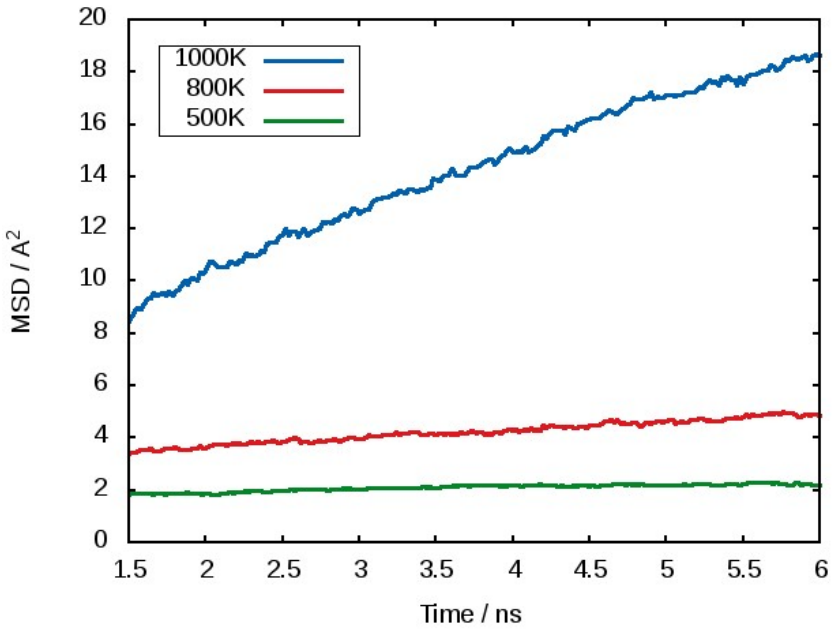

Figure 6.5: *Mean squared displacement (MSD) data for Mg^{2+} in $MgFeSiO_4$ at 500 K (green), 800 K (red) and 1000 K (blue).*

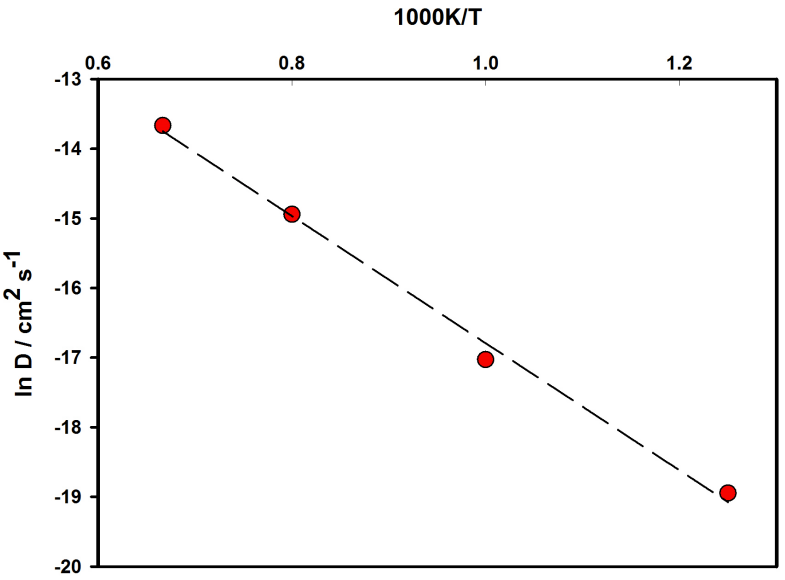

Figure 6.6: *Arrhenius plot of Mg ion diffusion coefficients D_{Mg} for $MgFeSiO_4$*

6.4 Dopant Substitution

It has previously been suggested that the incorporation of on dopants on certain sites of Li-ion cathode materials could improve the capacity of the material by increasing the amount of lithium available for intercalation by forming lithium interstitial defects.[219] Similar strategies could also be beneficial for magnesium cathode materials. While the divalent nature of the magnesium ion theoretically offers increased energy density over monovalent lithium, many structures only allow for the de/intercalation of half of the available magnesium. Incorporating dopants could create Mg interstitial defects that could consequently improve the capacity of the cathode material.

Here we investigate trivalent doping (Al, Ga and V) on the silicon site within the $MgFeSiO_4$ structure. The doping process is described by Equation 6.1, where M = Al, Ga or V.

$$M_2O_3 + 2Si_{Si}^{X} + MgO \rightarrow 2M_{Si}^{'} + Mg_i^{\bullet\bullet} + 2SiO_2 \tag{6.1}$$

Trivalent doping on the silicon site is charge compensated by the formation of a Mg interstitial. We also investigated an alternative charge-compensation mechanism involving O vacancies, which was found to be less favourable by more than 4 eV. Trivalent doping on other sites in the structure would yield oxygen vacancies as compensation, which would not improve the capacity or Mg^{2+} diffusion in the material.

Interatomic potentials were used to model the corresponding oxides of the dopant cations which were used. The potentials used are given in Table 6.6.[207,224] The dopant substitution energies were calculated by combining the appropriate defect and lattice energy terms, given in Table 6.7. This approach has been successfully applied to other silicate materials.[219]

Table 6.6: *Interatomic potential parameters for trivalent dopant cations*

Interaction	**A (eV)**	**ρ (Å)**	**C (eV.Å^6)**
Al^{3+}-O^{2-}	1114.9	0.3118	0.0
Ga^{3+}-O^{2-}	2901.12	0.2742	0.0
V^{3+}-O^{-2}	1790.2	0.3061	0.0

Table 6.7: *Trivalent dopant incorporation energies on the Si in $MgFeSiO_4$.*

Dopant	**Energy (eV)**
Al^{3+}	5.64
Ga^{3+}	8.99
V^{3+}	8.59

The large dopant values predicted for all three trivalent ions (Al, Ga and V) suggest a low degree of dopant solubility. From this we conclude such trivalent doping of $MgFeSiO_4$ is not a feasible method to improve capacity or Mg^{2+} migration.

6.5 Cell Voltage Trends

When developing new cathode materials for Mg batteries it is important to establish an adequate operating voltage (in the range of 2.0 - 3.0 V) while maintaining a high reversible capacity.[16,225]

DFT was used to calculate the cell voltage of cation-ordered $MgFeSiO_4$. The relevant Mg^{2+} ions were removed from the structure to carry out the calculations; different vacancy configurations were considered and the voltage was calculated using Equation 6.2 with the lowest energy configuration. Metallic Mg was used to calculate the chemical potential of magnesium ($\mu\{Mg\}$). This methodology has been applied successfully to other battery materials,[226–228] including silicates.[229,230]

$$V = \frac{\varepsilon\{MgFeSiO_4\} - \varepsilon\{Mg_xFeSiO_4\} - (x)\mu\{Mg\}}{2x} \tag{6.2}$$

The cell voltage of ordered $MgFeSiO_4$ was calculated to be 2.35 eV *vs.* Mg/Mg^{2+}, this is both within the desirable operating window and in good agreement with electrochemical data, which gives an average voltage of 2.4 V.[126]

Transition metal doping can be used as a method to 'tune' the cell voltage of cathode materials. Here we investigate how doping on the transition metal site of $MgFeSiO_4$ affects the cell voltage. Figure 6.7 shows the voltage trends of $MgFe_{1-x}M_xSiO_4$ (M = Ni, Co or Mn) *vs.* Mg/Mg^{2+} with increasing x values. When 50% of Fe is replaced by one of the doping transition metals the cell voltage follows the trend Mn (2.8 V) < Co (3.0 V) < Ni (3.4 V); a similar trend is reported for olivine $LiMPO_4$ systems.[44,231] It is worth noting that while the Mn and Co doped structures are within the operating window of current Mg ion electrolytes, Ni doping pushes the cell voltage above this window.

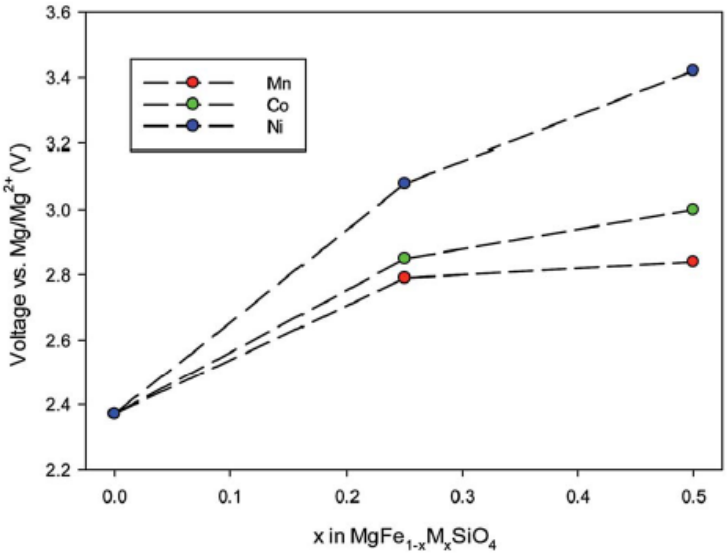

Figure 6.7: *Cell voltage trends (vs. Mg/Mg^{2+}) as a function of dopant (M = Co, Ni or Mn) on the Fe site in $MgFeSiO_4$*

6.6 Chapter Summary

The structural and electrochemical properties of the potential magnesium cathode material, ordered $MgFeSiO_4$, were analysed using atomistic modelling and DFT. The results are as follows:

(a) A Mg^{2+} migration energy of 0.6 eV was calculated along a one-dimensional curved pathway (similar to that in $LiFePO_4$) and a D_{Mg} in the range of 10^{-9} cm^2s^{-1} was derived for large-scale MD at 300 K. These results suggest favourable Mg^{2+} intercalation kinetics in this material.

(b) The incorporation energies of trivalent metal dopants on the silicon site were calculated and the process was predicted to be unfavourable and a low dopant solubility would be expected.

(c) The cell voltage for ordered $MgFeSiO_4$ was derived as 2.35 V *vs.* Mg/Mg^{2+} using DFT. This value is in good agreement with the available electrochemical data. Transition metal doping on the Fe site is predicted to increase the cell voltage in the cases of Co, Mn and Ni. However, in the case of Ni doping the voltage rises above the electrochemical stability window of current Mg electrolytes.

Overall this study suggests that ordered $MgFeSiO_4$ could be a viable cathode material for magnesium batteries.

7 | Conclusions and Future Work

7.1 General Remarks

This thesis presents computer modelling studies on a variety of cathode materials for sodium-ion and magnesium rechargeable batteries. This work has been motivated by the knowledge that emerging grid storage technologies require a new generation of batteries, beyond the current commercial Li-ion cells. The development of these new batteries depends on the evolution of new materials and an understanding of their properties on a scale difficult to probe using experimental techniques. Through atomic scale investigation of materials further insights into fundamental defect, ion-transport, cell voltage and surface related properties relevant to their performance within a battery have been provided. It is appropriate to conclude this thesis by reviewing each of the studies undertaken and suggesting possible future studies for each investigation.

7.2 Defect Chemistry and Na ion diffusion in $NaFePO_4$

In **Chapter 3** the defect and migration properties of both the olivine and maricite forms of $NaFePO_4$ were investigated using energy minimisation and molecular dynamics.

Conclusions

Anti-site defects were found to be the lowest energy intrinsic defect type in both the olivine and maricite forms of $NaFePO_4$. Na^+ ion diffusion was investigated in both structures using energy minimisation and MD. It was found that there is considerably more Na diffusion in olivine $NaFePO_4$ than in the maricite polymorph. Maricite $NaFePO_4$ was found to have a high energy barrier for Na diffusion and a low D_{Na} value of approximately 7 x 10^{-13} cm^2s^{-1} at 300 K. This lack of Na conductivity would make maricite $NaFePO_4$ a poor bulk cathode material for Na-ion batteries.

The Lowest energy pathway in olivine $NaFePO_4$ was found to be along the *b*-axis channels, in agreement with past work on $LiFePO_4$. A D_{Na} value of 4 x 10^{-9} cm^2s^{-1} was recorded at 300 K using MD, consistent with a high rate cathode material. The effect that the low energy anti-site defects have on the Na diffusion of this material was also considered. It was found that these defects impede Na diffusion to a much greater effect in this compound in $LiFePO_4$.

This atomistic study of olivine and maricite $NaFePO_4$ presents fundamental differences in their defect chemistry and bulk Na diffusion properties, helping to rationalise the electrochemical behaviour of these phases.

Future Work

This study could be extended through the use of DFT as a means to consider the voltage of olivine $NaFePO_4$. Olivine $NaFePO_4$ has a low operating voltage for a Na-ion cathode material, 2.7 V *vs.* Na/Na^+. Previous work has shown that

doping on the transition metal site of a polyanionic cathode material can tune its voltage properties. Divalent transition metals (Co^{2+}, Mn^{2+}, Ni^{2+} etc.) should be incorporated onto the Fe site to determine if this method could be used to increase the operating voltage of $NaFePO_4$. This could be further extended by considering mixed transition metal doping. For example both Co^{2+} and Ni^{2+} could be incorporated in small concentrations onto the Fe site.

7.3 Effect of Strain on Ion Migration and Defect Formation in Olivine $NaFePO_4$ and $LiFePO_4$

Chapter 4 presents a study on the effect of biaxial lattice strain on ion conduction properties of olivine $LiFePO_4$ and $NaFePO_4$, through the use of energy minimisation and MD calculations.

Conclusions

The application of biaxial strain is not predicted to change the dimensionality of diffusion in either $LiFePO_4$ or $NaFePO_4$. Both structures remain one-dimensional upon the application of both compressive and tensile strain. Diffusion barriers in the [010] direction significantly decrease in both materials with the application of tensile strain in the *ac*-plane. Tensile strain in the *ac*-plane also leads to increases in the diffusion coefficient for both materials. This offers a potential enhancement in ion conduction at room temperature.

The formation energies of blocking anti-site defects are found to be increased in both materials upon the application of *ac* tensile strain. An effect which is particularly prominent in $NaFePO_4$.

In general this study suggests that tensile strain applied in the *ac*-plane (perpendicular to migration channels) could improve the intercalation properties of olivine-type cathode materials. This discovery could lead to enhancements in ion conduction and rate performance of olivine cathodes, and provides a

framework for design optimisation of high rate cathode materials.

Future Work

DFT calculations could be used to expand this work. Nudged elastic band (NEB) calculations and *ab initio* MD would allow ion conduction to be examined with the inclusion of electronic structural aspects of these materials. NEB calculations would provide activation energies for ion migration and *ab initio* MD would predict diffusion coefficients. These results could be compared to those presented in this work providing a more extensive understanding the effect strain has on olivine-type materials, before experimental studies were performed.

Due to the nature of this computational study, interfacial effects such as grain boundaries and dislocations can not be considered. However, their presence may influence the enhancement which has been predicted. Therefore, experimental studies which implement this strain on either $LiFePO_4$ or $NaFePO_4$ would be able to offer key insights in this area.

7.4 Structural, Diffusion and Surface Properties of Layered Sodium Oxides

In **Chapter 5** the effect of Mg^{2+} doping on the intercalation and structural properties of P2-$Na_{\frac{2}{3}}[Ni_{\frac{1}{3}}Mn_{\frac{2}{3}}]O_2$ was investigated using energy minimisation and MD techniques. It is accompanied by experimental synthesis and structural analysis. This work is extended with an *ab initio* study of the surfaces and grain boundaries of P2-$NaCoO_2$.

Conclusions

The effect of Mg^{2+} doping on Na vacancy formation energies was considered. It was established that 10% Mg^{2+} doping on the Ni site would decrease the Na vacancy energy at all three Na sites.

D_{Na} values were calculated with MD for $Na_{0.6}[Ni_{0.33}Mn_{0.67}]O_2$ and $Na_{0.6}[Mg_{0.03}Ni_{0.3}Mn_{0.67}]O_2$. An order of magnitude decrease was recorded when the Mg^{2+} dopants were incorporated. Therefore an increase in Na^+ diffusion would be expected with 10% Mg^{2+} doping of P2-$Na_{\frac{2}{3}}[Ni_{\frac{1}{3}}Mn_{\frac{2}{3}}]O_2$.

Secondly, the structural changes that occur with Mg doping were studied using MD calculations. The magnesium ions were found to displace from the transition metal layer into the Na layer in $Na_{0.6}[Mg_{0.03}Ni_{0.3}Mn_{0.67}]O_2$. This is because Mg-O bonds are weaker than either Ni-O or Mn-O. The movement of the Mg^{2+} ions in the z-direction alters the electrostatic potential felt by Na ions and has a positive effect on Na^+ diffusion.

Twelve low energy surfaces of P2-$NaCoO_2$ were minimised in order to obtain their formation energies. Of these, the lowest in energy was predicted to be the $(10\bar{1}4)$ termination, while the highest was predicted as $(10\bar{1}0)$. The surface energy is related to the degree of coordination loss experienced by the Na and Co ions at the surface. Where a greater degree of coordination loss is experienced in the higher energy surfaces.

Grain boundary models were considered for the $(10\bar{1}4)$ and $(11\bar{2}0)$ surfaces. These were chosen as they represent the lowest energy termination and the low index surface with the lowest energy. The $(11\bar{2}0)$ boundary model had the lowest overall energy, despite the formation energy of this surface being higher than that of $(10\bar{1}4)$. The low energies calculated for both grain boundaries suggests that they will be present in high concentrations in $NaCoO_2$.

Future Work

There are several areas of future work that could be undertaken in order to extend this research.

Previous studies of P2-type oxide cathode materials for Na-ion batteries have considered doping of metals other than magnesium. These have included Li^+, Al^{3+}, Zn^{2+} and Ti^{4+}. It would be of interest to investigate how doping of these metals on the Ni site of P2-$Na_{\frac{2}{3}}[Ni_{\frac{1}{3}}Mn_{\frac{2}{3}}]O_2$ would affect its electrochemical and structural properties. Of particular significance would be any displacement of

these metals from the transition metal layer and subsequent changes in Na ion diffusion.

A more extensive study of the grain boundaries in P2-$NaCoO_2$ would be of considerable interest. To establish a better understanding on how the presence of grain boundaries influences Na^+ conduction *ab initio* MD calculations would be valuable. This would allow the prediction of surfaces which were most beneficial to Na^+ diffusion so they could be promoted during crystal growth.

Transition metal site doping of $NaCoO_2$ (and other Na oxide materials) is a common approach to tune material properties, such as ion conduction. It would be desirable to investigate, using DFT, how doping at the Co site with different metals, at varying concentrations, could effect surface formation.

A key area of interest would be the prediction of the morphology of $NaCoO_2$ using surface energy information. This would allow for comparison with previous computational and experimental determination of the morphology of structurally analogous $LiCoO_2$.

$Na_{0.7}CoO_2$ is a more commonly utilised cathode material than $NaCoO_2$. Through the knowledge obtained in this study, surface structures of the more complex $Na_{0.7}CoO_2$ material could be generated. The effect additional Na vacancies have on surface energies could provide insight into the formation of grain boundaries in synthesised $Na_{0.7}CoO_2$.

7.5 Diffusion Rates and Voltage Trends of $MgFeSiO_4$

Structural and electrochemical properties of ordered olivine $MgFeSiO_4$ were investigated in **Chapter 6** using atomistic modelling and DFT techniques.

Conclusions

The lowest energy Mg^{2+} diffusion pathway in $MgFeSiO_4$ was found to be along a one-dimensional curved pathway parallel to the *c*-axis, similar to that observed

in $LiFePO_4$. The migration energy in this direction was calculated to be 0.6 eV, which is low for a magnesium cathode material. Long time-scale MD was used to derive a D_{Mg} value in the range of 10^{-9} cm^2s^{-1} at 300 K. Suggesting favourable Mg^{2+} intercalation kinetics.

Trivalent metal doping at the silicon site was investigated. However, all incorporation energies were unfavourable and as such, low dopant solubility would be expected.

DFT calculations were used to predict a cell voltage of 2.35 V *vs.* Mg/Mg^{2+}, in good agreement with experimental data. Transition metal doping on the Fe site increases the cell voltage value in the cases of Co, Mn and Ni. However, in the case of Ni doping, the voltage rises above the electrochemical stability window of current Mg electrolytes.

The work presented here suggests that ordered $MgFeSiO_4$ could be a potential cathode material for magnesium batteries, due to its favourable Mg^{2+} kinetics.

Future Work

This chapter considered the ordered structure of $MgFeSiO_4$. Anti-site defects were found to easily form and then displace during the MD study. Extension of this work could consider the more thermodynamically stable, mixed Mg/Fe occupancy form of $MgFeSiO_4$ using MD calculations. It would be of interest to establish whether these anti-site defects are also able to easily form in this material, opening up clear diffusion pathways for Mg^{2+} ions. It could be that mobile anti-site defects would mean the mixed-occupancy form of $MgFeSiO_4$ is able to diffuse Mg^{2+} ions similarly to the ordered polymorph.

Bibliography

[1] H. Moriwake, A. Kuwabara, C. A. J. Fisher, R. Huang, T. Hitosugi, Y. H. Ikuhara, H. Oki and Y. Ikuhara, *Adv. Mater.*, 2013, **25**, 618–622.

[2] B. L. Ellis, K. T. Lee and L. F. Nazar, *Chem. Mater.*, 2010, **22**, 691–714.

[3] M. Sawicki and L. L. Shaw, *RSC Adv.*, 2015, **5**, 53129–53154.

[4] H. Pan, Y.-S. Hu and L. Chen, *Energy Environ. Sci.*, 2013, **6**, 2338–2360.

[5] B. Dunn, H. Kamath and J.-M. Tarascon, *Science*, 2011, **334**, 928–935.

[6] B. G. Pollet, I. Staffell and J. L. Shang, *Electrochim. Acta*, 2012, **84**, 235–249.

[7] V. Palomares, P. Serras, I. Villaluenga, K. B. Hueso, J. Carretero-González and T. Rojo, *Energy Environ. Sci.*, 2012, **5**, 5884.

[8] M. D. Slater, D. Kim, E. Lee and C. S. Johnson, *Adv. Funct. Mater.*, 2012, **23**, 947–958.

[9] N. Yabuuchi, K. Kubota, M. Dahbi and S. Komaba, *Chem. Rev.*, 2014, **114**, 11636–11682.

[10] S.-W. Kim, D.-H. Seo, X. Ma, G. Ceder and K. Kang, *Adv. Energy Mater.*, 2012, **2**, 710–721.

[11] B. L. Ellis and L. F. Nazar, *Curr. Opin. Solid State Mater. Sci.*, 2012, **16**, 168–177.

[12] V. Palomares, M. Casas-Cabanas, E. Castillo-Martínez, M. H. Han and T. Rojo, *Energy Environ. Sci.*, 2013, **6**, 2312–2337.

[13] D. Aurbach, Z. Lu, A. Schechter, Y. Gofer, H. Gizbar, R. Turgeman, Y. Cohen, M. Moshkovich and E. Levi, *Nature*, 2000, **407**, 724–727.

[14] P. Canepa, G. S. Gautam, D. C. Hannah, R. Malik, M. Liu, K. G. Gallagher, K. A. Persson and G. Ceder, *Chem. Rev.*, 2017, **117**, 4287–4341.

[15] H. D. Yoo, I. Shterenberg, Y. Gofer, G. Gershinsky, N. Pour and D. Aurbach, *Energy Environ. Sci.*, 2013, **6**, 2265–2279.

[16] M. M. Huie, D. C. Bock, E. S. Takeuchi, A. C. Marschilok and K. J. Takeuchi, *Coord. Chem. Rev.*, 2015, **287**, 15–27.

[17] J. M. Tarascon and M. Armand, *Nature*, 2001, **414**, 359–367.

[18] M. S. Islam and C. A. J. Fisher, *Chem. Soc. Rev.*, 2014, **43**, 185–204.

[19] M. S. Whittingham, *Chem. Rev.*, 2004, **104**, 4271–4302.

[20] M. R. Palacín, *Chem. Soc. Rev.*, 2009, **38**, 2565–2575.

[21] M. S. Whittingham, *Dalton Transactions*, 2008, 5424–5431.

[22] P. G. Bruce, *Chem. Commun.*, 1997, 1817–1824.

[23] C. M. Park, J. H. Kim, H. Kim and H. J. Sohn, *Chem. Soc. Rev.*, 2010, **39**, 3115–3141.

[24] J. Cabana, L. Monconduit, D. Larcher and M. R. Palacín, *Adv. Mater.*, 2010, **22**, E170–E192.

[25] L. Nazar, G. Goward, F. Leroux, M. Duncan, H. Huang, T. Kerr and J. Gaubicher, *Int. J. Inorg. Mater.*, 2001, **3**, 191–200.

[26] M. N. Obrovac, R. A. Dunlap, R. J. Sanderson and J. R. Dahn, *J Electrochem Soc*, 2001, **148**, A576–A588.

[27] H. Li, X. Huang and L. Chen, *Solid State Ionics*, 1999, **123**, 189–197.

[28] Y. Idota, T. Kubota and A. Matsufuji, *Science*, 1997, **276**, 1395–1397.

[29] J. M. Tarascon, P. Poizot, S. Laruelle, S. Grugeon and L. Dupont, *Nature*, 2000, **407**, 496–499.

[30] J. Fan, T. Wang, C. Yu, B. Tu, Z. Jiang and D. Zhao, *Adv. Mater.*, 2004, **16**, 1432–1436.

[31] W. Xu, N. L. Canfield, D. Wang, J. Xiao, Z. Nie and J. G. Zhang, *J. Power Sources*, 2010, **195**, 7403–7408.

[32] L. Ji, Z. Lin, M. Alcoutlabi and X. Zhang, *Energy Environ. Sci.*, 2011, **4**, 2682–2699.

[33] D. Deng, M. G. Kim, J. Y. Lee and J. Cho, *Energy Environ. Sci.*, 2009, **2**, 818–837.

[34] P. G. Bruce, *Solid State Ionics*, 2008, **179**, 752–760.

[35] A. K. Padhi, K. S. Najundaswamy and J. B. Goodenough, *J Electrochem Soc*, 1997, **144**, 1188–1194.

[36] K. Nanjundaswamy, A. K. Padhi, J. B. Goodenough, S. Okada, H. Ohtsuka, H. Arai and J.Yamaki, *Solid State Ionics*, 1996, **92**, 1–10.

[37] S. i. Nishimura, G. Kobayashi, K. Ohoyama, R. Kanno, M. Yashima and A. Yamada, *Nat. Mater.*, 2009, **7**, 707–711.

[38] C. A. J. Fisher, V. M. H. Prieto and M. S. Islam, *Chem. Mater.*, 2008, **20**, 5907–5915.

[39] M. Armand and J. M. Tarascon, *Nature*, 2008, **451**, 652–657.

[40] S. Y. Chung, S. Y. Choi, T. Yamamoto and Y. Ikuhara, *Phys. Rev. Lett.*, 2008, **100**, 1–4.

[41] S. Y. Chung, S. Y. Choi, T. Yamamoto and Y. Ikuhara, *Angew. Chem. Int. Ed.*, 2009, **48**, 543–546.

[42] K. Rissouli, K. Benkhouja, J. Ramos-Barrado and C. Julien, *Mater. Sci. Eng., B*, 2003, **98**, 185–189.

[43] S. Okada, S. Sawa, M. Egashira, J. ichi Yamaki, M. Tabuchi, H. Kageyama, T. Konishi and A. Yoshino, *J. Power Sources*, 2001, **97-98**, 430–432.

[44] A. Yamada, M. Hosoya, S. C. Chung, Y. Kudo, K. Hinokuma, K. Y. Liu and Y. Nishi, *J. Power Sources*, 2003, **119-121**, 232–238.

[45] M. Yonemura, A. Yamada, Y. Takei, N. Sonoyama and R. Kanno, *J Electrochem Soc*, 2004, **151**, A1352–A1356.

[46] G. R. Gardiner and M. S. Islam, *Chem. Mater.*, 2010, **22**, 1242–1248.

[47] H. Kim, H. Kim, Z. Ding, M. H. Lee, K. Lim, G. Yoon and K. Kang, *Adv. Energy Mater.*, 2016, **6**, 1600943.

[48] H. Vikström, S. Davidsson and M. Höök, *Appl. Energy*, 2013, **110**, 252–266.

[49] P. W. Gruber, P. A. Medina, G. A. Keoleian, S. E. Kesler, M. P. Everson and T. J. Wallington, *J. Ind. Ecol.*, 2011, **15**, 760–775.

[50] A. S. Nagelberg and W. L. Worrell, *J. Solid State Chem.*, 1979, **29**, 345–354.

[51] M. Whittingham, *Progress in Solid State Chemistry*, 1978, **12**, 41–99.

[52] C. Delmas, J. Braconnier, C. Fouassier and P. Hagenmuller, *Solid State Ionics*, 1981, **3-4**, 165–169.

[53] L. W. Shacklette, T. R. Jow and L. Townsend, *J Electrochem Soc*, 1988, **135**, 2669–2674.

[54] J. Tarascon and G. W. Hull, *Solid State Ionics*, 1986, **22**, 85–96.

[55] T. R. Jow, L. W. Shacklette, M. Maxfield and D. Vernick, *J Electrochem Soc*, 1987, **134**, 1730–1733.

[56] K. West, B. Zachau-Christiansen, T. Jacobsen and S. Skaarup, *Solid State Ionics*, 1988, **28-30**, 1128–1131.

[57] Y. Yamada, Y. Iriyama, T. Abe and Z. Ogumi, *Langmuir*, 2009, **25**, 12766–12770.

[58] D. Kim, S. H. Kang, M. Slater, S. Rood, J. T. Vaughey, N. Karan, M. Balasubramanian and C. S. Johnson, *Adv. Energy Mater.*, 2011, **1**, 333–336.

[59] S. P. Ong, V. L. Chevrier, G. Hautier, A. Jain, C. Moore, S. Kim, X. Ma and G. Ceder, *Energy Environ. Sci.*, 2011, **4**, 3680–3688.

[60] A. Ponrouch, C. Frontera, F. Bardé and M. R. Palacín, *Nat. Mater.*, 2015, **15**, 169–172.

[61] D. Kundu, E. Talaie, V. Duffort and L. F. Nazar, *Angew. Chem. Int. Ed.*, 2015, **54**, 3431–3448.

[62] T. D. Hatchard and M. N. Obrovac, *J. Electrochem. Soc.*, 2014, **161**, A1748–A1752.

[63] A. Ponrouch, R. Dedryvère, D. Monti, A. E. Demet, J. M. A. Mba, L. Croguennec, C. Masquelier, P. Johansson and M. R. Palacín, *Energy Environ. Sci.*, 2013, **6**, 2361–2369.

[64] Z. Wang, S. M. Selbach and T. Grande, *RSC Adv.*, 2014, **4**, 3973–3983.

[65] D. A. Stevens and J. R. Dahn, *J Electrochem Soc*, 2000, **147**, 1271–1273.

[66] D. A. Stevens and J. R. Dahn, *J Electrochem Soc*, 2001, **148**, A803–A811.

[67] K. Gotoh, T. Ishikawa, S. Shimadzu, N. Yabuuchi, S. Komaba, K. Takeda, A. Goto, K. Deguchi, S. Ohki, K. Hashi, T. Shimizu and H. Ishida, *J. Power Sources*, 2013, **225**, 137–140.

[68] Y. Kim, K. H. Ha, S. M. Oh and K. T. Lee, *Chem. Eur. J*, 2014, **20**, 11980–11992.

[69] W. Luo, F. Shen, C. Bommier, H. Zhu, X. Ji and L. Hu, *Acc. Chem. Res.*, 2016, **49**, 231–240.

[70] M. Dahbi, N. Yabuuchi, K. Kubota, K. Tokiwa and S. Komaba, *Phys. Chem. Chem. Phys.*, 2014, **16**, 15007–15028.

[71] W. Kang, Z. Zhang, P. K. Lee, T. W. Ng, W. Li, Y. Tang, W. Zhang, C. S. Lee and D. Y. W. Yu, *J. Mater. Chem. A*, 2015, **3**, 22846–22852.

[72] L. P. Wang, L. Yu, X. Wang, M. Srinivasan and Z. J. Xu, *J. Mater. Chem. A*, 2015, **3**, 9353–9378.

[73] C. Delmas, C. Fouassier and P. Hagenmuller, *Physica B+C*, 1980, **99**, 81–85.

[74] N. Yabuuchi and S. Komaba, *Sci. Technol. Adv. Mater.*, 2014, **15**, 043501.

[75] R. Berthelot, D. Carlier and C. Delmas, *Nat. Mater.*, 2010, **10**, 74–80.

[76] P. Zhang, R. B. Capaz, M. L. Cohen and S. G. Louie, *Phys. Rev. B*, 2005, **71**, 153102.

[77] M. Roger, D. J. P. Morris, D. A. Tennant, M. J. Gutmann, J. P. Goff, J. U. Hoffmann, R. Feyerherm, E. Dudzik, D. Prabhakaran, A. T. Boothroyd, N. Shannon, B. Lake and P. P. Deen, *Nature*, 2006, **445**, 631–634.

[78] Y. S. Meng, Y. Hinuma and G. Ceder, *J. Chem. Phys.*, 2008, **128**, 104708.

[79] Y. Takahashi, Y. Gotoh and J. Akimoto, *J. Solid State Chem.*, 2003, **172**, 22–26.

[80] Z. Lu and J. R. Dahn, *Chem. Mater.*, 2001, **13**, 2078–2083.

[81] Z. Lu and J. R. Dahn, *J. Electrochem. Soc.*, 2001, **148**, A1225–A1229.

[82] D. H. Lee, J. Xu and Y. S. Meng, *Phys. Chem. Chem. Phys.*, 2013, **15**, 3304–3312.

[83] J. Cabana, N. A. Chernova, J. Xiao, M. Roppolo, K. A. Aldi, M. S. Whittingham and C. P. Grey, *Inorg. Chem.*, 2013, **52**, 8540–8550.

[84] P. Moreau, D. Guyomard, J. Gaubicher and F. Boucher, *Chem. Mater.*, 2010, **22**, 4126–4128.

[85] R. Tripathi, S. M. Wood, M. S. Islam and L. F. Nazar, *Energy Environ. Sci.*, 2013, **6**, 2257–2264.

[86] S. M. Oh, S. T. Myung, J. Hassoun, B. Scrosati and Y. K. Sun, *Electrochem. Commun.*, 2012, **22**, 149–152.

[87] B. L. Ellis, W. R. M. Makahnouk, Y. Makimura, K. Toghill and L. F. Nazar, *Nat. Mater.*, 2007, **6**, 749–753.

[88] P. P. Prosini, C. Cento, A. Masci and M. Carewska, *Solid State Ionics*, 2014, **263**, 1–8.

[89] J. Kim, D. H. Seo, H. Kim, I. Park, J. K. Yoo, S. K. Jung, Y. U. Park, W. A. Goddard and K. Kang, *Energy Environ. Sci.*, 2015, **8**, 540–545.

[90] R. Kapaev, A. Chekannikov, S. Novikova, S. Yaroslavtsev, T. Kulova, V. Rusakov, A. Skundin and A. Yaroslavtsev, *J. Solid State Electrochem.*, 2017, **21**, 2373–2380.

[91] M. Casas-Cabanas, V. V. Roddatis, D. Saurel, P. Kubiak, J. Carretero-González, V. Palomares, P. Serras and T. Rojo, *J. Mater. Chem.*, 2012, **22**, 17421–17423.

[92] C. Zhu, L. Gu, L. Suo, J. Popovic, H. Li, Y. Ikuhara and J. Maier, *Adv. Funct. Mater.*, 2013, **24**, 312–318.

[93] M. Galceran, V. Roddatis, F. J. Zúñiga, J. M. Pérez-Mato, B. Acebedo, R. Arenal, I. Peral, T. Rojo and M. Casas-Cabanas, *Chem. Mater.*, 2014, **26**, 3289–3294.

[94] F. Boucher, J. Gaubicher, M. Cuisinier, D. Guyomard and P. Moreau, *J. Am. Chem. Soc.*, 2014, **136**, 9144–9157.

[95] J. Lu, S. C. Chung, S. ichi Nishimura and A. Yamada, *Chem. Mater.*, 2013, **25**, 4557–4565.

[96] N. N. Bramnik, K. Nikolowski, C. Baehtz, K. G. Bramnik and H. Ehrenberg, *Chem. Mater.*, 2007, **19**, 908–915.

[97] D. Aurbach, G. Suresh, E. Levi, A. Mitelman, O. Mizrahi, O. Chusid and M. Brunelli, *Adv. Mater.*, 2007, **19**, 4260–4267.

[98] P. Canepa, G. S. Gautam, R. Malik, S. Jayaraman, Z. Rong, K. R. Zavadil, K. Persson and G. Ceder, *Chem. Mater.*, 2015, **27**, 3317–3325.

[99] J. Muldoon, C. B. Bucur, A. G. Oliver, T. Sugimoto, M. Matsui, H. S. Kim, G. D. Allred, J. Zajicek and Y. Kotani, *Energy Environ. Sci.*, 2012, **5**, 5941–5950.

[100] N. Pour, Y. Gofer, D. T. Major and D. Aurbach, *J. Am. Chem. Soc.*, 2011, **133**, 6270–6278.

[101] D. Aurbach, H. Gizbar, A. Schechter, O. Chusid, H. E. Gottlieb, Y. Gofer and I. Goldberg, *J Electrochem Soc*, 2002, **149**, A115–A121.

[102] J. O. Besenhard and M. Winter, *ChemPhysChem*, 2002, **3**, 155–159.

[103] B. Peng, J. Liang, Z. Taoa and J. Chen, *J. Mater. Chem.*, 2009, **19**, 2877–2883.

[104] E. Levi, Y. Gofer and D. Aurbach, *Chem. Mater.*, 2010, **22**, 860–868.

[105] E. Levi, G. Gershinsky, D. Aurbach and O. Isnard, *Inorg. Chem.*, 2009, **48**, 8751–8758.

[106] C. R. andR. Chevrel, A. Jenny, P. Pecheur, H. Scherrer and S. Scherrer, *Phys Rev B*, 1999, **60**, 16442–16447.

[107] K. R. Kganyago, P. E. Ngoepe and C. R. A. Catlow, *Phys. Rev. B*, 2003, **67**, 104103.

[108] E. Levi, E. Lancry, A. Mitelman, D. Aurbach, G. Ceder, D. Morgan and O. Isnard, *Chem. Mater.*, 2006, **18**, 5492–5503.

[109] D. Aurbach, Y. Gofer, Z. Lu, A. Schechter, O.Chusid, H. Gizbar, Y. Cohen, V.Ashkenazi, M.Moshkovich, R.Turgeman and E.Levi, *J. Power Sources*, 2001, **97–98**, 28–32.

[110] D. Aurbach, M. D. Levi and E. Levi, *Solid State Ionics*, 2008, **179**, 742–751.

[111] P. G. Bruce, F. Krok, J. Nowinski, V. C. Gibson and K. Tavakkoli, *J. Mater. Chem.*, 1991, **1**, 705–706.

[112] P. G. Bruce, F. Krok, P. Lightfoot, J. L. Nowinski and V. C. Gibson, *Solid State Ionics*, 1992, **53-56**, 351–355.

[113] N. Amir, Y. Vestfrid, O. Chusid, Y. Gofer and D.Aurbach, *J. Power Sources*, 2007, **174**, 1234–1240.

[114] P. Lightfoot, F. Krok, J. L. Nowinski and P. G. Bruce, *J. Mater. Chem.*, 1992, **2**, 139–140.

[115] M. K. Aydinol, A. F. Kohan, G. Ceder, K. Cho and J. Joannopoulos, *Phys. Rev. B*, 1997, **56**, 1354–1365.

[116] Z. Rong, R. Malik, P. Canepa, G. S. Gautam, M. Liu, A. Jain, K. Persson and G. Ceder, *Chem. Mater.*, 2015, **27**, 6016–6021.

[117] G. S. Gautam, P. Canepa, A. Abdellahi, A. Urban, R. Malik and G. Ceder, *Chem. Mater.*, 2015, **27**, 3733–3742.

[118] G. S. Gautam, P. Canepa, R. Malik, M. Liu, K. Persson and G. Ceder, *Chem. Commun.*, 2015, **51**, 13619–13622.

[119] P. Novák, R. Imhof and O. Haas, *Electrochim. Acta*, 1999, **45**, 351–367.

[120] C. Kim, P. J. Phillips, B. Key, T. Yi, D. Nordlund, Y.-S. Yu, R. D. Bayliss, S.-D. Han, M. He, Z. Zhang, A. K. Burrell, R. F. Klie and J. Cabana, *Adv. Mater.*, 2015, **27**, 3377–3384.

[121] R. Enjalbert and J. Galy, *Acta Cryst. C*, 1986, **C42**, 1467–1469.

[122] Z. Feng, J. Yang, Y. NuLi, J. Wang, X. Wang and Z. Wang, *Electrochem. Commun.*, 2008, **10**, 1291–1294.

[123] Y. NuLi, Y. Zheng, Y. Wang, J. Yang and J. Wang, *J. Mater. Chem.*, 2011, **21**, 12437–12443.

[124] Y. NuLi, Y. Zheng, F. Wang, J. Yang, A. I. Minett, J. Wang and J. Chen, *Electrochem. Commun.*, 2011, **13**, 1143–1146.

[125] C. Ling, D. Banerjee, W. Song, M. Zhang and M. Matsui, *J. Mater. Chem.*, 2012, **22**, 13517–13523.

[126] Y. Orikasa, T. Masese, Y. Koyama, T. Mori, M. Hattori, K. Yamamoto, T. Okado, Z.-D. Huang, T. Minato, C. Tassel, J. Kim, Y. Kobayashi, T. Abe, H. Kageyama and Y. Uchimoto, *Sci. Rep.*, 2014, **4**, 5622.

[127] T. Mori, T. Masese, Y. Orikasa, Z.-D. Huang, T. Okado, J. Kim and Y. Uchimoto, *Phys. Chem. Chem. Phys.*, 2016, **18**, 13524–13529.

[128] S. A. T. Redfern, G. Artioli, R. Rinaldi, C. M. B. Henderson, K. S. Knight and B. J. Wood, *Phys. Chem. Miner.*, 2000, **27**, 630–637.

[129] S. Chatterjee, S. Sengupta, T. Saha-Dasgupta, K. Chatterjee and N. Mandal, *Phys. Rev. B*, 2009, **79**, 115103.

[130] S. Chatterjee, S. Bhattacharyya, S. Sengupta and T. Saha-Dasgupta, *Phys. Chem. Miner.*, 2010, **38**, 259–265.

[131] J. D. Gale, *J. Chem. Soc., Faraday Trans.*, 1997, **93**, 629–637.

[132] J. D. Gale and A. L. Rohl, *Mol. Simul.*, 2003, **29**, 291–341.

[133] S. Plimpton, *J. Comput. Phys.*, 1995, **117**, 1–19.

[134] G. Kresse and J. Furthmüller, *Phys. Rev. B*, 1996, **54**, 11169–11186.

[135] G. Kresse and D. Joubert, *Phys. Rev. B*, 1999, **59**, 1758–1775.

[136] A. R. Leach, *Molecular Modelling Principles and Applications*, 1996.

[137] C. R. A. Catlow, *Computer Modelling in Inorganic Crystallography*, 1997.

[138] A. K. Cheetham and P. Day, *Solid-State Chemistry Techniques*, 1987.

[139] D. Frenkel and B. Smit, *Understanding Molecular Simulation From Algorithms to Applications*, 1996.

[140] D. S. Sholl and J. A. Steckel, *Density Functional Theory: A Practical Introduction*, Wiley, 2009.

[141] W. Koch and M. C. Holthausen, *A Chemist's Guide to Density Functional Theory*, Wiley, 2001.

[142] R. A. Buckingham, *Proceedings of the Royal Society of London A*, 1938, **168**, 264–283.

[143] P. M. Morse, *Phys. Rev.*, 1929, **34**, 57–64.

[144] A. Pedone, G. Malavasi, M. C. Menziani, A. N. Cormack and U. Segre, *J. Phys. Chem. B*, 2006, **110**, 11780–11795.

[145] B. G. Dick and A. W. Overhauser, *Phys. Rev.*, 1958, **112**, 90–103.

[146] N. F. Mott and M. J. Littleton, *J. Chem. Soc. Faraday Trans.*, 1989, 485–499.

[147] L. Verlet, *Phys. Rev.*, 1967, **159**, 98–103.

[148] W. Kohn and L. J. Sham, *Phys. Rev.*, 1965, **140**, A1133–A1138.

[149] J. P. Perdew and A. Zunger, *Phys. Rev. B*, 1981, **23**, 5048–5079.

[150] J. P. Perdew, K. Burke and M. Ernzerhof, *Phys. Rev. Lett.*, 1996, **77**, 3865–3868.

[151] F. Bloch, *Zeitschrift fur Physik*, 1929, **52**, 555–600.

[152] P. W. Tasker, *J. Phys. C Solid State Phys.*, 1979, **12**, 4977–4984.

[153] W. Tang, X. Song, Y. Du, C. Peng, M. Lin, S. Xi, B. Tian, J. Zheng, Y. Wu, F. Pan and K. P. Loh, *J. Mater. Chem. A*, 2016, **4**, 4882–4892.

[154] C. Heubner, S. Heiden, M. Schneider and A. Michaelis, *Electrochim. Acta*, 2017, **233**, 78–84.

[155] K. T. Lee, T. N. Ramesh, F. Nan, G. Botton and L. F. Nazar, *Chem. Mater.*, 2011, **23**, 3593–3600.

[156] V. Koleva, T. Boyadzhieva, E. Zhecheva, D. Nihtianova, S. Simova, G. Tyuliev and R. Stoyanova, *Cryst. Eng. Comm.*, 2013, **15**, 9080–9089.

[157] M. Avdeev, Z. Mohamed, C. D. Ling, J. Lu, M. Tamaru, A. Yamada and P. Barpanda, *Inorg. Chem.*, 2013, **52**, 8685–8693.

[158] M. S. Islam, D. J. Driscoll, C. A. J. Fisher and P. R. Slater, *Chem. Mater.*, 2005, **17**, 5085–5092.

[159] R. Amin, P. Balaya and J. Maier, *Electrochem. Solid-State Lett.*, 2007, **10**, A13–A16.

[160] T. Shibata, W. Kobayashi and Y. Moritomo, *Appl. Phys Express*, 2013, **6**, 097101.

[161] T. Shibata, W. Kobayashi and Y. Moritomo, *Appl. Phys Express*, 2014, **7**, 067101.

[162] C. Tealdi, C. Spreafico and P. Mustarelli, *J. Mater. Chem.*, 2012, **22**, 24870–24876.

[163] C. Delacourt, P. Poizot, S. Levasseur and C. Masquelier, *Electrochem Solid-State Lett*, 2006, **9**, A352–A355.

[164] H. Huang, S. C. Yin and L. F. Nazar, *Electrochem. Solid-State Lett.*, 2001, **4**, A170 – A172.

[165] K. Zaghib, A. Guerfi, P. Hovington, A. Vijh, M. Trudeau, A. Mauger, J. Goodenough and C. Julien, *J. Power Sources*, 2013, **232**, 357–369.

[166] R. M. Ormerod, *Chem. Soc. Rev.*, 2002, **32**, 17–28.

[167] J. G. Swallow, W. H. Woodford, Y. Chen, Q. Lu, J. J. Kim, D. Chen, Y.-M. Chiang, W. C. Carter, B. Yildiz, H. L. Tuller and K. J. V. Vliet, *J. Electroceram.*, 2014, **32**, 3–27.

[168] J. Janek, M. Martin and K. D. Becker, *Phys. Chem. Chem. Phys.*, 2009, **11**, 3010–3010.

[169] A. Kushima and B. Yildiz, *J. Mater. Chem.*, 2010, **20**, 4809–4819.

[170] G. Dezanneau, J. Hermet and B. Dupé, *Int. J. Hydrogen Energy*, 2012, **37**, 8081–8086.

[171] T. J. Pennycook, M. J. Beck, K. Varga, M. Varela, S. J. Pennycook and S. T. Pantelides, *Phys. Rev. Lett.*, 2010, **104**, 1–4.

[172] M. J. D. Rushton and A. Chroneos, *Sci. Rep.*, 2014, **4**, 6068.

[173] R. A. D. Souza, A. Ramadan and S. Hörner, *Energy Environ. Sci.*, 2012, **5**, 5445–5453.

[174] S. Tan, Y. Zhang, M. Xia, Z. Ye, F. Chen, X. Xie, R. Peng, D. Xu, Q. Fan, H. Xu, J. Jiang, T. Zhang, X. Lai, T. Xiang, J. Hu, B. Xie and D. Feng, *Nat. Mater.*, 2013, **12**, 634–640.

[175] C. W. Hicks, D. O. Brodsky, E. A. Yelland, A. S. Gibbs, J. A. N. Bruin, M. E. Barber, S. D. Edkins, K. Nishimura, S. Yonezawa, Y. Maeno and A. P. Mackenzie, *Science*, 2014, **344**, 283–285.

[176] F. Nabeshima, Y. Imai, M. Hanawa, I. Tsukada and A. Maeda, *Appl. Phys. Lett.*, 2013, **103**, 172602.

[177] N. Sata, K. Eberman, K. Eberl and J. Maier, *Nature*, 2000, **408**, 946–949.

[178] J. H. Haeni, P. Irvin, W. Chang, R. Uecker, P. Reiche, Y. L. Li, S. Choudhury, W. Tian, M. E. Hawley, B. Craigo, A. K. Tagantsev, X. Q.

Pan, S. K. Streiffer, L. Q. Chen, S. W. Kirchoefer, J. Levy and D. G. Schlom, *Nature*, 2004, **430**, 758–761.

[179] S. A. Harrington, J. Zhai, S. Denev, V. Gopalan, H. Wang, Z. Bi, S. A. T. Redfern, S.-H. Baek, C. W. Bark, C.-B. Eom, Q. Jia, M. E. Vickers and J. L. MacManus-Driscoll, *Nat. Nanotechnol.*, 2011, **6**, 491–495.

[180] H. J. Yan, Z. Q. Wang, B. Xu and C. Ouyang, *Funct. Mater. Lett.*, 2012, **5**, 1250037.

[181] F. Ning, S. Li, B. Xu and C. Ouyang, *Solid State Ionics*, 2014, **263**, 46–48.

[182] J. Lee, S. J. Pennycook and S. T. Pantelides, *Appl. Phys. Lett.*, 2012, **101**, 033901.

[183] R. Shahid and S. Murugavel, *Phys. Chem. Chem. Phys.*, 2013, **15**, 18809–14.

[184] F. Sauvage, L. Laffont, J.-M. Tarascon and E. Baudrin, *J. Power Sources*, 2008, **175**, 495–501.

[185] S. Laref and A. Laref, *RSC Adv.*, 2015, **5**, 35667–35674.

[186] J. Chen, A. K. Thapa and T. A. Berfield, *J. Power Sources*, 2014, **271**, 406–413.

[187] A. Awarke, S. Lauer, M. Wittler and S. Pischinger, *Comput. Mater. Sci.*, 2011, **50**, 871–879.

[188] T. Kozawa, T. Murakami and M. Naito, *J. Power Sources*, 2016, **320**, 120–126.

[189] D. B. Ravnsbæk, K. Xiang, W. Xing, O. J. Borkiewicz, K. M. Wiaderek, P. Gionet, K. W. Chapman, P. J. Chupas, M. Tang and Y.-M. Chiang, *Nano Lett.*, 2016, **16**, 2375–2380.

[190] C. Tealdi, J. Heath and M. S. Islam, *J. Mater. Chem. A*, 2016, **4**, 6998–7004.

[191] S. Yang, X. Zhou, J. Zhang and Z. Liu, *J. Mater. Chem.*, 2010, **20**, 8086–8091.

[192] R. Chen, Y. Wu and X. Y. Kong, *J. Power Sources*, 2014, **258**, 246–252.

[193] G. J. Shu and F. C. Chou, *Phys. Rev. B*, 2008, **78**, 3–6.

[194] T. Jiang, G. Chen, A. Li, C. Wang and Y. Wei, *J. Alloys Compd.*, 2009, **478**, 604–607.

[195] J. Chen and J. Graetz, *ACS Appl. Mater. Interfaces*, 2011, **3**, 1380–1384.

[196] Z. Lu and J. R. Dahn, *J. Electrochem. Soc.*, 2001, **148**, A710.

[197] X. Wu, G. L. Xu, G. Zhong, Z. Gong, M. J. McDonald, S. Zheng, R. Fu, Z. Chen, K. Amine and Y. Yang, *ACS Appl. Mater. Interfaces*, 2016, **8**, 22227–22237.

[198] H. Yoshida, N. Yabuuchi, K. Kubota, I. Ikeuchi, A. Garsuch, M. Schulz-Dobrickb and S. Komaba, *Chem. Commun.*, 2014, **50**, 3677 – 3680.

[199] X. Wua, J. G. amd Dawei Wang, G. Zhong, M. J. McDonald and Y. Yangab, *J. Power Sources*, 2015, **281**, 18–26.

[200] B. Zhou, H. Shi, R. Cao, X. Zhang and Z. Jiang, *Phys. Chem. Chem. Phys.*, 2014, **16**, 18578–18585.

[201] W. Zhao, H. Kirie, A. Tanaka, M. Unno, S. Yamamoto and H. Noguchi, *Mater. Lett.*, 2014, **135**, 131–134.

[202] K. Hemalatha, M. Jayakumar, P. Berac and A. S. Prakash, *J. Mater. Chem.A*, 2015, **3**, 20908–20912.

[203] G. Singh, N. Tapia-Ruiz, J. M. L. del Amo, U. Maitra, J. W. Somerville, A. R. Armstrong, J. M. de Ilarduya, T. Rojo and P. G. Bruce, *Chem. Mater.*, 2016, **28**, 5087–5094.

[204] D. Kramer and G. Ceder, *Chem. Mater.*, 2009, **21**, 3799–3809.

[205] Y. Hinuma, Y. S. Meng and G. Ceder, *Phys. Rev. B*, 2008, **77**, 224111.

[206] B. Ammundsen, G. R. Burns, M. S. Islam, H. Kanoh and J. Rozière, *J. Phys. Chem. B*, 1999, **103**, 5175–5180.

[207] G. V. Lewis and C. R. Catlow, *J. Phys. C: Solid State Phys.*, 1985, **18**, 1149 – 1161.

[208] Z.-Y. Li, R. Gao, J. Zhang, X. Zhang, Z. Hu and X. Liu, *J. Mater. Chem. A*, 2016, **4**, 3453–3461.

[209] J. Xu, D. H. Lee, R. J. Clément, X. Yu, M. Leskes, A. J. Pell, G. Pintacuda, X.-Q. Yang, C. P. Grey, and Y. S. Meng, *Chem. Mater.*, 2014, **26**, 1260–1269.

[210] G. W. Watson, E. T. Kelsey, N. H. de Leeuw, D. J. Harris and S. C. Parker, *J. Chem. SOC., Faraday Trans.,*, 1996, **92**, 433–438.

[211] L. Wang, F. Zhou, Y. S. Meng and G. Ceder, *Phys. Rev. B*, 2007, **76**, 165435.

[212] T. Oyama, N. Wada, H. Takagi and M. Yoshiya, *Phys. Rev. B*, 2010, **82**, 134107.

[213] J. A. Dawson, H. Chen and I. Tanaka, *J. Phys. Chem. C*, 2014, **188**, 14485–14494.

[214] Y. Zheng, Y. NuLi, Q. Chen, Y. Wang, J. Yang and J. Wang, *Electrochim. Acta*, 2012, **66**, 75–81.

[215] M. S. Islam, R. Dominko, C. Masquelier, C. Sirisopanaporn, A. R. Armstrong and P. G. Bruce, *J. Mater. Chem.*, 2011, **21**, 9811–9818.

[216] S. Chatterjee and T. Saha-Dasgupta, *Phys. Rev. B*, 2010, **81**, 1–7.

[217] B. Zhang, R. Dugas, G. Rousse, P. Rozier, A. M. Abakumov and J. M. Tarascon, *Nat. Commun.*, 2016, **7**, 10308.

[218] J. Heath, H. Chen and M. S. Islam, *J. Mater. Chem. A*, 2017, **5**, 13161–13167.

[219] N. Kuganathan and M. S. Islam, *Chem. Mater.*, 2009, **21**, 5196–5202.

[220] A. R. Armstrong, N. Kuganathan, M. S. Islam and P. G. Bruce, *J. Am. Chem. Soc.*, 2011, **133**, 13031–13035.

[221] Y. Deng, C. Eames, J.-N. Chotard, F. Lalere, V. Seznec, S. Emge, O. Pecher, C. P. Grey, C. Masquelier and M. S. Islam, *J. Am. Chem. Soc.*, 2015, **137**, 9136–9145.

[222] S. M. Wood, C. Eames, E. Kendrick and M. S. Islam, *J. Phys. Chem. C*, 2015, 15935–15941.

[223] J. Wu, G. Gao, G. Wu, B. Liu, H. Yang, X. Zhou and J. Wang, *Phys. Chem. Chem. Phys.*, 2014, **16**, 22974–22978.

[224] M. Cherry, M. Islam and C. Catlow, *J. Solid State Chem.*, 1995, **118**, 125–132.

[225] P. Saha, M. K. Datta, O. I. Velikokhatnyi, A. Manivannan, D. Alman and P. N. Kumta, *Prog. Mater Sci.*, 2014, **66**, 1–86.

[226] M. Liu, Z. Rong, R. Malik, P. Canepa, A. Jain, G. Ceder and K. A. Persson, *Energy Environ. Sci.*, 2015, **8**, 964–974.

[227] A. R. Armstrong, C. Lyness, P. M. Panchmatia, M. S. Islam and P. G. Bruce, *Nat. Mater.*, 2011, **10**, 223–229.

[228] Y. Yuan, C. Zhan, K. He, H. Chen, W. Yao, S. Sharifi-Asl, B. Song, Z. Yang, A. Nie, X. Luo, H. Wang, S. M. Wood, K. Amine, M. S. Islam, J. Lu and R. Shahbazian-Yassar, *Nat. Commun.*, 2016, **7**, 13374.

[229] C. Eames, A. R. Armstrong, P. G. Bruce and M. S. Islam, *Chem. Mater.*, 2012, **24**, 2155–2161.

[230] M. A. de Dompablo, M. Armand, J. Tarascon and U. Amador, *Electrochem. Commun.*, 2006, **8**, 1292–1298.

[231] C. Masquelier and L. Croguennec, *Chem. Rev.*, 2013, **113**, 6552–6591.

[232] F. Kroger, *The Chemistry of Imperfect Crystals*, North-Holland:Amsterdam, 1974.

[233] E. J. Mittemeijer, *Crystallography. In: Fundamentals of Materials Science*, Springer, 2010.

Appendices

A | Kröger Vink Notation

Kröger-Vink notation is the most commonly used way of describing defects in crystal systems.[232] It is based on the following structure:

$$X_Z^Y \tag{A.1}$$

Here X describes the species present, Y is the net charge with respect to the crystal lattice and Z is the location of said species. The possible values of X, Y and Z are given in Table A.1.

Table A.1: *Components of Kröger-Vink notation used to describe point defects in crystal systems*

Component	Possible Values	Description
X	V	Vacancy
	H, Li, Be...	Atomic symbol of ion on lattice site
Y	X	neutral charge
	•	positive charge
	,	negative charge
Z	H, Li, Be...	Atomic symbol of species originally on site
	i	interstitial site

The number of • or ' indicate the net charge of the species. (ie. •• represents +2). So for example a sodium ion on a sodium site would be represented as

follows:

$$Na_{Na}^{X} \tag{A.2}$$

and an oxygen vacancy would be:

$$V_{O}^{\bullet\bullet} \tag{A.3}$$

Defect equations can be built up using these notations. For example, the formation of an oxygen interstitial is shown below.

$$O_{O}^{x} \rightarrow V_{O}^{\bullet\bullet} + O_{i}^{''} \tag{A.4}$$

This notation is used through the work presented here.

B | Isolated defect energies

Table B.1: *Isolated defect energies in olivine and maricite $NaFePO_4$*

Defect type	**Kröger-Vink notation**	**Defect energy olivine (eV)**	**Defect energy maricite (eV)**
Vacancy	V'_{Na}	5.88	5.68
Vacancy	V''_{Fe}	22.42	20.99
Vacancy	V''''_{P}	153.49	150.39
Vacancy	$V^{\bullet\bullet}_{O}$	24.35	23.32
Interstitial	$Na^{\bullet}_{i}$	-3.46	-3.40
Interstitial	$Fe^{\bullet\bullet}_{i}$	-16.78	-15.17
Impurity	Na'_{Fe}	-14.48	-14.65
Impurity	$Fe^{\bullet}_{Na}$	15.36	14.95

Table B.2: *Isolated defect energies in $MgFeSiO_4$*

Defect type	**Kröger-Vink notation**	**Defect energy (eV)**
Vacancy	V''_{Mg}	23.13
Vacancy	V''_{Fe}	24.77
Vacancy	V''''_{Si}	98.15
Vacancy	$V^{\bullet\bullet}_{O}$	24.11
Interstitial	$Mg^{\bullet\bullet}_{i}$	5.96
Interstitial	$Fe^{\bullet\bullet}_{i}$	7.52
Impurity	Mg^{X}_{Fe}	0.11
Impurity	Fe^{X}_{Mg}	-0.07

C | Hexagonal Miller Indices

The unit cell basis vectors can be described using **a, b** and **c**, with points on the axes given by $\frac{\mathbf{a}}{h}$, $\frac{\mathbf{b}}{k}$ and $\frac{\mathbf{c}}{l}$, where *h,k* and *l* are all integers, defining a plane in the lattice. Miller indices are used to describe the orientation of lattice planes within in a crystal system. A family of lattice planes can be fully identified with the indices *h,k* and *l*. These planes have interplannar distances denoted by d_{hkl}. Miller indices are presented as (hkl) and parallel front and back faces of a crystal are denoted by (hkl) and $(\bar{h}\bar{k}\bar{l})$. Miller indices only indicate the orientation of the lattice plane, they do not provide information regarding their position with respect to the atomic structure of the crystal.

For hexagonal crystal systems the derivation of a set of equivalent lattice planes is more complicated. An additional index, *i*, is included to yield the Miller-Bravais indices, $(hkil)$.Where $i = -(h + k)$ and therefore by knowing (hkl), i can be added according to $(hkil) = (hk(\bar{h} + \bar{k})l)$. For example:

$$(110) = (11(-1 - -1)0) = (11\bar{2}0) \tag{C.1}$$

The index of i is essentially artificial as it not necessarily need to indicate the orientation of the family of lattice planes. However, it is helpful to recognise equivalent lattice planes. For example in a hexagonal system, the (100) family of lattice planes is equivalent to the $(\bar{1}10)$.[233]

D | Example Datasets

Example GULP dataset

defe opti conp comp prop phonon

title 1

Dataset of olivine NaFePO4

name NaFePO4

cell

10.4109 6.2283 4.9521 90.0 90.0 90.0

frac

Na core 0.5 0.5 0.5

Fe2 core 0.7870 0.75 0.5137

P core 0.8917 1.25 0.5574

O1 core 0.6140 0.75 0.7476

O2 core 0.9685 0.75 0.3389

O3 core 0.8245 1.0554 0.6882

Fe2 shel 0.7870 0.75 0.5137

O1 shel 0.6140 0.75 0.7476

O2 shel 0.9685 0.75 0.3389

O3 shel 0.8245 1.0554 0.6882

space

p n m a

species

Na core 1.0

Fe2 core -0.997

Fe2 shel 2.997

P core 5.0

O core 0.96

O shel -2.96

buck

Na core O shel 560 0.32 0.0 0.0 12.0

buck

Fe2 shel O shel 1105.2409 0.3106 0.0 0.0 12.0

buck

P core O shel 897.2648 0.3577 0.0 0.0 12.0

buck

O shel O shel 22764.3 0.149 44.53 0.0 12.0

three

P core O core O core 1.3226 109.47 2.0 2.0 4.0

spring

Na 99999

spring

Fe2 19.26

spring

P 99999

spring

O 65.0

dump nafepo4.grs

Example LAMMPS data file

Title line: 1_10_vac

19872 atoms

0 bonds

0 angles

0 dihedrals

0 impropers

5 atom types
0 bond types
0 angle types
0 dihedral types
0 improper types

0.0 57.6780000000 xlo xhi
0.0 62.2554000000 ylo yhi
0.0 60.6090000000 zlo zhi

Masses

1 24.305
2 55.845
3 55.845
4 28.0855
5 15.9994

Atoms

1 1 1 1.2 36.048750000 5.187950000 0.000000000
2 1 1 1.2 36.048750000 5.187950000 3.030450000
3 1 1 1.2 33.645500000 0.000000000 3.030450000
4 1 1 1.2 33.645500000 0.000000000 0.000000000
5 1 1 1.2 40.855250000 5.187950000 0.000000000
6 1 1 1.2 40.855250000 5.187950000 3.030450000
7 1 1 1.2 38.452000000 0.000000000 3.030450000
8 1 1 1.2 38.452000000 0.000000000 0.000000000
9 1 1 1.2 45.661750000 5.187950000 0.000000000

10 1 1 1.2 43.258500000 0.000000000 3.030450000

11 1 1 1.2 43.258500000 0.000000000 0.000000000

12 1 1 1.2 50.468250000 5.187950000 3.030450000

...

Example LAMMPS input file

```
############################
#————Variables and cell————————#
############################
clear
units metal #eV,atomic charge,angstroms,ps,kelvin,bars,g/mol
dimension 3
boundary p p p
atom_style full
#processors * * * grid numa
read_data data.300_a_novac
group sodium type 1
#replicate 2 2 2
variable T1 equal 300
variable Timer equal step*dt

############################
#———Pair styles and electrostatics————#
############################

pair_style buck/coul/long 10.0
pair_coeff * * 0.0 1.0 0.0
pair_coeff 1 4 560 0.32 0.0
pair_coeff 2 4 1760 0.28 0.0
pair_coeff 3 4 1345.15 0.318 0
```

```
pair_coeff 4 4 22764.3 0.149 44.53

kspace_style pppm 1e-05

############################
# ————Run Minimization ————#
############################

reset_timestep 0
timestep 0.5
thermo 10
thermo_style custom step enthalpy fmax lx ly lz vol press
min_style cg
minimize 1e-25 1e-25 5000 10000

############################
# ———— Relax Cell ————————#
############################

reset_timestep 0
timestep 0.5
fix 1 all box/relax aniso 1.0 vmax 0.003
thermo 1
thermo_style custom step enthalpy fmax lx ly lz vol press
min_style cg
minimize 1e-25 1e-25 5000 10000
unfix 1

############################
# ————Run NPT T1——————————#
############################
```

```
reset_timestep 0
timestep 0.002
velocity all create $T1 4928459 rot yes dist gaussian
fix 2 all npt temp $T1 $T1 0.01 aniso 1.0 1.0 0.1
thermo_style custom step v_Timer cpu temp etotal fmax lx ly lz vol press
thermo 1000
run 2000
unfix 2

reset_timestep 0
timestep 0.002
compute mymsd sodium msd com yes
variable msdx equal "c_mymsd[1]"
variable msdy equal "c_mymsd[2]"
variable msdz equal "c_mymsd[3]"
variable msdtot equal "c_mymsd[4]"
fix msdT1 sodium ave/time 1 1
10000 v_msdx v_msdy v_msdz v_msdtot file msd$T1
fix 3 all nvt temp $T1 $T1 0.01
thermo_style custom step v_Timer cpu temp etotal fmax lx ly lz vol press
thermo 5000
dump dynamics all xyz 100 dynamics.xyz
run 5000000
unfix 3
unfix msdT1
```

Example VASP INCAR file

```
system = NaCoO2
PREC = accurate
```

ISTART = 1

ISMEAR = -5

SIGMA = 0.05

ENCUT = 520

ISIF = 3

ISPIN = 2

IBRION = 2

NELMIN = 4

#NELECT = 606

#NUPDOWN = 1

#AMIN = 0.01

#BMIX = 4.0001

NSW = 100

EDIFF = 1E-5

EDIFFG = -0.03

LORBIT = 11

ICHARG = 0

#EMIN = -3

#EMAX = 10.5

NEDOS = 500

NCORE = 8

#NPAR = 4

LREAL = Auto

ALGO = Fast

LDAU = .TRUE.

LDAUL = -1 2 -1

LDAUU = 0 3.3 0

LDAUJ = 0 1 0

LMAXMIX = 4

MAGMOM =45*0.6 45*0.6 90*0.6

LASPH = .TRUE.

#ISYM = 0

GGA = PS

#IDIPOL = 4

Example VASP KPOINTS file

K-Points

0

G

8 2 1

Example VASP POSCAR file

NA CO O

1.0000000000000000

2.8803896308416035 0.0000000001436935 -0.0000000014484826

5.7607796980967647 18.2817367108918241 -0.3851302946334665

-0.0000000166082866 -0.6976878301342934 32.6277557374248133

Na Co O

45 45 90

Direct

0.3836533852633624 0.0581732850276686 0.0416896169152167

0.0227133989694705 0.7386431398794331 0.0496238572832029

0.6986656679154428 0.4006671361953910 0.0263864302937550

0.7077448682487720 0.1461275211495849 0.1046548877953502

0.3685102998378168 0.8157447458361768 0.1095736144318227

0.0351858807137600 0.4824069832964967 0.1035322270879304

0.0439449364708910 0.2280275122776039 0.1685551281474190

0.7112809214208329 0.8943594797106925 0.1722230283709970

0.3787021663351817 0.5606488423704579 0.1712078511310962

0.3851927637905720 0.3074035436378175 0.2324856008220350

...

Example VASP POTCAR file

PAW_PBE Na 08Apr2002

1.00000000000000000

parameters from PSCTR are:

VRHFIN =Na: s1p0

LEXCH = PE

EATOM = 5.1581 eV, .3791 Ry

TITEL = PAW_PBE Na 08Apr2002

LULTRA = F use ultrasoft PP ?

IUNSCR = 1 unscreen: 0-lin 1-nonlin 2-no

RPACOR = 1.800 partial core radius

POMASS = 22.990; ZVAL = 1.000 mass and valenz

RCORE = 2.200 outmost cutoff radius RWIGS = 3.320; RWIGS = 1.757 wigner-seitz radius (au A)

ENMAX = 101.968; ENMIN = 76.476 eV

ICORE = 2 local potential

LCOR = T correct aug charges

LPAW = T paw PP

EAUG = 250.695

DEXC = -.224

RMAX = 4.566 core radius for proj-oper

RAUG = 1.300 factor for augmentation sphere

RDEP = 2.259 radius for radial grids

QCUT = -2.738; QGAM = 5.475 optimization parameters

Description

l E TYP RCUT TYP RCUT

0 .000 23 2.200

0 2.000 23 2.200

1 .000 23 2.200

2 .000 23 2.200

Error from kinetic energy argument (eV)

NDATA = 100

STEP = 20.000 1.050

.348 .334 .326 .310 .302 .284 .267 .258

.240 .222 .214 .197 .181 .166 .151 .137

.124 .112 .101 .853E-01 .760E-01 .674E-01 .559E-01 .490E-01

.428E-01 .347E-01 .277E-01 .237E-01 .186E-01 .143E-01 .109E-01 .814E-02

.600E-02 .437E-02 .315E-02 .227E-02 .150E-02 .115E-02 .878E-03 .781E-03

.729E-03 .720E-03 .719E-03 .706E-03 .674E-03 .622E-03 .554E-03 .458E-03

.380E-03 .292E-03 .221E-03 .179E-03 .144E-03 .125E-03 .118E-03 .117E-03

.116E-03 .112E-03 .102E-03 .878E-04 .713E-04 .558E-04 .437E-04 .350E-04

.317E-04 .309E-04 .307E-04 .295E-04 .259E-04 .215E-04 .163E-04 .124E-04

.103E-04 .973E-05 .968E-05 .927E-05 .801E-05 .626E-05 .453E-05 .365E-05

.338E-05 .335E-05 .313E-05 .253E-05 .185E-05 .142E-05 .129E-05 .127E-05

.116E-05 .917E-06 .668E-06 .563E-06 .549E-06 .520E-06 .423E-06 .321E-06

.275E-06 .272E-06 .250E-06 .201E-06

END of PSCTR-controll parameters

local part

85.0376694860515556

-.18316053E+02 -.18302544E+02 -.18269466E+02 -.18214418E+02 -.18137523E+02

-.18038955E+02 -.17918939E+02 -.17777753E+02 -.17615727E+02 -.17433244E+02

-.17230737E+02 -.17008687E+02 -.16767626E+02 -.16508124E+02 -.16230795E+02

-.15936287E+02 -.15625280E+02 -.15298485E+02 -.14956637E+02 -.14600495E+02

...

Example METADISE input

vasp

Na Co O

1.00000000000000

2.8737704376640858 0.0000000000000000 0.0000000000000000

-1.4368852188320429 2.4887582036461953 0.0000000000000000

0.0000000000000000 0.0000000000000000 15.2877768154666160

Na Co O

3 3 6

Direct

0.0000000000000000 0.0000000000000000 0.0000000000000000

0.6666666865499664 0.3333333432698495 0.3333333432699064

0.3333333432698495 0.6666666865396991 0.6666666865334108

0.0000000000000000 0.0000000000000000 0.5000000000000000

0.6666666865499664 0.3333333432698495 0.8333333432699064

0.3333333432698495 0.6666666865396991 0.1666666865334108

0.0000000000000000 0.0000000000000000 0.2308355948257130

0.0000000000000000 0.0000000000000000 0.7691644051742870

0.6666666865499664 0.3333333432698495 0.5641689380956194

0.6666666865499664 0.3333333432698495 0.1024977484441933

0.3333333432698495 0.6666666865396991 0.8975022813591238

0.3333333432698495 0.6666666865396991 0.4358310917076977

ends

poten

species

Na core 1.0000

Co core 3.0000

O core -2.0000

ends

ends

#force

#print vasp 1

#rdf

#stop

#grow 2 2 2

slab

#miller 0 0 1

start

miller

maxm 4

stackgen systematic

#coord Zr3 core O4 core 2.8

#from 15

#all

#step 1.01

#dipole

tole 0.2

bfgs 1

newt 0

start

stop

stop

E | Published Work

Publications

i. C. Tealdi, J. Heath and M. S. Islam, "Feeling the strain: enhancing ionic transport in olivine phosphate cathodes for Li- and Na-ion batteries through strain effects", *J. Mater. Chem. A*, **4**, 6998-7004 (2016).

ii. J. Heath, H. Chen and M. S. Islam, "$MgFeSiO_4$ as a potential cathode material for magnesium batteries: ion diffusion rates and voltage trends", *J. Mater. Chem. A*, **5**, 13161-13167 (2017).

iii. N. Tapia-Ruiz, W. M. Dose, N. Sharma, H. Chen, J. Heath, J. Somerville, U. Maitra, M. S. Islam and P. G. Bruce, High voltage P2-$Na_{2/3}Ni_{1/3-x}Mg_xMn_{2/3}O_2$ ($0 < x < 0.20$) cathodes; insights from neutron and in-situ X-ray diffraction, electrochemical and computational studies, *Energy Environ. Sci.* (Submitted).

Journal of Materials Chemistry A

PAPER

View Article Online
View Journal | View Issue

Cite this: J. Mater. Chem. A, 2016, 4, 6998

Feeling the strain: enhancing ionic transport in olivine phosphate cathodes for Li- and Na-ion batteries through strain effects†

Cristina Tealdi,*[a] Jennifer Heath[b] and M. Saiful Islam[b]

Received 20th November 2015
Accepted 21st February 2016

DOI: 10.1039/c5ta09418f

www.rsc.org/MaterialsA

Olivine-type phosphates $LiFePO_4$ and $NaFePO_4$ are among the most widely studied cathode materials for rechargeable batteries. To improve their rate behaviour for future electronic and vehicle applications, it is vital that the Li^+ and Na^+ conductivities be enhanced. In this study, atomistic simulation methods (including molecular dynamics) are used to investigate the effect of lattice strain on ion transport and defect formation in olivine-type $LiFePO_4$ and $NaFePO_4$, as these properties are directly related to their intercalation behaviour. The results suggest that lattice strain can have a remarkable effect on the rate performance of cathode materials, with a major increase in the ionic conductivity and decrease in blocking defects at room temperature. Such understanding is important for the future optimization of high-rate cathodes for rechargeable batteries, and is relevant to the growing interest in developing thin film solid-state batteries.

1. Introduction

The successful development of next-generation lithium- and sodium-ion batteries depends to a large degree on the ability to fabricate cathode materials with superior electrochemical and mechanical properties.[1–3] Cathodes based on olivine $LiFePO_4$ have been widely studied for this purpose and continue to be important.[4–6] One advantage of such polyoxyanion-type materials compared with the conventional layered transition metal oxides is that the binding of oxygen in the polyoxyanions enhances the material's stability and thus safety.[6,7] Sodium-ion battery materials such as $NaFePO_4$ have attracted increasing attention recently, largely because the high natural abundance of sodium should make them less expensive.[8,9] The development of cheap and safe cathode materials is a particularly important goal in the case of large-scale batteries. However, the improvement of the rate performance of both $LiFePO_4$ and $NaFePO_4$ for portable electronic or electric vehicle applications will require significantly improved ionic conductivities.

Previous strategies to optimize intercalation properties have mainly involved chemical doping and morphology modulation, with nanosizing and carbon coating so far proving to be the most successful approaches.[10,11] The charge/discharge rate performance of olivine-type $LiFePO_4$ has been improved by shortening the diffusion distances by preparing nanosized particles, but higher rates are required for specific applications such as electric vehicles.[4] Higher energy storage capability will also require materials with faster ionic transport so that thicker electrodes can be used.[5]

In the case of intercalation compounds, charge/discharge rates are related to lithium and sodium diffusion kinetics which, in turn, are highly dependent upon structural and defect properties. Manipulation of lattice strain is increasingly being considered as a possible design strategy to improve the functional properties of various materials, such as superconductivity,[12,13] ionic conductivity,[14] ferroelectricity[15] and colossal magnetoresistance.[16] In particular, there has been considerable interest in the application of lattice strain in the modulation of ionic conductivity in oxide materials for solid oxide fuel cells (SOFCs).[17,18] Several studies have highlighted the positive effect of tensile lattice strain on migration barriers and ion diffusion coefficients in SOFC electrolytes. Following the report of colossal ionic conductivity in epitaxial heterostructures formed by thin layers of Y/ZrO_2 and $SrTiO_3$,[19] lattice strain effects on fluorite- and perovskite-type materials have been systematically studied using computational techniques.[20–25] It should be noted that there is still much debate as to the nature of the charge-carriers with evidence pointing towards electronic conduction in $SrTiO_3$.[26] In contrast, the effects of mechanical strain on battery cathode materials have not been extensively considered, with only a limited number of studies to date.[27–34] Shahid *et al.*[30] report that at the nanoscale level for $LiFePO_4$ there is an order of magnitude enhancement in the electronic (polaron)

[a]Department of Chemistry, University of Pavia and INSTM, Viale Taramelli 16, 27100 Pavia, Italy. E-mail: cristina.tealdi@unipv.it

[b]Department of Chemistry, University of Bath, Bath, BA2 7AY, UK

† Electronic supplementary information (ESI) available: List of potential parameters; comparison between calculated and experimental structures; alkali-ion migration barrier for along path A and C; formation energy for pair clusters in the case of *ab* and *bc* biaxial applied strain. See DOI: 10.1039/c5ta09418f

conductivity, which they attribute to lattice strain on reduction of the particle size.

Chemical or electrochemical delithiation and subsequent sodiation of the Li counterpart is currently the only known synthesis route to obtain olivine-type $NaFePO_4$.[35–38] Epitaxial deposition of thin films, and eventually strained thin films or multilayers, represents an effective strategy to stabilize metastable polymorphs under ambient conditions.[39] Such strategies have not yet been explored for maricite-type $NaFePO_4$, the thermodynamically most stable polymorph of this compound.[40] Strain due to lattice mismatch may also be present at the interfaces of powder samples of intercalating materials which undergo a two-phase mechanism during intercalation, such as $LiFePO_4/FePO_4$.[41]

It is apparent that there are limited fundamental studies in this area comparing Li- and Na-ion systems. Here we investigate the effect of lattice strain on the ion conduction and defect properties of both $LiFePO_4$ and $NaFePO_4$ olivine-type cathode materials using atomistic simulation techniques. In general, the results highlight the importance of lattice strain effects as an alternative strategy to optimize the electrochemical properties of Li- and Na-ion intercalation compounds.

2. Methodology

The atomistic computational methods used in this study are well-established techniques[42] (embodied in the GULP code[43]), and have been applied successfully to a range of polyanionic battery materials.[44] They are based on the specification of a pair potential model that describes the interactions between ions within the crystal structure. For the olivine-type compounds, short-range interactions were modelled with a Buckingham potential, with an additional three-body term to describe the angle-dependent nature of the P–O–P bonds in the PO_4^{3-} units (Table S1-ESI†). Potential parameters for this study were taken from previous successful work on the olivine-type phosphate systems.[45,46] Ion polarisability was taken into account through the use of the well-known shell model.[47] Lattice relaxation around charged defects and migrating ions was treated through the two-region Mott–Littleton scheme,[48] which allows the explicit relaxation of a large number of ions (>800) to be simulated. To calculate energy barriers for Li^+ or Na^+ migration, the conventional hopping model for diffusion into adjacent vacancies was used.

Olivine-type $LiFePO_4$ and $NaFePO_4$ unit cells (*Pnma* space group) were allowed to relax at constant pressure with zero applied strain. Subsequently, the energy minimized cells were subjected to biaxial compressive (<0%) and tensile (>0%) strains between −3% and +3% in the *ab*, *ac* and *bc* planes. Besides representing a physically accessible range of values, this strain range was chosen in order to avoid instabilities due to structure failure. Energy minimization of the structures with respect to the third cell parameter and all the atomic coordinates was then carried out. The strained energy-minimized structures were used as the starting configurations for ion migration and defect calculations. Similar methodology has been applied successfully to the study of SOFC oxide-ion conductors.[23,25]

For the MD simulations, 4 × 4 × 8 supercells with composition $Li_{0.9}FePO_4$ and $Na_{0.9}FePO_4$ were constructed and energy minimized (using the GULP code) at both zero and 3% tensile strain applied in the *ac* plane. Alkali ion vacancies were randomly distributed within the supercells and charge compensation was achieved through a corresponding change in the average Fe oxidation state. As in our previous MD work on Li_xFePO_4,[53] the shell model for electronic polarizability was applied to the oxygen ions (with a spring constant of 130 eV $Å^{-2}$), which ensured stability of the system during the MD simulations at high temperature.

MD simulations were performed, using the DL_Poly code,[49] at 500 K. Such an elevated temperature was chosen to allow both efficient thermalization of the defective solid and sufficient ionic diffusion during the simulation time span, thereby improving the statistics of the calculations. The unstrained system was first equilibrated at the desired temperature for 100 ps with a time step of 0.5 fs. The main simulation run of 750 ps was then performed in the NVT ensemble (Nose–Hoover thermostat). For the strained systems, the energy-minimized cell parameters were expanded according to the thermal expansion coefficient derived for the same composition in the absence of applied strain. Simulations in the NVT ensemble were then carried out as described above. Data analysis was performed using the Visual Molecular Dynamics package (VMD).[50]

3. Results and discussion

3.1 Strain effects on structures and ion conduction

The set of interatomic potential and shell model parameters used in this study have been shown to reliably reproduce the structural features of unstrained $LiFePO_4$ and $NaFePO_4$, as well as their defect, transport and surface properties,[45,46,50–53] providing a good starting point for our calculations. The good reproduction of the experimental structures of both $LiFePO_4$ and $NaFePO_4$ is shown in Table S2-ESI.†

For experimental work, lattice strain in thin film samples is generated by substrate/film mismatch (*i.e.* differences in *d* spacing), as schematically shown in Fig. 1a. In the case of similar or related lattice symmetries and small mismatch values, a coherent interface is often formed. The lattice mismatch leads to in-plane tensile or compressive strain in the deposited layer. In the case of thin films deposited onto

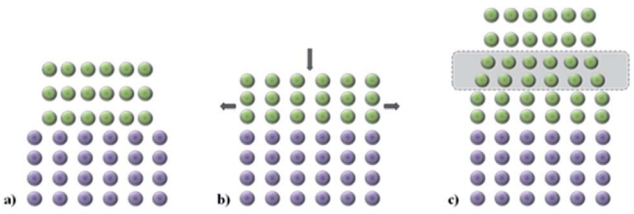

Fig. 1 Schematic representation of the effect of tensile lattice strain in a thin film (green) due to lattice mismatch with the substrate (purple). (a) No mismatch accommodation; (b) tensile-strained thin film; (c) partially strained film showing strain release far from the substrate interface for a sufficiently thick film.

a crystalline substrate, this will be a biaxial strain. For perfectly elastic systems, the unit cell volume remains unchanged and the out-of-plane cell parameters increase or decrease as appropriate (Fig. 1b). In practice, most oxide materials have a Poisson coefficient, ν, in the range $0 < \nu < 0.5$,[54] which means that in the case of in-plane tensile strain, the out-of-plane parameter decreases in a way such that film undergoes a net positive volume change. The effect of lattice strain due to film/substrate mismatch is restricted to thin films on the nanometre scale; in thick film samples, the strain is released as the greater distance from the film/substrate interface into the bulk of the film (Fig. 1c).

Since many electrical properties are strongly influenced by the type and number of defects and ion diffusion barriers in a crystalline material, strained systems may exhibit behaviour different from the corresponding bulk material. The application of biaxial strain on the olivine system, regardless of the plane considered, has the effect of producing a net change in unit cell volume (Fig. 2), indicative of non-ideal Poisson behaviour commonly exhibited by oxide materials.[54]

Li^+ migration pathways in $LiFePO_4$, as initially predicted from theoretical calculations[45] and subsequently confirmed by neutron diffraction maximum entropy methods,[55] zigzag along the [010] direction (path B of Fig. 3). Na^+ migration in olivine-type $NaFePO_4$ was subsequently shown to follow the same zigzag path, characterized by a lower migration barrier compared to the Li analogue (0.31 *vs.* 0.55 eV).[46]

Fig. 4 shows the calculated migration barrier along the [010] direction as a function of applied strain for $LiFePO_4$ and $NaFePO_4$. For both systems, the energy barrier increases slightly along with the applied strain for the *ab* and *bc* cases. Interestingly, the migration energy decreases along with strain for the *ac* case, reaching a value that is approximately half the value for the unstrained system, corresponding to 3% tensile strain. The calculated migration barrier for Li^+ decreases from 0.55 eV to 0.28 eV while the migration barrier for Na^+ decreases from 0.37 eV to 0.16 eV. This significant reduction in migration energy with tensile strain is consistent with a previous DFT study of Lee *et al.*[29] on olivine $LiFePO_4$.

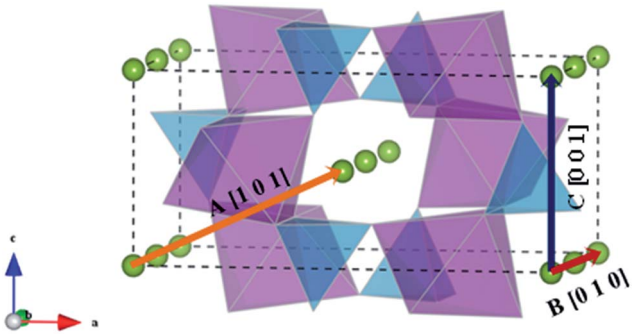

Fig. 3 Schematic representation of the possible migration paths in olivine-type $AFePO_4$ (A = Li^+ or Na^+). Blue: PO_4 tetrahedra; purple: FeO_6 octahedra; green: Li/Na.

Changes in migration barrier for ion diffusion can be interpreted in terms of structural modifications. In particular, our results show a relation between the variation in migration barrier and the ion–ion hopping distance along with the applied strain. For example, in the case of $LiFePO_4$, the Li–Li hopping distance for migration along the [010] direction decreases for the *ac* strained case, while it increases for the other two cases (Fig. S2a†). A decrease in ion hopping distance is expected to favour alkali-ion diffusion in the structure. Other structural parameters such as the available free volume at the saddle point position may also influence the migration barrier. Hence, the overall variation of the migration barrier along with strain is the

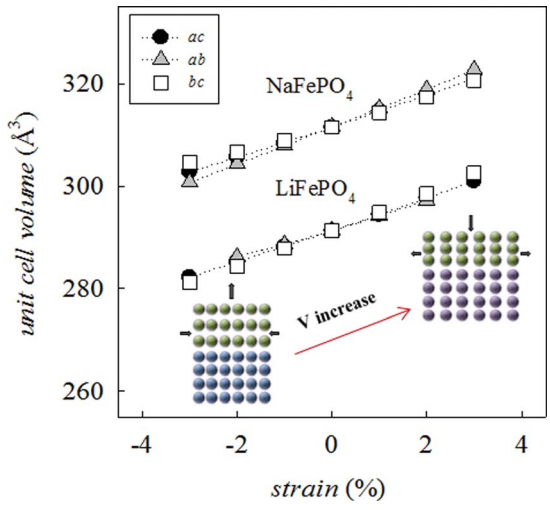

Fig. 2 Change in the calculated unit cell volume as a function of strain for $LiFePO_4$ and $NaFePO_4$ together with a schematic representation of the effect of compressive (<0%) or tensile (>0%) lattice strain on the thin film system.

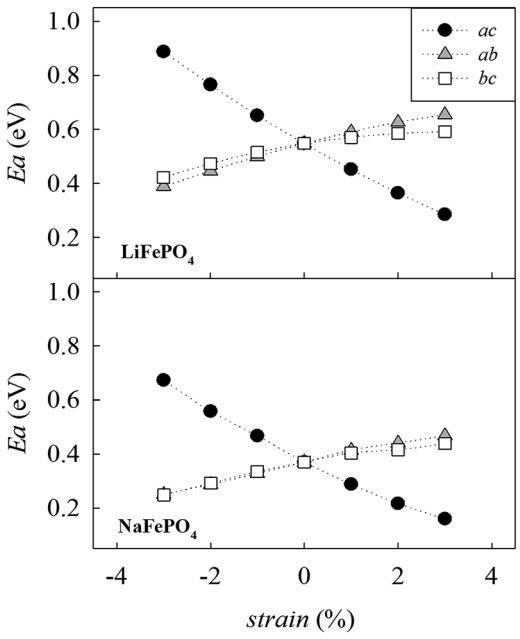

Fig. 4 Change in the alkali-ion migration barrier along the [010] direction as a function of strain for $LiFePO_4$ (upper panel) and $NaFePO_4$ (lower panel).

result of a fine interplay between different structural parameters whose nature depends on the particular structure and the migration path considered (Fig. S2-ESI†).

In the olivine system, two other migration paths are potentially accessible, labelled in Fig. 3 as paths A (along the [101] direction) and C (along the [001] direction). Both paths are characterized by energy barriers >2.5 eV for the unstrained system and, as a consequence, alkali-ion transport in olivine-type materials is considered a one dimensional process. In order to determine if the dimensionality of Li^+ and Na^+ ion transport is affected by applied strain, the activation energies for paths A and C were calculated as a function of the applied strain. Calculated activation energies for migration along the [001] and [101] directions still remain above 2 eV for the 3% tensile strained systems (Fig. S1-ESI†) and therefore they are not comparable to the most favourable migration path running parallel to the *b* axis (Fig. 4). This result suggests that, even for the strained systems, Li^+ and Na^+ ion transport will remain a 1D diffusion process, as is found for unstrained $LiFePO_4$ and $NaFePO_4$.[45,46]

MD simulations performed on both the unstrained and the *ac*-plane strained systems confirmed that Li and Na ion diffusion proceeds through a zig-zag path parallel to the *b*-axis. The 1D and curved nature of such paths are not altered by the application of tensile strain, as shown in Fig. 5 for the Na-based system, selected as an example.

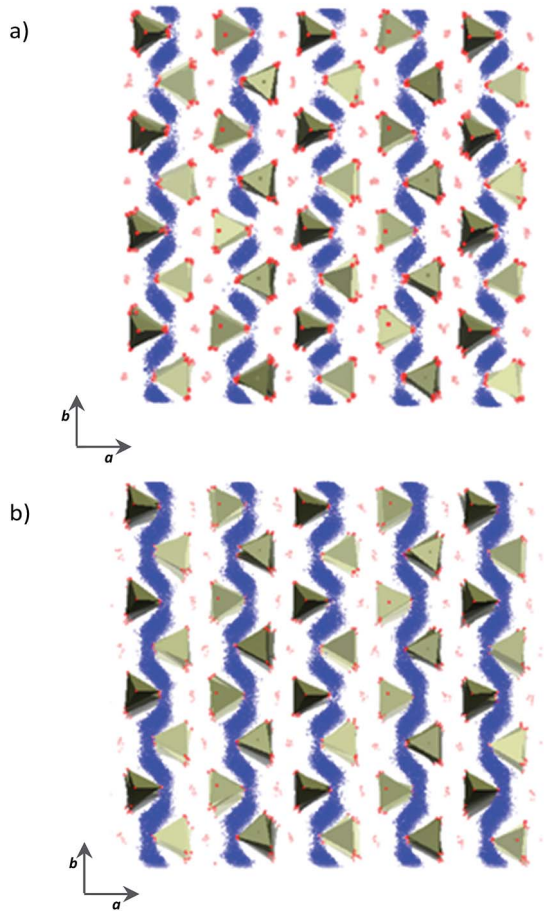

Fig. 5 Na-ion trajectory plot for (a) unstrained $Na_{0.9}FePO_4$ and (b) 3% *ac*-strained $Na_{0.9}FePO_4$ showing the Na-ion zig-zag path. Projection along the *c* axis. Blue spheres represent the positions occupied by Na ions over the simulation time; pink spheres represent the Fe ions in their final configuration while the tetrahedra represent the PO_4 units.

Visual analysis of Fig. 5 already indicates that the application of tensile strain has a positive effect on the alkali-ion mobility within the system showing greater Na-ion density in the trajectory plot. To better quantify such effects, Li and Na ion diffusion coefficients were derived from the slope of the mean square displacement (MSD) parameters *vs.* simulation time plots (Fig. 6) through the use of the following standard relation:

$$\langle |r_i(t) - r_i(0)|^2 \rangle = 6D + B \quad (1)$$

where on the left side the quadratic displacement of the Li/Na atom from its initial position is represented, D is the diffusion coefficient and B is the atomic displacement parameter attributed to thermal vibration. The diffusion coefficients (D) derived for the systems under investigation are reported in Table 1. Direct comparison with experiment is not straightforward due to significant scatter in measured values of diffusion coefficients. Nevertheless, our calculated D_{Li} and D_{Na} are consistent with available observed values for $LiFePO_4$ and related Na-ion cathode materials.[56–58]

Analysis of the MD results indicate two main points: first, Na-ion diffusion coefficients are predicted to be higher than Li-ion diffusion coefficients in the olivine system, in line with the calculated difference in the absolute values between Na-ion and Li-ion migration barriers (Fig. 4); second, the application of tensile strain increases the alkali-ion diffusion. The predicted effect is comparable for Li and Na-based systems and, at the simulation temperature used in this study (500 K), is roughly one order of magnitude.

The overall results derived from MD simulations are in good agreement with the trend observed from static lattice simulations, *i.e.* tensile strain applied perpendicularly to the main diffusion direction is enhancing ion transport in the system.

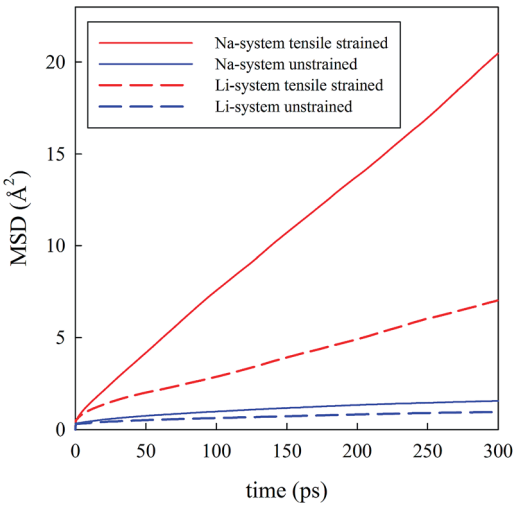

Fig. 6 Mean square displacement (MSD) *vs.* time for $Li_{0.9}FePO_4$ (dashed lines) and $Na_{0.9}FePO_4$ (solid lines).

Table 1 Comparison between the Li and Na ion calculated diffusion coefficients at 500 K for the unstrained and the 3% tensile strained systems

Strain (%)	D_{Li} ($cm^2\ s^{-1}$)	D_{Na} ($cm^2\ s^{-1}$)
0.0	3.36×10^{-8}	6.69×10^{-8}
3.0	3.42×10^{-7}	1.08×10^{-6}

Based on the calculated changes in activation energy along with strain (Fig. 4), we can estimate the change in ionic conductivity due to the application of 3% biaxial strain in the *ac* plane based on standard Arrhenius equations. Previous work of De Souza[23] shows that with regard to oxygen diffusion in fluorite-type CeO_2, ΔH^{mig} can be conveniently approximated by the calculated activation barrier, E_{mig}, within a certain range of applied strain. Using the values shown in Fig. 4, and approximating ΔH^{mig} by the calculated activation barrier, E_{mig}, we can predict an enhancement in Li^+ and Na^+ conductivity of approximately three orders of magnitude at room temperature. We recognize that the calculated enhancement based on MD results is significantly lower. However, a number of factors should be taken into consideration. First, MD simulations were conducted at 500 K while the estimation of conductivity increase based on the static lattice simulations result was performed at 300 K. The predicted change in activation energy along with strain (Fig. 4) suggests that differences in conductivity will be more pronounced as the temperature is reduced; for example, this has been computationally predicted[20] and experimentally observed[59] for oxygen diffusion in strained fluorite structures and perovskite-type materials.[60] This is also in line with the predicted large effect of temperature in the exponential factor of the Arrhenius equation.

Therefore, the key conclusion of this study is that tensile biaxial strain applied in the plane perpendicular to the main diffusion path will promote alkali-ion diffusion. Even within the limits of our estimate, this is a major enhancement in ionic conductivity which should greatly improve the rate behaviour of olivine-type cathode materials. Even taking into account possible effects of interfaces (*e.g.* dislocations, grain boundaries and space charge regions), the ionic conductivity should undergo a significant enhancement. There are of course experimental technical challenges associated with the fabrication of epitaxial thin-films (using, for example, pulsed laser deposition) and their electrical characterisation. In particular, the evolution of dislocation defects may introduce a lower degree of strain compared to that expected on the basis of substrate/lattice mismatch. Nevertheless, our clear predictions warrant further investigation.

3.2 Strain effects on defect formation

Due to the 1D nature of alkali-ion transport in olivine-type materials, the presence of intrinsic anti-site defects (eqn (2) and (3), and Fig. 7), which involve the exchange of an Li/Na ion for a neighbouring Fe atom, can be detrimental to ion intercalation properties:

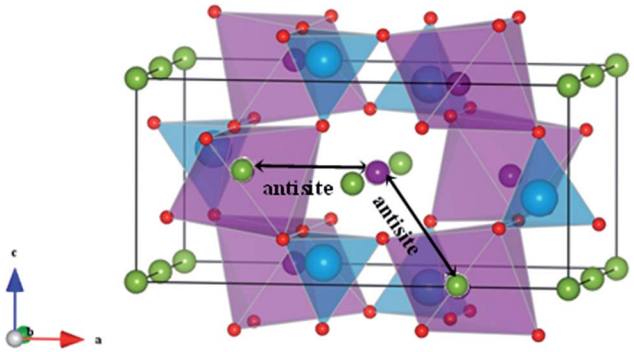

Fig. 7 Schematic representation of two configurations of Li/Fe or Na/Fe anti-site defects in olivine-type $AFePO_4$ ($A = Li^+$ or Na^+).

$$Li_{Li}^{\times} + Fe_{Fe}^{\times} \rightarrow Fe_{Li}^{\cdot} + Li'_{Fe} \quad (2)$$

$$Na_{Na}^{\times} + Fe_{Fe}^{\times} \rightarrow Fe_{Na}^{\cdot} + Na'_{Fe} \quad (3)$$

Such intersite cation exchanges represent the most energetically favourable intrinsic defect in olivine-type materials.[45] Their formation has been frequently observed experimentally, for example, by refinement of site occupancies in diffraction experiments[61] or by direct visualization using electron microscopy methods.[62] Since alkali-ion transport in olivine-type materials occurs one-dimensionally along [010], these types of defect negatively affect the intercalation properties by blocking the ion transport pathways.

In order to determine if the application of biaxial strain affects the formation energy of such defects, we calculated the energies of anti-site pair cluster formation and the binding energies for such defects as a function of strain. Fig. 8 shows the

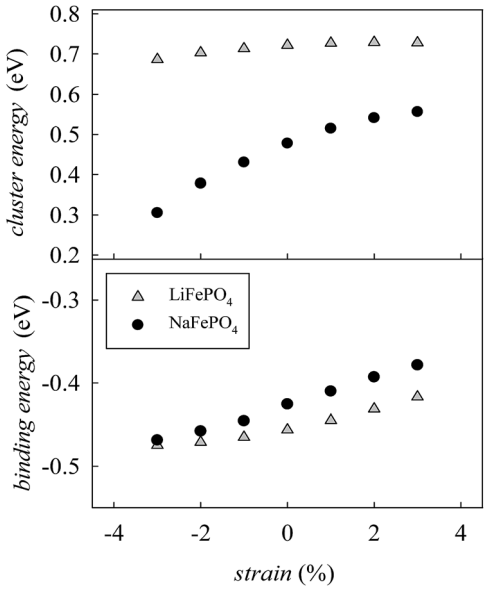

Fig. 8 Anti-site defect energies for olivine-type $AFePO_4$ ($A = Li^+$ or Na^+) as a function of the applied biaxial tensile/compressive strain in the *ac* plane; (upper) cluster formation energy (based on eqn (1) and (2)); (lower) binding energy.

anti-site pair cluster formation energy as a function of the imposed strain in the *ac* plane for the $LiFePO_4$ and $NaFePO_4$ systems. The first point to note is that the formation of the anti-site defect for $NaFePO_4$ is more favourable than for the Li analogue, in agreement with previous studies.[46] Interestingly, the dependence of this defect formation parameter on the applied strain is more pronounced for the Na-based system. In particular, as the imposed strain increases from compressive to tensile strain, the anti-site cluster formation energy for $LiFePO_4$ does not change greatly (Fig. 8), suggesting that strain in this system is not a crucial parameter to modulate the anti-site defect population.

In contrast, the variation with strain is much more pronounced for $NaFePO_4$, with tensile strain making the formation of anti-site defect clusters less favourable. While compressive strain increases the energy required for a Na ion to occupy an Fe site, due to size restraints with the large Na ion, the energy needed for an Fe ion to sit on a Na site is reduced to a greater extent, resulting in the predicted reduction in cluster energy. Elongation of the *b*-axis, caused by the application of *ac* strain is attributed to this change in formation energy.

Binding energies for the anti-site pair clusters were calculated as the difference between the cluster energy and the sum of the energies of the isolated defects. Negative values of binding energy imply that the cluster is bound. As shown in Fig. 8, binding energies become less negative as the applied strain increases, suggesting that tensile strain makes the Li/Na–Fe clusters less strongly bound, with a lower tendency for anti-site defect association.

Finally, the effect of strain on the anti-site cluster formation energy is negligible ($LiFePO_4$) or positive ($NaFePO_4$) when tensile strain in applied in the *ac* plane. The application of biaxial strain in directions different from the *ac* plane is predicted to be unfavourable for the intercalation properties of olivine-type materials since it is expected to increase the amount of anti-site defects in the system (Fig. S3-ESI†).

4. Conclusions

The effect of lattice strain on the ion conduction properties of olivine-type cathode materials for lithium- and sodium-ion batteries has been investigated using atomistic simulation techniques. Compressive or tensile strain is not found to affect the dimensionality of ion transport in either $LiFePO_4$ or $NaFePO_4$, which remains 1D. More importantly, the Li^+ and Na^+ migration barriers along the [010] direction decrease significantly when tensile strain is applied in the *ac* plane. It is predicted that this decrease in activation energy corresponds to a striking enhancement in ionic conductivity at room temperature. The highly positive effect of tensile strain on alkali-ion diffusion is confirmed through the use of molecular dynamics simulations. Tensile strain is also predicted to reduce the binding energies of blocking anti-site defects, and slightly increase their formation energy (especially for $NaFePO_4$). These results suggest that tensile strain applied perpendicularly to the alkali-ion migration channels will improve the intercalation properties of olivine-type cathode materials.

We recognise that interface effects (*e.g.* dislocations, grain boundaries and space charge regions) may influence the effective enhancement. Despite the technical challenges, related experimental work on epitaxial thin-film fabrication and their electrical characterisation would be extremely interesting.

In general, the intriguing results reported here suggest that lattice strain can lead to significant enhancements in ionic conduction and rate performance of Li- and Na-ion cathode materials. Such insights provide a framework for the future design and optimization of high-rate cathodes, and are also relevant to the development of thin-film solid-state batteries. Indeed, one of the aims of this work is to stimulate further studies on strain effects in related battery materials.

Acknowledgements

C. T. gratefully acknowledges the Cariplo Foundation and Regione Lombardia for grant 2015-0753. For a PhD studentship (J. H.) and research funding, we are grateful to the University of Bath URS scheme, the EPSRC Programme Grant on energy materials (EP/K016288/1) and the MCC/Archer consortium (EP/L000202/1).

Notes and references

1 B. Dunn, H. Kamath and J.-M. Tarascon, *Science*, 2011, **334**, 928.
2 V. Etacheri, R. Marom, R. Elazari, G. Salitra and D. Aurbach, *Energy Environ. Sci.*, 2011, **4**, 3243.
3 N. Yabuuchi, K. Kubota, M. Dahbi and S. Komaba, *Chem. Rev.*, 2014, **114**, 11636.
4 K. Zaghib, A. Guerfi, P. Hovington, A. Vijh, M. Trudeau, A. Mauger, J. B. Goodenough and C. M. Julien, *J. Power Sources*, 2013, **232**, 357.
5 M. S. Whittingham, *Chem. Rev.*, 2014, **114**, 11414.
6 J. Wang and X. Sun, *Energy Environ. Sci.*, 2015, **8**, 1110.
7 C. Masquelier and L. Croguennec, *Chem. Rev.*, 2013, **113**, 6552.
8 B. L. Ellis and L. F. Nazar, *Curr. Opin. Solid State Mater. Sci.*, 2012, **16**, 168.
9 S.-W. Kim, D.-H. Seo, X. Ma, G. Ceder and K. Kang, *Adv. Energy Mater.*, 2012, **2**, 710.
10 C. Delacourt, P. Poizot, S. Levasseur and C. Masquelier, *Electrochem. Solid-State Lett.*, 2006, **9**, A352.
11 H. Huang, S. C. Yin and L. F. Nazar, *Electrochem. Solid-State Lett.*, 2001, **4**, A170.
12 C. W. Hicks, D. O. Brodsky, E. A. Yelland, A. S. Gibbs, J. A. N. Bruin, M. E. Barber, S. D. Edkins, K. Nishimura, S. Yonezawa, Y. Maeno and A. P. Mackenzi, *Science*, 2014, **344**, 283; S. Tan, Y. Zhang, M. Xia, Z. Ye, F. Chen, X. Xie, R. Peng, D. Xu, Q. Fan, H. Xu, J. Jiang, T. Zhang, X. Lai, T. Xiang, J. Hu, B. Xie and D. Feng, *Nat. Mater.*, 2013, **12**, 634.
13 F. Nabeshima, Y. Imai, M. Hanawa, I. Tsukada and A. Maeda, *Appl. Phys. Lett.*, 2013, **103**, 172602.
14 N. Sata, K. Eberman, K. Eberl and J. Maier, *Nature*, 2000, **408**, 21.

15 J. H. Haeni, P. Irvin, W. Chang, R. Uecker, P. Reiche, Y. L. Li, S. Choudhury, W. Tian, M. E. Hawley, B. Craigo, A. K. Tagantsev, X. Q. Pan, S. K. Streiffer, L. Q. Chen, S. W. Kirchoefer, J. Levy and D. G. Schlom, *Nature*, 2004, **430**, 758; S. A. Harrington, J. Zhai, S. Denev, V. Gopalan, H. Wang, Z. Bi, S. A. T. Redfern, S.-H. Baek, C. W. Bark, C.-B. Eom, Q. Jia, M. E. Vickers and J. L. MacManus-Driscoll, *Nat. Nanotechnol.*, 2011, **6**, 491.
16 A. J. Millis, T. Darling and A. Migliori, *J. Appl. Phys.*, 1998, **83**, 1588; K. H. Ahn, T. Lookman and A. R. Bishop, *Nature*, 2004, **428**, 401.
17 N. Schichtel, C. Korte, D. Hesse and J. Janek, *Phys. Chem. Chem. Phys.*, 2009, **11**, 3043–3048.
18 K. Wen, W. Lv and W. He, *J. Mater. Chem. A*, 2015, **3**, 20031.
19 J. Garcia-Barriocanal, A. Rivera-Calzada, M. Varela, Z. Sefrioui, E. Iborra, C. Leon, S. J. Pennycook and J. Santamaria, *Science*, 2008, **321**, 676.
20 A. Kushima and B. Yildiz, *J. Mater. Chem. A*, 2010, **20**, 4809.
21 T. J. Pennycook, M. J. Beck, K. Varga, M. Varela, S. J. Pennycook and S. T. Pantelides, *Phys. Rev. Lett.*, 2010, **104**, 115901.
22 M. J. D. Rushton, A. Chroneos, S. J. Skinner, J. A. Kilner and R. W. Grimes, *Solid State Ionics*, 2013, **230**, 37.
23 R. A. De Souza, A. Ramadan and S. Horner, *Energy Environ. Sci.*, 2012, **5**, 5445.
24 U. Aschauer, R. Pfenninger, S. M. Selbach, T. Grande and N. A. Spaldin, *Phys. Rev. B: Condens. Matter Mater. Phys.*, 2013, **88**, 054111.
25 C. Tealdi and P. Mustarelli, *J. Phys. Chem. C*, 2014, **118**, 29574.
26 A. Cavallaro, M. Burriel, J. Roqueta, A. Apostolidis, A. Bernardi, A. Tarancón, R. Srinivasan, S. N. Cook, H. L. Fraser, J. A. Kilner, D. W. McComb and J. Santiso, *Solid State Ionics*, 2010, **181**, 592.
27 H.-J. Yan, Z.-Q. Wang, B. Xu and C. Ouyang, *Funct. Mater. Lett.*, 2012, **5**, 1250037.
28 F. Ning, S. Li, B. Xu and C. Ouyang, *Solid State Ionics*, 2014, **263**, 46.
29 J. Lee, S. J. Pennycook and S. T. Pantelides, *Appl. Phys. Lett.*, 2012, **101**, 033901.
30 R. Shahid and S. Murugavel, *Phys. Chem. Chem. Phys.*, 2013, **15**, 18809.
31 F. Sauvage, L. Laffront, J.-M. Tarascon and E. Baudrin, *J. Power Sources*, 2008, **175**, 495.
32 S. Laref and A. Laref, *RSC Adv.*, 2015, **5**, 35667.
33 A. K. Chen, T. A. Thapa and J. Berfield, *J. Power Sources*, 2014, **271**, 406.
34 A. Awarke, S. Lauer, M. Wittler and S. Pischinger, *Comput. Mater. Sci.*, 2011, **50**, 871.
35 P. Moreau, D. Guyomard, J. Gaubicher and F. Boucher, *Chem. Mater.*, 2010, **22**, 4126.
36 S.-M. Oh, S.-T. Myung, J. Hassoun, B. Scrosati and Y.-K. Sun, *Electrochem. Commun.*, 2012, **22**, 149.
37 M. Casas-Cabanas, V. V. Roddatis, D. Saurel, P. Kubiak, J. Carretero-Gonzalez, V. Palomares, P. Serras and T. Rojo, *J. Mater. Chem.*, 2012, **22**, 17421.
38 K. T. Lee, T. N. Ramesh, F. Nan, G. Botton and L. F. Nazar, *Chem. Mater.*, 2011, **23**, 3593.
39 A. Gupta, *Curr. Opin. Solid State Mater. Sci.*, 1997, **2**, 23.
40 B. L. Ellis, W. R. M. Makahnouk, Y. Makimura, K. Toghill and L. F. Nazar, *Nat. Mater.*, 2007, **6**, 749.
41 N. Meethong, H.-Y. Shadow Huang, S. A. Speak-man, W. Craig Carter and Y.-M. Chaing, *Adv. Funct. Mater.*, 2007, **17**, 1115.
42 C. R. A. Catlow, *Computer Modelling in Inorganic Crystallography*, Academic Press, San Diego, CA, 1997.
43 J. D. Gale, *J. Chem. Soc., Faraday Trans.*, 1997, **93**, 629; J. D. Gale and A. L. Rohl, *Mol. Simul.*, 2003, **29**, 291.
44 M. S. Islam and C. A. J. Fisher, *Chem. Soc. Rev.*, 2014, **43**, 185.
45 M. S. Islam, D. J. Discroll, C. A. J. Fisher and P. R. Slater, *Chem. Mater.*, 2005, **17**, 5085.
46 R. Tripathi, S. M. Wood, M. S. Islam and L. F. Nazar, *Energy Environ. Sci.*, 2013, **6**, 2257.
47 B. G. Dick and A. W. Overhauser, *Phys. Rev.*, 1958, **112**, 90.
48 N. F. Mott and M. J. Littleton, *Trans. Faraday Soc.*, 1938, **34**, 485.
49 I. T. Todorov, W. Smith, K. Trachenko and M. T. Dove, *J. Mater. Chem.*, 2006, **16**, 1911.
50 W. Humphrey, A. Dalke and K. Schulten, *J. Mol. Graphics*, 1996, **14**, 33.
51 C. A. J. Fisher and M. S. Islam, *J. Mater. Chem.*, 2008, **18**, 1209.
52 A. Whiteside, C. A. J. Fisher, S. C. Parker and M. S. Islam, *Phys. Chem. Chem. Phys.*, 2014, **16**, 21788.
53 C. Tealdi, C. Spreafico and P. Mustarelli, *J. Mater. Chem.*, 2012, **22**, 24870.
54 G. N. Greaves, A. L. Greer, R. S. Lakes and T. Rouxel, *Nat. Mater.*, 2011, **10**, 823.
55 S. C. Nishimura, G. Kobayashi, K. Ohoyama, Y. Kanno, M. Yashima and A. Yamada, *Nat. Mater.*, 2008, **7**, 707.
56 R. Amin, P. Balaya and J. Maier, *Electrochem. Solid-State Lett.*, 2007, **10**, A13; R. R. Chen, Y. X. Wu and X. Y. Kong, *J. Power Sources*, 2014, **258**, 246; S. L. Yang, X. F. Zhou, J. G. Zhang and Z. P. Liu, *J. Mater. Chem.*, 2010, **20**, 8086.
57 G. J. Shu and F. C. Chou, *Phys. Rev. B: Condens. Matter Mater. Phys.*, 2008, **78**, 052101.
58 T. Jiang, G. Chen, A. Li, C. Wang and Y. Wei, *J. Alloys Compd.*, 2009, **478**, 604.
59 W. Shen, J. Jiang and J. L. Hertz, *RSC Adv.*, 2014, **4**, 21625.
60 T. Mayeshiba and D. Morgan, *Phys. Chem. Chem. Phys.*, 2015, **17**, 2715.
61 J. Chen and J. Graetz, *ACS Appl. Mater. Interfaces*, 2011, **3**, 1380.
62 S. Y. Chung, S. Y. Choi, T. Yamamoto and Y. Ikuhara, *Phys. Rev. Lett.*, 2008, **100**, 125502.

Journal of Materials Chemistry A

PAPER

View Article Online
View Journal | View Issue

Cite this: J. Mater. Chem. A, 2017, 5, 13161

$MgFeSiO_4$ as a potential cathode material for magnesium batteries: ion diffusion rates and voltage trends†

Jennifer Heath, Hungru Chen and M. Saiful Islam *

Received 12th April 2017
Accepted 30th May 2017

DOI: 10.1039/c7ta03201c

rsc.li/materials-a

Developing rechargeable magnesium batteries has become an area of growing interest as an alternative to lithium-ion batteries largely due to their potential to offer increased energy density from the divalent charge of the Mg ion. Unlike the lithium silicates for Li-ion batteries, $MgFeSiO_4$ can adopt the olivine structure as observed for $LiFePO_4$. Here we combine advanced modelling techniques based on energy minimization, molecular dynamics (MD) and density functional theory to explore the Mg-ion conduction, doping and voltage behaviour of $MgFeSiO_4$. The Mg-ion migration activation energy is relatively low for a Mg-based cathode, and MD simulations predict a diffusion coefficient (D_{Mg}) of 10^{-9} cm^2 s^{-1}, which suggest favourable electrode kinetics. Partial substitution of Fe by Co or Mn could increase the cell voltage from 2.3 V *vs.* Mg/Mg^{2+} to 2.8–3.0 V. The new fundamental insights presented here should stimulate further work on low-cost silicate cathodes for Mg batteries.

1. Introduction

The Li-ion battery currently dominates the portable energy storage market, powering mobile phones, laptop computers and electric vehicles. But the next generation of electronics will rapidly overtake the limit of what is theoretically possible with traditional Li-ion systems. While there are new approaches, such as the development of Na-ion batteries and solid-state Li-ion batteries, that could potentially offer cost, specific energy and safety advantages, there are few options to improve energy density. One strategy to improve energy density beyond the capability of Li^+ systems is to utilise multivalent cations, specifically the Mg^{2+} ion, owing to its similar size to Li^+.[1–6] Improvements in energy density originate from the ability to use a metal anode rather than an insertion structure. In addition, dendrite formation, which prevents the use of Li metal anodes for Li-ion batteries, does not occur with Mg metal anodes.[2]

Due to the difficulty of Mg^{2+} insertion/extraction in host structures, the choice of cathode materials for Mg batteries is limited. This is thought to be due to stronger ionic interactions and harder charge redistribution of Mg^{2+} ions in comparison to Li^+ ions.[3] Approaches used to improve the diffusivity of Mg^{2+} ions in cathode materials have included decreasing the particle size of the cathode,[7] charge shielding of the inserted Mg^{2+} ions[8,9] and redistribution of the electrons donated by Mg to transition metal clusters.[3,10–12]

Various potential cathode materials for Mg batteries have been considered, such as V_2O_5,[13–17] polymorphs of MnO_2,[18–24] molybdenum chalcogenides,[1,3,25] and spinel sulphides and oxides.[26–29] Recently, olivine-type Mg silicates have been reported to show promising cathode performance for Mg batteries, with some indication of reversible Mg intercalation.[30–36] This follows extensive work on lithium-based silicates, Li_2FeSiO_4 and Li_2MnSiO_4, as possible low-cost and stable cathodes due to the high natural abundance of silicon and the strong Si–O bonds.[37]

It has previously been reported that the olivine phase of $MgFeSiO_4$ exhibits a degree of mixing between octahedral Mg and Fe crystallographic sites.[38–40] However, ordered phases of the $MgFeSiO_4$ structure have been synthesised through high temperature methods. A synthesis temperature of up to approximately 900 °C yields a structure where Mg^{2+} occupies M2 octahedral sites and Fe^{2+} prefers M1 octahedral sites. However above this temperature, the site preference switches, with Mg^{2+} and Fe^{2+} residing in M1 and M2 positions, respectively.[38] Therefore, above 900 °C $MgFeSiO_4$ can be synthesised with a structure analogous to $LiFePO_4$, where the Mg^{2+} ions form one-dimensional channels along the *c*-axis.

In previous studies, Mg^{2+} has been inserted into disordered olivine $FePO_4$ with a measured capacity of only ~13 mA h g^{-1}. This poor performance was found to be linked to surface amorphisation that prevented the electrochemical reaction from penetrating the bulk, rather than poor Mg^{2+} mobility in the structure.[41] A first-principles study on the magnesium silicates reports the redox and thermodynamic behaviour of these

Department of Chemistry, University of Bath, Bath, BA2 7AY, UK. E-mail: m.s.islam@bath.ac.uk

† Electronic supplementary information (ESI) available. See DOI: 10.1039/c7ta03201c

compounds,[33] revealing a similarity between lithium- and magnesium-insertion processes. However, these calculations did not consider kinetic processes, such as the transport of Mg^{2+} ions in the host lattice, which are essential to the performance of ion intercalation electrodes.

It is well established that the underlying transport and electronic properties of battery cathode materials are crucial to the greater understanding of their electrochemistry, but are not fully characterised for $MgFeSiO_4$. Here we investigate the solid-state features that influence the electrochemical performance of ordered $MgFeSiO_4$ (with a structure analogous to olivine $LiFePO_4$), by employing advanced modelling methods to probe the Mg-ion transport properties and voltage trends from transition metal doping.

2. Methods

The methods used here are well established and detailed elsewhere.[42,43] Previous studies on inorganic solids have successfully applied these potential-based methods, including olivine-structured $LiFePO_4$ and $NaFePO_4$ (ref. 44–46) and Li and Na silicate cathode materials.[47–50] Interactions between ions in the silicate framework were described using the Born-model framework, with a long-range coulombic term and a short-range term to model electron–electron repulsions and van der Waals interactions. The inclusion of a three-body term was necessary in order to model the angle-dependent nature of the SiO_4 unit.[47] The shell model[51] was used to account for the ionic polarisability effects. The interatomic potentials used here (listed in Table S1 in ESI†) were taken from previous studies on related oxides and silicates.[47,49,52] The Mott–Littleton approach is used to simulate the lattice relaxation around defects and migrating ions, which is incorporated within the GULP code.[53]

Molecular dynamics (MD) calculations, which introduce kinetic energy to the system by solving Newton's equations of motion for an ensemble of ions at finite temperatures, were performed using the LAMMPS code.[54] The calculations were carried out on a simulation box, with periodic boundary conditions, made up of 12 × 6 × 10 unit cells, consisting of 20 160 atoms. The initial configuration of the structure contained 10% Mg vacancies (and corresponding Fe^{3+} species), which were randomly distributed. The Pedone model[55] was used for the MD simulations, which was employed successfully in recent studies on Na-ion conducting battery materials.[50,56] Three initial configurations were investigated and the results of the three structures were averaged. Simulation runs were carried out using the NVT ensemble and a time step of 2 fs for long runs of 6 ns, at temperatures in the range 300–1500 K. Pre-equilibrium runs of 4 ps with NVE and NPT ensembles were first used for stable configurations. Computer simulations have been used to investigate a range of materials for lithium and sodium batteries.[40,42,56–59]

Density functional theory (DFT) calculations were performed using a plane wave basis set implemented in the VASP code.[60] A cutoff energy of 440 eV and k-point mesh of 2 × 4 × 5 were needed to converge the forces and energies. PAW potentials[61,62] and the spin-polarized generalised gradient approximation (GGA) with the PBEsol functional[63] were used. DFT+U methodology was used to account for the metal d-orbitals with an effective Hubbard $U_{eff} = U - J = 4.3$, 3.9, 3.3 and 6.0 eV ($J = 1.0$ eV) for Fe, Mn, Co and Ni, respectively.[56] A ferromagnetic arrangement of the unpaired 3d electrons was assumed. The Mg^{2+}/Mg cell voltage for the Fe^{2+}/Fe^{3+} redox couple was calculated using the following equation:

$$V = \frac{\varepsilon\{MgFeSiO_4\} - \varepsilon\{Mg_xFeSiO_4\} - (x)\mu\{Mg\}}{2x} \quad (1)$$

The chemical potential of magnesium ($\mu\{Mg\}$) was calculated using Mg metal. Such DFT techniques have been applied to other battery materials[29,42,57,59] including Li-ion silicate cathodes.[58,64]

3. Results and discussion

3.1 Structural modelling

The olivine-type structure of the cation-ordered $MgFeSiO_4$ belongs to the *Pmnb* space group (Fig. 1),[34] and consists of corner sharing FeO_6 octahedra along the *bc* plane. SiO_4 tetrahedra share corners and edges with the FeO_6 octahedra. Mg ions are located in channels along the *c*-axis. The starting point of the study was to reproduce the experimentally observed structure of $MgFeSiO_4$. A comparison between the calculated unit cell parameters based on effective potentials and those of the experimental structures is given in Table 1 (and further details on potential models are given in Table S2†).

The lattice parameters were computed to within 1% of the experimental values. Reproduction of the lattice parameters adds validity to the interatomic model used for simulating defects and Mg-ion migration.

3.2 Energetics and pathways for Na-ion migration

Examination of the intrinsic Mg-ion mobility in $MgFeSiO_4$ is of interest when considering its use as a cathode material for magnesium batteries. In the olivine structure there are three potential pathways for Mg-ion migration, as shown in Fig. 2a. The activation energies of Mg migration along these pathways in $MgFeSiO_4$ are listed in Table 2, along with the Mg–Mg distances. The activation energy is significantly lower for pathway A (parallel to the *c*-axis) than for pathways B and C. This

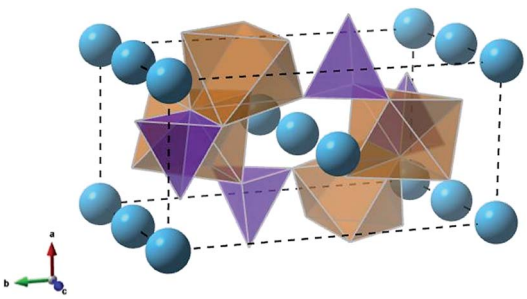

Fig. 1 Olivine-type structure of $MgFeSiO_4$ (orange octahedra: FeO_6, purple tetrahedra: SiO_4, light blue spheres: Mg^{2+} ions).

Table 1 Calculated and experimental lattice parameters and bond lengths for $MgFeSiO_4$

Parameter	Experimental[38] (Å)	Calculated (Å)	Δ (Å)
a	4.807	4.854	0.047
b	10.376	10.336	−0.040
c	6.061	6.026	−0.035
Mg–O	2.168	2.131	−0.037
Fe–O	2.125	2.140	0.015
Si–O	1.624	1.639	0.015

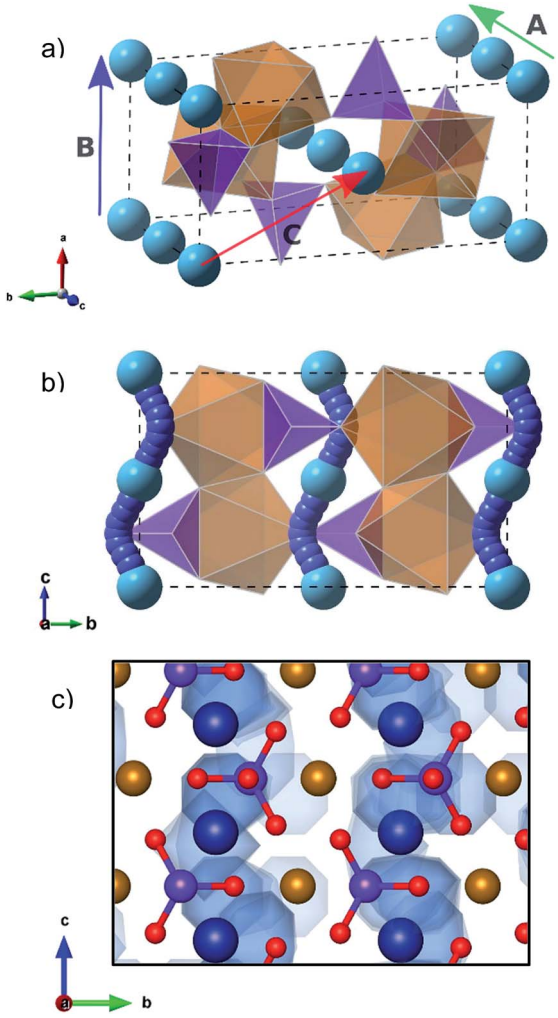

Fig. 2 (a) Mg-ion migration pathways in olivine $MgFeSiO_4$. (b) Lowest energy Mg-ion curved pathway, parallel to *c*-axis (brown octahedra: FeO_6, purple tetrahedra: SiO_4, blue spheres: Mg^{2+} ions); (c) Mg density plot from MD simulations showing Mg diffusion pathways (brown spheres: Fe^{2+} ions; dark blue spheres: Mg^{2+} ions; purple spheres silicon; red spheres: oxygen. Light blue channels mark diffusion pathway).

is similar to the results obtained for olivine $LiFePO_4$,[44] where the lowest energy pathway is along open channels that run parallel to the *b*-axis. The activation energies for pathways B and C are both prohibitively high and so Mg ion migration is not likely in

Table 2 Mg–Mg separations and activation energies of Mg migration in $MgFeSiO_4$

Pathway	Mg–Mg distance (Å)	E_a Mg (eV)
A	3.01	0.60
B	4.85	5.18
C	5.71	5.43

these directions. This can be rationalised by considering the structure of $MgFeSiO_4$; the distance between neighbouring Mg^{2+} ions in pathways B and C is greater than pathway A. In addition, pathway B has a smaller channel size than pathway A. Pathway C would involve migration directly past both Fe–O and Si–O bonds, both of which would contribute to the high migration energy found.

Fig. 2b shows the curved pathways along which Mg-ion migration is predicted to take place in $MgFeSiO_4$. These same migration pathways have also been simulated in olivine $LiFePO_4$,[44] and subsequently confirmed by diffraction measurements and maximum entropy studies.[65] The calculated migration energy for this pathway was 0.60 eV, just 0.05 eV higher than that calculated for $LiFePO_4$.[44]

A previous first-principles study carried out by Rong *et al.*[66] reports the migration energies of different multivalent ions in olivine $FePO_4$, layered NiO_2 and spinel Mn_2O_4. Here Mg^{2+} diffusion in the olivine structure was calculated to require approximately 0.7 eV, lower than multivalent cation diffusion in the layered and spinel structures, calculated at approximately 1.1 and 0.8 eV, respectively. The relativity low migration energies predicted for both olivine $FePO_4$ and $MgFeSiO_4$ suggest favourable Mg^{2+} ion transport in the olivine structure.

MD techniques, used here at long timescales, are well suited to examine ion motion. The curved pathways predicted using energy minimisation techniques were also generated using MD, as shown in the energy density plot in Fig. 2c.

A small degree of anti-site defects (the exchange of Mg^{2+}/Fe^{2+} on neighboring sites) is found in the MD calculations; an example can be seen in Fig. 2c, where Mg-ion density is found near the Fe sites. These defects were anticipated given the high levels of Mg/Fe mixing in the thermodynamically stable form of $MgFeSiO_4$.[38–40] This type of defect has been reported to cause blocking of the 1D migration pathways in olivine $LiFePO_4$.[67] However, major blocking of the Mg channels was not observed in our MD simulations, which is likely to be important for reversible Mg intercalation. Hence, we predict that while anti-site defects may form causing a localised blocking effect, the Fe^{2+} ions are able to migrate back into their original sites allowing Mg^{2+} ions to diffuse through uninterrupted channels. Also there was no evidence of inter-channel hopping of the displaced Mg^{2+} ions.

The mean squared displacement (MSD) of Mg ions, $[r(t)]^2$, for $MgFeSiO_4$ is shown in Fig. 3. The MSD data can be used to derive the Mg-ion diffusion coefficient (D_{Mg}) using:

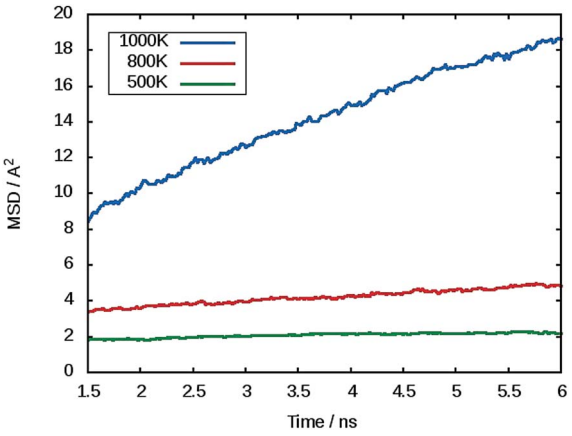

Fig. 3 Representative mean squared displacement (MSD) data for magnesium ions in $MgFeSiO_4$ at 500 K (green), 800 K (red) and 1000 K (blue).

$$D = \left(\frac{1}{6t}\right)\left\langle [r(t)]^2 \right\rangle \quad (2)$$

At 300 K a D_{Mg} value of 1.1×10^{-9} cm^2 s^{-1} was calculated. To our knowledge there no experimental or calculated diffusion coefficients for ordered $MgFeSiO_4$ for direct comparison. A previous study on tavorite $FeSO_4F$ as a potential cathode for Mg batteries, quoted an estimated D_{Mg} in the range of 10^{-9} cm^2 s^{-1}, the same order of magnitude as observed for Li diffusion in the same structure.[68] Interestingly, Mg batteries may be more suitable for high temperature environments where the diffusion rate (and electrode kinetics) would be higher.

An Arrhenius plot for Mg^{2+} diffusion in $MgFeSiO_4$ is shown in Fig. 4, which can be used to estimate the activation energy of migration. An activation energy of 0.79 eV was derived. While this value is slightly higher than that predicted using energy minimisation, it is still relatively low for a Mg-based cathode material. This result and the prediction of D_{Mg} in the range of Li-ion cathode materials, suggests favourable Mg^{2+} intercalation kinetics for ordered $MgFeSiO_4$.

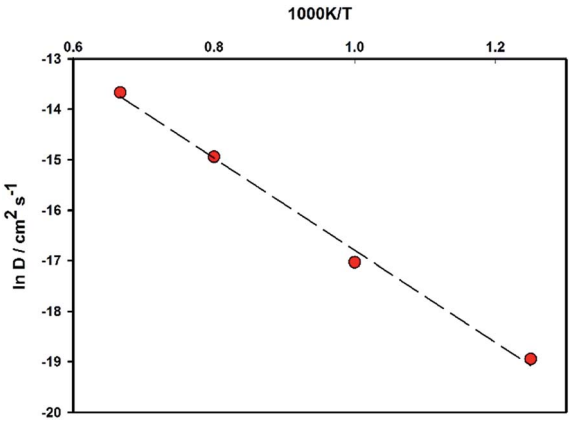

Fig. 4 Arrhenius plot of Mg-ion diffusion coefficients D_{Mg} for $MgFeSiO_4$.

3.3 Dopant substitution

Previous dopant studies on lithium-ion battery cathodes have suggested that the incorporation of dopants on certain sites could potentially improve the capacity of the material by increasing the amount of lithium available for extraction through formation of lithium interstitial defects.[47] Doping strategies could also be beneficial for magnesium-ion cathode materials. While the divalent nature of the magnesium ion offers increased energy density over monovalent lithium, many structures only allow for the de/intercalation of half of the available magnesium. The incorporation of dopants could create Mg interstitial defects that could consequently improve the capacity of the cathode material.

Here we investigate trivalent doping (Al, Ga and V) on the Si site within the $MgFeSiO_4$ structure. The doping process is described using the following equation (where M = Al, Ga or V):

$$M_2O_3 + 2Si_{Si}^{\times} + MgO \rightarrow 2M'_{Si} + Mg_i^{\cdot\cdot} + 2SiO_2 \quad (3)$$

M^{3+} doping on the Si site is charge compensated by the formation of an Mg interstitial. We note that the alternative charge-compensation mechanism involving oxygen vacancies is less favourable by more than 4 eV. Trivalent doping on other sites in the structure would yield Fe vacancy as compensation, which would not improve the capacity or Mg diffusion in the material.

The dopant substitution reaction energies were calculated by combining the appropriate defect and lattice energy terms, listed in Table 3. Interatomic potentials used to model the corresponding binary oxides of the dopant cations were used in each case (Table S3†). This systematic approach to dopant incorporation has been applied successfully to other silicate systems.[47]

The large incorporation energies (in Table 3) for trivalent Al, Ga and V doping in $MgFeSiO_4$ to create Mg interstitials are unfavourable, and suggest a low degree of dopant solubility. Therefore, we conclude such trivalent doping of $MgFeSiO_4$ is not a viable method to improve its capacity or Mg diffusion properties.

3.4 Cell voltage trends

One challenge to overcome when developing new cathode materials for magnesium-ion batteries is to establish an adequate operating voltage (in the range of approximately 2.0–3.0 V) while simultaneously retaining a high reversible capacity.[69,70] V_2O_5 is reported to have a voltage of 2.66 V when paired with Mg/Mg^{2+}, within the appropriate range. However, as a cathode material it suffers from slow magnesium diffusion.[71]

Table 3 Calculated energies of trivalent dopant incorporation on the Si site in $MgFeSiO_4$

Dopant	Energy (eV)
Al^{3+}	5.64
Ga^{3+}	8.99
V^{3+}	8.59

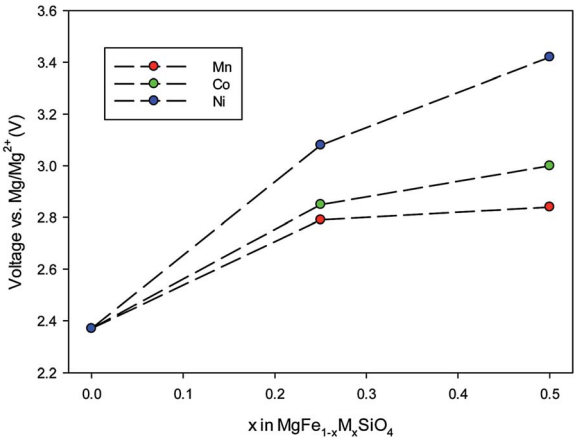

Fig. 5 Trends in cell voltage (*vs.* Mg/Mg^{2+}) as a function of increasing dopant (M = Co, Ni, Mn) on the Fe site in $MgFeSiO_4$.

Other potential cathode materials for Mg batteries have displayed voltages much lower than the optimal window, such as the Chevrel phase Mo_6S_8 and spinel $MgTi_2S_4$ both of which display a cell voltage of 1.2 V (ref. 1 and 26) and the cation-disordered phase of $MgFeSiO_4$ at 1.6 V.[72]

DFT was used to calculate the cell voltage of cation-ordered $MgFeSiO_4$. Similar to the potential-based calculations, the experimental structure was reproduced to a high degree of accuracy (Table S4†). To carry out the calculations relevant Mg^{2+} ions were removed from the optimised structure; various different vacancy configurations were considered and the voltage was calculated using eqn (1) with the lowest energy configuration.

First, the cell voltage of ordered $MgFeSiO_4$ was calculated to be 2.35 V *vs.* Mg/Mg^{2+}, within the operating window, and in good accord with electrochemical data showing an average voltage of 2.4 V.[34] Transition metal doping can be used to tailor the cell voltage for optimal energy density. Here we investigate how doping on the transition metal site affects the cell voltage of $MgFeSiO_4$. The voltage trends of $MgFe_{1-x}M_xSiO_4$ (M = Ni, Co and Mn) *vs.* Mg/Mg^{2+} with varied x values are shown in Fig. 5. $MgFe_{1-x}M_xSiO_4$ structures, where $x = 0.5$, follow the trend Mn (2.8 V) < Co (3.0 V) < Ni (3.4 V); we note that olivine-structured $LiMPO_4$ cathode materials follow a similar trend.[73,74] The cell voltage values of the Ni doped structures are above the adequate operating voltage for current Mg-ion electrolytes, while the Mn and Co doped structures are within this electrochemical stability window. We note that future work could include examining conversion reactions as a result of transition metal doping, a topic that goes beyond the scope of this current study.

4. Conclusions

Our fundamental study of olivine-structured $MgFeSiO_4$ as a potential cathode material for Mg batteries shows good reproduction of the experimentally observed structure and reveals key atomic-scale insights into its electrochemical properties. First, we derive an Mg-ion migration energy of 0.6 eV along the 1D channel through a curved pathway (similar to $LiFePO_4$), and a diffusion coefficient (D_{Mg}) of 10^{-9} cm^2 s^{-1} at 300 K from large-scale MD. These ion transport results suggest favourable Mg^{2+} intercalation kinetics.

Secondly, doping of trivalent Al, Ga or V ions on Si sites is unfavourable and suggests low dopant solubility.

Finally, the DFT derived cell voltage for $MgFeSiO_4$ of 2.35 V *vs.* Mg/Mg^{2+} agrees well with the available electrochemical data. Mn or Co doping of this structure on the Fe site is predicted to increase the cell voltage to greater than 2.70 V. However, in the case of Ni doping this brings the voltage outside of the useable electrochemical stability range of current electrolytes. Overall, the fundamental insights presented here will inform the future optimisation of silicate electrodes for magnesium batteries.

Acknowledgements

We gratefully acknowledge support from the EPSRC for the Energy Materials Programme grant (EP/K016288) and Archer HPC facilities through the Materials Chemistry Consortium (EP/L000202). J. H acknowledges PhD funding from the University of Bath URS Studentship. We also thank Dr Pier-emanuele Canepa (Bath) for useful discussions.

References

1 D. Aurbach, Z. Lu, A. Schechter, Y. Gofer, H. Gizbar, R. Turgeman, Y. Cohen, M. Moshkovich and E. Levi, *Nature*, 2000, **407**, 724–727.
2 H. D. Yoo, I. Shterenberg, Y. Gofer, G. Gershinsky, N. Pour and D. Aurbach, *Energy Environ. Sci.*, 2013, **6**, 2265–2279.
3 E. Levi, Y. Gofer and D. Aurbach, *Chem. Mater.*, 2010, **22**, 860–868.
4 R. Van Noorden, *Nature*, 2014, **507**(7490), 26–28.
5 P. Canepa, G. Sai Gautam, D. C. Hannah, R. Malik, M. Liu, K. G. Gallagher, K. A. Persson and G. Ceder, *Chem. Rev.*, 2017, **117**, 4287–4341.
6 J. Muldoon, C. B. Bucur and T. Gregory, *Chem. Rev.*, 2014, **114**, 11683–11720.
7 N. Amir, Y. Vestfrid, O. Chusid, Y. Gofer and D. Aurbach, *J. Power Sources*, 2007, **174**, 1234–1240.
8 P. Novak and J. Desilvestro, *J. Electrochem. Soc.*, 1993, **140**, 140–144.
9 P. Novak, W. Scheifele, F. Joho and O. Haas, *J. Electrochem. Soc.*, 1995, **142**, 2544–2550.
10 E. Levi, E. Lancry, A. Mitelman, D. Aurbach, O. Isnard and D. Djurado, *Chem. Mater.*, 2006, **18**, 3705–3714.
11 E. Levi, E. Lancry, A. Mitelman, D. Aurbach, G. Ceder, D. Morgan and O. Isnard, *Chem. Mater.*, 2006, **18**, 5492–5503.
12 E. Levi, A. Mitelman, O. Isnard, M. Brunelli and D. Aurbach, *Inorg. Chem.*, 2008, **47**, 1975–1983.
13 D. B. Le, S. Passerini, F. Coustier, J. Guo, T. Soderstrom, B. B. Owens and W. H. Smyrl, *Chem. Mater.*, 1998, **10**, 682–684.
14 S. H. Lee, R. A. DiLeo, A. C. Marschilok, K. J. Takeuchi and E. S. Takeuchi, *ECS Electrochem. Lett.*, 2014, **3**, 87–90.
15 N. Y. Sa, H. Wang, D. L. Proffit, A. L. Lipson, B. Key, M. Liu, Z. X. Feng, T. T. Fister, Y. Ren, C. J. Sun, J. T. Vaughey,

P. A. Fenter, K. A. Persson and A. K. Burrell, *J. Power Sources*, 2016, **323**, 44–50.
16 Y. W. Cheng, Y. Y. Shao, V. Raju, X. L. Ji, B. L. Mehdi, K. S. Han, M. H. Engelhard, G. S. Li, N. D. Browning, K. T. Mueller and J. Liu, *Adv. Funct. Mater.*, 2016, **26**, 3446–3453.
17 S. Tepavcevic, Y. Z. Liu, D. H. Zhou, B. Lai, J. Maser, X. B. Zuo, H. Chan, P. Kral, C. S. Johnson, V. Stamenkovic, N. M. Markovic and T. Rajh, *ACS Nano*, 2015, **9**, 8194–8205.
18 R. G. Zhang, X. Q. Yu, K. W. Nam, C. Ling, T. S. Arthur, W. Song, A. M. Knapp, S. N. Ehrlich, X. Q. Yang and M. Matsui, *Electrochem. Commun.*, 2012, **23**, 110–113.
19 N. Kumagai, S. Komaba and H. Sakai, *J. Power Sources*, 2001, **97**, 515–517.
20 X. Q. Sun, V. Duffort, B. L. Mehdi, N. D. Browning and L. F. Nazar, *Chem. Mater.*, 2016, **28**, 534–542.
21 C. Ling, R. G. Zhang, T. S. Arthur and F. Mizuno, *Chem. Mater.*, 2015, **27**, 5799–5807.
22 K. W. Nam, S. Kim, S. Lee, M. Salama, I. Shterenberg, Y. Gofer, J. S. Kim, E. Yang, C. S. Park, S. S. Lee, W. S. Chang, S. G. Doo, Y. N. Jo, Y. Jung, D. Aurbach and J. W. Choi, *Nano Lett.*, 2015, **15**, 4071–4079.
23 L. Wang, K. Asheim, P. E. Vullum, A. M. Svensson and F. Vullum-Bruer, *Chem. Mater.*, 2016, **28**, 6459–6470.
24 R. Zhang, T. S. Arthur, C. Ling and F. Mizuno, *J. Power Sources*, 2015, **282**, 630–638.
25 L. W. F. Wan, B. R. Perdue, C. A. Apblett and D. Prendergast, *Chem. Mater.*, 2015, **27**, 5932–5940.
26 X. Q. Sun, P. Bonnick, V. Duffort, M. Liu, Z. Q. Rong, K. A. Persson, G. Ceder and L. F. Nazar, *Energy Environ. Sci.*, 2016, **9**, 2273–2277.
27 J. C. Knight, S. Therese and A. Manthiram, *ACS Appl. Mater. Interfaces*, 2015, **7**, 22953–22961.
28 C. Kim, P. J. Phillips, B. Key, T. H. Yi, D. Nordlund, Y. S. Yu, R. D. Bayliss, S. D. Han, M. N. He, Z. C. Zhang, A. K. Burrell, R. F. Klie and J. Cabana, *Adv. Mater.*, 2015, **27**, 3377–3384.
29 M. Liu, Z. Q. Rong, R. Malik, P. Canepa, A. Jain, G. Ceder and K. A. Persson, *Energy Environ. Sci.*, 2015, **8**, 964–974.
30 Z. Feng, J. Yang, Y. NuLi, J. Wang, X. Wang and Z. Wang, *Electrochem. Commun.*, 2008, **10**, 1291–1294.
31 Y. NuLi, Y. Zheng, Y. Wang, J. Yang and J. Wang, *J. Mater. Chem.*, 2011, **21**, 12437–12443.
32 Y. NuLi, Y. Zheng, F. Wang, J. Yang, A. I. Minett, J. Wang and J. Chen, *Electrochem. Commun.*, 2011, **13**, 1143–1146.
33 C. Ling, D. Banerjee, W. Song, M. Zhang and M. Matsui, *J. Mater. Chem.*, 2012, **22**, 13517–13523.
34 Y. Orikasa, T. Masese, Y. Koyama, T. Mori, M. Hattori, K. Yamamoto, T. Okado, Z. D. Huang, T. Minato, C. Tassel, J. Kim, Y. Kobayashi, T. Abe, H. Kageyama and Y. Uchimoto, *Sci. Rep.*, 2014, **4**, 5622.
35 Y. Zheng, Y. NuLi, Q. Chen, Y. Wang, J. Yang and J. Wang, *Electrochim. Acta*, 2012, **66**, 75–81.
36 T. Mori, T. Masese, Y. Orikasa, Z. D. Huang, T. Okado, J. Kim and Y. Uchimoto, *Phys. Chem. Chem. Phys.*, 2016, **18**, 13524–13529.
37 M. S. Islam, R. Dominko, C. Masquelier, C. Sirisopanaporn, A. R. Armstrong and P. G. Bruce, *J. Mater. Chem.*, 2011, **21**, 9811–9818.
38 S. A. T. Redfern, G. Artioli, R. Rinaldi, C. M. B. Henderson, K. S. Knight and B. J. Wood, *Phys. Chem. Miner.*, 2000, **27**, 630–637.
39 S. Chatterjee, S. Sengupta, T. Saha-Dasgupta, K. Chatterjee and N. Mandal, *Phys. Rev. B: Condens. Matter Mater. Phys.*, 2009, **79**, 115103.
40 S. Chatterjee, S. Bhattacharyya, S. Sengupta and T. Saha-Dasgupta, *Phys. Chem. Miner.*, 2011, **38**, 259–265.
41 R. G. Zhang and C. Ling, *ACS Appl. Mater. Interfaces*, 2016, **8**, 18018–18026.
42 M. S. Islam and C. A. J. Fisher, *Chem. Soc. Rev.*, 2013, **43**, 185–204.
43 C. R. A. Catlow, *Computer Modelling in Inorganic Crystallography*, Academic Press, 1997.
44 M. S. Islam, D. J. Driscoll, C. A. J. Fisher and P. R. Slater, *Chem. Mater.*, 2005, **17**, 5085–5092.
45 C. Tealdi, J. Heath and M. S. Islam, *J. Mater. Chem. A*, 2016, **4**, 6998–7004.
46 R. Tripathi, S. M. Wood, M. S. Islam and L. F. Nazar, *Energy Environ. Sci.*, 2013, **6**, 2257–2264.
47 N. Kuganathan and M. S. Islam, *Chem. Mater.*, 2009, **21**, 5196–5202.
48 C. A. J. Fisher, N. Kuganathan and M. S. Islam, *J. Mater. Chem. A*, 2013, **1**, 4207–4214.
49 A. R. Armstrong, N. Kuganathan, M. S. Islam and P. G. Bruce, *J. Am. Chem. Soc.*, 2011, **133**, 13031–13035.
50 J. C. Treacher, S. M. Wood, M. S. Islam and E. Kendrick, *Phys. Chem. Chem. Phys.*, 2016, **18**, 32744–32752.
51 B. G. Dick and A. W. Overhauser, *Phys. Rev.*, 1958, **112**, 90–103.
52 G. V. Lewis and C. R. A. Catlow, *J. Phys. C: Solid State Phys.*, 1985, **18**, 1149–1161.
53 J. D. Gale and A. L. Rohl, *Mol. Simul.*, 2003, **29**, 291–341.
54 S. Plimpton, *J. Comput. Phys.*, 1995, **117**, 1–19.
55 A. Pedone, G. Malavasi, M. C. Menziani, A. N. Cormack and U. Segre, *J. Phys. Chem. B*, 2006, **110**, 11780–11795.
56 S. M. Wood, C. Eames, E. Kendrick and M. S. Islam, *J. Phys. Chem. C*, 2015, **119**, 15935–15941.
57 A. R. Armstrong, C. Lyness, P. M. Panchmatia, M. S. Islam and P. G. Bruce, *Nat. Mater.*, 2011, **10**, 223–229.
58 C. Eames, A. R. Armstrong, P. G. Bruce and M. S. Islam, *Chem. Mater.*, 2012, **24**, 2155–2161.
59 Y. Yuan, C. Zhan, K. He, H. Chen, W. Yao, S. Sharifi-Asl, B. Song, Z. Yang, A. Nie, X. Luo, H. Wang, S. M. Wood, K. Amine, M. S. Islam, J. Lu and R. Shahbazian-Yassar, *Nat. Commun.*, 2016, **7**, 13374.
60 G. Kresse and J. Furthmuller, *Phys. Rev. B: Condens. Matter Mater. Phys.*, 1996, **54**, 11169–11186.
61 G. Kresse and D. Joubert, *Phys. Rev. B: Condens. Matter Mater. Phys.*, 1999, **59**, 1758–1775.
62 P. E. Blochl, *Phys. Rev. B: Condens. Matter Mater. Phys.*, 1994, **50**, 17953–17979.
63 J. P. Perdew, K. Burke and M. Ernzerhof, *Phys. Rev. Lett.*, 1996, **77**, 3865–3868.
64 M. E. Arroyo-de Dompablo, M. Armand, J. M. Tarascon and U. Amador, *Electrochem. Commun.*, 2006, **8**, 1292–1298.

65 S.-I. Nishimura, G. Kobayashi, K. Ohoyama, R. Kanno, M. Yashima and A. Yamada, *Nat. Mater.*, 2008, **7**, 707–711.
66 Z. Q. Rong, R. Malik, P. Canepa, G. S. Gautam, M. Liu, A. Jain, K. Persson and G. Ceder, *Chem. Mater.*, 2015, **27**, 6016–6021.
67 C. Tealdi, C. Spreafico and P. Mustarelli, *J. Mater. Chem.*, 2012, **22**, 24870–24876.
68 J. D. Wu, G. H. Gao, G. M. Wu, B. Liu, H. Y. Yang, X. W. Zhou and J. C. Wang, *Phys. Chem. Chem. Phys.*, 2014, **16**, 22974–22978.
69 M. M. Huie, D. C. Bock, E. S. Takeuchi, A. C. Marschilok and K. J. Takeuchi, *Coord. Chem. Rev.*, 2015, **287**, 15–27.
70 P. Saha, M. K. Datta, O. I. Velikokhatnyi, A. Manivannan, D. Alman and P. N. Kumta, *Prog. Mater. Sci.*, 2014, **66**, 1–86.
71 G. Gershinsky, H. D. Yoo, Y. Gofer and D. Aurbach, *Langmuir*, 2013, **29**, 10964–10972.
72 Z. Z. Feng, J. Yang, Y. N. NuLi and J. L. Wang, *J. Power Sources*, 2008, **184**, 604–609.
73 A. Yamada, M. Hosoya, S. C. Chung, Y. Kudo, K. Hinokuma, K. Y. Liu and Y. Nishi, *J. Power Sources*, 2003, **119**, 232–238.
74 C. Masquelier and L. Croguennec, *Chem. Rev.*, 2013, **113**, 6552–6591.

High voltage P2-$Na_{2/3}Ni_{1/3-x}Mg_xMn_{2/3}O_2$ ($0 \leq x \leq 0.20$) cathodes; insights from neutron and in-situ X-ray diffraction, electrochemical and computational studies

Nuria Tapia-Ruiz, Wesley M. Dose, Neeraj Sharma, Hungru Chen, Jennifer Heath, James Somerville, Urmimala Maitra, M. Saiful Islam and Peter G. Bruce

INTRODUCTION

Lithium-ion batteries (LIBs) are strong candidates to meet future worldwide energy demands due to their high-energy density. However, there are serious concerns about the cost of lithium due to its scarcity and geographically concentrated availability. In this context, sodium-ion batteries (SIBs) have emerged as a promising alternative, especially when volumetric and gravimetric energy density requirements are not as stringent, *e.g.* grid storage, thereby addressing the issues related to cost and sources [1,2].

A wide variety of sodium battery materials have been explored in the past few years. Among the sodium cathodes reported to date, layered oxide compounds with formula Na_xTMO_2 (TM = transition metal) adopting P2-type and O3-type structures [3] have become strong contenders for application. In these structures P and O refer to the Na coordination, *i.e.* trigonal prismatic or octahedral, respectively, while the numerals designate the repeated transition metal oxide stacking within the unit cell (ABBA and ABCABC for "2" and "3", respectively). Layered P2-type compounds have shown enhanced electrochemical performance as they generally undergo fewer structural transitions when (de)intercalating Na-ions compared to O3 [1]. In particular, P2-$Na_{2/3}Ni_{1/3}Mn_{2/3}O_2$ has shown promise due to its high theoretical capacity (*ca.* 170 mAh g^{-1}) and high average voltage (*ca.* 3.5 V) because of the presence of the active Ni^{2+}/Ni^{4+} redox couple. Nevertheless, the material possesses a poor cycle life, which has been attributed to the gliding of the transition metal layers at high voltages and subsequent formation of the O2 phase [4,5]. In addition, plateaux occurring upon charge/discharge have been attributed to specific sodium ordering patterns in the edge-shared and face-shared sodium sites when sodium contents are 1/2 and 1/3 [6].

Sodium ordered compounds are thermodynamically more stable than their disordered counterparts, impeding Na^+ mobility, which results in poorer performance at high current rates [6,7]. To date, researchers have made considerable efforts to improve the electrochemical performance of P2-$Na_{2/3}Ni_{1/3}Mn_{2/3}O_2$ by strategic doping of this material with selected cations, namely Li^+, Al^{3+}, Zn^{2+} and Ti^{4+} [8-12]. Mg^{2+} substitution for Ni^{2+} has shown great promise and hence is one of the most studied approaches [12,13], although the non-redox active behaviour of Mg^{2+} in theory causes a penalty on the overall charge stored in the material. However, there is still a need for greater fundamental understanding of important effects: the structural role of Mg in the Ni^{2+}/Mn^{4+} honeycomb layers (along

the *ab* plane) and *c* axis, and how its presence/absence affects the Na^+-vacancy order/disorder in these materials and the phases obtained at the end of charge. A more complete understanding of this behaviour will allow us to design battery materials with promising electrochemical performance in terms of cyclability and rate capability. In this study, a series of P2-type $Na_{2/3}Ni_{1/3-x}Mg_xMn_{2/3}O_2$ ($0 \leq x \leq 0.20$) materials were prepared by a conventional solid-state method and were structurally characterised using mainly X-ray and neutron diffraction techniques. Cycling data was performed in half-cells vs. Na at room temperature. Ab initio simulation studies were conducted to examine structural and Na-ion diffusion properties on Mg doping, complementing the experimental insights.

RESULTS

Crystal structure

P2-$Na_{2/3}Ni_{1/3-x}Mg_xMn_{2/3}O_2$ materials (where $0 \leq x \leq 0.20$) were synthesised from their respective oxides *via* solid-state methods. Elemental analysis from inductively coupled plasma (ICP) spectroscopy confirms the compositions are as targeted (Table S1). Particles of 1-10 µm of diameter and hundreds of nanometers of thickness and hexagonal morphologies were observed (Figure S1). Powder X-ray diffraction (PXRD) was used to confirm the purity of the samples (Figure S2). All Bragg reflections from each individual sample could be assigned to a P2-type layered structure with $P6_3/mmc$ (n° 194) space group. The lattice parameters for the undoped sample are comparable to those reported in the literature [5]. A broad reflection at d = 4.2 Å (1/3 1/3 0) (not shown here) was observed in the Mg-doped samples, corresponding to long-range in-plane ordering represented by [$(Mg^{2+}/Mn^{4+})O_6$] honeycomb units (in a $\sqrt{3}a \times \sqrt{3}a$ type supercell) [14] (Figure S2). As intuitively expected, this Bragg reflection becomes more significant at high levels of Mg dopant. The Mg^{2+}/Mn^{4+} honeycomb-type ordering occurs due to the large differences in radii and charge (*ca.* Mg^{2+}/Mn^{4+} = 1.38) [7]. By contrast, elucidation of Ni^{2+}/Mn^{4+} ordering, which is analogous to the Mg^{2+}/Mn^{4+} ordering, was easily evidenced using neutron diffraction (ND) due to their different neutron scattering lengths (see experimental section). A comparison between X-ray and neutron data for the undoped sample is shown in Figure 1a.

ND data at room temperature for the P2-$Na_{2/3}Ni_{1/3-x}Mg_xMn_{2/3}O_2$ ($0 \leq x \leq 0.20$) series is shown in Figures 1b and 1c. Selected Rietveld refined crystallographic parameters from ND data are presented in the SI. An increase in the lattice parameters was observed upon Mg-doping due to the larger size of Mg^{2+} (0.72 Å) when compared to Ni^{2+} (0.69 Å) in octahedral coordination). The cell parameters of $Na_{2/3}Ni_{1/3}Mn_{2/3}O_2$ are in good agreement with those from X-ray data and the literature [5]. Data were refined using the Rietveld method using an AB-type crystallographic model ($P6_3$ space group) [15,16]. This structural model considers a larger hexagonal unit cell than that described by the $P6_3/mmc$ space group, with in-plane [$((Ni^{2+}/Mg^{2+})/Mn^{4+})O_6$] honeycomb stacking layers which are not superimposed along the c-axis, hence the A-B nomenclature. This superstructure differs from the AA-type, reported in the $Na_{2/3}Mg_{1/3}Mn_{2/3}O_2$ material by Paulsen et al., where honeycomb ordered layers overlay along the c axis [16]. In the model, we have considered that Ni^{2+} and Mg^{2+} ions are located at the same octahedral 2b sites due to their identical pristine charge and relatively similar sizes, whereas Mn^{4+} atoms are located in both 2a and 2b sites in the MO_2 layers; larger Na ions are located in between MO_2 layers in trigonal

prismatic sites (*i.e.* 6c sites predominantly (*ca.* 75% Na available) as these correspond to the more stable edge sites and in a lower amount in the face-shared 2a and 2b sites). In-plane and inter-plane ordering patterns are characterised by the reflections observed in the 3.4 < d < 4.5 Å range (Figure 1c) [15]. In-plane Ni(Mg)/Mn long-range ordering is characterised by the 010 and 012 reflections at 4.35 and 3.45 Å respectively, whereas intra-plane Ni(Mg)/Mn long-range ordering is characterised by the 011 reflection at 4.1 Å. These peaks have been indicated in Figure 1c with a (*) sign and are still present in the ND data, even at the largest magnesium content. The AA-type structure differs from the AB-type structure on the absence of the reflection at 4.1 Å [15].

The reflections at *d* = 3.15 and 3.25 Å are coincident to those observed by Meng et al. when describing the large zig-zag (LZZ)-sodium ordering in prismatic sites on P2-$Na_{2/3}Ni_{1/3}Mn_{2/3}O_2$] (Figure 1c). However, it was not possible to observe in these data the Bragg reflection at *ca.* 3.04 Å reported by Meng et al. [6]. These reflections broaden at the highest Mg content studied here, i.e. *x* = 0.20 (data shown in pink in Figure 1c). Instead, two extra peaks (marked with a (+) sign) were observed in this sample in the d spacing range studied. These peaks were also observed in the X-ray data (Figure S2(b)). These peaks were matched to a second phase (*ca.* 20 wt%) that could be refined as a $\sqrt{7}$ *a* x $\sqrt{7}$ *a*- type ordered superstructure with hexagonal space group *P*6_3/m (nº 176), isostructural to $K_4Co_7O_{14}$, and with lattice parameters *a* = 7.706(3) Å and *c* = 11.051(6) Å. This structural model was previously used by Imanishi et al. to describe a unique Na ordering in $Na_{0.58}CoO_2$ structure, with Na atoms in two inequivalent Na sites (2b and 6h) which induce a shift of the Co-atom trimers parallel to the c- axis [18].

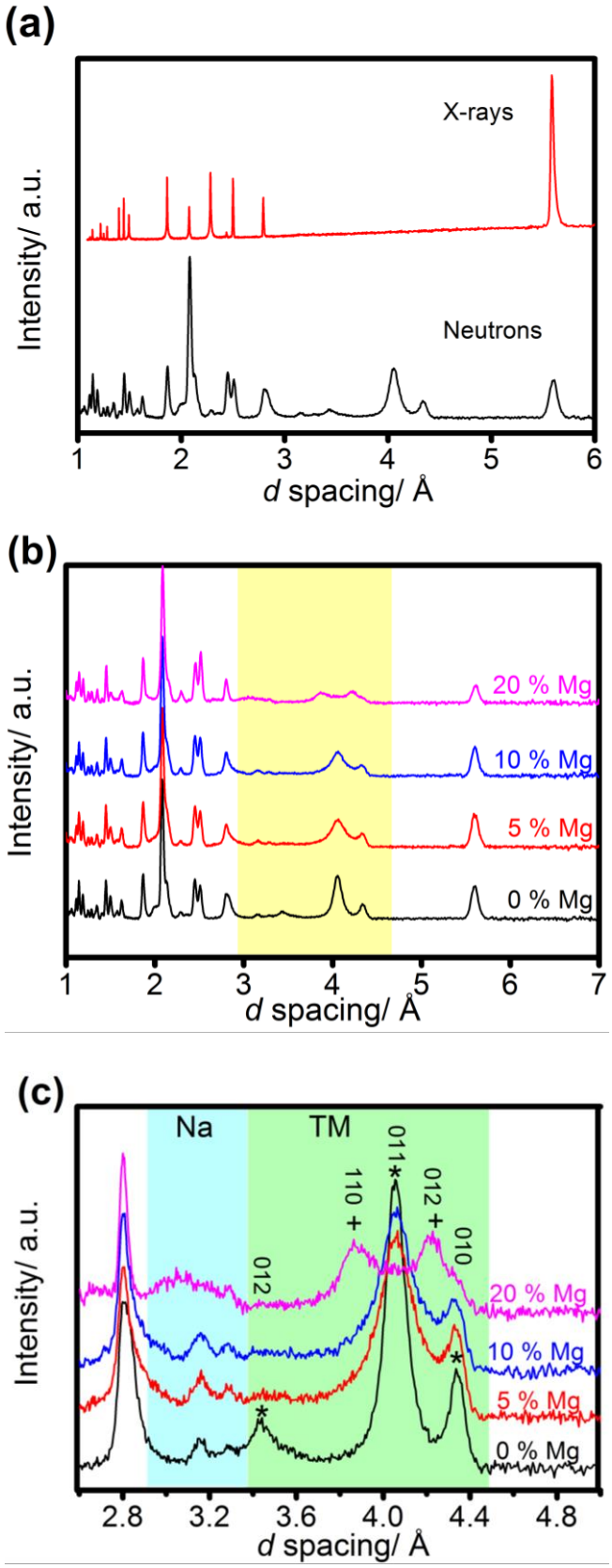

Figure 1. a) X-ray and neutron data comparison for $Na_{2/3}Ni_{1/3-x}Mg_xMn_{2/3}O_2$, where x = 0; b) Stacked plots showing neutron diffraction data for $Na_{2/3}Ni_{1/3-x}Mg_xMn_{2/3}O_2$, where $0 \leq x \leq 0.20$. Yellow-highlighted region represents the d spacing range where ordering features related to sodium and transition metal

atoms have been observed; and c) zoom of the yellow-highlighted region in Figure 2b. Blue-highlighted area shows evolution of peaks related to the zig-zag Na ordered distribution upon Mg concentration. Green-highlighted area shows peaks attributed to inter-plane and intra-plane transition metal ordering. (*) indicates *hkl* reflections indexed using $P6_3$ the space group (nº 173); and (+) indicates *hkl* reflections indexed using the $P6_3/m$ space group (nº 176).

Electrochemical performance in Na-half cells

Charge/discharge galvanostatic curves of the $Na_{2/3}Ni_{1/3-x}Mg_xMn_{2/3}O_2$ ($0 \leq x \leq 0.20$) samples in the voltage range 2-4.5 V are shown in Figure 2a. The experimental capacities obtained in the undoped material are comparable to those reported in the literature [5,6]. Contrary to our calculations where we consider exclusively the electrochemical oxidation of Ni^{2+} (found in the pristine materials using XANES (Figure S3)) to Ni^{4+}, we have observed experimental capacities larger than expected in the magnesium doped samples. Here, we have assumed that the Mn^{4+} observed by XANES in the pristine materials does not have any electrochemical activity, i.e. does not undergo Mn^{5+} as described in other reports [17]. This behaviour is notably more significant when x = 0.20, where an extra 38 mAh g^{-1} was achieved on the first charge. Similar electrochemical behaviour was reported by Yabuuchi et al. in P2-$Na_{0.67}Mg_{0.28}Mn_{0.72}O_2$ and their explanation for the abnormally high capacity (about 100 extra mAh g^{-1}) was attributed to oxygen participation [14]. The substitution of Ni^{2+} by Mg^{2+} ions favours the initial capacity retention on cycling [12,13], with a higher cycling efficiency when $x \geq 0.10$ (Figure 2b). The enhanced capacity retention in magnesium-doped samples compared to the undoped material has been explained with the switch from the detrimental O2 phase, observed in the undoped material at high voltages, to the intergrowth OP4 phase [13]. Furthermore, smoother charge and discharge curves were observed upon Mg^{2+} substitution (these being optimal when x = 0.2), indicating a predominant solid-solution reaction mechanism. This is clearly evidenced in the dq dV^{-1} curves shown in Figure 2c. Single phase reactions on cycling caused by Na^+ vacancy disorder have been related to high Na^+ conductivity and excellent high-rate electrochemical performance [7]. Structural changes upon cycling of these samples are analysed by *in operando* diffraction methods in the section below.

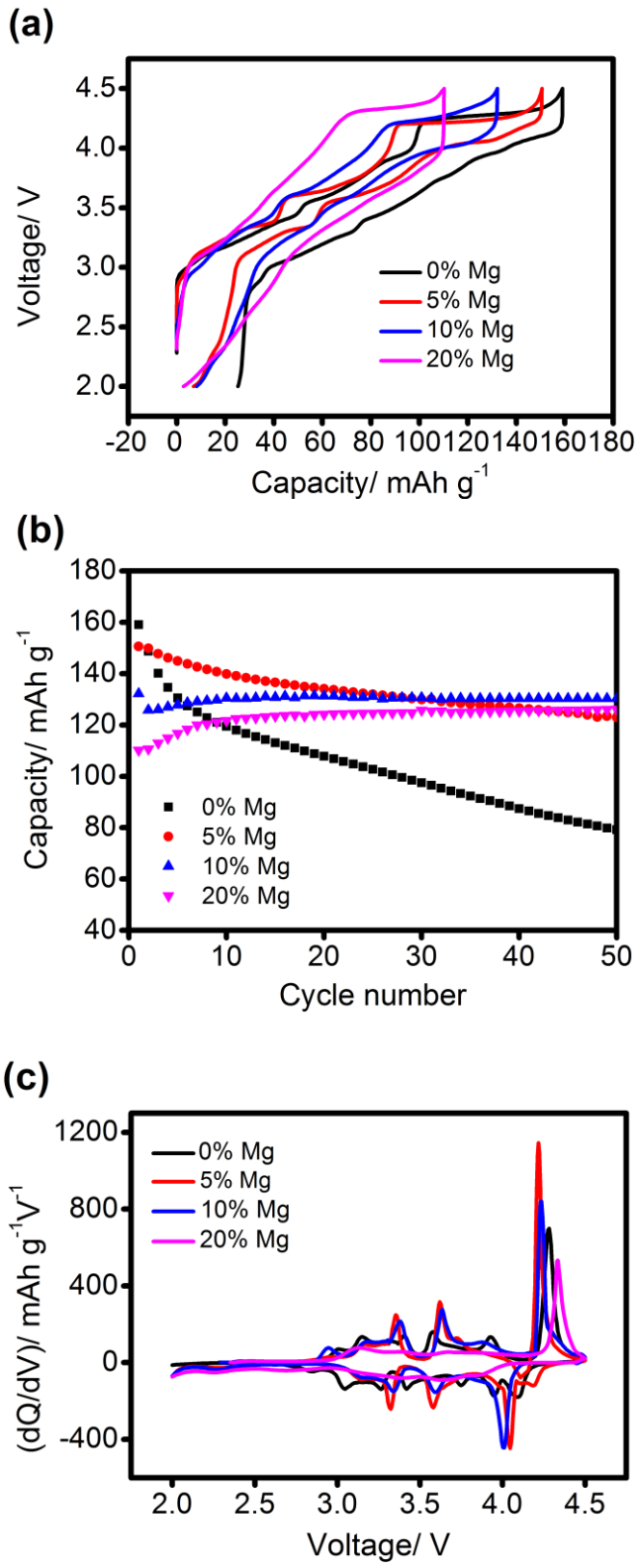

Figure 2. First charge and discharge curves for $Na_{2/3}Ni_{1/3-x}Mg_xMn_{2/3}O_2$, where $0 \leq x \leq 0.20$, in the voltage range 2-4.5 V at 10 mA g^{-1}; b) Cycling data (up to 50 cycles) for data shown in Figure 1; and c) Differential capacity curves for data shown in Figure 2a.

In operando X-ray diffraction studies

Structural evolution determined from the *in operando* synchrotron XRD experiments during sodium (de)intercalation in the P2-$Na_{2/3}Ni_{1/3-x}Mg_xMn_{2/3}O_2$ ($0 \leq x \leq 0.20$) series is shown in Figure 3 for the (002) and (100) reflections (space group $P6_3/mmc$). Rietveld analysis of the patterns collected before cycling (Tables S7-S9) were in good agreement with the powder-only structural models. In general, during charge (sodium removal) the 00*l* reflections shift to lower angles, an expansion of the *c* axis; while the *h*00 and *h*0*l* reflections shift to higher angles, a contraction in the *a* axis. The reverse trends were observed during discharge (sodium insertion), in agreement with those reported previously from *ex-situ* data for x = 0 [5,6].

Undoped evolution

Without Mg substitution (x = 0) the structure undergoes a series of two-phase reactions during overall expansion and contraction below 4.0 V, and above 4.2 V. As reported in earlier work, the phase transformation from P2 to O2 occurs above 4.2 V on charge and is associated with the 4.28 V plateau [5,7]. Increased repulsion between successive O layers (directly facing each other in the P2 structure (ABBA)) at low sodium content prompts the MO_2 sheets to glide in the a-b plane to transform into the O2 structure (ABCB), that energy calculations have shown to be the more stable phase after removing all Na ions [6]. Lu and Dahn first proposed that the voltage plateaux at 3.0 and 3.6 V correspond to specific Na ion ordering at x = 1/2 and 1/3 [5]. More recently Meng and co-workers [6] used first principle calculations to model the nature of the ordering and the structure of these intermediate phases. The high resolution *in operando* synchrotron XRD experiments described in this work provide experimental evidence for the intermediate phases, and demonstrate how these phases evolve with respect to time and potential. Sequential Rietveld refinements were carried out to determine the lattice parameters and weight fraction of the respective phases (Figure 4, and details of the fits are given in the SI). On charge at 50 mA g^{-1} two phases were clearly resolved prior to the P2-O2 phase transition. The new phase appears at 3.5 V, coinciding with the first voltage step, and the lattice parameters of this new phase evolve rapidly (*a* decreased while *c* increased) through to 3.8 V and the second voltage step, after which they stabilised at their minimum and maximum values, respectively. Discharge (sodium insertion) was performed specifically at a slower rate (10 mA g^{-1}) to give better resolution of the phase changes, and thus these are discussed in more detail.

Upon sodium insertion, the P2 and O2 phases coexist from the charged state to the end of the 4.0 V plateau. Three P2 phases were observed thereafter, corresponding to the 3.6, 3.0 and 2.3 V plateaux. The lattice parameters of the three P2 phases (at the maximum phase weight fraction) are compared to the x = 1/3, 1/2 and 2/3 sodium ordered structures reported by Meng and co-workers (*ex-situ* data) [6] in Figure 5. Although Figure 5 compares the dynamic/metastable structure (this work) with the relaxed/equilibrium structure [6], there is a good agreement between these data. Therefore, based on the comparisons of the structures and the approximate composition (derived from the electrochemistry) it can be concluded that the intermediate phases observed in our *in operando* work agree with the proposed compositions in the literature. This is the first time that experimental evidence for the Na ion

ordered structures are reported and discussed in $Na_{2/3}Ni_{1/3-x}Mn_{2/3}Mg_xO_2$, confirming the calculated structures reported previously [6].

Mg-doped evolution

From a visual inspection of the *in operando* synchrotron XRD pattern evolution (Figure 3) and the electrochemical profiles (Figure 2a) it is clear that Mg-doping has had a significant effect on the phase evolution.

Effect of doping above 4 V

Doping with 10 % Mg (x = 0.1) was sufficient to supress the P2 to O2 phase transition, in agreement with Wang *et al.* [19]. However, upon sodium removal above 4.3 V we observed a loss of reflection intensity and a broad reflection at 2θ = 7.35° (Figure S8), which is not discussed in ref. [19]. This phase transition we identify as the P2 to OP4 transition, where the OP4 phase shows alternate stacking of octahedral and trigonal prismatic sodium layers along the c axis, as has been previously identified in $Na_{2/3}Fe_{1-y}Mn_yO_2$ materials [20]. While substitution of 20 % Mg did not prevent the P2 reflections losing intensity in the charged state, the OP4 reflection was no longer observed in the first charged state (Figure 6). However, asymmetric broadening of the (002) reflection indicated the presence of stacking faults. DFT calculations presented below have shown that Mg substitution in $Na_{2/3}Ni_{1/3-x}Mn_{2/3}Mg_xO_2$ inhibits the P2 to O2 phase transformation.

Effect of doping below 4 V

Mg doping smoothed the charge/discharge profile below 4 V [19]. Comparison of the *in operando* XRD patterns revealed that at x = 0.1 this was caused by subtler P2 to $P2_{new}$ phase changes (both showing similar lattice parameters) (SI). These are more distinct at faster cycling rates, with clearer two-phase behaviour observed during charge at 100 mA g^{-1} than discharge at 8.5 mA g^{-1}. By increasing the Mg fraction to x = 0.2, however, the two-phase behaviour is replaced by continuous reflection evolution characteristic of a solid solution reaction. This correlates with the electrochemical observations of smoother charge/discharge curves and illustrates the “removal” of the ordered structures during charge/discharge. These more gradual structural changes upon Na (de)intercalation have also been observed in P2 $Na_{2/3}Mn_{1-y}Mg_yO_2$ [ref: DOI: 10.1039/c6ee01750a], where *ex situ* ^{23}Na solid state MAS NMR was used to demonstrate that Mg doping leads to more continuous changes in the Na resonances and to fewer, sharper peaks during the first cycle. The absence of ordered structures or the insertion/extraction reactions via disordered states, especially in terms of Na^+-vacancy disorder, have been related to high Na^+ conductivity and excellent high-rate performance [7]. Our work provides direct evidence for the variation in structural order as a function of Mg concentration with respect to electrochemical processes.

Effect of doping on volume change

As discussed above, Mg substitution gave rise to an overall increase in the unit cell volume. In turn, this results in reduced volume contraction/expansion on sodium extraction/insertion. At x = 0.1 and 0.2, the unit cell contraction of the P2 phase on first charge is over half that of the undoped material (% vol. contraction of 0.56 % and 0.52 %, respectively, compared to 1.30 % for x = 0). The subsequent % vol. expansion of the x = 0.2 material (0.11 %) is also considerably less than either the x = 0 (0.93 %) or x = 0.1 (0.58 %) doping levels. The trend in the volume change with Mg substitution agrees well with the electrochemical performance effect, where increased doping contents improve performance.

In operando synchrotron XRD data has conclusively revealed that during charge-discharge below 4 V the Na ion ordered intermediates are removed as the Mg concentration increases, which in turn leads to smoother charge/discharge profiles and better electrochemical performance. Additionally, the x = 0.1 Mg dopant suppresses the formation of the O2 phase, transitioning instead to the intermediate OP4 structure, while higher Mg concentrations of x = 0.2 appear to minimise the transition to the OP4. This correlates with the dramatic reduction in the volume change during charge/discharge as the Mg concentration is increased. All these structural factors point towards superior electrochemical performance of the Mg-doped samples.

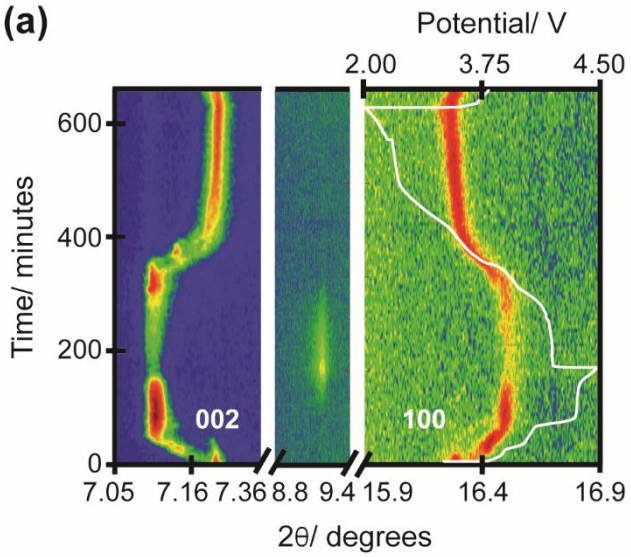

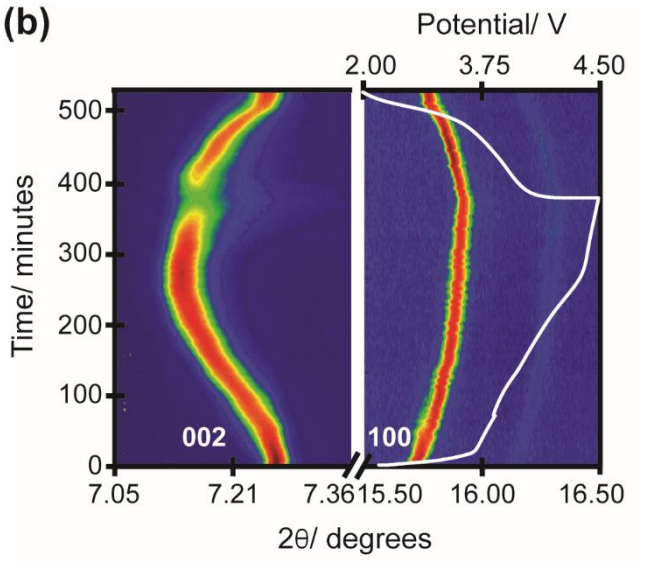

Figure 3. Selected 2θ regions of *in operando* synchrotron XRD data highlighting the evolution of the (002) and (100) reflections for $Na_{2/3}Ni_{1/3-x}Mg_xMn_{2/3}O_2$ where a) x = 0; and b) x = 0.2. The colour scale represents reflection intensity and the potential profiles are included.

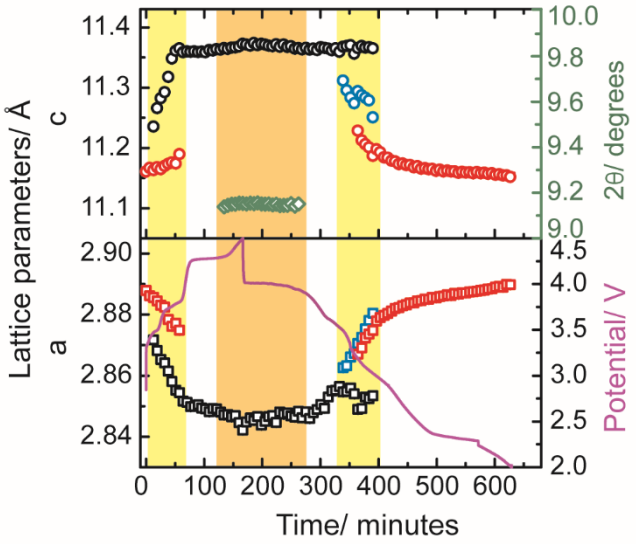

Figure 4. Changes in *a* and *c* lattice parameters of the $Na_{2/3}Ni_{1/3}Mn_{2/3}O_2$ electrode (x = 0) during charge-discharge, together with the electrochemical profile. The lattice parameters of the P2 ordered phases are shown in black (1/3 Na), blue (1/2 Na) and red (2/3 Na), and the 2θ position of the 002 reflection from the O2 phase is shown in green. Error bars are within the symbols. The two yellow shaded regions indicate the phase transitions between P2 sodium ordered structures and the orange shaded region indicates the P2 to O2 phase transition.

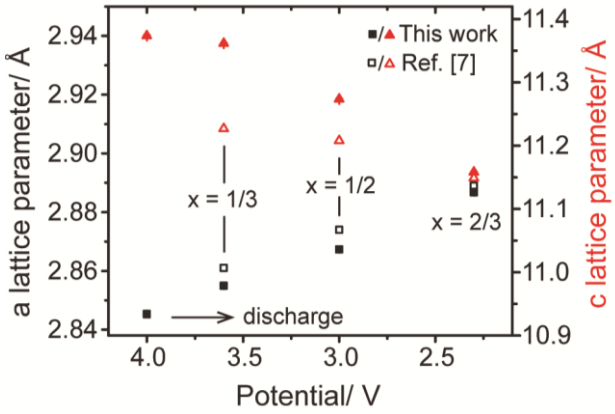

Figure 5. Comparison of the lattice parameters at the 4.0 V, 3.6 V, 3.0 V and 2.3 V plateaux on discharge collected *in operando* in this work (filled data) with the lattice parameters of the x = 1/3, 1/2 and 2/3 ordered structures (4.0 V, 3.5 V and before charging respectively) collected *ex-situ* during charge by Meng and co-workers (open data) [6]. Error bars are included within the symbols.

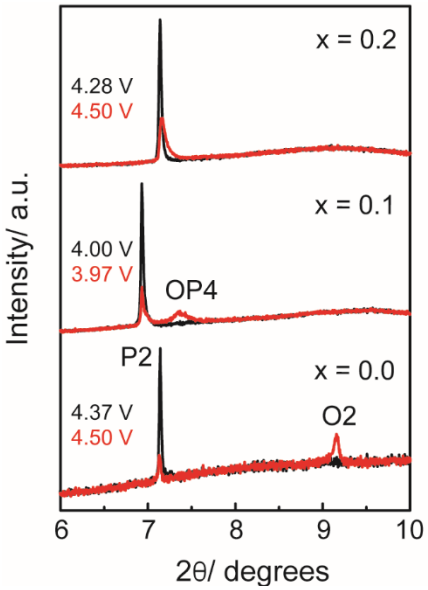

Figure 6. *In operando* XRD patterns for $Na_{2/3}Ni_{1/3-x}Mg_xMn_{2/3}O_2$, where $0 \leq x \leq 0.20$, prior to the charged state (black) and in the charged state (red) between 6° and 10° 2θ. The red XRD pattern shown for x = 0.1 is 10 minutes after the charged state (3.97 V) where the OP4 reflection is most intense.

Effects of Mg doping on Na^+ diffusion

Na-ion diffusion in P-type layered oxide compounds has been shown to be faster than in O-type compounds [21,22]. Strong in-plane Na-Na interactions makes Na-ion diffusion highly correlated [21]. It is therefore necessary to perform molecular dynamics simulations to probe such diffusion mechanisms and to complement the experimental measurements. The simulated Na diffusion in $Na_{0.56}Ni_{0.33}Mn_{0.67}O_2$ and $Na_{0.56}Mg_{0.11}Ni_{0.22}Mn_{0.67}O_2$ from ab initio molecular dynamics (AIMD) simulations are shown in Figure 7. In agreement with the galvanostatic intermittent titration technique

(GITT) and nuclear magnetic resonance (NMR) measurements on this family of compounds [13], our simulations suggest that the Mg doping causes an increase in Na-ion diffusivity. Na diffusion coefficients (D_{Na}) derived from classical MD also predict this increase of Na diffusion with Mg doping; values of 2.5 x 10^{-9} cm^2 s^{-1} and 1.2 x 10^{-8} cm^2 s^{-1} (at 300 K) are obtained for $Na_{0.56}Ni_{0.33}Mn_{0.67}O_2$ and $Na_{0.56}Mg_{0.11}Ni_{0.22}Mn_{0.67}O_2$ respectively. The enhancement in Na diffusion has been attributed to the enlargement of interlayer spacing upon Mg doping [23]. However, the estimated change in interlayer separation is very small (less than 0.05 Å).

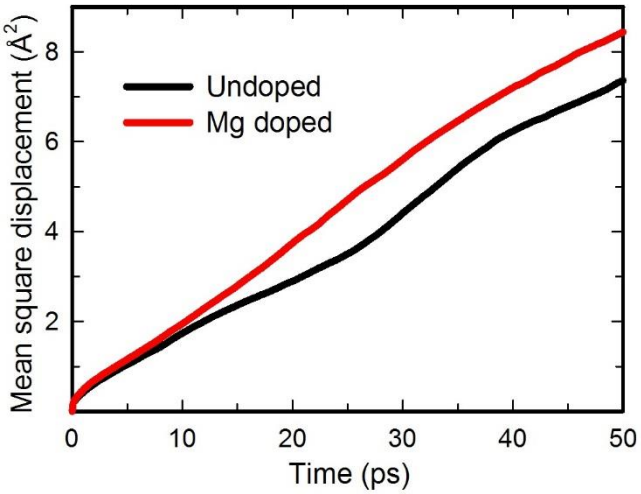

Figure 7. Mean square displacements of Na ions in $Na_{0.56}Ni_{0.33}Mn_{0.67}O_2$ and $Na_{0.56}Mg_{0.11}Ni_{0.22}Mn_{0.67}O_2$ during AIMD simulations.

Here possible effects of Mg doping on Na diffusion are discussed. Electrochemical data of $Na_{2/3}Ni_{1/3}Mn_{2/3}O_2$ have shown sodium ordering and phase separation (Figure 2a), which results in rich structural and electronic phase diagrams [24-27]. The electrochemically inactive Mg^{2+} (with fixed 2+ charge) and its random distribution over Ni sites can effectively suppress the development of long-range charge ordering within the MO_2 sheet and hence inhibit long-range sodium ordering (see x = 0.2 experimental case detailed above). As a result, charge and discharge would proceed through a more solid-solution like reaction with a higher Na diffusivity, as reflected in a more sloping charge-discharge profile (Figures 2a and 3c). Furthermore, our AIMD simulation on $Na_{0.56}Mg_{0.11}Ni_{0.22}Mn_{0.67}O_2$, shows that the Mg can displace along the z direction with a larger amplitude than both Ni and Mn, as shown in Figure 8. This can be attributed to the ionic nature of the Mg-O bond and hence less rigid MgO_6 octahedra. In contrast, the relatively higher degree of covalency in Ni-O and Mn-O bonds, owing to strong 3d-2p orbital hybridizations [28,29], makes the NiO_6 and MnO_6 octahedra more rigid. The large displacement of Mg^{2+} in the z direction consequently alters the electrostatic potential felt by Na^+ ions and has a positive effect on Na diffusion. An interesting comparison includes a previous NMR study indicating that Li^+ ions (which have a very similar ionic radius to Mg^{2+}) were displaced from transition metal layers to the Na layers in the P2-$Na_x[Li_yNi_zMn_{1-y-z}]O_2$ material [30].

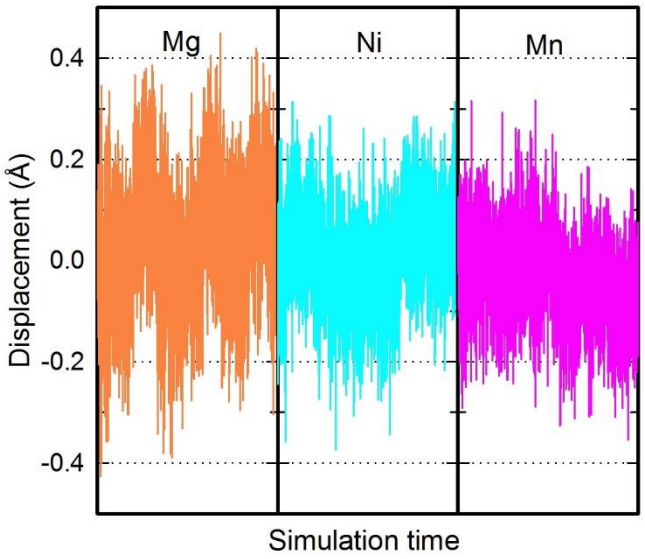

Figure 8. The displacement of Mg, Ni and Mn along the z-direction in $Na_{0.56}Mg_{0.11}Ni_{0.22}Mn_{0.67}O_2$ during the 50 ps AIMD simulation.

Effects of Mg doping on the phase transition

Without Mg doping, all Na^+ ions can theoretically be extracted from the structure of $Na_{2/3}Ni_{1/3}Mn_{2/3}O_2$ at the end of the charge, accompanied by the oxidation of Ni^{2+} to Ni^{4+}. Empty Na layers then enables the gliding of MO_2 sheets and results in the transformation from P2 to O2 structures [5,6,30]. In $Na_{2/3}Ni_{1/3-x}Mg_xMn_{2/3}O_2$ compounds, two Na^+ ions must stay in the vicinity of an Mg^{2+} dopant at high voltages (*ca.* 4.2 V), in order to keep the local charge neutrality. This prevents the formation of consecutive empty Na layers and hence the transformation to O2 structure is inhibited. Figure 9 shows two possible local structures around the Mg^{2+} dopant during the P2-OP4 phase transformation. The first situation, (a), is where both Na^+ ions are located on the same side of the MO_2 sheet and so one Na layer is completely empty. The empty layer then enables gliding of MO_2 sheets resulting in O type stacking. The second situation, (b), is where the two Na^+ ions are located on each side of the MO_2 sheet. Our DFT calculations indicate that the first configuration is more energetically stable, which is consistent with the experimentally observed P2 to OP4 transition in the Mg doped samples, especially for x = 0.1.

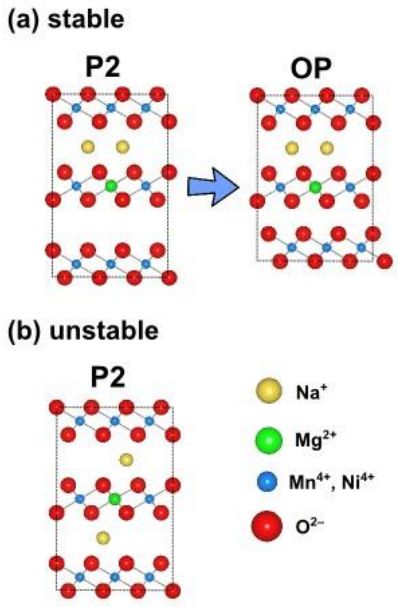

Figure 9. Two possible local structures around the Mg^{2+} ion at 4.2 V. (a) The low energy configuration, where two Na ions are located at the same side of the MO_2 sheet and the empty Na layer allows the transformation from P stacking to O stacking. (b) The high energy configuration, where two Na ions are located on each side of the MO_2 sheet.

CONCLUSIONS

In this work we have demonstrated the effects of Mg doping on the structure of a series of P2-$Na_{2/3}Ni_{1/3-x}Mg_xMn_{2/3}O_2$ compounds. Combined XRD and neutron analysis shows that magnesium substitutes nickel in the Ni-Mn honeycomb structure. Furthermore, our data shows that when doping with Mg, the P2-$Na_{2/3}Ni_{1/3}Mn_{2/3}$-type structure still remains of an AB-type, as in the undoped material. Hence there is no structural re-arrangement in the c-axis when doping with Mg. Finally, we have shown that high levels of Mg dopant in the structure (*i.e.* x = 0.2) lead to an overall more disordered distribution of sodium in the pristine material. Electrochemical data corroborate our structural data by showing a solid-solution profile. Importantly, this is the highest level of Mg dopant substituted in the P2-$Na_{2/3}Ni_{1/3-x}Mn_{2/3}O_2$ compound reported to this date. The high resolution *in operando* synchrotron XRD experiments provide evidence for the x = 1/2 and x = 1/3 intermediate Na^+-vacancy ordered phases in P2-$Na_{2/3}Ni_{1/3}Mn_{2/3}O_2$, and demonstrate how these phases evolve with respect to time and potential. Furthermore, we have shown that Mg doping effectively disrupts the Na^+-vacancy ordering leading to more gradual structural changes, and suppresses the P2-O2 transition at high voltages, switching it to an OP4 phase. Ab initio molecular dynamics studies have indicated that Na-ion diffusivity increases on Mg doping, and that the OP4 phase is the most thermodynamically stable at high voltages for the Mg-doped compounds.

The results of this work have shed new light on major dopant effects in the P2-$Na_{2/3}Ni_{1/3}Mn_{2/3}O_2$ system.

Understanding the structural and electrochemical changes occurring in cathode materials when a dopant is added to the system is of paramount importance in the design of novel materials with enhanced electrochemical performance.

EXPERIMENTAL

Synthesis

Samples were synthesised by ball milling a mixture of Na_2CO_3 anhydrous (Fisher Chemicals), NiO (Sigma Aldrich, nanopowder, < 50 nm particle size), MnO_2 (Sigma Aldrich, -325 mesh, 99%) and MgO (Sigma Aldrich, -325 mesh, $\geq$ 99% trace metal basis) in acetone in stoichiometric ratios in a Planetary Ball Mill PM 100 (Retsch) for 1 h at 450 rpm using a 2:1 ball-to-powder-ratio. The mixture was left to dry in air and the powders were pressed as pellets under a load of 4 tons cm^{-2} before calcining at 800-850 °C for 12 h in air followed by slow cooling in the furnace. Samples were kept in an Ar filled glove box maintained at < 0.1 ppm H_2O and O_2.

Characterisation

Powder X-ray diffraction (PXRD) patterns were recorded on a 9 KW Rigaku Smartlab diffractometer using Cu $K\alpha_1$ radiation (λ = 1.54051 Å). A customized air-tight sample holder covered with Kapton film was used to avoid severe air/moisture contact during measurement.

Chemical analyses were performed by Inductively Coupled Plasma (ICP) using a Perkin Elmer Elan 6100 DRC ICP-MS.

Time-of-flight powder neutron diffraction data were collected on the GEM high-intensity, medium-resolution instrument at ISIS, Rutherford Appleton Laboratories. Neutron scattering lengths of 0.363, 1.03, 0.566, -0.373 and 0.5803 (all × 10^{-12} cm) were assigned to Na, Ni, Mg, Mn, and O, respectively [31].

Electrodes were prepared by mixing the active material with Super S carbon and a 5 wt% solution of PVDF (Polyvinylidene fluoride) in NMP (N-Methyl-2-pyrrolidone) in a 75:15:10 weight ratio. Slurries of the mixtures were prepared by adding *ca.* 1 ml of NMP to the mixture under constant stirring for 3-4 h. The slurry was cast onto Al foil that acts as current collector in an argon-filled glovebox. Loading of active material for the galvanostatic cycling is 2-3 mg cm^{-2}. The coated foil was dried under vacuum at 80 ° C for 2 h and electrodes of 20 mm were punched out and pressed under a load of 4 tons cm^{-2}.

Galvanostatic charging/discharging tests were performed in CR2325 coin cells using 1 M $NaPF_6$ (99.99% Sigma Aldrich) in PC (propylene carbonate) as the electrolyte solution and sodium metal as the counter electrode. Coin cells were charged/discharged at 10 mA g^{-1} in the 2-4.5 V range.

In operando X-ray diffraction

Customised half cells with 3 mm diameter holes in the casing and 5 mm diameter holes in the stainless spacer were used for the construction of the coin cells for the *in operando* measurements. The coin

cells contained the electrodes described above, Na metal (~ 1 mm thickness), a glass fibre separator and 1 M $NaPF_6$ in PC (propylene carbonate) electrolyte solution. *In operando* synchrotron XRD experiments were performed within 1-2 days after cell construction. Data were collected on the Powder Diffraction beamline [32] at the Australian Synchrotron with a wavelength (λ) of 0.70772(2) Å for 0% and 10% and 0.70793(2) Å for 20%, where the wavelength is determined by refining a structural model with data collected on a NIST 660b LaB_6 standard reference material. XRD data were collected continuously in transmission geometry every 4.4(1) minutes for the 10% and 20% samples and 6.4 minutes for the 0% sample. In conjunction, the *in operando* cells were first charged to 4.5 V at relatively fast rates between 30-100 mA g^{-1} and then subsequently discharged to 2 V and charged to 4.5 V at lower rates between 10-30 mA g^{-1}. The electrode loading varied from 1-4 mg cm^{-2} and the current rates were adjusted to accommodate this variation. PXRD and ND data were refined by the Rietveld method using the GSAS software suite with the EXPGUI software interface [33].

COMPUTATIONAL METHODS

Density functional theory (DFT) calculations were performed using the Vienna *ab initio* simulation package (VASP) [34]. Valence electrons were described by a planewave basis set with a cut-off energy of 450 eV. The interactions between valence and core electrons were treated using the projector augmented-wave (PAW) method [35]. The k-space was sampled with k-point mesh spacing smaller than 0.05 $Å^{-1}$. Spin-polarization was enabled and ferromagnetic coupling between magnetic manganese cations was assumed. Structural optimization was performed until the residue force on each atom is smaller than 0.03 eV/Å. Similar DFT methods have been applied successfully to a range of battery materials [36-39].

Ab initio molecular dynamics (AIMD) simulations were carried out to study Na^+ ion diffusion in $Na_{0.56}Ni_{0.33}Mn_{0.67}O_2$ and $Na_{0.56}Mg_{0.11}Ni_{0.22}Mn_{0.67}O_2$ with a supercell containing 54 formula units, 192 atoms. Each composition was first equilibrated for 10 picoseconds. Statistical properties were then obtained by the following 50 picoseconds simulations using the NVT ensemble with a Nosé-Hoover thermostat [40, 41]. All molecular dynamics simulations were performed at 500 K with a time step of 2 femtoseconds. Gamma-point only was used in the k-space sampling in order to keep the computational cost affordable.

REFERENCES

1. Palomares, V.; Serras, P.; Villaluenga, I.; Hueso, K. B.; Carretero-González, J.; Rojo, T. Na-ion batteries, recent advances and present challenges to become low cost energy storage systems. *Energy Environ. Sci.* **2012**, 5, 5884–5901.

2. Kundu, D.; Talaie, E.; Duffort, V.; Nazar, L. F. The emerging chemistry of sodium ion batteries for electrochemical energy storage. *Angew. Chem. Int. Ed.* **2015**, 54, 2–20.

3. Delmas, C.; Fouassier, C.; Hagenmuller, P. Structural classification and properties of the layered oxides. *Phys. B+C* **1980**, 99, 81–85.

4. Lu, Z.; Dahn, J. R. Can all the lithium be removed from T2-$Li_{2/3}[Ni_{1/3}Mn_{2/3}]O_2$? *J. Electrochem. Soc.* **2001**, 148, A710–A715.

5. Lu, Z.; Dahn, J. R. In-situ X-ray diffraction study of P2-$Na_{2/3}[Ni_{1/3}Mn_{2/3}]O_2$. *J. Electrochem. Soc.* **2001**, 148, A1225–A1229.

6. Lee, D. H.; Xu, J.; Meng, Y. S. An advanced cathode for Na-ion batteries with high rate and excellent structural stability. *Phys. Chem. Chem. Phys.* **2013**, 15, 3304–3312.

7. Wang, Y.; Xiao, R.; Hu, Y.-S.; Avdeev, M.; Chen, L. P2-$Na_{0.6}[Cr_{0.6}Ti_{0.4}]O_2$ cation-disordered electrode for high-rate symmetric rechargeable sodium-ion batteries. *Nature Comm.* **2015**, 6, 1–9.

8. Wu, X.; Xu, G.-L.; Zhong, G.; Gong, Z.; McDonald, J.; Zheng, S.; Fu, R.; Chen, Z.; Amine, K.; Yang, Y. Insights into the effects of zinc doping on structural phase transition of P2-type sodium nickel manganese oxide cathodes for high-energy sodium ion batteries. *ACS Appl. Mater. Interfaces* **2016**, 8, 22227–22237.

9. Yoshida, H.; Yabuuchi, N.; Kubota, K.; Ikeuchi, I.; Garsuch, A.; Schulz-Dobrickb, M.; Komaba, S. P2-type $Na_{2/3}Ni_{1/3}Mn_{2/3-x}Ti_xO_2$ as a new positive electrode for higher energy Na-ion batteries. *Chem. Comm*. **2014**, 50, 3677–3680.

10. Wu, X.; Guo, J.; Wang, D.; Zhong, G.; McDonald, M. J.; Yang, Y. P2-type $Na_{0.66}Ni_{0.33-x}Zn_xMn_{0.67}O_2$ as new high-voltage cathode materials for sodium-ion batteries. *J. Power Sources* **2015**, 281, 18–26.

11. Kim, D.; Kang, S.-H.; Slater, M.; Rood, S.; Vaughey, J. T.; Karan, N.; Balasubramanian, M.; Johnson, C. S. Enabling sodium batteries using lithium-substituted sodium layered transition metal oxide cathodes. *Adv. Energy Mater.* **2011**, 1, 333–336.

12. Zhao, W.; Kirie, H.; Tanaka, A.; Unnoa, M.; Yamamoto, S.; Noguchi, H. Synthesis of metal ion substituted P2-$Na_{2/3}Ni_{1/3}Mn_{2/3}O_2$ cathode material with enhanced performance for Na ion batteries. *Mater. Lett.* **2014**, 135, 131–134.

13. Singh, G.; Tapia-Ruiz, N.; Lopez del Amo, J. M.; Maitra, U.; Somerville, J. W.; Armstrong, A. R.; Martinez de Ilarduya, J.; Rojo, T.; Bruce, P. G. High Voltage Mg-Doped $Na_{0.67}Ni_{0.3-x}Mg_xMn_{0.7}O_2$ (x = 0.05, 0.1) Na-Ion Cathodes with Enhanced Stability and Rate Capability. *Chem. Mater.* **2016**, 28, 5087–5094.

14. Yabuuchi, N.; Hara, R.; Kubota, K.; Paulsen, J.; Kumakura, S.; Komaba, S. New electrode material for rechargeable sodium batteries: P2-type $Na_{2/3}[Mg_{0.28}Mn_{0.72}]O_2$ with anomalously high reversible capacity. *J. Mater. Chem. A* **2014**, 2, 16851–16855.

15. Yabuuchi, N.; Hara, R.; Kajiyama, M.; Kubota, K.; Ishigaki, T.; Hoshikawa, A.; Komaba, S. New O2/P2-type Li-excess layered manganese oxides as promising multi-functional electrode materials for rechargeable Li/Na batteries. *Adv. Energy Mater.* **2014**, 1301453.

16. Paulsen, J M.; Donaberger, R. A.; Dahn, J. Layered T2-, O6-, O2-, and P2-type $A_{2/3}[M'^{2+}_{1/3}M^{4+}_{2/3}]O_2$ bronzes, A = Li, Na; M´= Ni, Mg; M= Mn, Ti, *Chem. Mater.* **2000**, 12, 2257-2267

17. Freire, M.; Kosova, N. V.; Jordy, C.; Chateigner, D.; Lebedev, O. I.; Maignan, A.; Pralong V. A new active Li–Mn–O compound for high energy density Li-ion batteries, *Nature Mater.* **2016**, 15, 173.

18. Igarashi, D.; Miyazaki, Y. Kajitani, T. Disorder-order transitions in Na_xCoO_2 (x ~0.58), Phys. Rev. B **2008**, 78, 184112.

19. Wang, P.-F.; You, Y.; Yin, Y.-X.; Wang, Y.-S.; Wan, L.-J.; Gu, L.; Guo, Y.-G. Suppressing the P2-O2 phase transition of $Na_{0.67}Mn_{0.67}Ni_{0.33}O_2$ by magnesium substitution for improved sodium-ion batteries. *Angew. Chem. Int. Ed.* **2016**, 55, 7445–7449.

20. Yabuuchi, N.; Kajiyama, M.; Iwatate, J.; Nishikawa, H.; Hitomi, S.; Okuyama, R.; Usui, R.; Yamada, Y.; Komaba, S. P2-type Na(x)[Fe(1/2)Mn(1/2)]O2 made from earth abundant elements for rechargeable Na batteries. *Nat. Mater.* **2012**, 11, 512–517.

21. Mo, Y.; Ong, S. P.; Ceder, G. Insights into Diffusion Mechanisms in P2 Layered Oxide Materials by First-Principles Calculations. *Chem. Mater.* **2014**, 26, 5208–5214.

22. Katcho, N. A.; Carrasco, J.; Saurel, D.; Gonzalo, E.; Han, M.; Aguesse, F.; Rojo, T. Origins of Bistability and Na Ion Mobility Difference in P2- and O3-$Na_{2/3}Fe_{2/3}Mn_{1/3}O_2$ Cathode Polymorphs. *Adv. Energy Mater.* **2016**, 7, 1601477.

23. Li, Z-Y.; Gao, R.; Zhang, J.; Zhang, X.; Hu, Z.; Liu, X. New insights into designing high-rate performance cathode materials for sodium ion batteries by enlarging the slab-spacing of the Na-ion diffusion layer. *J. Mater. Chem. A* **2016**, 4, 3453–3461.

24. Roger, M.; Morris, D. J. P.; Tennant, D. A.; Gutmann, M. J.; Goff, J. P.; Hoffman, J. -U.; Feyerherm, R.; Dudzik, E.; Prabhakaran, D.; Boothroyd, A. T.; Shannon, N.; Lake, B.; Deen, P. P. Patterning of sodium ions and the control of electrons in sodium cobaltate. *Nature* **2006**, 445, 631–634.

25. Julien, M.-H.; de Vaulx, C.; Mayaffre, H.; Berthier, C.; Horvatić, M.; Simonet, V.; Wooldridge, J.; Balakrishnan, G.; Lees, M. R.; Chen, D. P.; Lin, C. T.; Lejay, P. Electronic Texture of the Thermoelectric Oxide $Na_{0.75}CoO_2$. *Phys. Rev. Lett.* **2008**, 100, 096405.

26. Lang, G.; Bobroff, J.; Alloul, H.; Collin, G.; Blanchard, N. Spin correlations and cobalt charge states: Phase diagram of sodium cobaltates. *Phys. Rev. B* **2008**, 78, 155116.

27. Ning, F. L.; Golin, S. M.; Ahilan, K.; Imai, T.; Shu, G. T.; Chou, F. C. ^{59}Co NMR Evidence for Charge Ordering below TCO ~ 51 K in $Na_{0.5}CoO_2$. *Phys. Rev. Lett.* **2008**, 100, 086405.

28. de Groot, F. M. F.; Grioni, M.; Fuggle, J. C.; Ghijsen, J.; Sawatzky, G. A.; Petersen, P. Oxygen 1s x-ray-absorption edges of transition-metal oxides. *Phys. Rev. B* **1989**, 40, 5715.

29. Cox, P. A. Transition Metal Oxides: An Introduction to Their Electronic and Properties. *Oxford University Press* **1992**.

30. Xu, J.; Lee, D. H.; Clément, R. J.; Yu, X.; Leskes, M.; Pell, A. J.; Pintacuda, G.; Yang, X.-Q.; Grey, C. P.; Meng, Y. S. Identifying the Critical Role of Li Substitution in P2–$Na_x[Li_yNi_zMn_{1-y-z}]O_2$ (0 < x, y, z < 1) Intercalation Cathode Materials for High-Energy Na-Ion Batteries. *Chem. Mater.* **2014**, 26, 1260–1269.

31. Sears, V. F. Neutron scattering lengths and cross sections, *Neutron News*, **1992**, 3, 26.

32. Wallwork, K. S.; Kennedy, B. J.; Wang, D. The high resolution powder diffraction beamline for the Australian Synchrotron. *AIP Conf. Proc.* **2006**, 879.

33. Larson A. C.; Von Dreele, R. B. in Los Alamos National Laboratory Report LAUR 86-748, **1994**; Toby, B. H. J. *Appl. Cryst.* **2001**, 34, 210–213.

34. Kresse, G.; Furthmüller, J. Efficient iterative schemes for *ab initio* total-energy calculations using a plane-wave basis set. *Phys. Rev. B* **1996**, 54, 11169–11186.

35. Blöchl, P. E. Projector augmented-wave method. *Phys. Rev. B* **1994**, 50, 17953–17979.

36. Islam M. S. and Fisher C. A. J., Lithium and sodium battery cathode materials: computational insights into voltage, diffusion and nanostructural properties, *Chem. Soc. Rev.* **2014,** 43, 185-204.

37. Armstrong A. R., Lyness C., Panchmatia P., Islam M. S. and Bruce P. G., The lithium intercalation process in the low voltage lithium battery anode $Li_{1+x}V_{1-x}O2$, *Nature. Mater*. **2011,** 10, 223.

38. Eames C. and Islam M. S., Ion Intercalation into Two-Dimensional Transition-Metal Carbides: Global Screening for New High-Capacity Battery Materials, *J. Am. Chem. Soc.* **2014**, 136, 16270.

39. S. P. Ong, V. L. Chevrier, G. Hautier, A. Jain, C. Moore, S. Kim, X. Ma and G. Ceder, *Energy Environ. Sci.* **2011**, 4, 3680.

40. Nosé, S. A unified formulation of the constant temperature molecular dynamics methods. *J. Chem. Phys.* **1984**, 81, 511–519.

41. Hoover, W. G. Canonical dynamics: equilibrium phase-space distribution. *Phys. Rev. A* **1985**, 31, 1695–1697.

"Master gave Dobby a sock...

Dobby is free"

J. K. Rowling,

Harry Potter and the Chamber of Secrets